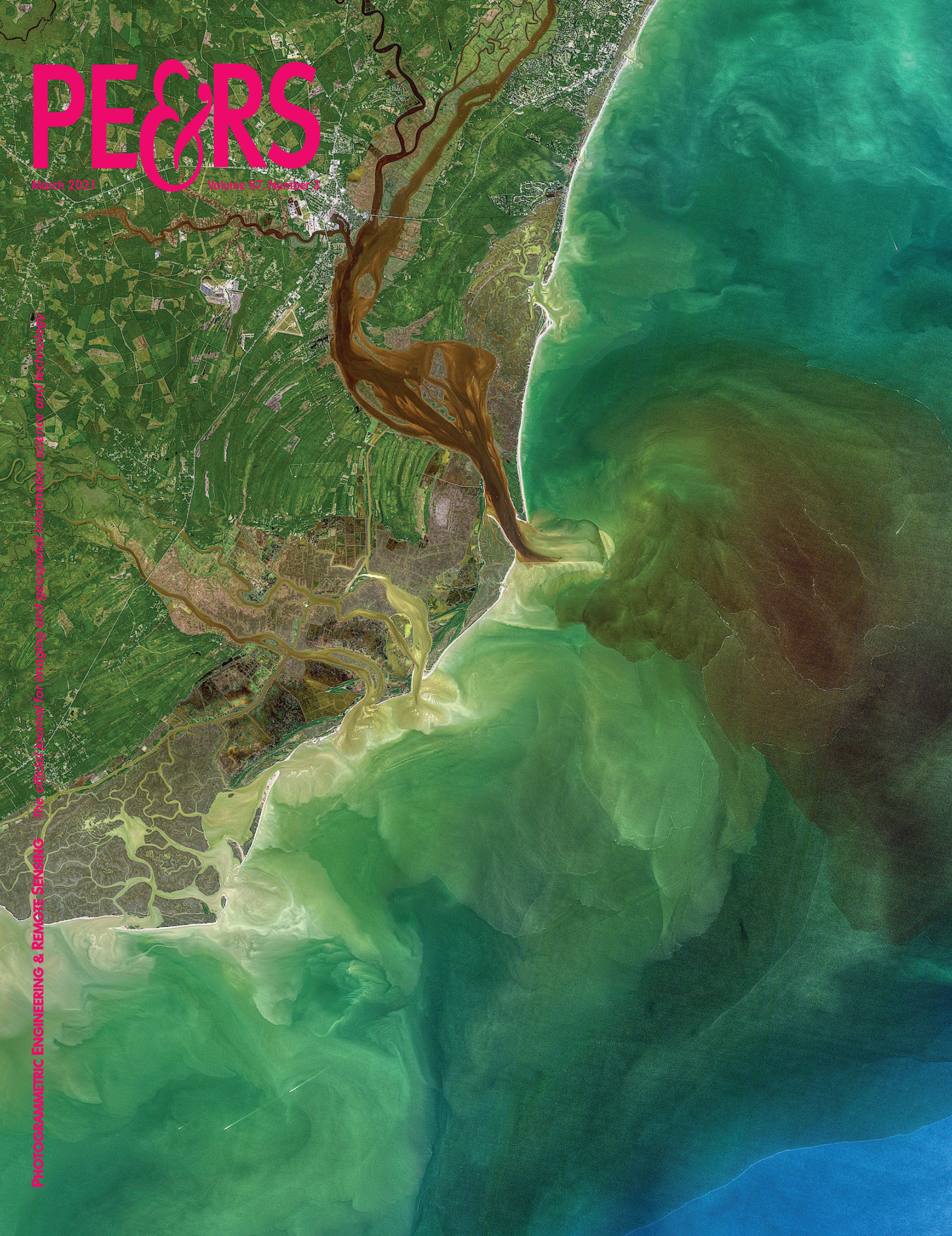


# PE&RS

March 2021

Volume 57, Number 3

PHOTOGRAMMETRIC ENGINEERING & REMOTE SENSING The official journal for imaging and geospatial information science and technology





**asprs** THE IMAGING & GEOSPATIAL  
INFORMATION SOCIETY

# ASPRS 2021

## *Annual Conference*

March 29- April 2, 2021

### **SAVE THE DATE!**

Due to the ongoing COVID pandemic, ASPRS is going to be conducting its 2021 Annual Conference virtually. The conference program will consist of:

- » a multi-day series of technical sessions, including oral presentations, Ignite-Style talks, and invited panel discussions
- » 2-hour and 4-hour workshops conducted as live, instructor-led webinars
- » vendor spotlights and product demos\*
- » the ASPRS Annual Business Meeting, which includes the Installation of Officers and Directors, Presidential Address, and presentation of 2021 Awards and Scholarships.
- » annual Division, Council, and Committee meetings
- » The entire conference program will be recorded and made available on-demand for all registrants on the ASPRS online learning platform.

**<http://conferences.asprs.org/asprs-2021/>**

## ANNOUNCEMENTS

AEC Next Technology Expo & Conference, **International Lidar Mapping Forum**, and **SPAR 3D Expo & Conference** are coming together to form **Geo Week 2022** and will take place February 6-8, 2022 in Denver, Colorado. The joining of these events reflects the increased integration between the built environment, advanced airborne/terrestrial technologies, and commercial 3D technologies. Geo Week is at the forefront of this integration, providing education, technology, and resources for professionals in industries including AEC, Asset & Facility Management, Disaster & Emergency Response, Earth Observation & Satellite Applications, Energy & Utilities, Infrastructure & Transportation, Land & Natural Resource Management, Mining & Aggregates, Surveying & Mapping, and Urban Planning/Smart Cities.

“We’ve witnessed the growing convergence between geospatial and the built world, and we received positive feedback from customers about holding the events together, which had been the plan for 2020 and 2021 before the pandemic forced us to cancel due to the unavoidable consequence of the worsening magnitude of the public health and safety issues caused by the COVID-19,” said Lee Corkhill, Marketing Director at Diversified Communications. “We believe the market is ready and eager for this next step of leveraging the confluence of what are becoming ubiquitous technologies for improved collaboration, increased efficiency, and better outcomes. Much of the conference content and technology being showcased will reflect and support this increasing integration.” An Advisory Board of industry leaders will guide conference programming and event development.

In addition to Diversified Communications’ technology events coming together, powerful partnership events will also take place at Geo Week, including the ASPRS (American Society for Photogrammetry and Remote Sensing) Annual Conference and USIBD’s (U.S. Institute of Building Documentation) Annual Symposium. ASPRS, USIBD and other events have supported and taken place with ILMF, AEC Next and SPAR 3D when the latter events took place separately. Bringing all these brands together as a new powerhouse event under the Geo Week umbrella is a fitting evolution that recognizes the increasing convergence of the technologies.

**Karen Schuckman, PLS, CP, CMS and Managing Director of ASPRS**, said, “Bringing ASPRS and ILMF together beginning in 2018 reunited the photogrammetry, remote sensing, and lidar professionals and vendors who enthusiastically welcomed the opportunity to attend one consolidated event; an event where they could roam one large exhibit hall and attend educational workshops to broaden their expertise into related disciplines. Bringing the built world into this mix through AEC Next and SPAR 3D acknowledges not only the richness and complexity of the technologies we have available for spatial analysis and decision making, it also give us all the opportunity to explore and invent new analysis methods that leverage the

fusion of imagery, elevation, and bathymetry with 3D models of the built world. The merging of these disciplines IS the future. Co-locating our annual conferences and expositions facilitates us traveling into the future on a multi-lane superhighway.”

“The coming together of professionals from the geospatial and built environment communities is long overdue,” said John Russo, AIA, President of USIBD. “Finally, one event, one place where we can all gather to network and gain insight into the convergence of our worlds. The USIBD is excited to participate in GeoWeek and share its expertise in reality capture, BIM, digital twin and more!”

Geo Week counts a broad range of industry organizations, publications, and portals as supporters during this unprecedented period of transformation and disruption driving the rapid expansion of the internet of things, the development of smart cities, and a data revolution altering how people live and work. At the center of this revolution are geospatial, 3D, and location-based technologies. Geo Week is the only platform-neutral event in North America that brings together industry leaders to harness these technologies and explore the myriad applications they empower.

According to Corkhill, there will also be content that addresses the built environment, advanced airborne/terrestrial technologies, and commercial 3D technologies independently of one another.

“The event represents a continuum, with individuals and organizations from all corners of industry at differing levels of adoption. Geo Week will support a future vision, in which professionals and organizations that understand the full spectrum of data needs, work processes, software integration, and standards in both geospatial and BIM will be tomorrow’s technology leaders.”

The event will feature multiple tracks with content clearly identified as relevant to one or more of the audience groups feeding into Geo Week. The International Lidar Mapping Forum (ILMF) audience has historically been comprised of precision measurement professionals in surveying and mapping who use airborne and terrestrial lidar and related remote sensing technologies. The AEC Next audience has historically been comprised of professionals in architecture, engineering, and construction (AEC) that use technologies such as reality capture, automation, AI and XR to bid and manage projects and improve workflows. The SPAR 3D audience has historically been comprised of professionals who use 3D capture, scanning, visualization and modeling technologies across a variety of verticals. “We will use these familiar brands to designate content and make it easy and accessible for all stakeholders to find the solutions, connections, and education they need, no matter which vertical or industry segment they originated from.” says Corkhill. To this end, the organizers will also continue to publish Geo Week ENewsletter, SPAR3D ENewsletter, and AEC ENewsletter.

URISA is pleased to announce the Exemplary Systems in Government (ESIG) Awards process for 2021. This year marks the milestone 40th Anniversary of URISA ESIG Awards, which recognize extraordinary achievements in the use of geospatial information technology that have improved the delivery and quality of government services.

The award competition is open to all public agencies at the national/federal, state/provincial, regional, and local levels. Winners will be recognized during the Awards Luncheon on October 5 during GIS-Pro 2021 in Baltimore, Maryland. Submissions are invited in two categories Single Process Systems and Enterprise Systems.

Submissions are due on or before Monday, June 7, 2021. A detailed application requiring details about the Jurisdiction/Organization, System Design, Implementation, Organizational Impact, and System Resources is available <https://www.urisa.org/awards/exemplary-systems-in-government-awards/>.

## ACCOMPLISHMENTS

**Woolpert's** Mark Mockus has been promoted to market director. He will lead the firm's private market, directing architecture and engineering projects for private sector clients. Mockus has more than 34 years of architecture and management experience, specializing in high-intensity, innovative and complex design.

Mockus has been with Woolpert since late 2019, serving as a program director out of the firm's Chicago office. He has been integral to the firm's pursuit of retail rollout projects, like Best Buy and 7-Eleven. Mockus said his goals in this new role are to continue to expand the firm's design clientele, to draw bigger and more impactful architecture projects, and to increase and amplify Woolpert's top talent.

"We have leading designers and architects accomplishing great things already, including Tim Reber, Jason Golub, Jon Grzywa, Tony Martin, Chris Perry—and so many more," Mockus said. "We're planning to make a strategic shift to major metro areas moving forward. Currently our Chicago office is in the suburbs, but it needs to move downtown. Emerging and established talent gravitates toward the bigger cities, even with the pandemic."

Mockus also aims to extend and leverage the cross-service capabilities within Woolpert. He said having architecture, engineering, geospatial (AEG) and strategic consulting services in-house gives the firm an unparalleled advantage in the industry, and it is a differentiator the firm plans to wield more liberally.

"If a client has any questions regarding services or wants to get project consultants together, they make one call instead of five," Mockus said. "It's the true one-point of contact. I've been on the owner's side of the equation and I would have greatly appreciated working with a firm that collaborates behind the scenes like Woolpert does."

Woolpert Sector Leader Todd Duwel said he foresees heightened growth and creativity under Mockus.

"Mark hasn't been with Woolpert long, but he has illustrated a focused ambition that will constructively elevate Woolpert's private market," Duwel said. "He already has made the firm better, and our current and future clients will have Mark to thank for making their companies better, as well. We're excited to have him in this role."

## EVENTS

ARSET-Use of Solar Induced Fluorescence and Lidar to Assess Vegetation Change and Vulnerability Online Training

- 16 March, Part I—Lidar and its Applications
- 18 March, Part II—Accessing and Analyzing Lidar Data for Vegetation Studies
- 23 March, Part III—Solar Induced Fluorescence and its Applications
- 25 March, Part IV—Accessing and Analyzing SIF Data for Vegetation Studies

For more information, visit <https://appliedsciences.nasa.gov/join-mission/training/english/arset-use-solar-induced-fluorescence-and-lidar-assess-vegetation>.

## CALENDAR

- 16, 18, 23, 25 March, **ARSET-Use of Solar Induced Fluorescence and Lidar to Assess Vegetation Change and Vulnerability**. For more information, visit <https://appliedsciences.nasa.gov/join-mission/training/english/arset-use-solar-induced-fluorescence-and-lidar-assess-vegetation>.
- 29 March - 2 April, **ASPRS 2021 Annual Conference**, For more information, visit [www.asprs.org/](http://www.asprs.org/).
- 23-25 April, **GISTAM 2021**, Prague, Czech Republic. For more information, visit [www.gistam.org/](http://www.gistam.org/).
- 17-19 May, **2021 Stratus Conference**, Buffalo, New York. For more information, visit <http://stratus-conference.com/>.
- 7-11 June, **URISA GIS Leadership Academy**, Minneapolis, Minnesota. For more information, visit [www.urisa.org/education-events/urisa-gis-leadership-academy/](http://www.urisa.org/education-events/urisa-gis-leadership-academy/).
- 16-20 August, **URISA GIS Leadership Academy**, Portland, Oregon. For more information, visit <https://www.urisa.org/education-events/urisa-gis-leadership-academy/>.
- 3-6 October, GIS-Pro 2021, Baltimore, Maryland. For more information, visit [www.urisa.org/gis-pro](http://www.urisa.org/gis-pro).
- 8-12 November, **URISA GIS Leadership Academy**, St. Petersburg, Florida. For more information, visit [www.urisa.org/education-events/urisa-gis-leadership-academy/](http://www.urisa.org/education-events/urisa-gis-leadership-academy/).
- 6-8 February 2022, **Geo Week 2022**, Denver, Colorado. For more information, visit [www.geo-week.com/](http://www.geo-week.com/).



## 149 Top Geospatial Trends to Watch in 2021

By Qassim Abdullah, Ph.D., PLS, CP

### COLUMNS

#### 152 Signatures

The Column of the Student Advisory Council

#### 155 Book Review—*Smarter Government—How to Govern for Results in the Information Age*

#### 157 Grids and Datums Update

This month we look at Federal Democratic Republic of Ethiopia

### ANNOUNCEMENTS

#### 159 Headquarters News—ASPRS Announces Student Conference Presentation Grants!

#### 159 New ASPRS Members

Join us in welcoming our newest members to ASPRS.

#### 160 Call for Submissions—*PE&RS* Special Issue on Remote Sensing Monitoring for Urban Environment

### DEPARTMENTS

#### 145 Industry News

#### 146 Calendar

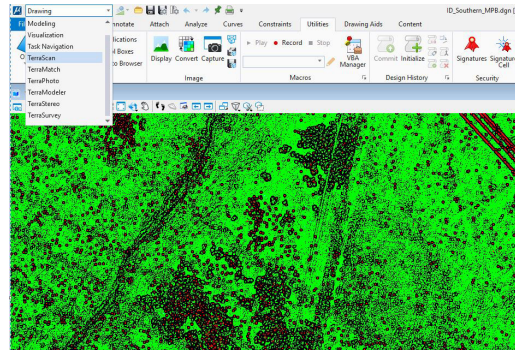
#### 188 In-Press *PE&RS* Articles

#### 196 Who's Who in ASPRS

#### 216 ASPRS Sustaining Members

#### 217 2019-2020 *PE&RS* Reviewers

#### 219 ASPRS Media Kit



**153 GIS Tips & Tricks—**  
**Tired of Looking at Tiny Icons in TerraScan? Here's a Solution...**

#### 161 Extraction of Impervious Surface Using Sentinel-1A Time-Series Coherence Images with the Aid of a Sentinel-2A Image

Wenfu Wu, Jiahua Teng, Qimin Cheng, and Songjing Guo

The continuous increasing of impervious surface (IS) hinders the sustainable development of cities. Using optical images alone to extract IS is usually limited by weather, which obliges us to develop new data sources. The obvious differences between natural and artificial targets in interferometric synthetic-aperture radar coherence images have attracted the attention of researchers. In this paper, we used time-series coherence images and introduced multi-resolution segmentation as a postprocessing step to extract IS.

#### 171 Road Extraction from Cartosat-2F Multispectral Data with Object-Oriented Analysis

Chumbitha Leena, Manoj Raj Saxena, and Ravi Shankar Dwivedi

For detection of a road network, high-resolution satellite data have been used following the object-oriented classification approach. In this paper, we use object-based feature extraction algorithms for detection of road networks from a high resolution Cartosat-2F multispectral data in an Indian city with varying terrain conditions ranging from a compact built-up area to a predominantly vegetated area.

#### 181 Digital Surface Model Refinement Based on Projected Images

Jiali Wang and Yannan Chen

Currently, the practical solution to remove the errors and artifacts in the digital surface models (DSM) through stereo images is still manual or semiautomatic editing those affected patches. Although some degrees of semiautomation can be gained, the DSM refinement remains a labor consuming and expensive process. This paper proposes a new method to correct errors in DSM or/and refine an existing coarse DSM.

#### 189 Remote Sensing for Ecosystem Services and Urban Sustainability

John C. Trinder

The purpose of this paper is to demonstrate how geospatial technologies, especially remote sensing, can play a leading role in defining urban sustainability based on the evaluation of demand and supply of ecosystem services (ES).

#### 197 Monitoring Work Resumption of Wuhan in the COVID-19 Epidemic Using Daily Nighttime Light

Zhenfeng Shao, Yun Tang, Xiao Huang, and Deren Li

This paper analyzes the characteristics of nighttime light (NTL) radiance variation, aiming to demonstrate the possibility of using NTL to monitor work resumption and evaluate the impact of COVID-19 on economic activities in Wuhan, China.

#### 207 Progressive TIN Densification with Connection Analysis for Urban Lidar Data

Tao Wang, Lianbin Deng, Yuhong Li, and Hao Peng

Urban lidar data are advantageous for capturing the terrain surface of built-up areas, which can be directly used to provide digital surface models. Cloud points are classified into ground points to obtain digital terrain models. This paper proposes a method to improve the progressive triangulated irregular network (TIN) densification method using a TIN connection analysis algorithm, namely, connection analysis via slope analysis.

**See the Cover Description on Page 148**

# COVER DESCRIPTION

Four blackwater rivers—the Waccamaw, Pee Dee, Black, and Sampit—feed into Winyah Bay, an estuary in eastern South Carolina. All of them flow through swamps, wetlands, and forests that are rich with decaying vegetation and other organic matter. The dead leaves and debris stain the rivers and wetlands a transparent brown color as several natural chemical substances found in plants—tannin, phenol, and humic acid—seep into the water. The same process gives tea its yellow or brown color.

After heavy rains, stained floodwaters can get flushed out of swamps and wetlands into the estuary and ocean. That was happening on October 1, 2020, when the Operational Land Imager (OLI) on Landsat 8 acquired this natural-color image of Winyah Bay. Many waterways were swollen following heavy rains from Hurricane Sally.

When measuring the phenomenon with optical instruments, scientists describe heavily stained waters as being high in colored dissolved organic matter (CDOM). On October 1, a National Oceanic and Atmospheric Administration water quality monitoring system at North Inlet-Winyah Bay National Estuarine Research Reserve measured CDOM levels that were roughly 50 percent higher than the long-term average for that date, said Erik Smith, the head of the research reserve.

Blackwater flows can have important consequences for aquatic ecosystems because they change the color of the light available to phytoplankton for photosynthesis. “The compounds that make up CDOM absorb blue light wavelengths extremely well, so blue light does not penetrate very deep into the water. The red wavelengths are the ones left behind, hence the brownish-red appearance of the water,” explained Tammi Richardson, an oceanographer at the University of South Carolina. “If phytoplankton do not have pigments that can absorb red light, then they will not be able to photosynthesize.”

Since phytoplankton photosynthesis is a centerpiece of the ocean food web, CDOM levels can affect the productivity of the entire Winyah Bay estuary. In practice, cryptophytes and diatoms tend to do well in blackwater, while other types of phytoplankton tend to suffer.

Blackwater holds an interesting place in maritime history in this region. In the early years of European exploration and colonization of North America, mariners sought out blackwater streams to refill their casks because the water was thought to minimize the spread of disease. Sailors did not know why at the time, but the high acidity and presence of certain phenols have anti-bacterial properties.

Among those early sailors may have been the Spanish explorer Lucas Vázquez de Ayllón. He led an expedition of six ships that reached Winyah Bay in August 1526, and established San Miguel de Gualdape, the first European settlement in the contiguous United States. It preceded Pensacola, Roanoke, and Jamestown by decades, but is often overlooked by historians because of how unsuccessful and short-lived it was.

Upon arrival in Winyah Bay, the Spaniards immediately lost their main supply ship—the Capitana—when it ran aground on a sandbar near the modern town of Georgetown. In the chaos that followed, the Native American guides and interpreters they had captured from the area during a previous expedition deserted and slipped into the forest. After about a month in Winyah Bay, Ayllón moved the colony of 500 Europeans and 100 enslaved Africans to a new location. Where exactly they went is unclear, but historians think they settled along Sapelo Sound in what is now Georgia.

However, unusually cold weather, disease, and lack of food quickly turned a difficult situation into a catastrophe for the colonists. Settlers died in large numbers by mid-October, including Ayllón himself. His death triggered a battle for leadership of the struggling colony. In the confusion, the African slaves revolted and escaped, meaning the first ever documented slave uprising in North America happened at San Miguel de Gualdape. The 150 Europeans who were still alive after the uprising soon abandoned the colony and set sail for Hispaniola. The escaped slaves, meanwhile, were likely taken in by Native American communities in the area.

For more information, visit <https://landsat.visibleearth.nasa.gov/view.php?id=147517>

NASA image by Norman Kuring/NASA's Ocean Color Web, using Landsat data from the U.S. Geological Survey. Story by Adam Voiland, with information from James Morris (University of South Carolina).



## PHOTOGRAMMETRIC ENGINEERING & REMOTE SENSING

JOURNAL STAFF

Publisher ASPRS

Editor-In-Chief Alper Yilmaz

Assistant Director — Publications Rae Kelley

Electronic Publications Manager/Graphic

Artist Matthew Austin

*Photogrammetric Engineering & Remote Sensing* is the official journal of the American Society for Photogrammetry and Remote Sensing. It is devoted to the exchange of ideas and information about the applications of photogrammetry, remote sensing, and geographic information systems. The technical activities of the Society are conducted through the following Technical Divisions: Geographic Information Systems, Photogrammetric Applications, Lidar, Primary Data Acquisition, Professional Practice, and Remote Sensing Applications. Additional information on the functioning of the Technical Divisions and the Society can be found in the Yearbook issue of *PE&RS*.

Correspondence relating to all business and editorial matters pertaining to this and other Society publications should be directed to the American Society for Photogrammetry and Remote Sensing, 425 Barlow Place, Suite 210, Bethesda, Maryland 20814-2144, including inquiries, memberships, subscriptions, changes in address, manuscripts for publication, advertising, back issues, and publications. The telephone number of the Society Headquarters is 301-493-0290; the fax number is 225-408-4422; web address is [www.asprs.org](http://www.asprs.org).

**PE&RS.** *PE&RS* (ISSN0099-1112) is published monthly by the American Society for Photogrammetry and Remote Sensing, 425 Barlow Place, Suite 210, Bethesda, Maryland 20814-2144. Periodicals postage paid at Bethesda, Maryland and at additional mailing offices.

**SUBSCRIPTION.** For the 2021 subscription year, ASPRS is offering two options to our *PE&RS* subscribers — an e-Subscription and the print edition. E-subscribers can plus-up their subscriptions with printed copies for a small additional charge. Print and Electronic subscriptions are on a calendar-year basis that runs from January through December. We recommend that customers who choose both e-Subscription and print (e-Subscription + Print) renew on a calendar-year basis.

The rate of the e-Subscription (digital) Site License Only for USA and Non-USA is \$1000.00 USD. e-Subscription (digital) Site License Only for Canada\* is \$1049.00 USD. e-Subscription (digital) Plus Print for USA is \$1365.00 USD. e-Subscription (digital) Plus Print for Canada\* is \$1424.00 USD. e-Subscription (digital) Plus Print for Non-USA is \$1395.00 USD. Printed-Subscription Only for USA is \$1065.00 USD. Printed-Subscription Only for Non-USA is \$1195.00 USD. \*Note: e-Subscription/Printed-Subscription Only/e-Subscription Plus Print for Canada include 5% of the total amount for Canada's Goods and Services Tax (GST #135123065). **PLEASE NOTE: All Subscription Agencies receive a 20.00 USD discount.**

**POSTMASTER.** Send address changes to *PE&RS*, ASPRS Headquarters, 425 Barlow Place, Suite 210, Bethesda, Maryland 20814-2144. CDN CPM #/40020812)

**MEMBERSHIP.** Membership is open to any person actively engaged in the practice of photogrammetry, photointerpretation, remote sensing and geographic information systems; or who by means of education or profession is interested in the application or development of these arts and sciences. Membership is for one year, with renewal based on the anniversary date of the month joined. Membership Dues include a 12-month electronic subscription to *PE&RS*. Or you can receive the print copy of *PE&RS* Journal which is available to all member types for an additional fee of \$60.00 USD for shipping USA, \$65.00 USD for Canada, or \$75.00 USD for international shipping. Dues for ASPRS Members outside of the U.S. will now be the same as for members residing in the U.S. Annual dues for Regular members (Active Member) is \$150.00 USD; for Student members \$50.00 USD for USA and Canada \$53.00 USD; \$60.00 USD for Other Foreign members. A tax of 5% for Canada's Goods and Service Tax (GST #135123065) is applied to all members residing in Canada.

**COPYRIGHT 2021.** Copyright by the American Society for Photogrammetry and Remote Sensing. Reproduction of this issue or any part thereof (except short quotations for use in preparing technical and scientific papers) may be made only after obtaining the specific approval of the Managing Editor. The Society is not responsible for any statements made or opinions expressed in technical papers, advertisements, or other portions of this publication. Printed in the United States of America.

# Top Geospatial Trends to Watch in 2021

By Qassim Abdullah, Ph.D., PLS, CP  
Woolpert Vice President and Chief Scientist



**It's** that time of the year, when we review geospatial methods and technology trends and I use my piercing crystal ball to see what's on the horizon for the new year. While the pandemic changed the way we conduct business, geospatial sensor technologies continued their upward trend. As I have in the past, I'll revisit the trends I forecasted at this time last year, note how those predictions panned out, and project how these and other trends are expected to evolve throughout 2021 and beyond.

---

### Data Democratization: Big Data Needs Big Tools

Data democratization, or providing streamlined access to technical expertise, continued to evolve in 2020. Although still a work in progress, the geospatial community became more educated in many new and complex data topics like machine learning in application development. It also became more adept at sharing those tools and techniques so they can be easily understood by those without extensive experience, skills or training. An example of this increased awareness is the growing trend in the Geospatial Knowledge Infrastructure\*, which is being tackled by the United Nations and its global strategic partners.

Crowd sourcing, big data and data science have been aggressively pursued by tech companies, whether they are for honest data gathering or for those who want to sell location-based data to the highest bidder. Location-based applications including smart buildings, self-driving cars and crowd sourcing will continue their upward growth and potential this year. These data, if used properly, can be a great service to diverse sectors that include planning, construction, utilities, transportation, government and energy.

However, although there is growing number of niche companies and services offering creative solutions, the mainstream geospatial industry witnessed sluggish growth in the creative methods and tools needed to mine, extract and convert these data into knowledge. These niche companies are mainly small business startups focused on innovative solutions that serve a segmented or specialized market. Often, they are snatched up upon arrival by giant tech companies before the industry has had a chance to work with them. The situation is different for the giant tech companies like Google and Amazon, which have continued their advancement of machine learning, artificial intelligence and deep learning. Their sophisticated methods and tools were developed for their use rather than for the geospatial community at large, but some of their developments are benefiting geospatial users on a limited scale.

---

### Think Small—Miniaturized Sensors

Last year, I envisioned companies like Google, Apple and LG would invest more in advancing and integrating miniaturized imaging and lidar systems within their devices for mapping applications.

The latest imaging capabilities of some smartphones exceeded my expectations, and I was pleased to see that Apple

has a lidar sensor on its iPhone 12 Pro. Once I heard about it, of course I had to purchase one. I am still figuring out how it works. Based on the article posted on LinkedIn by Rami Tamimi, an Ohio State University student working toward his doctorate in geodetic engineering, the iPhone 12 Pro lidar looks awesome and is a great foray into sharing this technology with the masses. I expect other phone manufacturers will emulate Apple by incorporating this technology in 2021.

---

### Living in the Cloud

Last year, I acknowledged that progress was made by agencies moving computing powers to the cloud. Many more companies are offering business models for cloud data hosting and processing. Amazon, Google and Microsoft continue to lead that market and offer users and developers sophisticated platforms like serverless cloud computing. These platforms enable developers to run apps and services without having to manage and operate costly and complicated server infrastructure.

Among members of the geospatial community who are utilizing the cloud for data storage and application development, the majority are interested in serverless cloud computing architecture. This supports our favorite geospatial applications, map libraries and GIS clients like ArcGIS Online, ArcGIS Desktop or QGIS. This trend will continue to evolve and grow strongly throughout 2021.

---

### Lidar, Lidar, Everywhere

In 2020, lidar manufacturers continued to make huge technological advances, both in traditional linear-mode lidar and in newer lidar technologies, like single photon. These advancements will continue this year, offering more efficient data acquisition and more affordable lidar data to support national programs, such as the U.S. Geological Survey's 3D Elevation Program†.

For a glimpse of the industry's current capabilities in aerial lidar mapping, here are some figures I presented during the Geo Week webinar "Airborne Lidar and Actionable Data," that was held earlier this month. In my presentation, I noted that Woolpert has collected dense lidar data over 700,000 square kilometers worldwide in the last three years. As part of those collections, 100,000 km<sup>2</sup> was topo-bathy lidar. Before lidar and its immense capabilities, we used to generate topographic maps using traditional stereophotogrammetry. This manual, labor-intensive method, in many cases, could not match the quality or the accuracy of a lidar-derived digital terrain model. It also would take us decades to compile a 700,000 km<sup>2</sup> DTM using stereo imagery.

Lately, we've seen lidar manufacturers start to invest a great deal of energy into the development of AI-based applications that will help users weed through the massive number of point clouds to extract the information they need.

Improvements in lidar data density, quality and accuracy continued to attract new users and new applications in 2020, and this trend will continue for years to come. Unmanned aircraft system, or drone-based, lidar data acquisition also witnessed massive growth in 2020 as new lidar systems emerged. The most impressive development was the recent introduction of a flash lidar sensor with 200-meter range by

---

Photogrammetric Engineering & Remote Sensing  
Vol. 87, No. 3, March 2021, pp. 149–151.  
0099-1112/21/149–151

© 2021 American Society for Photogrammetry  
and Remote Sensing  
doi: 10.14358/PERS.87.3.149

---

\* <https://geospatialmedia.net/pdf/GKI-Discussion-Document-Ver1.0.pdf>  
† <https://www.usgs.gov/core-science-systems/ngp/3dep>

Sense Photonics. Although the flash lidar concept is not new to the industry, its 200-meter range capability and its ability to be mass produced for the automobile industry will also make it an attractive lidar option for UAS.

The great thing about flash lidar is that it is lightweight and has no moving parts. All UAS-based lidar systems other than flash lidar are based on a scanning mechanism that can introduce unstable geometry and therefore compromise the positional accuracy of the resulting product. Another UAS lidar development worth mentioning is DJI lidar. Like other DJI products, DJI lidar is considered to be the least expensive lidar acquisition method for drones. Affordable and efficient lidar systems such as this will force manufacturers and integrators to lower the cost of UAS-based lidar, which is win-win for the geospatial industry.

---

### Topo-Bathy Lidar

This year, the importance of the bathymetric survey has earned its own section in this forecast. The reason for this is two-fold. First, manufacturers have excelled in providing the industry with an awesome new breed of lidar systems that can be used for the dual data acquisition for topographic and bathymetric survey. These new systems made it much more practical to survey coastlines without the need for two types of lidar systems—topographic and bathymetric. The second reason is that on Jan. 5, 2021, the White House Council on Environmental Quality and the Office of Science and Technology Policy released an implementation plan for the “National Strategy for Ocean Mapping, Exploring and Characterizing of the United States Exclusive Economic Zone.” The implementation plan was drafted by the National Oceanic and Atmospheric Administration. This presidential memorandum applies to an oceanic area larger than the terrestrial landmass of the United States. This is good news for the geospatial industry, since we will help implement the plan.

---

### Marrying BIM to GIS and Digital Twin

Building information modeling, virtual reality and augmented reality will continue their growth within the geospatial and engineering communities. The mapping and geospatial industry must refine its tools and methods by building efficient GIS databases and applications to take advantage of upcoming opportunities. This year, we will hear more about the concept of the digital twin and its importance to planning and decision-making. If you are not familiar with the concept, I would define digital twin as “the digital surrogate of the physical environment, which you can use and abuse without harming or disturbing the physical environment representing your project site.”

The digital twin opens huge opportunities for the geospatial community, since lidar is becoming the most efficient tool from which to generate data and build a model. The geospatial community needs to familiarize itself with the digital twin concept and what it entails to enhance geospatial modeling technologies moving forward.

Another interesting development in the BIM arena in 2020 was combining the power of indoor mapping and digital facility management services. This integration enables companies to manage their workspaces and provide property managers with the ability to edit floor plans in real time and to share those changes immediately with employees and facility users. Imagine if a leasing manager or builder gave you access to the dynamic digital floor plan of a new project or of your new apartment before you moved in. Having a 3D digital twin of that space before you sign a lease or purchase contract can provide the kind of empowerment that leads to a better

quality of life. This capability was recently introduced to the market by Mappedin of Waterloo, Canada.

---

### A “Smart” Revolution

The concepts of smart cities and intelligent transportation systems will continue their healthy growth in 2021. This growth will be accelerated by geospatial trends cited here, most notably digital twin methods, big data, machine learning and deep learning. Helping this growth are the continued advancements in utilizing the Internet of Things for cloud data storage and processing in near-real time.

Autonomous driving will continue to make strides as more car manufacturers go down this road. Self-driving cars require artificial intelligence and geospatial data to understand infrastructure details and conditions. As predicted last year, our geospatial community is poised to earn a substantial market share of the services and technologies needed to support and navigate the smart revolution.

---

### Mapping-as-a-Service

Gradually, the term mapping-as-a-service is expanding to encompass all cloud-based geospatial data solutions, including data-as-a-service, software-as-a-service, and online analytical solutions based on AI and machine learning. There is not expected to be any substantial development in speculated data acquisition, on-demand geospatial data and data subscription services in 2021, largely due to the pandemic. I expected this sector to grow in 2020 but unfortunately our geospatial business, like everything else, was impacted by COVID-19. However, MaaS capabilities are expected to see measurable growth in 2022.

I ended my article from last year with: “These geospatial trends will continue to blossom throughout 2020, as the need for advanced technologies continues to rise. I look forward to seeing what the year will bring.” Well, we all know now what 2020 brought to us. However, our geospatial community is resilient, and we will survive the wrath of 2020. Our success will require the collaboration of multiple tiers of government, the private sector, public utilities, community activists, building owners, average citizens, etc. It will also require hard work on several levels as we advance application developments like dashboards and databases to achieve real-time situational awareness, and scientific datasets and analysis to create technology solutions for use around the world.

**Happy New Year!**

---

*Woolpert Vice President and Chief Scientist Qassim Abdullah, Ph.D., PLS, CP, has more than 40 years of combined industrial, R&D and academic experience in analytical photogrammetry, digital remote sensing, and civil and surveying engineering. When he's not presenting at geospatial conferences around the world, Qassim teaches photogrammetry and remote sensing courses at the University of Maryland and Penn State, authors a monthly column for the ASPRS journal PE&RS, and mentors R&D activities within Woolpert.*

*Previously published on <https://woolpert.com/media/blogs/>*

*The contents of this column reflect the views of the author, who is responsible for the facts and accuracy of the data presented herein. The contents do not necessarily reflect the official views or policies of the American Society for Photogrammetry and Remote Sensing.*

# GREETINGS FROM THE ASPRS STUDENT ADVISORY COUNCIL (SAC)!

**A**s we continuously network with our ASPRS Chapter community, we are highlighting the San Diego State University Student Chapter of the ASPRS for their continued commitment to emerging technology, education, engagement, and fellowship.

**GO AZTECS!** The San Diego State University Student Chapter of the ASPRS is made up of both graduate and undergraduate students interested in remote sensing; GIS; and geospatial education, research, and outreach. Advised by Distinguished Professor Emeritus Dr. Douglas Stow, the current chapter includes students affiliated with both the Department of Geography and the Department of Biology (Ecology Program Area).

The SDSU chapter aims to connect students interested in geospatial technologies, provide opportunities to meet with professionals in GIS and remote sensing fields, discuss research ideas and planned methodology, and lead or participate in technical workshops. Over the years, the student chapter has hosted a variety of workshops, to include sessions focused on: object-based image classification approaches, structure-for-motion (SfM) processing, and spectral unmixing techniques. With the Department of Geography being home to a few drones and a handheld spectrometer, student chapter advisors and members have organized and led demos using these tools.

The chapter's main focus is on the annual Spring Technical Meeting it hosts for the ASPRS Pacific Southwest (PSW) Region, usually held on the SDSU campus and open to the public. This meeting features three-to-four short presentations and concludes with a longer keynote presentation (often given by the acting ASPRS President). Followed by a student chapter-hosted social hour, students and members of the community have the opportunity to meet the speakers and dive deeper into what was shared during the day's presentations.

Due to 2020's COVID-19-related restrictions, the SDSU student chapter postponed its originally planned wildland fire-themed Spring Technical Meeting and worked with the PSW Region to create the 1<sup>st</sup> Annual ASPRS PSW Remote Sensing & Wildland Fire Symposium (RS Fire 2020). Each session featured speakers who are respected and well known in the remote sensing and GIS, landscape ecology, and wildland firefighting communities; the primary goal was to help open lines of communication between imaging scientists and firefighters. Held over four Monday afternoons in November and chaired by the SDSU Student Chapter President, Krista West, this new symposium series was a success.

Faculty Involvement			
	 <p>Dr. Douglas Stow – Faculty Advisor</p> <ul style="list-style-type: none"> <li>• Stow Research Group</li> <li>• Primary instructor of remote sensing courses at SDSU and the Co-Director of the Center for Earth Systems Analysis Research</li> </ul>	 <p>Lloyd (Pete) Coulter</p> <ul style="list-style-type: none"> <li>• SDSU Programmer/Analyst</li> <li>• ASPRS PSW Region Director</li> </ul>	
Student Officers	 <p>Krista West</p>	 <p>Keaton Shennan</p>	 <p>William Nicewonger</p>
Position	President	Vice President	Secretary-Treasurer
Degree	PhD Student	MS Student	BS Student
Major	Geography	Geography	Geography/ Interdisciplinary Studies)

#### ASPRS STUDENT ADVISORY COUNCIL

YOUSSEF KADDOURA  
COUNCIL CHAIR

EVAN VEGA  
DEPUTY COUNCIL CHAIR

JASON MCGLAUGHLIN  
EDUCATION COUNCILOR

GERARDO ROJAS  
DEPUTY EDUCATION COUNCILOR

TERRA MCKEE  
COMMUNICATIONS COUNCILOR

JEFF PU  
DEPUTY COMMUNICATIONS COUNCILOR

MADISON FUNG  
SOCIAL MEDIA COMMITTEE CHAIR

AUSTIN STONE  
NETWORKING COUNCILOR

VICTORIA SCHOLL  
DEPUTY NETWORKING COUNCILOR

LAUREN MCKINNEY-WISE  
CHAPTERS COMMITTEE CHAIR

DAVID LUZADER  
SAC EPCP LIASON

# GIS Tips & Tricks

Michael Baranowski, CLT, GISP, and  
Al Karlin, Ph.D. CMS-L, GISP

## Tired of Looking at Tiny Icons in TerraScan? Here's a Solution...

Sometimes small improvements and useful tips pay off big in terms of time and convenience, especially when using geospatial software in a production mode. Small icons, crowded onto toolbars, can confuse new users and infuriate long-time users. Then, some software products require the user to hold down multiple keyboard keys and/or a combination of mouse buttons to navigate the interface. This is the case with the Terrascan MDL (MicroStation Development Library) application that runs within MicroStation. While Terrascan MDL with MicroStation is the “industry standard” for lidar editing, here is a tip to update Terrascan MDL user interface.

When loading the Terrascan MDL Application into MicroStation you have a small docked Window with 16 icons to choose tools from. The standard method requires a combination of (1) continuous firm pressure (push down/click) with the left mouse button each icon, to (2) activate all the sub tools that can be opened. Then, (3) you have to move your cursor down the row of tools, making sure not to let up with the left mouse hold to select the tool you want to use, as in the “standard” sequence, Figures 1-4. Throughout this process, a user may need to search through several options to find the desired toolbar.

This Terrasolid “active workflow ribbon” library allows the Terrasolid toolbar to be viewed in the typical MicroStation/CAD ribbon format rather than the “standard” Terrascan mode. The new active workflow ribbon has condensed the tools into fewer tabs (9 for Terrascan), and with each tab you now can see the tools across the ribbon, as in the ribbon sequence, Figures 5-8. Each tool is clearly described and the

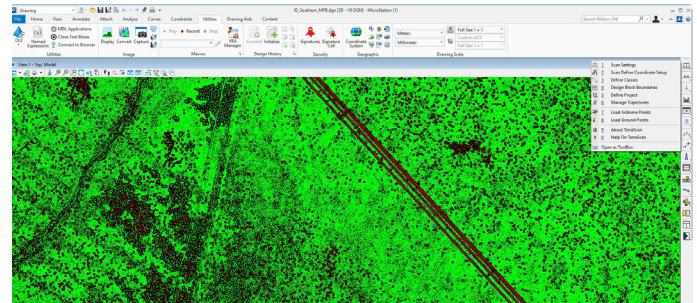


Figure 2: Step 2—Standard Terrascan interface- Mouse-click to open panel of icons.

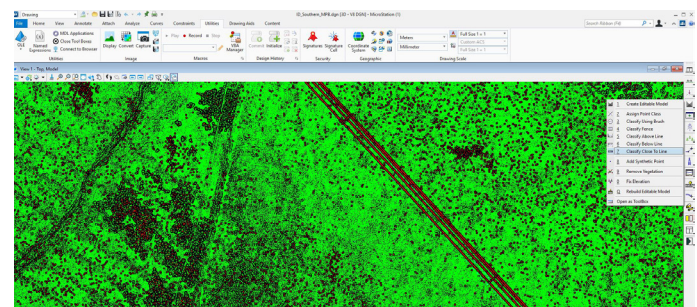


Figure 4: Step 4—Standard Terrascan interface-After dragging the mouse through the interface, the selected tool activates.

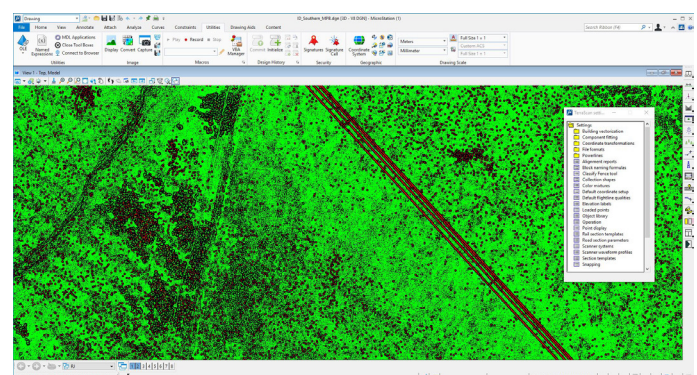


Figure 3: Step 3—Standard Terrascan interface- Tool panel opens after additional mouse-click; two clicks deep into interface.

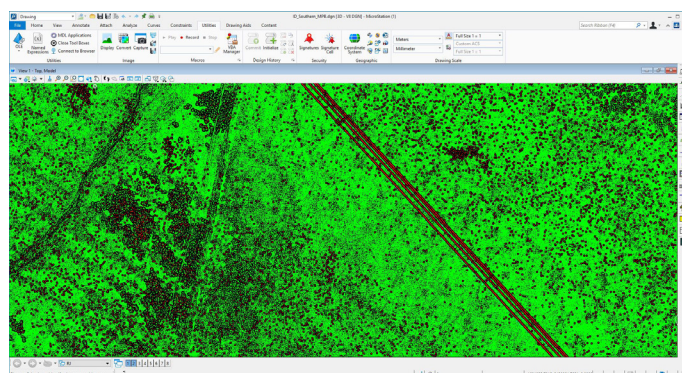


Figure 1: Step 1— Standard Terrascan interface – no ribbon.

Photogrammetric Engineering & Remote Sensing  
Vol. 87, No. 3, March 2021, pp. 153–154.

0099-1112/21/153–154

© 2021 American Society for Photogrammetry  
and Remote Sensing

doi: 10.14358/PERS.87.3.153

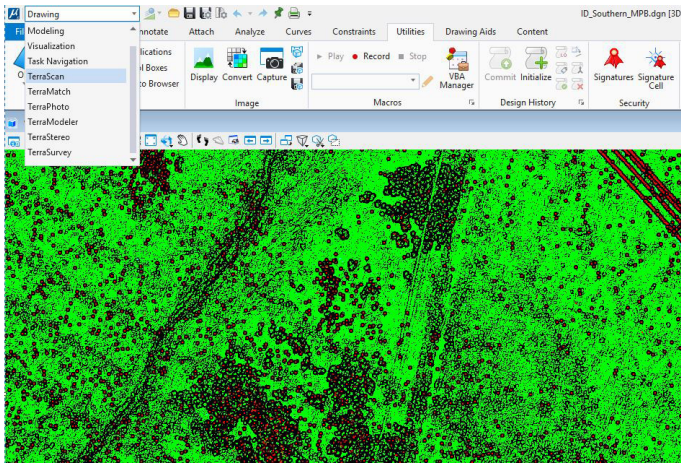


Figure 5: Step 1—The Active Workflow Ribbon – once design library has been installed, all available Terrasolid ribbons are visible.

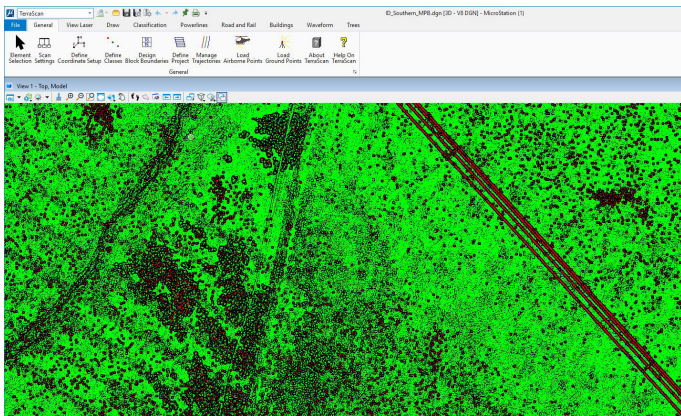


Figure 6: Step 2—The Active Workflow Ribbon – after selecting the TerraScan Tools workflow ribbon, the 16 subgroups are now displayed as 9 tabs on the ribbon

icon symbol ready for you to click and open the tool. This streamlining results in fewer click and drags, and eliminates searching through multiple levels of interface. The active workflow ribbon library does not replace the “standard” interface, so if you still prefer the standard interface, both options are available on-screen.

For additional installation instructions, Geocue has a support document at: <https://support.geocue.com/terrasolid-design-library/>.

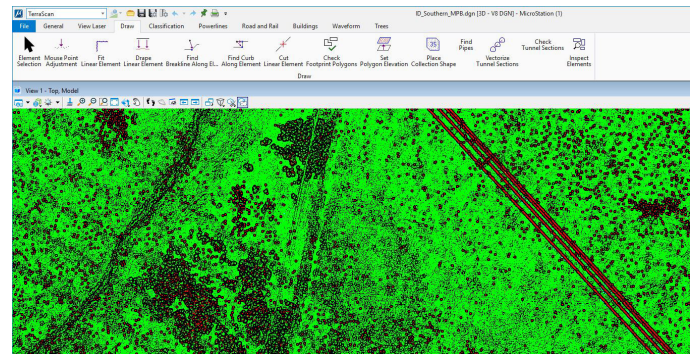


Figure 7: Step 3—The Active Workflow Ribbon – Example of all available Draw Tab tools with descriptions of each written out below the icon.

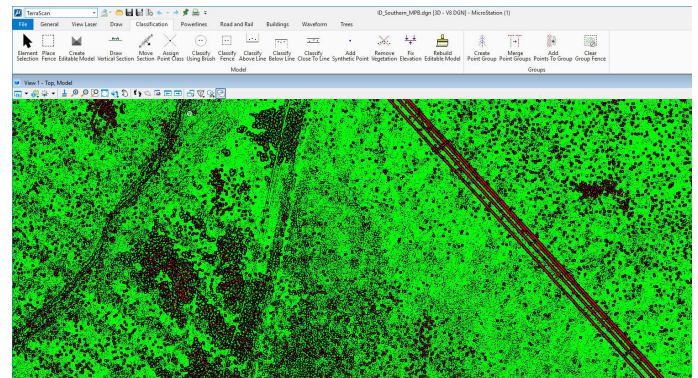


Figure 8: Step 4—The Active Workflow Ribbon – all classification sub-tools now can be found under a single tab.

And it is that easy to update the TerraScan interface!

**Michael Baranowski, CLT, GISP and Al Karlin, Ph.D., CMS-L, GISP** are with Dewberry’s Geospatial and Technology Services group in Tampa, FL. Mike is a Senior Geospatial Analyst at Dewberry who manages many aspects of lidar production along with resource allocation. As a senior geospatial scientist, Al works with all aspects of Lidar, remote sensing, photogrammetry, and GIS-related projects.

Please e-mail questions or comments to [GISTT@ASPRS.org](mailto:GISTT@ASPRS.org).

## ASPRS WORKSHOP SERIES

It’s not too late to earn Professional Development Hours

Miss one of our Geo Week 2020 Live Online Workshops? Not to worry! You can purchase the workshops now and watch when you are ready! Check out the workshops offered by visiting:

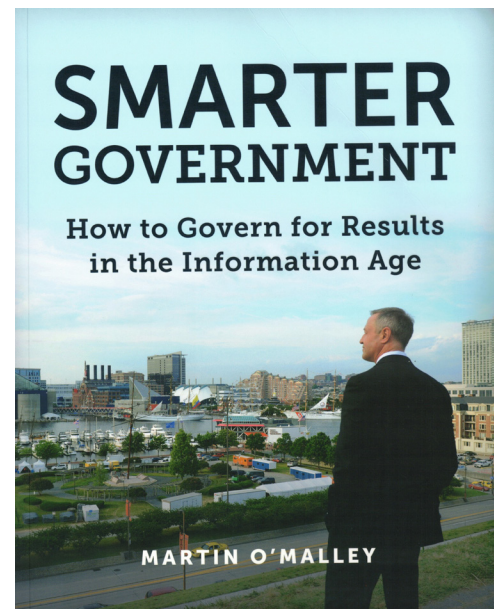
<https://conferences.asprs.org/geoweek-2020/workshops/>

The book authored by Martin O'Malley, the former Maryland Governor, clearly sends the message that technology is a key to better government and improved results in the information age. He makes the case for using improved technologies, specifically GIS (Geographic Information System) technology, to gather, manage, and analyze data to enhance government performance and service delivery. The governor states that "First as mayor of Baltimore and then as governor of Maryland, I experienced firsthand the power of GIS ... Whether the goal is improving public education, reducing violent crime, or restoring the health of our natural environment, GIS provides a powerful platform for progress. GIS is making government smarter." The governor's intent is to share how the data, the map, and the method for achieving dramatic public-sector progress during his service helped him to work with his administration to achieve measurable results using GIS technology.

The author provides his reasons for running for Baltimore Mayor and the challenges his administration faced with lagging information from various unrelated and outdated systems that made governing difficult. He brought CompStat, a combination of management, philosophy, and organizational management tools, to his police department. Moving forward, the mayor brought on CityStat, a new system for governing the whole of city government. The author detailed the implementation and achievements of StateStat that is based on the CityStat Techniques across the entire state after he became the governor of Maryland.

He tells the story of his meeting with ESRI co-founder Jack Dangermond, who introduced him to the concepts of GIS, from which the governor saw the power of the GIS map as "The Power of Information Shared by All," a new platform and new tools that can be integrated into the government system so the results can be seen through GIS maps and internet. In his own words, "The capacity that a common operating platform provides for managing dynamic and sometimes fast-moving problems with real-time data is a big innovation in government. In fact, these new technologies – GIS and the Internet of Things (IoT) – and the ability these technologies give us to model belief space – that is to say, to model the changing dynamics of our built and natural environments – are ushering in a whole new way of governing in the Information Age."

There are 14 chapters in the book. Each chapter includes a "Learn & Explore" section that provides a link to the book's website ([www.smartergovernment.com](http://www.smartergovernment.com)). On this website, the user can watch videos, explore the story maps, dashboards, books, blogs, data resources, and examples that support the concepts and ideas presented in the book and other infor-



## Smarter Government—How to Govern for Results in the Information Age

Martin O'Malley

Foreword by Stephen Goldsmith

ISBN: 9781589485242 2019 332 pages Paperback List Price: 39.99\* (\* Individual store prices may vary)

**Reviewed by** Connie Li Krampf, CP, CMS, MSCS,  
Project Manager - Photogrammetry, Weston &  
Sampson, Cary, North Carolina.

mation related to the book. Study and Discussion questions based on the chapters are listed in Appendix A of the book. The user can also find those questions on the aforementioned website.

GIS exercises for each chapter can be found in Appendix B of the book, from there, a user can get hands-on experience with the GIS software and learn the technology by working with real data. Esri provides free trial software and student licenses so users can learn the technology at their convenience with little financial burden.

The book is by no means a highly technical tome; however,

Photogrammetric Engineering & Remote Sensing  
Vol. 87, No. 3, March 2021, pp. 155–156.  
0099-1112/21/155–156

© 2021 American Society for Photogrammetry  
and Remote Sensing  
doi: 10.14358/PERS.87.3.155

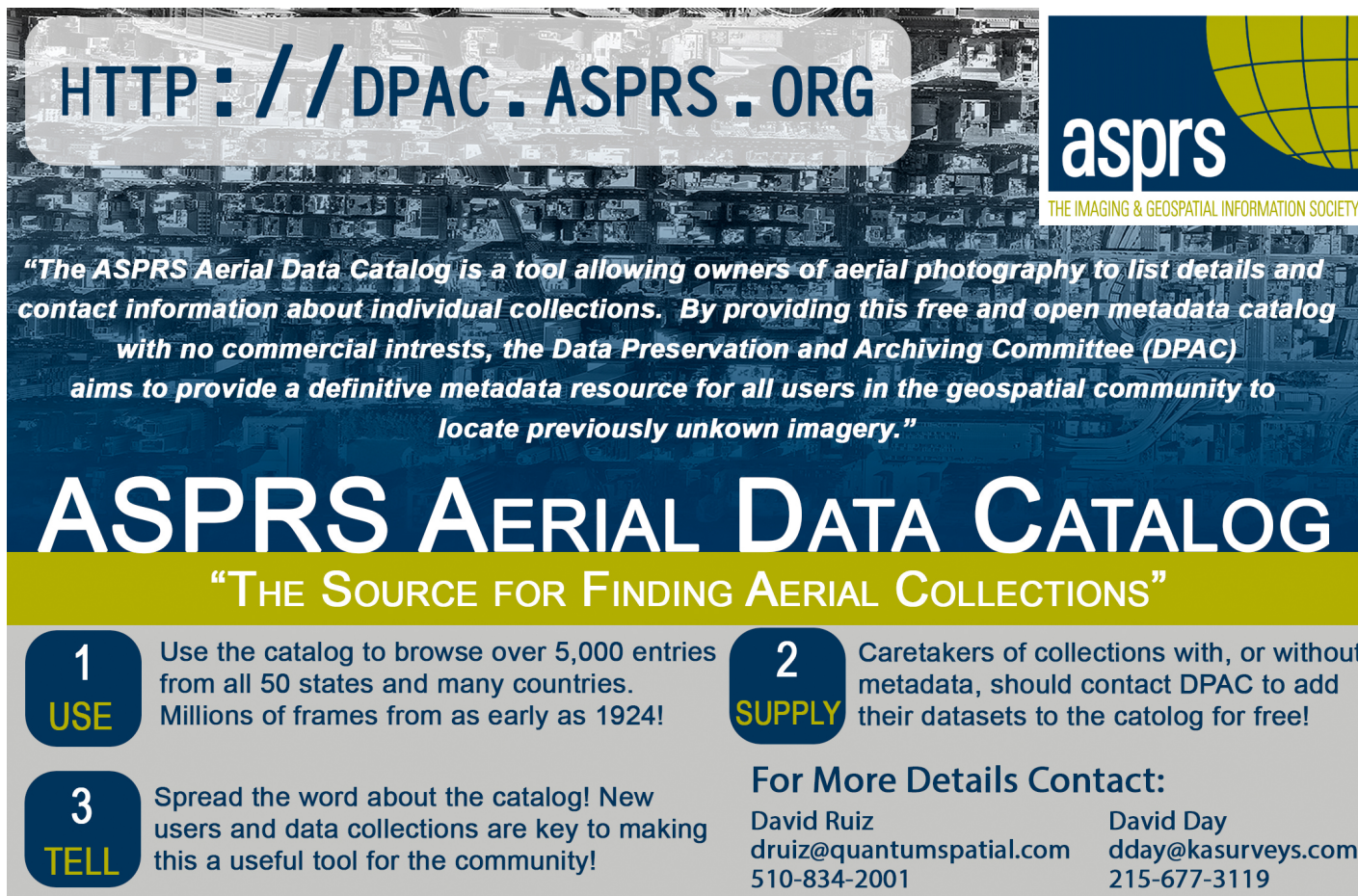
users can find a good deal of helpful technological information through the sidebars. There are interesting stories about how the technologies were used by the governor's administration.

The author lays out "A New Way of Governing," about a method that emphasizes the relationship between the governed and the trust required for governing. This new way of governing is based on data collection, management, and analysis, showing and measurement of results through GIS technology. Maps, pictures, charts, and illustrations are provided to help the reader understand the concepts the author attempts to convey in the book. Additional sections include "Acknowledgments," a list of "Contributors" and a long list of "Credits".

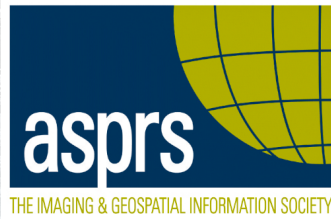
The book totals 332 pages; is well written and easy to read. Each chapter begins with a meaningful, relatable, artistic, and beautiful picture. Maps, charts, and other illustrations in the book are thoughtfully chosen and well placed. The book has relevant stories, pictures, leadership practices, and nuggets of wisdom.

This book could serve as a textbook for undergraduate or graduate students with majors in Geospatial Science as well as Political Science, History, or other related disciplines. The book's website is well designed and easy to navigate. The study and discussion questions are carefully written and closely related to the context of the book. The GIS exercises and data are appropriate and challenging enough to benefit the student. It can also serve as a reference resource for government leaders to consider applications to improve governance. A few small improvements could be made, for example, the map elements such as a north arrow, scale bar, or legend could be added to the map on page 255 to display clearer and more meaningful information.

The governor showcases the power of GIS technology and ways it can be used to govern and lead in the Information Age. GIS is not just a sterile geospatial technology but an evolutionary tool for human societies to live smarter and better. For that, GIS should be written as a chapter in a modern history book.



**HTTP://DPAC.ASPRS.ORG**



**"The ASPRS Aerial Data Catalog is a tool allowing owners of aerial photography to list details and contact information about individual collections. By providing this free and open metadata catalog with no commercial interests, the Data Preservation and Archiving Committee (DPAC) aims to provide a definitive metadata resource for all users in the geospatial community to locate previously unknown imagery."**

# ASPRS AERIAL DATA CATALOG

**"THE SOURCE FOR FINDING AERIAL COLLECTIONS"**

- 1 USE** Use the catalog to browse over 5,000 entries from all 50 states and many countries. Millions of frames from as early as 1924!
- 2 SUPPLY** Caretakers of collections with, or without metadata, should contact DPAC to add their datasets to the catalog for free!
- 3 TELL** Spread the word about the catalog! New users and data collections are key to making this a useful tool for the community!

**For More Details Contact:**

David Ruiz druiz@quantumspatial.com 510-834-2001	David Day dday@kasurveys.com 215-677-3119
--	---



# & GRIDS & DATUMS

BY Clifford J. Mugnier, CP, CMS, FASPRS

The Grids & Datums column has completed an exploration of every country on the Earth. For those who did not get to enjoy this world tour the first time, *PE&RS* is reprinting prior articles from the column. This month's article on the Federal Democratic Republic of Ethiopia was originally printed in 2003 but contains updates to their coordinate system since then.

**E**thiopia, occasionally called Abyssinia, is an ancient country in Northeast Africa. It is bounded on the north by Eritrea (912 km), on the east by Djibouti (337 km) and Somalia (1,626 km), on the south by Somalia and Kenya (830 km), and on the west by Sudan (1,606 km). Ethiopia has an area slightly less than twice the size of Texas, it is landlocked, and is mainly high plateau with a central mountain range divided by the Great Rift Valley. The lowest point is Denakil (-125 m), and the highest point is Ras Dashen Terara (4,620 m). Modern Ethiopia began with the reign of Tewodros II and the conquest of other chiefs in 1855. Later coming under Italian rule in 1882 and claimed as an Italian Protectorate by the Treaty of Ucciali in 1889, the coastal region was made a separate Italian Colony in 1890 and named Eritrea. Territorial integrity of Ethiopia was recognized by Great Britain, France, and Italy in 1906. Invaded by the Italians in 1935, and organized with Eritrea and Italian Somaliland as the Empire of Italian East Africa, the region was liberated by the British in 1941. The new constitution was adopted in 1987. Ethiopia's entire coastline along the Red Sea was lost with the *de jure* independence of Eritrea on 27 April 1993.

Very little mapping was done of Ethiopia in the 19<sup>th</sup> century. One of the earliest investigations of the region resulted in a "Report of the German Expedition to East Africa, 1861 and 1862," published in 1864 by Munzinger. The British explorer, Sir Samuel Baker, wrote of the region in 1867 in "The Nile Tributaries of Abyssinia." The Italians made some ground surveys in the region of Eritrea from 1888 to 1891, and these surveys formed the basis of the old *Carta della Colonia Eritrea* (Map of the Colony of Eritrea) at a scale of 1:50,000 which was published from 1909 through

## FEDERAL DEMOCRATIC REPUBLIC OF ETHIOPIA



1938. Another series was also published during the same time by the Italians at a scale of 1:100,000. New surveys of 1935 through 1938 resulted in one sheet being compiled on a Santoni stereoplotter with 50-meter contours. Smaller scale series were derivative compilations at the time.

The Ethiopian Datum of 1936 was established by the Italians at the West End of Metahara Base (10,083.560 m) where  $\Phi_0 = 8^\circ 53' 22.53'' \pm 0.18''$  N,  $\Lambda_0 = 39^\circ 54' 24.99''$  East of Greenwich, the reference azimuth to Monte Fantalli was  $\alpha_0 = 13^\circ 05' 21.97'' + 0.43''$ , and the presumed ellipsoid of reference was the International 1924 where  $a = 6,378,188$  m and  $1/f = 297$ . The check base for the chain commencing at Metahara was Giggiga base, which was 12,962.620 m in length. Halfway north from Metahara base to the now Eritrean port city of Massawa was the North End of Alomalà base (18,211.982 m) where  $\Phi_0 = 12^\circ 24' 56.56'' \pm 0.13''$  N,  $\Lambda_0 = 39^\circ 33' 30.42'' \pm 0.30''$  East of Greenwich, and the reference azimuth to the South End of Alomalà base was  $\alpha_0 = 180^\circ 00' 03.88'' \pm 0.18''$ . The old Italian 1:50,000-scale series mentioned above is based on the old datum origin located in the (now) Eritrean capitol city of Asmara. The coordinates of that origin elude me, and I suspect that the observations

Photogrammetric Engineering & Remote Sensing  
Vol. 87, No. 3, March 2021, pp. 157–158.

0099-1112/21/157–158

© 2021 American Society for Photogrammetry  
and Remote Sensing

doi: 10.14358/PERS.87.3.157

may have been made by the Italian navy rather than by the Istituto Geografico Militare of Firenze (Florence). In any case, there was no grid printed on any of the above series, even though the cartographic and geodetic work was done by the Italian military!

The Blue Nile River Basin Investigation Project was funded by the United States, and the geodetic work was performed by the U.S. Coast & Geodetic Survey. The origin of the geodetic work was in southern Egypt near Abu Simbel, south of Lake Nasser, at station Adindan where  $\Phi_0 = 22^\circ 10' 07.1098''$  N,  $\Lambda_0 = 31^\circ 29' 21.6079''$  East of Greenwich, the deflection of the vertical  $\zeta = +2.38''$  and  $\eta = -2.51''$ , and the ellipsoid of reference was the Clarke 1880 (modified) where  $a = 6,378,249.145$  m and  $1/f = 293.465$ . The Blue Nile Datum of 1958 appears to be the established classical datum of Ethiopia and much of North Africa. Adindan is the name of the origin, it is not the name of the datum; a most common mistake found in many "reference works." The Ethiopian Transverse Mercator grid is based on a central meridian where  $\lambda_0 = 37^\circ 30' E$ , scale factor at origin where  $m_0 = 0.9995$ , False Easting = 450 km, and False Northing = 5,000 km.

Ethiopia and Kenya signed a boundary treaty on 09 June 1970, and the field surveys for the demarcation of the border were performed by British surveyors. The datum used for

that survey was the Arc 1960 Datum, referenced to the Clarke 1880 (modified) ellipsoid. The grid system used at the time was the East Africa Transverse Mercator Belts H, J, and K where the central meridians are  $\lambda_0 = 37^\circ 30' (H)$ ,  $42^\circ 30' (J)$ , and  $47^\circ 30' (K)$ ; the scale factors at origin are all where  $m_0 = 0.9995$ , all False Eastings = 400 km, and False Northings = 4,500 km.

An International Boundary Commission has been formed by the United Nations to establish and demarcate a boundary between Ethiopia and Eritrea. The boundary has been researched and established, but the demarcation remains to be performed at the present time. The 125-page document published by the United Nations in April 2002 makes for some fascinating reading. The datum of record of the Commission is the WGS84, and will be used for the demarcation survey someday.

There are two sets of parameters published by NIMA for transforming from the Blue Nile Datum of 1958 to the WGS84 Datum: the mean solution for Sudan and Ethiopia is based on a 22-station solution where  $\Delta X = -166m \pm 5m$ ,  $\Delta Y = -15m \pm 5m$ , and  $\Delta Z = 204m \pm 5m$ . The solution for Ethiopia is based on an eight-station solution where  $\Delta X = -165m \pm 3m$ ,  $\Delta Y = -11m \pm 3m$ , and  $\Delta Z = +206m \pm 3m$ .

### Ethiopia Update

A 2019 thesis covers a detailed analysis of datum transformations in the northwest area of Ethiopia, but has no new data points, just more elaborate math models:

- Determination of Parameters for Datum Transformation between WGS 84 and ADINDAN-Ethiopia, Hassen, A. M.
- <http://etd.aau.edu.et/bitstream/handle/123456789/23487/Abubeker%20Mohammed.pdf?sequence=1&isAllowed=y>

As referenced in the original column, the United Nations has now published some boundary monuments in a report:

- Eritrea-Ethiopia Claims Commission - Statement by the Eritrea-Ethiopia Boundary Commission with Annex (List of Boundary Points and Coordinates) 27 November 2006.
- [https://legal.un.org/riaa/cases/vol\\_XXVI/771-799.pdf](https://legal.un.org/riaa/cases/vol_XXVI/771-799.pdf)

The contents of this column reflect the views of the author, who is responsible for the facts and accuracy of the data presented herein. The contents do not necessarily reflect the official views or policies of the American Society for Photogrammetry and Remote Sensing and/or the Louisiana State University Center for GeoInformatics (C<sup>4</sup>G).

This column was previously published in *PE&RS*.



**Too young to drive the car? Perhaps!**

**But not too young to be curious about geospatial sciences.**

The ASPRS Foundation was established to advance the understanding and use of spatial data for the betterment of humankind. The Foundation provides grants, scholarships, loans and other forms of aid to individuals or organizations pursuing knowledge of imaging and geospatial information science and technology, and their applications across the scientific, governmental, and commercial sectors.

**Support the Foundation, because when he is ready so will we.**

**[asprsfoundation.org/donate](http://asprsfoundation.org/donate)**



## JOURNAL STAFF

### Editor-In-Chief

Alper Yilmaz, Ph.D., PERSEditor@asprs.org

### Associate Editors

Rongjun Qin, Ph.D., qin.324@osu.edu

Michael Yang, Ph.D., michael.yang@utwente.nl

Petra Helmholtz, Ph.D., Petra.Helmholtz@curtin.edu.au

Bo Wu, Ph.D., bo.wu@polyu.edu.hk

Clement Mallet, Ph.D., clemallet@gmail.com

Jose M. Pena, Ph.D., jmpena@ica.csic.es

Prasad Thenkabail, Ph.D., pthenkabail@usgs.gov

Ruisheng Wang, Ph.D., ruishengwang@ucalgary.ca

Desheng Liu, Ph.D., liu.738@osu.edu

Valérie Gouet-Brunet, Ph.D., valerie.gouet@ign.fr

Dorota Iwaszczuk, Ph.D., dorota.iwaszczuk@tum.de

Qunming Wang, Ph.D., wqm11111@126.com

Filiz Sunar, Ph.D., fsunar@itu.edu.tr

Norbert Pfeifer, np@ipf.tuwien.ac.at

Jan Dirk Wegner, jan.wegner@geod.baug.ethz.ch

Hongyan Zhang, zhanghongyan@whu.edu.cn

Dongdong Wang, Ph.D., dddwang@umd.edu

Zhenfeng Shao, Ph.D., shaozhenfeng@whu.edu.cn

Ribana Roscher, Ph.D., ribana.roscher@uni-bonn.de

Sidike Paheding, Ph.D., spahedin@mtu.edu

### Contributing Editors

#### Highlight Editor

Jie Shan, Ph.D., jshan@ecn.purdue.edu

#### Feature Articles

Michael Joos, CP, GISP, featureeditor@asprs.org

#### Grids & Datums Column

Clifford J. Mugnier, C.P., C.M.S., cjmce@lsu.edu

#### Book Reviews

Sagar Deshpande, Ph.D., bookreview@asprs.org

#### Mapping Matters Column

Qassim Abdullah, Ph.D., Mapping\_Matters@asprs.org

#### Sector Insight

Lucia Lovison-Golob, Ph.D., lucia.lovison@sat-drones.com

Bob Ryerson, Ph.D., FASPRS, bryerson@kimgeomatics.com

#### GIS Tips & Tricks

Alvan Karlin, Ph.D., CMS-L, GISP akarlin@Dewberry.com

### ASPRS Staff

#### Assistant Director — Publications

Rae Kelley, rkelly@asprs.org

#### Electronic Publications Manager/Graphic Artist

Matthew Austin, maustin@asprs.org

#### Advertising Sales Representative

Bill Spilman, bill@innovativemediasolutions.com

## ASPRS ANNOUNCES STUDENT CONFERENCE PRESENTATION GRANTS!

ASPRS, with support of the ASPRS Foundation, has identified funding to sponsor Student Presentations in the upcoming ASPRS 2021 Annual Conference, which will be held virtually from March 29 – April 2, 2021. Individuals who are awarded Student Presentation Grants will have their conference registration fees waived, and will receive a complementary one-year student membership in ASPRS. Click the link above for full details.

### How do I know if I qualify for a Student Conference Presentation Grant?

- The student must be the conference Presenter; other non-students may be listed as co-authors.
- The student will be asked to provide proof of current enrollment before receiving final approval for a conference grant. Proof of current enrollment could be a copy of a student ID, an unofficial transcript, registration record for the current semester, or a letter from a supporting faculty member on institution letterhead.
- Abstracts that are accepted by the Technical Program Committee but not chosen to receive grants will still be eligible to participate in the conference. The presenters will be required to register and pay appropriate fees.

## NEW ASPRS MEMBERS

ASPRS would like to welcome the following new members!

### At Large

Ryan A. Burley  
Michael Corry Dye

Tom Tallada  
Crystal C. Thomas, PE, PS

### Cascadia

Matt Barker  
Forrest Corcoran  
Maria Krivova  
Lauren Eileen McKinney-Wise  
Chase Simpson  
Sudeera Wickramaratna

**Northeastern**  
Ralph Howe, III  
Jonathan Mikolin

**Pacific Southwest**  
Jacob Ryan Nesslage  
Gabriel Armas

### Potomac

Nazmul Huda  
Justin Lee  
Trung Tran

### Rocky Mountain

Robin E. Angulo  
Trent Casi  
Caitlin Elizabeth Dee Betancur  
Joseph D. Fargnoli  
Sarah Jaffe  
Stephen J. Leisz, Ph.D.  
Zach Taraschi

### Florida

Michael Barretto  
Matthew D. Deal  
Leo Harry Meirose, III

### Mid South

James Cannon  
Alisa Coffin  
James F. Kelly, Jr.  
Andy Vigstol  
Michael Williams

### North Atlantic

Jonathan Sayre

FOR MORE INFORMATION ON ASPRS MEMBERSHIP,  
VISIT [HTTP://WWW.ASPRS.ORG/JOIN-NOW](http://www.asprs.org/join-now)

*Your Path To Success In The Geospatial Community*

# Call for Submissions

## Remote Sensing Monitoring for Urban Environment

*Photogrammetric Engineering and Remote Sensing (PE&RS)* is seeking submissions for a special issue on Remote Sensing Monitoring for Urban Environment.

Urban remote sensing provides images with multiple spatio-temporal-spectral attributes, which can provide qualitative, quantitative, dynamic and comprehensive information and support for urban environmental monitoring and evaluation, and serve urban planning and management, ecological environment protection. In recent decades, global urban areas have been rapidly expanding, especially in developing countries. Rapid urbanization, along with manufacturing industries and large number of vehicles has resulted in serious environmental problems, called “urban diseases”, including increased vulnerability to natural hazards, natural vegetation cover decline and arable land loss, urban heat islands, air pollution, hydrological circle alteration and biotic homogenization. Urban ecosystems are strongly influenced by anthropogenic activities. Considering this, this special issue of PE&RS is aimed at reporting novel studies on exploiting remote sensing big data to monitor and improve urban environment, and showing the potential of remote sensing in developing sustainable cities, including but not limited to:

- Urban thermal-environment remote sensing
- Remote sensing image acquisition and processing for urban environment
- Remote sensing dynamic monitoring of urban expansion
- Remote sensing change detection of urbanization
- Remote sensing retrieval of urban ecological environment
- Remote sensing evaluation of urban human settlements
- Urban sustainability indicators and assessment
- Urban environmental monitoring

Papers must be original contributions, not previously published or submitted to other journals. Submissions based on previous published or submitted conference papers may be considered provided they are considerably improved and extended. Papers must follow the instructions for authors at <http://asprs-pers.edmgr.com/>.

### Important Dates (Tentative)

- March 1, 2021—Submission system opening
- September 31, 2021—Submission system closing
- Planned publication date is December 2021
- Submit your manuscript to <http://asprs-pers.edmgr.com/> by September 31, 2021.

### Guest Editors

#### **Zhenfeng Shao, Wuhan University, China**

Prof. Zhenfeng Shao, Professor at the State Key Laboratory of Information Engineering in Surveying, Mapping and Remote Sensing, Wuhan University, China. His research interests include urban remote sensing. He is now an associate editor of Email: [shaozhenfeng@whu.edu.cn](mailto:shaozhenfeng@whu.edu.cn).

#### **Orhan Altan, Istanbul Technical University, Turkey**

Prof. Orhan ALTAN, Professor at the Department of Geomatics Engineering, Istanbul Technical University, Turkey. He is Past President and Honorary Member of ISPRS, Honorary Member of Science Academy. He has published more than 200 scientific papers in scientific journals and conferences, and editor or co-editor of more than 20 international books. Email: [oaltan@itu.edu.tr](mailto:oaltan@itu.edu.tr).

#### **J.L.van Genderen, University of Twente, Netherlands**

Professor J.L.van Genderen, Professor at the Department of Earth Observation Science, Faculty of Geo-information Science and Earth Observation(ITC),University of Twente, Netherlands, he is an Associate Editor of the international journal GEO Spatial Information Science. His research interests include urban remote sensing and new technologies for urban management. Email: [Genderen@alumni.itc.nl](mailto:Genderen@alumni.itc.nl).

# Extraction of Impervious Surface Using Sentinel-1A Time-Series Coherence Images with the Aid of a Sentinel-2A Image

Wenfu Wu, Jiahua Teng, Qimin Cheng, and Songjing Guo

## Abstract

The continuous increasing of impervious surface (IS) hinders the sustainable development of cities. Using optical images alone to extract IS is usually limited by weather, which obliges us to develop new data sources. The obvious differences between natural and artificial targets in interferometric synthetic-aperture radar coherence images have attracted the attention of researchers. A few studies have attempted to use coherence images to extract IS—mostly single-temporal coherence images, which are affected by de-coherence factors. And due to speckle, the results are rather fragmented. In this study, we used time-series coherence images and introduced multi-resolution segmentation as a postprocessing step to extract IS. From our experiments, the results from the proposed method were more complete and achieved considerable accuracy, confirming the potential of time-series coherence images for extracting IS.

## Introduction

Impervious surface (IS) as an indicator for the urban environment can reflect the status of urban development to some extent (Liu *et al.* 2019; Gong *et al.* 2020). An increase in IS usually brings a series of problems, including urban heat islands (Xu 2010) and a decrease in cultivated land (Shao *et al.* 2020). Therefore, monitoring the distribution of IS makes a lot of sense and can advance the implementation of the United Nations 2030 Sustainable Development Agenda. Satellite remote sensing has become the most effective tool to monitor IS due to its advantages of low cost, large imaging range, and short revisit cycle (Shao *et al.* 2020).

Numerous urban IS extraction methods based on remote sensing have been proposed, mainly including visual interpretation (Zhou and Wang 2008; X. Zhang *et al.* 2013), spectral mixing analysis (C. Wu and Murray 2003; Z. Zhang *et al.* 2015), urban-index methods (Deng and Wu 2012; Liu *et al.* 2013; Shao, Tian and Shen 2014; Wang *et al.* 2015), image-classification methods (Shao and Liu 2014; Li and Gong 2016; L. Zhang, Weng and Shao 2017), and multi-source image-fusion methods (H. Zhang *et al.* 2019; Lin *et al.* 2020). Nevertheless, these methods have some limitations. For

example, although visual interpretation is very accurate, it is time-consuming and laborious, especially to extract IS at city, region, or larger scales. Spectral mixing analysis methods are mainly used in low- and medium-resolution images, and are proposed to solve the problem of mixed pixels and obtain results at sub-pixel scale. But the selection of end members remains challenging in heterogeneous urban areas. It is suitable to use high-resolution images in urban areas (Shao *et al.* 2020). Image-classification methods are the most used, but they face some problems, such as spectrum confusion. Multi-source data fusion is considered a promising method for mapping IS (Weng 2012). There are three levels (pixel, feature, and decision) for image fusion. For pixel-level fusion, fusion rules must be carefully designed to improve the extraction of IS (W. Wu, Guo and Cheng 2020). Unfortunately, the design of fusion rules is very difficult, without clear rules that can be obeyed.

Due to the all-weather and day-night imaging ability of synthetic-aperture radar (SAR), it has become an important data source for IS extraction (Y. Zhang, Zhang and Lin 2014). Interferometric SAR (InSAR), an important branch of SAR, is widely used in surface deformation (Zhao *et al.* 2018) and earthquake deformation (Cheloni *et al.* 2017). As an intermediate product of InSAR processing, coherence images have attracted the attention of researchers and been used in many fields, such as land cover classification (Jiang *et al.* 2017; Yun *et al.* 2019), change detection (Del Frate, Pacifici and Solimini 2008), and human-settlement detection (Corbane *et al.* 2018). In coherence images, human-made targets generally are stable with high coherence, while natural targets have low coherence with great fluctuation. This property is useful for distinguishing IS and pervious surface (NIS). Therefore, a few studies have attempted to introduce coherence images into IS extraction, with most using a single image which is sensitive to temporal de-coherence factors (L. Yang *et al.* 2009). In addition, the results are fragmented due to inherent speckle. In view of this, a time-series analysis technique may be an effective solution. But the potential of time-series coherence images for IS extraction has still not been fully explored.

In this study, based on the assumption that urban land covers do not change significantly in a few months, we used *Sentinel-1A* time-series coherence images to extract IS with a random-forest (RF) algorithm. To further relieve the effect of speckle, we introduced multi-resolution segmentation as a postprocessing step. First we generated the time-series coherence images. Second, we used the time-series coherence images with the RF classifier to obtain preliminary IS results. Third, we performed multi-resolution segmentation on *Sentinel-2A*

---

Wenfu Wu is with the School of Remote Sensing and Information Engineering, Wuhan University, Wuhan, China.

Jiahua Teng is with the Ministry of Ecology and Environment Center for Satellite Application on Ecology and Environment, Beijing, China.

Qimin Cheng is with the School of Electronics Information and Communications, Huazhong University of Science and Technology, Wuhan, China (chengqm@hust.edu.cn).

Songjing Guo is with the School of Geography and Information Engineering, China University of Geosciences, Wuhan, China.

---

Photogrammetric Engineering & Remote Sensing  
Vol. 87, No. 3, March 2021, pp. 161–170.  
0099-1112/21/161–170

© 2021 American Society for Photogrammetry  
and Remote Sensing  
doi: 10.14358/PERS.87.3.161

data and obtained the final IS result. Finally, we assessed and compared the accuracy of the results. The overall workflow of the study will be described in detail later.

## Study Area and Data Source

### Study Area

Tianjin is the study area (Figure 1), situated in northern China close to the capital, Beijing. It is at the confluence and estuary of the Hai River, the South Canal, the Ziya River, the Daqing River, the Yongding River, and the North Canal. The Hai River goes all the way through Tianjin to enter the sea. Due to its advantageous geographical position, Tianjin has occupied an important strategic position over the long history of China. Since the implementation of the reform and opening-up policy, Tianjin has ushered in a period of rapid development. Now it is one of the national central cities, with an urbanization rate of 84% by 2019. Such a high urbanization rate has increased the area of IS and brought a series of serious environmental problems. Therefore, monitoring the spatial distribution of IS in Tianjin is of high significance and is helpful for the city's sustainable development.

### Data Source and Preprocessing

*Sentinel-1A* and *Sentinel-2A* are the two data sources used in this study. We downloaded the data freely from the European Space Agency (<https://scihub.copernicus.eu/>). The acquisition dates of these images are listed in Table 1. The *Sentinel-1A* satellite was successfully launched on 3 April 2014, carrying a C-band SAR antenna with VV (vertical transmit and vertical receive) and VH (vertical transmit and horizontal receive) polarization modes. *Sentinel-1A* can

Table 1. Acquisition dates in 2017 of *Sentinel-1A* and *Sentinel-2A* data used in this study

Satellite	Acquisition Dates
<i>Sentinel-1A</i>	7 January
	19 January
	31 January
	12 February
	24 February
	8 March
	20 March
	1 April
	25 April
7 May	
<i>Sentinel-2A</i>	14 June

provide four modes of data—Strip Maps, Interferometric Wide Swath, Extra Wide Swath, and Wave Mode—but only three of them (Strip Maps, Interferometric Wide Swath, and Extra Wide Swath) can be downloaded freely. The Interferometric Wide Swath Single Look Complex products with VV and VH polarization were used in this study. Preprocessing such as speckle filtering, radiometric calibration, terrain correction, and interference calculation was carried out in the Sentinel Application Platform (SNAP) version 7.0 software.

A *Sentinel-2A* MultiSpectral Instrument Level-1C image was used for multi-resolution segmentation. *Sentinel-2A* images have a total of 12 bands: three bands with 60-m resolution, five with 20-m resolution, and four with 10-m resolution. We selected a nearly cloud-free image covering the study area. Since Level-1C data were topographically corrected but not atmospheric, we used the sen2cor SNAP plug-in to conduct atmospheric correction on Level-1C data and got Level-2A data.

The images used here first need to be registered. We used the automatic registration module of ENVI 5.3 software and coordinated with manual inspection for image registration. The root-mean-square error for registration was less than one pixel. After preprocessing, images were registered to the georeference system of the Universal Transverse Mercator projection (Zone 50N) and Datum World Geodetic System 84.

### Method

Figure 2 shows the overall workflow of this study. The main steps are generating the coherence image, applying the RF classifier, running postprocessing, and assessing accuracy. In this section, we will describe them in detail.

#### Generating the Coherence Image

Coherence images are one intermediate product generated in InSAR processing. The value of a coherence image illustrates the quality of the interferogram—the larger the value, the better the interferogram quality. During InSAR processing, it is often used to determine the filter parameters of the interference fringe and generate mask files to guide phase unwrapping. Coherence can be calculated using the equation

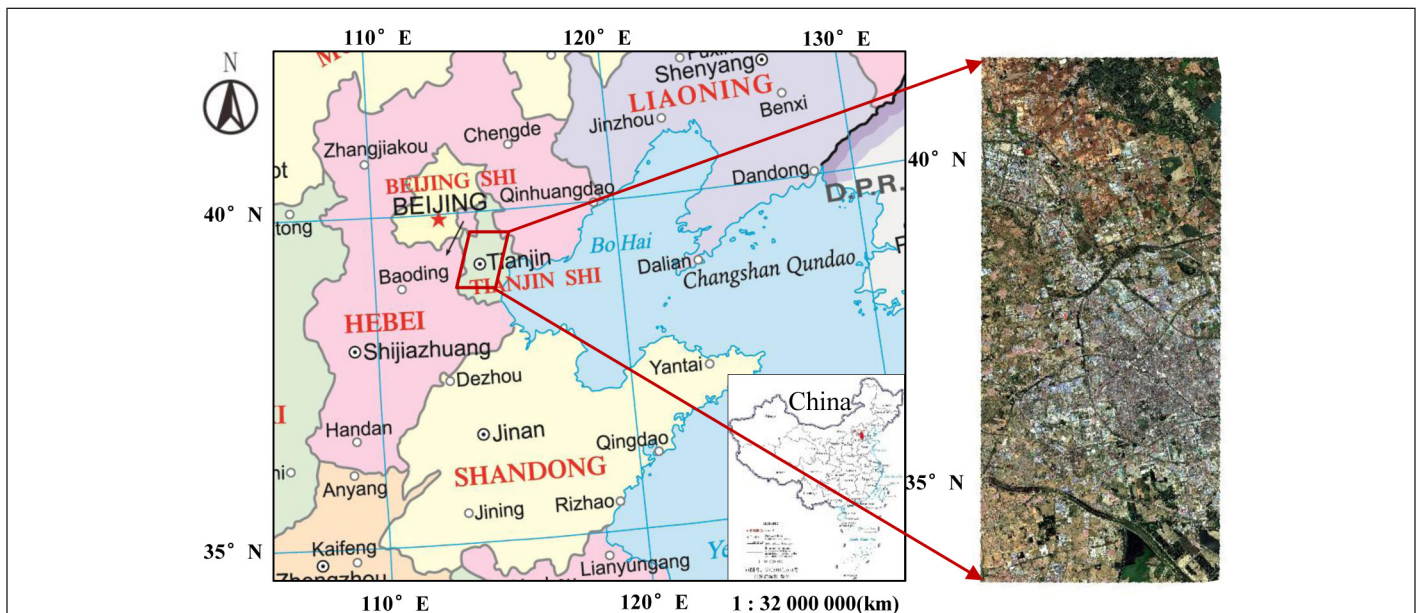


Figure 1. The geographical location of the study area and the corresponding *Sentinel-2A* image (R: Band 4, G: Band 3, B: Band 2).

$$\gamma = \frac{|E(s_1 s_2^*)|}{\sqrt{E(s_1 s_1^*) E(s_2 s_2^*)}} \quad (1)$$

where  $E(*)$  is the mathematical expectation,  $*$  is complex conjugate multiplication, and  $s_1$  and  $s_2$  are two co-registered single-look complex images

$$s_1 = \rho_1(R_1) \exp(-j\varphi_1) = \rho_1(R_1) \exp\left(-j\left[2\pi\left(\frac{2R_1}{\lambda}\right) + \varphi_0\right]\right) \quad (2)$$

$$s_2 = \rho_2(R_2) \exp(-j\varphi_2) = \rho_2(R_2) \exp\left(-j\left[2\pi\left(\frac{2R_2}{\lambda}\right) + \varphi_0\right]\right), \quad (3)$$

with  $\varphi_1$  and  $\varphi_2$  the phase value of a ground object obtained by the two images,  $\rho_1(R_1)$  and  $\rho_2(R_2)$  the amplitude value,  $R_1$  and  $R_2$  the distance between the satellite and the ground object during imaging, and  $\varphi_0$  a random phase.

Generally, in order to reduce the influence of speckle and based on the assumption that the random process of the scatter in a certain region size is stable and ergodic the mean value of the whole region can be replaced with the spatial average of a local region. So the coherence can be calculated through a sliding window, allowing us to rewrite Equation (1) as

$$\bar{\gamma} = \frac{\left| \sum_{n=1}^N \sum_{m=1}^M s_1(n, m) \cdot s_2^*(n, m) \right|}{\sqrt{\sum_{n=1}^N \sum_{m=1}^M |s_1(n, m)|^2} \sqrt{\sum_{n=1}^N \sum_{m=1}^M |s_2(n, m)|^2}}, \quad (4)$$

where  $N \times M$  is the size of the sliding window. In general,  $N$  and  $M$  are the same. The window size will affect the calculation of coherence: a large window will not only reduce the spatial resolution but may also be mixed with ground objects

that are not the same type as the central pixel, resulting in deviation of the coherence (Amitrano *et al.* 2016). Although a smaller window can keep the coherence image at a higher resolution, the estimation will be more biased (Touzi *et al.* 1999). Previous research has shown that a window size of  $5 \times 5$  is suitable for urban areas (Schneider *et al.* 2006). Therefore, we used that size in this study. The value of coherence ranges from 0 to 1; the larger the value, the better the coherence, and vice versa.

### Random-Forest Algorithm

Random forest is a typical ensemble learning algorithm, first proposed by Breiman (Breiman *et al.*, 2001), which consists of several decision trees. The bootstrap sample technique was used to select the training set for each decision tree. The final decision is made by voting the results of multiple decision trees. Compared with a decision-tree algorithm, RF conquers the problem of overfitting, is not sensitive to noise and outliers, and has scalability and parallelism for high-dimensional data classification. It also has significant advantages compared with state-of-the-art methods such as deep learning. First, it needs less training time and is easy to implement. Second, it is a white box, which yields explicable results. Finally, it can attain considerable performance with fewer samples. Therefore, RF has been widely used in the field of remote sensing and has achieved considerable results (Y. Zhang *et al.* 2014; Shao *et al.* 2016, 2019; for detailed information on RF, see Breiman *et al.* 2001).

### Postprocessing

Due to the inherent speckle, the IS extracted from the coherence image at the pixel level is fragmented, which is illustrated in Figure 3. Image segmentation can obtain homogeneous regions with less noise. Inspired by this idea, we introduced multi-resolution segmentation as a postprocessing step to assist the IS extraction.

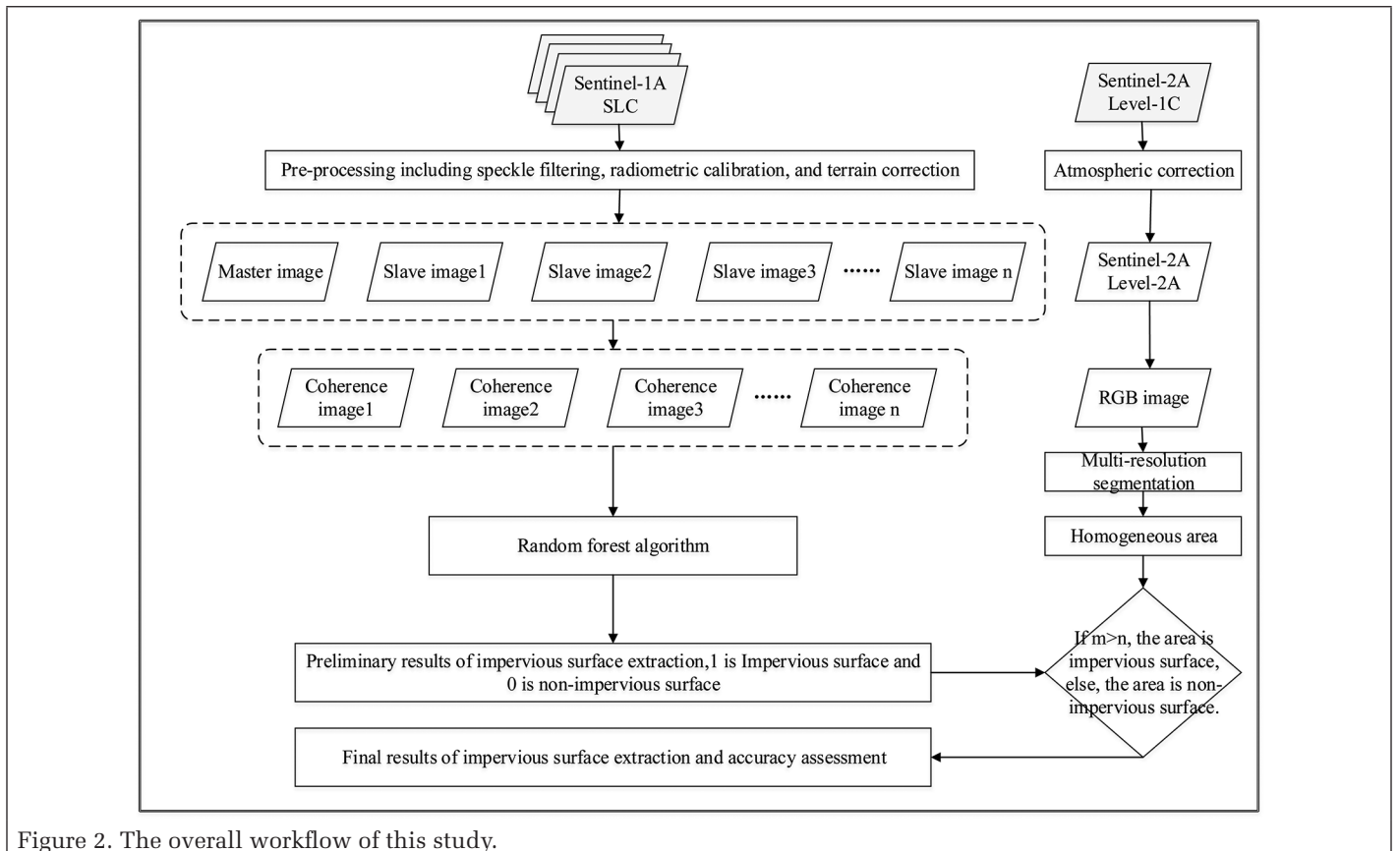


Figure 2. The overall workflow of this study.

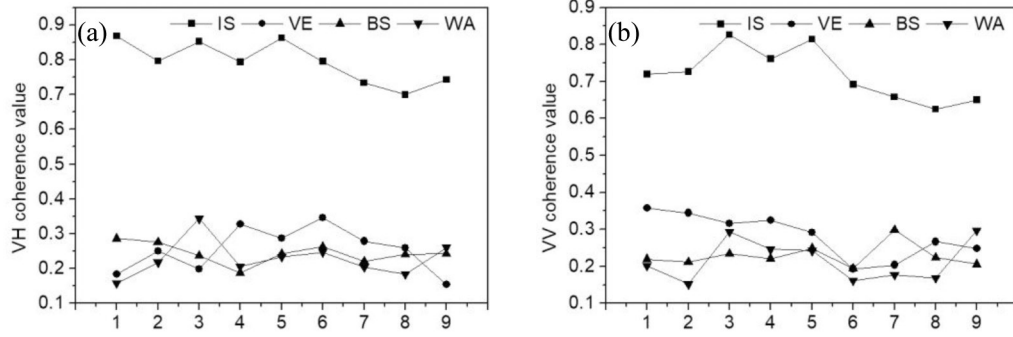


Figure 3. Schematic illustration of impervious-surface extraction using VH time-series coherence images at the pixel level.

### False-Color Image Composition

Multi-resolution segmentation is performed on the *Sentinel-2A* image. In this study, we do not use the *Sentinel-2A* image for segmentation directly; we use false-color image composed of the normalized difference vegetation index (NDVI), normalized difference built-up index (NDBI), and modified normalized difference water index (MNDWI). The three indices perform well in urban-area extraction. For example, NDVI, a commonly used index, can effectively detect vegetation. MNDWI can extract water bodies in the urban environment and distinguish them from shadow (Xu 2006). NDBI is often used to extract built-up area (Zha, Gao and Ni 2003). In this study, we only need to obtain homogeneous regions, not specific classification labels. Therefore, we used NDVI (red), NDBI (green), and MNDWI (blue) to compose a false-color image with homogeneous regions. NDVI, NDBI, and MNDWI can be calculated by

$$\text{NDVI} = \frac{\rho_{\text{NIR}} - \rho_{\text{Red}}}{\rho_{\text{NIR}} + \rho_{\text{Red}}} = \frac{\rho_{\text{Band8}} - \rho_{\text{Band4}}}{\rho_{\text{Band8}} + \rho_{\text{Band4}}} \quad (5)$$

$$\text{NDBI} = \frac{\rho_{\text{MIR}} - \rho_{\text{NIR}}}{\rho_{\text{MIR}} + \rho_{\text{NIR}}} = \frac{\rho_{\text{Band11}} - \rho_{\text{Band8}}}{\rho_{\text{Band11}} + \rho_{\text{Band8}}} \quad (6)$$

$$\text{MNDWI} = \frac{\rho_{\text{Green}} - \rho_{\text{NIR}}}{\rho_{\text{Green}} + \rho_{\text{NIR}}} = \frac{\rho_{\text{Band3}} - \rho_{\text{Band8}}}{\rho_{\text{Band3}} + \rho_{\text{Band8}}}, \quad (7)$$

where  $\rho_{\text{NIR}}$ ,  $\rho_{\text{Red}}$ ,  $\rho_{\text{MIR}}$ , and  $\rho_{\text{Green}}$  are the reflectance in the near-infrared, red, mid-infrared, and green bands, respectively.

### Multi-Resolution Segmentation

Multi-resolution segmentation is an object-oriented method. It is a technique of merging regions based on minimum heterogeneity from the bottom to the top using spectral, textural, and shape features (Duro, Franklin and Dubé 2012). We must first set a proper scale parameter. Then we start from a random pixel of the image and calculate the heterogeneity after merging with the adjacent pixel, and compare it with the scale parameter. If the heterogeneity is less than the square of the scale parameter, we continue to merge the adjacent pixel; otherwise we end the segmentation process (Tian and Chen 2007). The region heterogeneity is obtained by the weight sum of spectral and shape heterogeneity:

$$f = \omega \cdot \Delta h_{\text{color}} + (1 - \omega) \cdot \Delta h_{\text{shape}}, \quad \omega \in [0, 1], \quad (8)$$

where  $f$  is the region heterogeneity,  $\omega$  is the weight, and  $\Delta h_{\text{color}}$  and  $\Delta h_{\text{shape}}$  are the spectral and shape heterogeneity, respectively, which can be estimated by

$$\Delta h_{\text{color}} = \sum_c \omega_c \cdot \sigma_c \quad (9)$$

$$\Delta h_{\text{shape}} = \omega_{\text{compact}} \cdot \Delta h_{\text{compact}} + (1 - \omega_{\text{compact}}) \cdot \Delta h_{\text{smooth}}, \quad \omega_{\text{compact}} \in [0, 1], \quad (10)$$

with  $C$  the number of bands,  $\omega_c$  the weight corresponding to each band, and  $\sigma_c$  the spectral reflectance. Shape heterogeneity is determined by compactness and smoothness, with respective parameters of  $\Delta h_{\text{compact}}$  and  $\Delta h_{\text{smooth}}$ , and  $\omega_{\text{compact}}$  is the weight of compactness.

For a detailed mathematical formulation of multi-resolution segmentation, please refer to previous studies (Tian and Chen 2007; Duro *et al.* 2012).

### Extraction of IS and Assessment of Accuracy

In this study, we focus on the extraction of just IS; the other land covers are not our concern. So only two land cover types were identified: IS and NIS. First, we produced time-series coherence images, and then we inputted them into the configured RF classifier to obtain a preliminary extraction result. The IS was labeled 1, and the NIS was labeled 0. Second, we performed multi-resolution segmentation on the NDVI-NDBI-MNDWI false-color image to get a series of homogeneous regions which can be regarded as a single type (H. Yang *et al.* 2018). Third, we obtained the final IS extraction result. For each homogeneous region, if the number of IS pixels was greater than the number of NIS pixels, the region was classified as IS, and vice versa.

To assess the accuracy of IS extraction, five accuracy indices were used: overall accuracy (OA), kappa coefficient, user's accuracy (UA), producer's accuracy (PA), and  $F_1$  score. Before classification, we need to make training and testing samples to train and test the RF model. In this study, a total of 1113 samples were randomly selected with the aid of visual interpretation of the *Sentinel-2A* image and China's 2-m-resolution IS map produced by our group (Shao *et al.* 2018); 526 were IS and 587 were NIS. Two-thirds of these samples were used to train the model, and the rest were used to validate it.

### Experiment and Results

In this section, we first generated time-series coherence images. Then we optimized two key parameters in the RF model and implemented multi-resolution segmentation for the NDVI-NDBI-MNDWI false-color image. Finally, we extracted the IS and assessed the accuracy.

#### Generation of Time-Series Coherence Images

In the coherence image, natural targets are more sensitive to temporal de-coherence factors, such as changes in moisture, vegetation growth, and wind direction. But these factors have little effect on artificial targets. So the coherence of NIS will change over time with low coherence, whereas IS is stable target that can maintain good coherence over a long time. According to this property, a moderate extension of the time baseline is helpful to distinguish IS and NIS. Therefore, the *Sentinel-1A* image acquired on 7 January 2017 is used as the master image in this study, and the other images were used as the slave images, and time-series coherence images were generated. Table 2 shows the coherence-image pairs. There

are nine coherence pairs here. The time baseline is gradually increased and the perpendicular baseline is short, indicating a better quality of the coherence image. Figure 4 shows the VV and VH polarization temporal-coherence profiles of land covers. IS can still maintain good coherence when the time baseline is 120 days. The coherence value of other land covers is low and fluctuates greatly. The time-series coherence difference between IS and NIS is obvious.

### Parameter Optimization for RF Model

In this study, a total of nine features (time-series coherence images with VH or VV polarization) were inputted into the RF model. In the RF model, two parameters—the number of decision trees (Ntree) and the number of variables for splitting each node (Ntry)—affect the accuracy of the model. The grid-search technique, which is an exhaustive search method for specifying parameters, is often used to optimize the two parameters. The possible values of both parameters are combined and form a grid. Each combination is then used to configure the RF model, and the accuracy of the model is evaluated using cross validation. The parameters corresponding to the highest accuracy are selected. In our experiment, we also used the grid-search method to optimize the two parameters of the RF model, with the cross validation set to 10. The value of Ntree ranged from 1 to 500 with steps of 10, and Ntry from 1 to 9 with steps of 1. The accuracy is evaluated by the out-of-bag score (OOB\_Score).

Figure 5 shows the optimization of the parameters with VH and VV time-series coherence images. For VH and VV polarization, the performance of the RF model is similar. Compared to Ntry, Ntree has a stronger effect on the performance of RF model. When we fixed Ntree and gradually increased Ntry, the accuracy was not greatly improved. However, when we fixed Ntry and gradually increased Ntree, the accuracy continued to increase until Ntree reached 100 and OOB\_Score reached above 0.95. When Ntree is greater than 100, the RF model becomes stable and the OOB\_Score changes very little with further increases of Ntree. For VH polarization, the optimal values of Ntree and Ntry are 391 and 1, respectively. For VV polarization, the optimal values of Ntree and Ntry are 411 and 4, respectively. These optimal parameters will be configured into the RF model for subsequent IS extraction.

### Segmentation of the NDVI-NDBI-MNDWI False-Color Image

Scale, shape, and compactness are three important parameters to be set for multi-resolution segmentation. Unfortunately, there are no clear rules for determining the optimal values of these parameters. Their ideal values are usually determined by trial and error. In this study, the experiments were implemented in eCognition software. We first determined the scale parameter. After determining the scale parameter, we set both

shape and compactness parameters to 0.5 and then adjusted the scale gradually. According to the experiment results, the smaller the scale is, the more fragmented the segmentation result. Given the complexity of the urban scene, a segmentation result with a scale of 20 is satisfactory. Then we continued to determine the shape and compactness parameters using the same method.

Figure 6 illustrates the partial segmentation results with different parameters. We found that the best result was obtained when the shape was 0.4 and the compactness 0.6. The result with a compactness of 0.6 is more fragmented than that with a compactness of 0.5, but the boundaries are more curved and consistent with the boundaries of ground objects. The result with a shape parameter of 0.5 is more fragmented than that with a shape parameter of 0.4. When moderate values (0.5) of shape and compactness are taken, the

Table 2. Time-series coherence images.

Numerical Order	Coherence-Image Pair	Temporal Baseline (d)	Perpendicular Baseline (m)	Doppler Baseline (Hz)
1	20170107, 20170119	-12	-52.36	0.21
2	20170107, 20170131	-24	-23.32	4.25
3	20170107, 20170212	-36	-148.87	4.89
4	20170107, 20170224	-48	-63.74	2.87
5	20170107, 20170308	-60	-34.11	-2.81
6	20170107, 20170320	-72	82.23	4.24
7	20170107, 20170401	-84	-42.8	-2.71
8	20170107, 20170425	-108	-66.79	2.06
9	20170107, 20170507	-120	-56.42	2.80

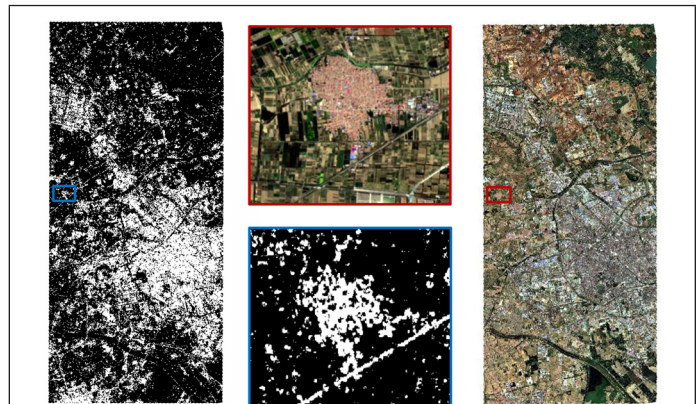


Figure 4. Temporal coherence profiles of impervious surface (IS), vegetation (VE), bare soil (BS), and water body (WA). (a, b) VH and VV polarization, respectively. The horizontal axis corresponds to the coherence-image pairs in Table 2.

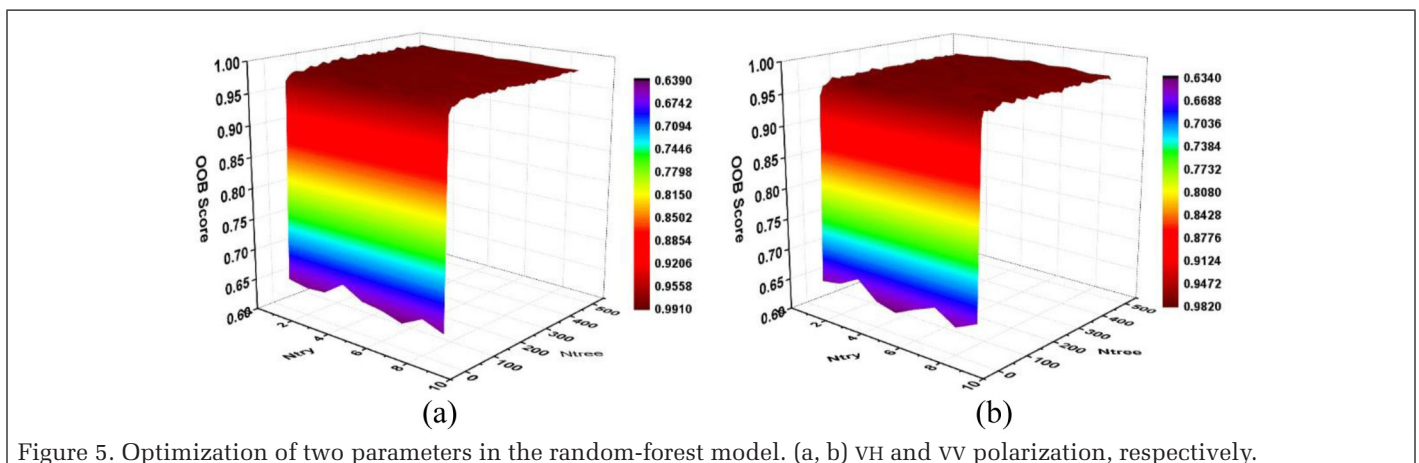


Figure 5. Optimization of two parameters in the random-forest model. (a, b) VH and VV polarization, respectively.

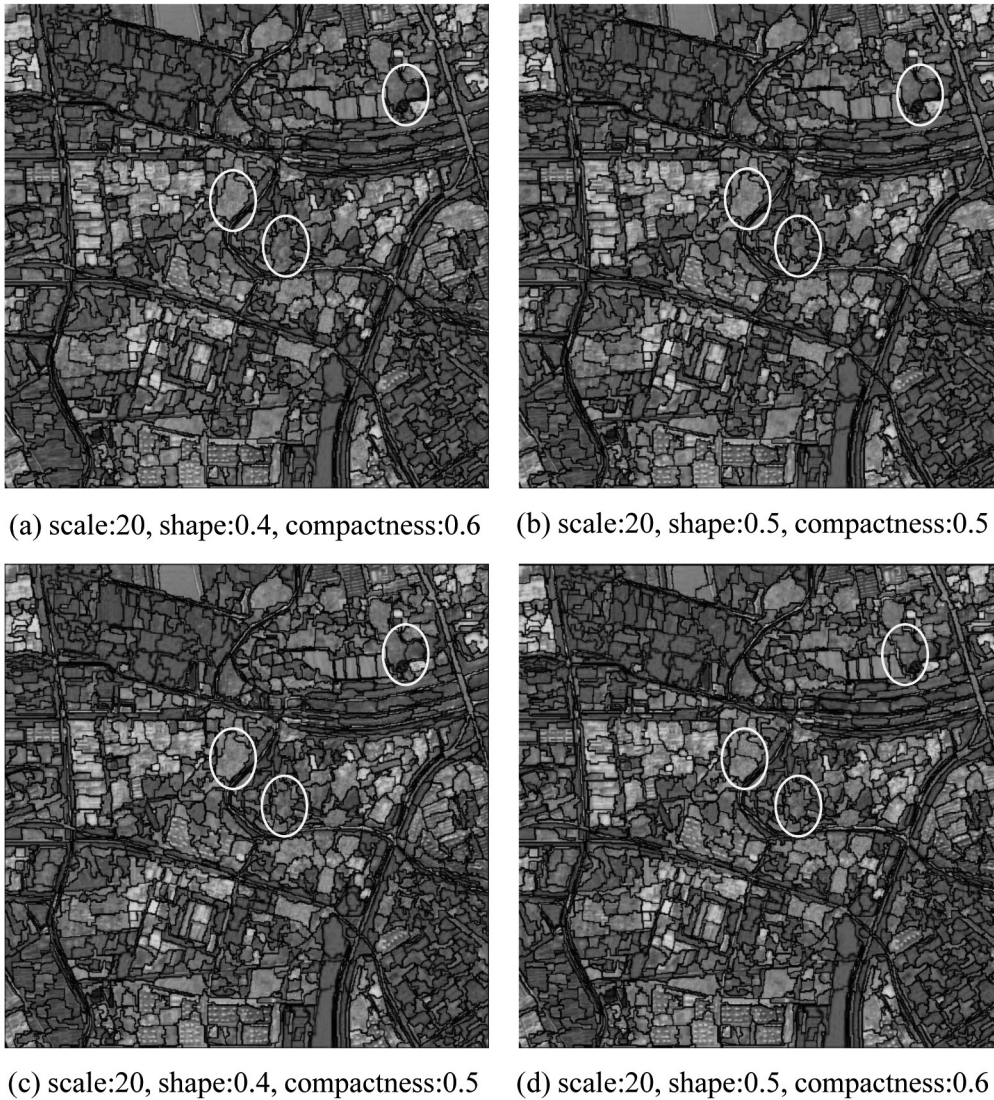


Figure 6. Results of multi-resolution segmentation with different parameters.

segmentation results are not satisfactory. To sum up, a small shape parameter combined with a large compactness parameter can achieve a better segmentation result. Therefore, we ultimately set the values of the scale, shape, and compactness at 20, 0.4, and 0.6, respectively.

#### IS Extraction and Accuracy Assessment

In order to achieve better extraction results, the optimal parameters of the RF model determined earlier were used to configure the RF classifier. In this study, two land cover types are identified: IS and NIS. Figure 7 illustrates the IS extraction results using the proposed method. From Figure 7, we can make a good distinction between urban and suburban areas of Tianjin. In the spatial distribution of IS and NIS in the Tianjin urban area, the connected IS covers most of the area, with NIS occupying only a small part. This indicates that the urbanization rate of Tianjin is relatively high. In the suburban area, IS is distributed sporadically, and NIS occupies most of the area. According to Figure 7, several differences at the bottom of the results can be found. Through comparing and checking the different areas carefully with the aid of high-resolution Google Earth imagery and China's 2-m-resolution IS map, we found that IS was overestimated in the vv polarization time-series coherence images.

Table 3 shows the accuracy of IS extraction. For the result with vv polarization coherence images, the PA values for IS

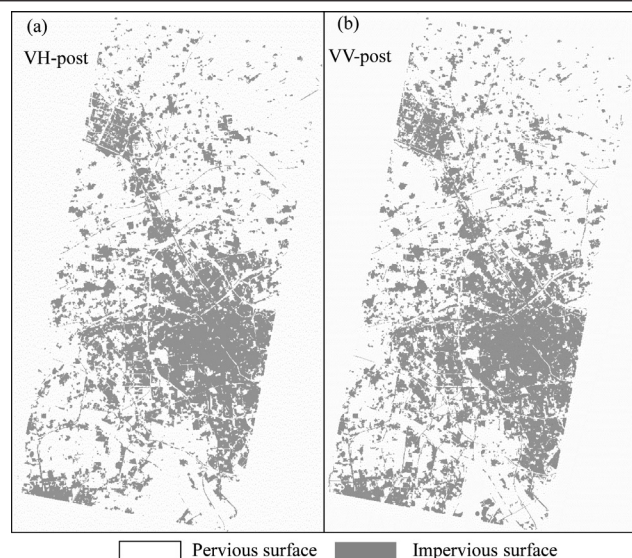


Figure 7. The impervious-surface extraction results with the proposed method. (a, b) VH and VV polarization, respectively. and NIS are 88.65% and 83.99%; the UA values are 87.64%

and 85.25%. For the result with VH polarization coherence images, the PA values are 94.62% and 85.47% and the UA values are 89.29% and 92.53%, which are higher than those of the VV polarization coherence images. In addition, the OA, kappa coefficient, and  $F_1$  scores of the result with VH polarization are 90.6%, 0.8076, and 0.9188, respectively, which are higher than those of VV polarization by 3.99%, 0.8, and 0.0174. Comparatively speaking, VH polarization time-series coherence images have better performance for IS extraction.

## Discussion

In this section, we first discuss the choice of coherence images. The effect of time-series coherence images is then analyzed. The contribution of the postprocessing and the effect of polarization for *Sentinel-1A* are discussed.

### The Choice of Coherence Images

According to equations 1–4, a coherence image contains both the amplitude and the phase information about ground objects. Compared with backscatter coefficients, the information contained in a coherence image is significantly richer and more valuable. So many researchers have begun to extract information from coherence images based on the coherence difference between ground objects. For example, Y. Li, Martinis, and Wieland (2019) have used it to map urban flood area, and Yun *et al.* (2019) have explored its performance in land cover classification. Similarly, we also propose a method based on the property, but our work is different. Those researchers need to analyze the coherence of each land cover carefully to get a satisfactory result, but the difference of coherence images may be not a good data source for land cover classification. However, in this study, IS is our concern. Coherence images have a better ability to identify artificial and natural targets. Therefore, they are a suitable data source and we choose a coherence image to extract the IS.

### Contribution of Time-Series Coherence Images

Although a coherence image has a better ability to identify artificial and natural targets, the coherence of ground objects is susceptible to the following factors (Zebker *et al.* 1992):

$$\gamma = \gamma_{\text{thermal}} \cdot \gamma_{\text{process}} \cdot \gamma_{\text{DC}} \cdot \gamma_{\text{geometric}} \cdot \gamma_{\text{temporal}} \quad (11)$$

where  $\gamma_{\text{thermal}}$  is thermal-noise incoherence,  $\gamma_{\text{process}}$  is data-processing incoherence,  $\gamma_{\text{DC}}$  is Doppler center-of-mass incoherence,  $\gamma_{\text{geometric}}$  is spatial incoherence, and  $\gamma_{\text{temporal}}$  is temporal incoherence.

Due to these factors, using a single coherence image to extract IS will lead to uncertainty. To investigate the contribution of time-series coherence images, we extracted IS from nine single-temporal coherence images with VH and VV polarization and compared them with time-series coherence images. Figure 8 illustrates the comparison of OA and kappa coefficients of results. There are some interesting findings. First, as expected, the accuracy of results using time-series coherence images is higher than that of most results using single-temporal coherence images. This confirms the potential of using time-series coherence images for mapping IS. Second, with the increase in the time baseline, the change trends of the accuracy of VH and VV are different. The accuracy of VV increases until the time baseline is 84 days, then decreases. The OA and kappa of VH fluctuate around 80% and 0.6, respectively, also reaching a maximum at the time baseline of 84 days. The accuracy of VH and VV results at the time baseline of 84 days are very close to that of time-series coherence images. This demonstrates that using single-temporal coherence images for mapping IS has strong uncertainty, and selecting a proper time baseline is very important. Using time-series

Table 3. Accuracy of impervious-surface extraction with the proposed method.

Parameter	VH Polarization			VV Polarization		
	IS	NIS	UA	IS	NIS	UA
IS	492	59	89.29%	461	65	87.64%
NIS	28	347	92.53%	59	341	85.25%
PA	94.62%	85.47%		88.65%	83.99%	
OA	90.6%	$\kappa$	0.8076	86.61%	$\kappa$	0.7276
$F_1$	0.9188			0.8814		

IS = impervious surface; NIS = nonimpervious surface; OA = overall accuracy; PA = producer's accuracy; UA = user's accuracy; VH = vertical transmit, horizontal receive; VV = vertical transmit and receive.

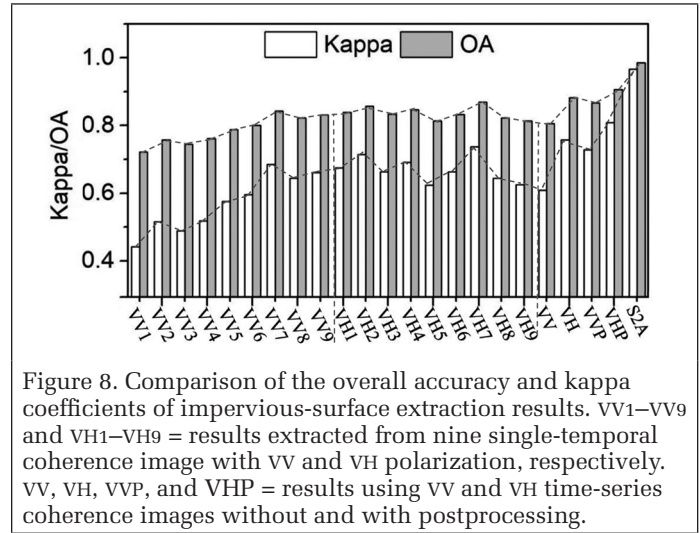


Figure 8. Comparison of the overall accuracy and kappa coefficients of impervious-surface extraction results. VV1–VV9 and VH1–VH9 = results extracted from nine single-temporal coherence image with VV and VH polarization, respectively. VV, VH, VVP, and VHP = results using VV and VH time-series coherence images without and with postprocessing.

coherence images can decrease the uncertainty, so that occasional fluctuations do not affect the overall trend of ground-object coherence. The difficulty of selecting a proper time baseline can also be avoided. All these findings prove that our proposed method of using time-series coherence images is feasible and can get better results.

### Contribution of the Postprocessing Step

One important and contributing step of the proposed method is to introduce multi-resolution segmentation as a postprocessing step. The intention in adding this step is to solve the problem of fragmentation in the IS extraction result using time-series coherence images at the pixel level. To better understand the contribution of the postprocessing, we compared the results with and without postprocessing. Figure 9 shows the results without postprocessing. Through visual interpretation, we found that although the IS extraction results of VV and VH polarization without postprocessing can also reflect the approximate distribution of IS in Tianjin, they have obvious noise, especially VV polarization. To clearly demonstrate the details and effects of postprocessing, three subregions are zoomed in on and shown in Figure 10. We can observe that postprocessing significantly reduced the noise and made the results more complete. Table 4 reflects the accuracy of the results without postprocessing. The OA, kappa coefficient, and  $F_1$  score of the result of VH polarization are 88.12%, 0.7568, and 0.8972, respectively. However, the result of VV polarization is not satisfactory. Although its OA and  $F_1$  score are also relatively high, its kappa coefficient is very low—only 0.6074. The PA and UA of the VV result are lower than those of VH polarization. Comparing Tables 3 and 4, the accuracy measures of results without postprocessing are all lower than the corresponding measure with postprocessing. From Figure 8, we can see that the results obtained using time-series coherence images without postprocessing have lower accuracy than

some results obtained with single-time coherence images; this does not occur in the results using time-series coherence images with postprocessing. On the whole, the introduction of multi-resolution segmentation proved to be an effective step.

### Comparison of VH and VV Polarization of Sentinel-1A

*Sentinel-1A* data have two polarization modes: VH and VV. This section will discuss the performance of VH and VV polarization in extracting IS. Figure 4 shows the coherence characteristics of land covers with VH and VV polarization. We can see that the coherence of IS with VH polarization is higher than with VV polarization. According to this finding, the coherence of VH polarization may be of greater benefit in the extraction

of IS. We used both VH and VV polarization coherence to extract IS. The experimental results (Figures 7–9 and Tables 3 and 4) illustrate that VH time-series coherence images have higher accuracy than VV time-series coherence images, which proves our assumption. In order to find out the reason for this phenomenon, we analyzed the histogram of each coherence image of VH and VV polarization, as shown in Figure 11. For VH polarization, the distribution of pixels is similar. We can also see that the coherence decreases with the increase of the temporal baseline, and the number of low-coherence pixels with a long temporal baseline is larger than that with a short temporal baseline. When the temporal baseline is short (less than 84 days in our study), the histogram of VV polarization differs greatly from that of VH polarization, and the number of high-coherence (>0.4) pixels is larger than with VH polarization. When the temporal baseline is large (108 and 120 days in our study), the distribution of pixels in the VV polarization coherence image tends to be consistent, which is similar to VH polarization. This indicates that VV polarization is more sensitive to coherence changes. When the temporal baseline is short, more ground objects, including bare soil, show strong coherence, which is easily confused with IS. This is the reason why the performance of the VH polarization coherence image is better than that of the VV polarization coherence image.

Table 4. Accuracy of impervious-surface extraction without postprocessing.

Parameter	VH Polarization			VV Polarization		
	IS	NIS	UA	IS	NIS	UA
IS	480	70	7.27%	420	80	84%
NIS	40	336	89.36%	100	326	76.52%
PA	92.31%	82.76%		80.77%	80.3%	
OA	88.12%	$\kappa$	0.7568	80.56%	$\kappa$	0.6074
$F_1$	0.8972			0.8235		

IS = impervious surface; NIS = nonimpervious surface; OA = overall accuracy; PA = producer's accuracy; UA = user's accuracy; VH = vertical transmit, horizontal receive; VV = vertical transmit and receive.

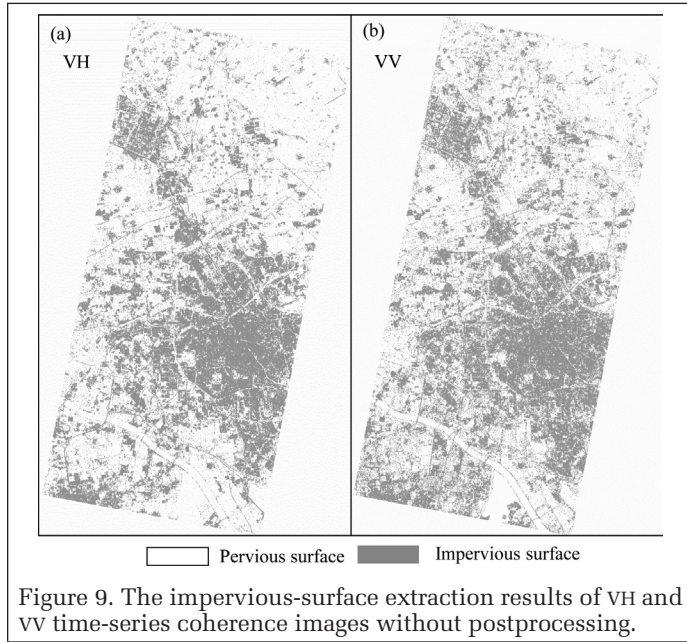


Figure 9. The impervious-surface extraction results of VH and VV time-series coherence images without postprocessing.

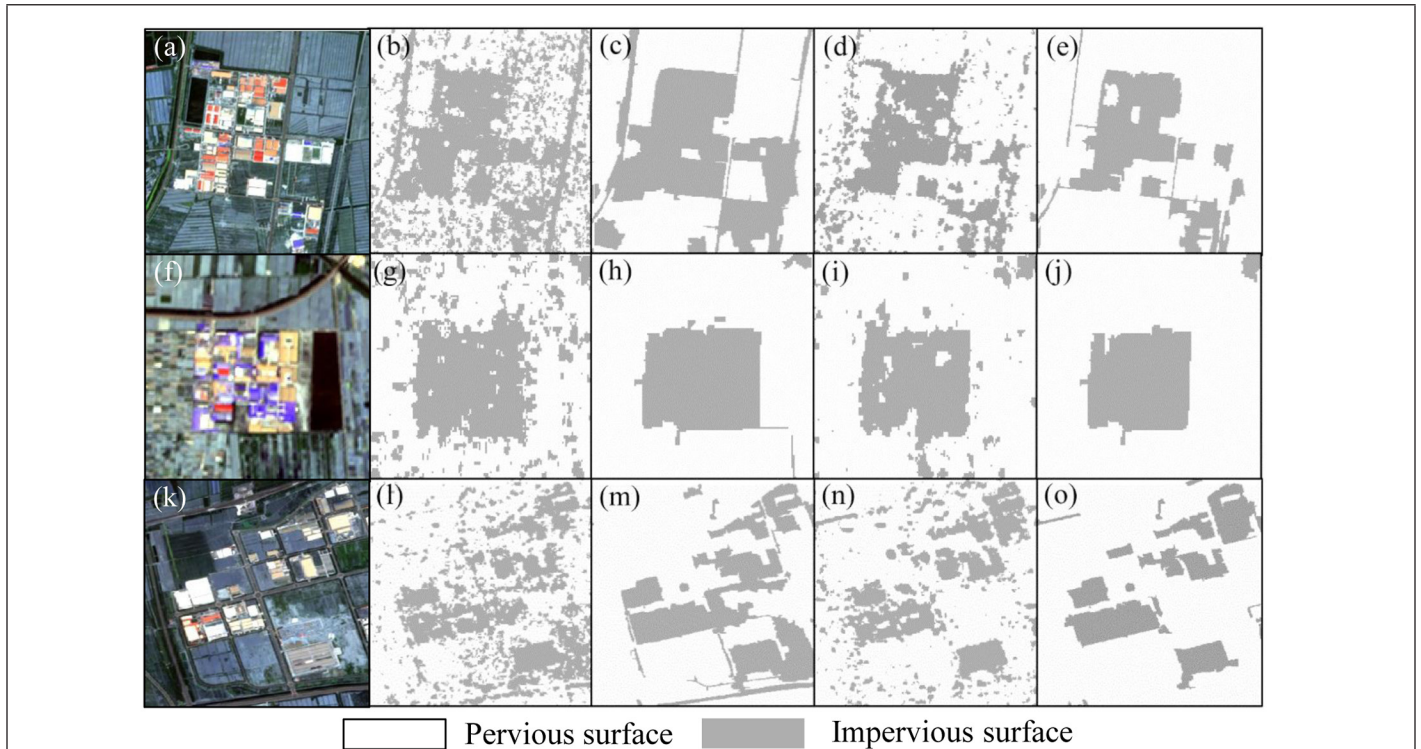


Figure 10. The impervious-surface extraction results of three subregions. (Left to right) *Sentinel-2A* image, results of VV time-series coherence images without and with postprocessing, VH time-series coherence images without and with postprocessing.

## Conclusion

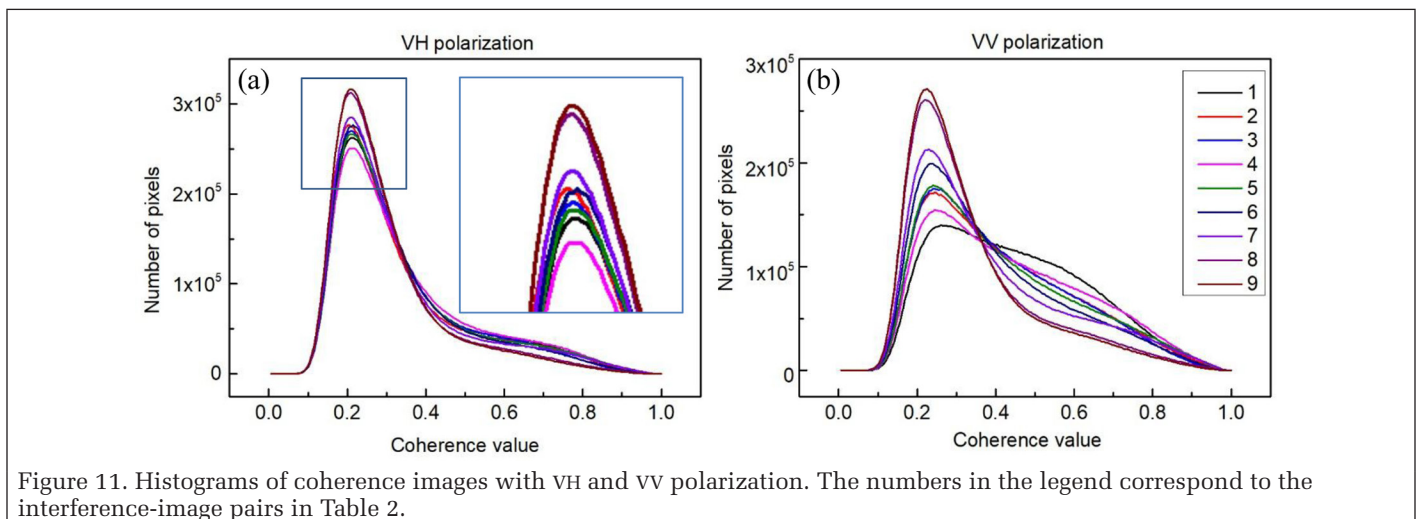
Impervious surface has been used as an important indicator for measuring the ecological environment. Monitoring the spatial distribution of impervious surface is of high significance. Coherence images, and intermediate product of InSAR processing, have been used in many fields, including land cover classification. In this study, based on the coherence differences between natural and artificial targets, we explored the potential of time-series coherence images to extract IS and introduced multi-resolution segmentation as a postprocessing step to alleviate the problem of speckle in coherence images. Our experiments indicated first that time-series coherence images can reduce the effect of de-coherence factors and obtain acceptable results. Second, multi-resolution segmentation is an effective postprocessing step which can suppress the influence of speckle and further improve the extraction of IS. Finally, time-series coherence images with VH polarization have better accuracy than those with VV polarization. Our study confirmed the potential of time-series coherence images and provided a new data source for IS extraction. However, the proposed method needs the aid of optical images. In future work, we can improve the quality of coherence images and then use them alone to extract IS.

## Acknowledgments

This work was supported in part by the National Key R & D Plan on Strategic International Scientific and Technological Innovation Cooperation Special Project under grant 2016YFE0202300; the National Natural Science Foundation of China under grants 61671332, 41771452, 51708426, 41890820, and 41771454; the Natural Science Fund of Hubei Province in China under grant 2018CFA007; and the Independent Research Projects of Wuhan University under grant 2042018kf0250.

## References

- Amitrano, D., V. Belfiore, F. Cecinati, G. Di Martino, A. Iodice, P.-P. Mathieu, S. Medagli, D. Poreh, D. Riccio and G. Ruello. 2016. Urban areas enhancement in multitemporal SAR RGB images using adaptive coherence window and texture information. *IEEE Journal of Selected Topics in Applied Earth Observations and Remote Sensing* 9 (8):3740–3752.
- Breiman, L., L. Breiman and R. A. Cutler. 2001. Random forests machine learning. *Journal of Clinical Microbiology* 2:199–228.
- Cheloni, D., V. De Novellis, M. Albano, A. Antonioli, M. Anzidei, S. Atzori, A. Avallone, C. Bignami, M. Bonano, S. Calcaterra, R. Castaldo, F. Casu, G. Cecere, C. De Luca, R. Devoti, D. Di Bucci, A. Esposito, A. Galvani, P. Gambino, R. Giuliani, R. Lanari, M. Manunta, M. Manzo, M. Mattone, A. Montuori, A. Pepe, S. Pepe, G. Pezzo, G. Pietrantonio, M. Polcaro, F. Riguzzi, S. Salvi, V. Sepe, E. Serpelloni, G. Solaro, S. Stramondo, P. Tizzani, C. Tolomei, E. Trasatti, E. Valerio, I. Zinno and C. Doglioni. 2017. Geodetic model of the 2016 Central Italy earthquake sequence inferred from InSAR and GPS data. *Geophysical Research Letters* 44 (13): 6778–6787.
- Corbane, C., G. Lemoine, M. Pesaresi, T. Kemper, F. Sabo, S. Ferri and V. Syrris. 2018. Enhanced automatic detection of human settlements using Sentinel-1 interferometric coherence. *International Journal of Remote Sensing* 39 (3):842–853.
- Del Frate, F., F. Pacifici and D. Solimini. 2008. Monitoring urban land cover in Rome, Italy, and its changes by single-polarization multitemporal SAR images. *IEEE Journal of Selected Topics in Applied Earth Observations and Remote Sensing* 1 (2):87–97.
- Deng, C. and C. Wu. 2012. BCI: A biophysical composition index for remote sensing of urban environments. *Remote Sensing of Environment* 127:247–259.
- Duro, D. C., S. E. Franklin and M. G. Dubé. 2012. A comparison of pixel-based and object-based image analysis with selected machine learning algorithms for the classification of agricultural landscapes using SPOT-5 HRG imagery. *Remote Sensing of Environment* 118:259–272.
- Gong, P., B. Chen, X. Li, H. Liu, J. Wang, Y. Bai, J. Chen, X. Chen, L. Fang, S. Feng, Y. Feng, Y. Gong, H. Gu, H. Huang, X. Huang, H. Jiao, Y. Kang, G. Lei, A. Li, X. Li, X. Li, Y. Li, Z. Li, Z. Li, C. Liu, C. Liu, M. Liu, S. Liu, W. Mao, C. Miao, H. Ni, Q. Pan, S. Qi, Z. Ren, Z. Shan, S. Shen, M. Shi, Y. Song, M. Su, H. P. Suen, B. Sun, F. Sun, J. Sun, L. Sun, W. Sun, T. Tian, X. Tong, Y. Tseng, Y. Tu, H. Wang, L. Wang, X. Wang, Z. Wang, T. Wu, Y. Xie, J. Yang, J. Yang, M. Yuan, W. Yue, H. Zeng, K. Zhang, N. Zhang, T. Zhang, Y. Zhang, F. Zhao, Y. Zheng, Q. Zhou, N. Clinton, Z. Zhu and B. Xu. 2020. Mapping essential urban land use categories in China (EULUC-China): Preliminary results for 2018. *Science Bulletin* 65 (3):182–187.
- Jiang, M., B. Yong, X. Tian, R. Malhotra, R. Hu, Z. Li, Z. Yu and X. Zhang. 2017. The potential of more accurate InSAR covariance matrix estimation for land cover mapping. *ISPRS Journal of Photogrammetry and Remote Sensing* 126:120–128.
- Li, X. and P. Gong. 2016. An “exclusion-inclusion” framework for extracting human settlements in rapidly developing regions of China from Landsat images. *Remote Sensing of Environment* 186:286–296.



- Li, Y., S. Martinis and M. Wieland. 2019. Urban flood mapping with an active self-learning convolutional neural network based on TerraSAR-X intensity and interferometric coherence. *ISPRS Journal of Photogrammetry and Remote Sensing* 152:178–191.
- Lin, Y., H. Zhang, H. Lin, P. E. Gamba and X. Liu. 2020. Incorporating synthetic aperture radar and optical images to investigate the annual dynamics of anthropogenic impervious surface at large scale. *Remote Sensing of Environment* 242:111757.
- Liu, C., Z. Shao, M. Chen and H. Luo. 2013. MNDISI: A multi-source composition index for impervious surface area estimation at the individual city scale. *Remote Sensing Letters* 4 (8):803–812.
- Liu, C., Q. Zhang, H. Luo, S. Qi, S. Tao, H. Xu and Y. Yao. 2019. An efficient approach to capture continuous impervious surface dynamics using spatial-temporal rules and dense Landsat time series stacks. *Remote Sensing of Environment* 229:114–132.
- Schneider, R. Z., K. P. Papathanassiou, I. Hajnsek and A. Moreira. 2006. Polarimetric and interferometric characterization of coherent scatterers in urban areas. *IEEE Transactions on Geoscience and Remote Sensing* 44 (4):971–984.
- Shao, Z., H. Fu, P. Fu and L. Yin. 2016. Mapping urban impervious surface by fusing optical and SAR data at the decision level. *Remote Sensing* 8 (11):945.
- Shao, Z., H. Fu, D. Li, O. Altan and T. Cheng. 2019. Remote sensing monitoring of multi-scale watersheds impermeability for urban hydrological evaluation. *Remote Sensing of Environment* 232:111338.
- Shao, Z., C. Li, D. Li, O. Altan, L. Zhang and L. Ding. 2020. An accurate matching method for projecting vector data into surveillance video to monitor and protect cultivated land. *ISPRS International Journal of Geo-Information* 9 (7):448.
- Shao, Z. and C. Liu. 2014. The integrated use of DMSP-OLS nighttime light and MODIS data for monitoring large-scale impervious surface dynamics: A case study in the Yangtze River Delta. *Remote Sensing* 6 (10):9359–9378.
- Shao, Z., P. Tang, Z. Wang, N. Saleem, S. Yam and C. Sommai. 2020. BRRNet: A fully convolutional neural network for automatic building extraction from high-resolution remote sensing images. *Remote Sensing* 12 (6):1050.
- Shao, Z., Y. Tian and X. Shen. 2014. BASI: A new index to extract built-up areas from high-resolution remote sensing images by visual attention model. *Remote Sensing Letters* 5 (4):305–314.
- Shao, Z., Y. Zhang, X. Huang, X. Zhu, L. Wu and B. Wan. 2018. Mapping impervious surface with 2 m using multi-source high resolution images. *Geomatics and Information Science of Wuhan University* 43 (12):1909–1915.
- Shao, Z., W. Zhou, X. Deng, M. Zhang and Q. Cheng. 2020. Multilabel remote sensing image retrieval based on fully convolutional network. *IEEE Journal of Selected Topics in Applied Earth Observations and Remote Sensing* 13:318–328.
- Tian, J. and D.-M. Chen. 2007. Optimization in multi-scale segmentation of high-resolution satellite images for artificial feature recognition. *International Journal of Remote Sensing* 28 (20):4625–4644.
- Touzi, R., A. Lopes, J. Bruniquel and P. W. Vachon. 1999. Coherence estimation for SAR imagery. *IEEE Transactions on Geoscience and Remote Sensing* 37 (1):135–149.
- Wang, Z., C. Gang, X. Li, Y. Chen and J. Li. 2015. Application of a normalized difference impervious index (NDII) to extract urban impervious surface features based on Landsat TM images. *International Journal of Remote Sensing* 36 (4):1055–1069.
- Weng, Q. 2012. Remote sensing of impervious surfaces in the urban areas: Requirements, methods, and trends. *Remote Sensing of Environment* 117:34–49.
- Wu, C. and A. T. Murray. 2003. Estimating impervious surface distribution by spectral mixture analysis. *Remote Sensing of Environment* 84 (4):493–505.
- Wu, W., S. Guo and Q. Cheng. 2020. Fusing optical and synthetic aperture radar images based on shearlet transform to improve urban impervious surface extraction. *Journal of Applied Remote Sensing* 14 (2):024506.
- Xu, H. 2006. Modification of normalised difference water index (NDWI) to enhance open water features in remotely sensed imagery. *International Journal of Remote Sensing* 27 (14):3025–3033.
- Xu, H. 2010. Analysis of impervious surface and its impact on urban heat environment using the normalized difference impervious surface index (NDISI). *Photogrammetric Engineering and Remote Sensing* 76 (5):557–565.
- Yang, H., B. Pan, W. Wu and J. Tai. 2018. Field-based rice classification in Wuhua county through integration of multi-temporal Sentinel-1A and Landsat-8 OLI data. *International Journal of Applied Earth Observation and Geoinformation* 69:226–236.
- Yang, L., L. Jiang, H. Lin and M. Liao. 2009. Quantifying sub-pixel urban impervious surface through fusion of optical and InSAR imagery. *GIScience & Remote Sensing* 46 (2):161–171.
- Yun, H.-W., J.-R. Kim, Y.-S. Choi and S.-Y. Lin. 2019. Analyses of time series InSAR signatures for land cover classification: Case studies over dense forestry areas with L-band SAR images. *Sensors* 19 (12):2830.
- Zebker, H. A., S. N. Madsen, J. Martin, K. B. Wheeler, T. Miller, Y. Lou, G. Alberti, S. Vetrilla and A. Cucci. 1992. The TOPSAR interferometric radar topographic mapping instrument. *IEEE Transactions on Geoscience and Remote Sensing* 30 (5):933–940.
- Zha, Y., J. Gao and S. Ni. 2003. Use of normalized difference built-up index in automatically mapping urban areas from TM imagery. *International Journal of Remote Sensing* 24 (3):583–594.
- Zhang, H., L. Wan, T. Wang, Y. Lin, H. Lin and Z. Zheng. 2019. Impervious surface estimation from optical and polarimetric SAR data using small-patched deep convolutional networks: A comparative study. *IEEE Journal of Selected Topics in Applied Earth Observations and Remote Sensing* 12 (7):2374–2387.
- Zhang, L., Q. Weng and Z. Shao. 2017. An evaluation of monthly impervious surface dynamics by fusing Landsat and MODIS time series in the Pearl River Delta, China, from 2000 to 2015. *Remote Sensing of Environment* 201:99–114.
- Zhang, X., D. Pan, J. Chen, Y. Zhan and Z. Mao. 2013. Using long time series of Landsat data to monitor impervious surface dynamics: A case study in the Zhoushan Islands. *Journal of Applied Remote Sensing* 7 (1):073515.
- Zhang, Y., H. Zhang and H. Lin. 2014. Improving the impervious surface estimation with combined use of optical and SAR remote sensing images. *Remote Sensing of Environment* 141:155–167.
- Zhang, Z., C. Liu, J. Luo, Z. Shen and Z. Shao. 2015. Applying spectral mixture analysis for large-scale sub-pixel impervious cover estimation based on neighbourhood-specific endmember signature generation. *Remote Sensing Letters* 6 (1):1–10.
- Zhao, C., C. Liu, Q. Zhang, Z. Lu and C. Yang. 2018. Deformation of Linfen-Yuncheng Basin (China) and its mechanisms revealed by  $\Pi$ -RATE InSAR technique. *Remote Sensing of Environment* 218:221–230.
- Zhou, Y. and Y. Q. Wang. 2008. Extraction of impervious surface areas from high spatial resolution imagery by multiple agent segmentation and classification. *Photogrammetric Engineering and Remote Sensing* 74 (7):857–868.

# Road Extraction from Cartosat-2F Multispectral Data with Object-Oriented Analysis

Chumbitha Leena, Manoj Raj Saxena, and Ravi Shankar Dwivedi

## Abstract

For detection of a road network, high-resolution satellite data have been used following the object-oriented classification approach. We used object-based feature extraction algorithms for detection of road networks from a high resolution Cartosat-2F multispectral data in an Indian city with varying terrain conditions ranging from a compact built-up area to a predominantly vegetated area. The approach involves multi-resolution segmentation (MRS) and spectral difference segmentation (SDS) followed by road extraction using fuzzy rule-based algorithm based on various object features, viz. gray-level co-occurrence matrix homogeneity, density, rectangular fit, etc. With overall accuracies ranging from 77.46% to 92% SDS approach performed better than MRS which could afford 60.46% to 75.0% only. However, both of these approaches score over the classical Gaussian maximum likelihood classifier which could register only 50.0% to 68.0% overall accuracy. Furthermore, the maximum overall accuracy was obtained in compact built-up site (85% to 92%) followed by sparsely built-up site (75.0% to 88%) and predominantly vegetated site (60.46% to 77.14%).

## Introduction

Timely and reliable information on the current status of road networks and changes therein due to incessant developmental activities is a prerequisite for planning and implementation of road network. High spatial resolution (HSR) satellite images offer immense potential in deriving such information in a timely and cost-effective manner. Different road features in an image have different image characteristics. For instance, geometric features have the direct relationship with the road shapes. Photometric features relate to the gray levels or colors of roads, and topological features and functional features are relatively simple but very difficult to apply in real applications (Wang *et al.* 2016). Various methods of road extraction from HSR satellite images have been developed (Mena 2003; Wang *et al.* 2016; Kahraman *et al.* 2018). These methods can be grouped into three categories: (1) pixel-based methods, (2) knowledge-based methods, and (3) object-oriented methods (Shi *et al.* 2014).

## Pixel-Based Methods

The per-pixel classifiers typically develop a spectral signature by combining the spectra of all training-set pixels for a given feature. The resulting signature contains the contributions of all materials present in the training pixels. Per-pixel classification algorithms can be parametric or nonparametric. The parametric classifiers assume that a normally distributed data set exists, and that the statistical parameters (e.g., mean vector and covariance matrix) generated from the training samples are representative of the ground features. With nonparametric

classifiers, the assumption of a normal distribution of the data set is not required. No statistical parameters are needed to separate image classes. These classifiers are, thus, especially suitable for the incorporation of nonspectral data into a classification procedure. Included in the per-pixel classifiers category are Gaussian maximum likelihood classifier (GMLC), neural networks, space vector machine (SVM), and expert systems.

## Knowledge-Based Methods

Owing to difficulties in extracting the roads from remote sensing images based solely on the local spectrum and texture information, and due to the stripe structure of the road, remote sensing data could not be input to the classifier directly. Parameter models such as the energy function can be used to operate on the maximum value of the energy function. The knowledge-based methods which use higher level information, e.g., a vision-based system (Poullis and You 2010), Gabor filtering and tensor voting for geospatial-feature classification have, therefore, been developed for feature detection. These models usually extract some structural elements according to the relationship among them and detect the specific structure. Wang and Zheng (1998) proposed a method for detection of roads and bridges from synthetic aperture radar (SAR) images by using geometric features to extract general objects and subsequently adopted the mathematical morphology and Hough transform to extract the small regions and to connect the discontinuous segments. Similarly, Grote *et al.* (2012) integrated radiometric and geometric features derived from remote sensing images to extract road networks. Initially, the normalized cut algorithm was used to segment the images; the segments were subsequently grouped.

## Object-Oriented Methods

In contrast to per-pixel classification, which relies solely on the spectral information in each pixel, object-oriented methods are based on information from a set of similar pixels called segments or image objects. Image objects or segments are groups of pixels that are similar to one another based on the spectral properties, i.e., color, size, shape, and texture, as well as context from a neighborhood surrounding the pixels. These methods entail segmentation of the images into regions/"objects"/"segments" first, followed by detection of roads using contextual image characteristics like image spectrum, texture, and structure, and other features (Sun *et al.* 2006; Zhong *et al.* 2014).

## Image Segmentation

Image segmentation is a computer-based process of dividing digital image and other raster data into spectrally and/or texturally homogeneous groups of pixels, referred to as segments or image objects (Hamilton *et al.* 2007). The segments or image objects, thus formed, meet the homogeneity criteria based

---

Chumbitha Leena and Ravi Shankar Dwivedi are with Jawaharlal Nehru Technological University, Hyderabad, India (rsdwivedi51@gmail.com).

Manoj Raj Saxena is with National Remote Sensing Centre, Department of Space, Govt. of India, Hyderabad- 500037, India.

---

Photogrammetric Engineering & Remote Sensing  
Vol. 87, No. 3, March 2021, pp. 171–180.  
0099-1112/21/171–180

© 2021 American Society for Photogrammetry  
and Remote Sensing  
doi: 10.14358/PERS.87.3.171

on the parameter or the threshold and spatial contingency defined by the user. Several image segmentation algorithms including the classical Otsu threshold segmentation (Otsu 1979) algorithm, fuzzy c-means clustering algorithm (Bezdek *et al.* 1984), K-means algorithm (Wagstaff *et al.* 2001), and watershed algorithm (Bieniek and Moga 2000) have been developed for segmentation of gray-scale images (Zhou *et al.* 2019). For segmentation of HSR multispectral image with multiple bands and abundant spectral information, the multi-scale or multi-resolution segmentation has been used (Gao *et al.* 2018).

Multi-resolution segmentation (MRS) is a bottom-up region-growing approach used to generate image object segments as the first step of an object-oriented classification (Benz *et al.* 2004). It is based on the fact that not all ground features occur at the same physical scale. The best segmentation result has been found to be achievable by segmenting an image at different scales (Burnett and Blaschke 2003). The segmentation process begins with each pixel forming one image segment or object. The objects (segments) are merged gradually in an iterative process. During segmentation, the image is converted into object primitives that share a certain spectral behavior, shape, and context. These preliminary object features are then segmented at a higher level (Gao 2009).

The spectral difference segmentation (SDS) is a merging algorithm where neighboring objects with a spectral mean below the given threshold (maximum spectral difference) are merged to produce the final objects. To use this segmentation algorithm, an already segmented image is required. Like multi-resolution segmentation, SDS is also a bottom-up segmentation approach designed to refine the results of multi-resolution segmentation. While performing spectral difference segmentation, the user needs to set the image-object domain and level settings as appropriate followed by setting the maximum spectral difference. The algorithm merges neighboring image objects/segments that have a spectral difference less than the user-defined maximum. As with multi-resolution segmentation, conditions, layer weights, and thematic-layer usage can all be set or varied to modify the results of the segmentation. The segmented image is subsequently classified for extraction of terrain features of interest.

#### Classification

Unlike per-pixel classification in which pixels are considered individually and assigned to land cover classes independent of one another, object-oriented classification treats each segment or object as the smallest unit of analysis in the decision making process (Gao 2009). The segmented image is classified using several algorithms, including nearest neighbor based on fuzzy logic. Several researchers have developed the object-oriented methods for extraction of road network from high spatial resolution remote sensing images (Zhong *et al.* 2014; Shi *et al.* 2014; Ok 2017; Chen *et al.* 2018; Zhau *et al.* 2019).

Zhong *et al.* (2014) proposed a hybrid approach for detection of road network involving object-oriented (OO) algorithm and conditional random fields (CRF) classification framework from QuickBird, IKONO, and hyperspectral (hyperspectral digital imagery collection experiment, or HYDICE) images. The approach comprises three main steps: the probabilistic pixel-wise classification, the CRF classification framework, and classification fusion. To begin with, the SVM classifier, a probabilistic pixel-wise classification, is used to classify the HSR image and to generate the corresponding probability map. The CRF classification framework consists of log unary potential (CRF-LOG) and the quasi-gamma unary potential (CRF-QG). The CRF classification is performed on the probability map, thus generated, and on the original HSR imagery to obtain the segmentation map by a connected-component labelling algorithm. In fact, CRF directly models the posterior probability of the labels for classification of probability map and HSR images

given the image data  $P(x|y)$  (Lafferty *et al.* 2001; Kumar and Hebeert 2006) with the following form:

$$P(x|y) = \frac{1}{Z(y)} \exp \left\{ -\sum_{\alpha \in C} \psi_{\alpha}(x_{\alpha}, y) \right\} \quad (1)$$

where  $Z(y) = \sum_x \exp \left\{ -\sum_{\alpha \in C} \psi_{\alpha}(x_{\alpha}, y) \right\}$  is the partition function,

and the term  $\psi_{\alpha}(x_{\alpha}, y)$  denotes the potential function, which has been widely used for classification of remote sensing image. A commonly used example of a CRF energy can be written as the sum of the unary and pair-wise potentials, i.e.,

$$E(x) = \sum_{i \in V} \psi_i(x_i) + \lambda \sum_{i \in V, j \in N_i} \psi_{ij}(x_i, x_j) \quad (2)$$

where  $\psi_i(x_i)$  is the unary potential term, and  $\psi_{ij}$  is the pair-wise potential term, which is computed over the local neighborhood  $N_i$  of pixel  $i$ . The nonnegative constant  $\lambda$  trades off the strength of the pair-wise potential against the unary potential.

The last step involves the fusion of the CRF-LOG and CRF-QG classification results obtained in the second step by the connected-component labelling algorithm is the last step. Object-oriented classification maps are then generated by a majority voting strategy using the segmentation map and the classification map.

For extraction of urban main-road centerlines from high spatial resolution ZIYUAN-3 satellite optical image, Shi *et al.* (2014) proposed an integrated method with four main steps. First, spectral-spatial classification to segment the images into two categories: road and nonroad groups using general adaptive neighborhood algorithm. Second, fusion of road groups and homogeneous property, measured by local Geary's C, to improve road-group accuracy. Third, road shape features are used to extract reliable road segments. Finally, local linear kernel smoothing regression is performed to extract smooth road centerlines. Road networks are then generated using tensor voting. Local Geary's C (Anselin 1995) is defined as:

$$c_i = \frac{1}{\frac{1}{n} \sum_{j=1}^n (y_j - \bar{y})^2} \sum_{j=1}^n w_{ij} [(y_i - \bar{y}) - (y_j - \bar{y})]^2 \quad (3)$$

$$= \frac{1}{\frac{1}{n} \sum_{j=1}^n (y_j - \bar{y})^2} \sum_{j=1}^n w_{ij} (y_i - y_j)^2 \quad (4)$$

where  $n$  is the number of georeferenced observations,  $y_i$  is the value of the observation at the  $i$ th location,  $\bar{y}$  is the mean of the observations, and  $w_{ij}$  is the weight of spatial relations between points  $i$  and  $j$  (ENVI 2013). The local Geary's C index identifies areas of high variability between a pixel value and its neighboring pixels. It is useful for detecting edge areas between clusters and other areas with dissimilar neighboring values (ENVI 2013).

Chen *et al.* (2018) put forward a two-stage method for detection of roads by combining edge information and region characteristics. The method involves the execution of convolutions by applying Gabor wavelets in the best scale to detect Gabor features with location and orientation information. The features are then merged into one response map for connection analysis. A Gabor filter is an appropriate linear filter for edge detection and analysis because it provides scale and direction information. The core of the two-dimensional Gabor filter for texture-feature extraction can be defined in spatial domain as follows (Kamarainen 2012):

$$g_{\lambda, \theta, \sigma, \varphi, k}(x, y) = \exp\left(-\frac{x'^2 + \kappa^2 y'^2}{2\sigma^2}\right) \cos\left(2\pi \frac{x}{\lambda} + \varphi\right) \quad (5)$$

$$\begin{aligned} x' &= x \cos\theta + y \sin\theta \\ y' &= -x \sin\theta + y \cos\theta \end{aligned}$$

where  $\lambda = 1/f$  is the wavelength,  $\theta$  is the orientation,  $\varphi$  is the phase offset,  $\sigma^2$  is the variance, and  $k = \gamma/\eta$  is the spatial aspect ratio. In the second stage, highly complete and connected Gabor features are used as edge constraints to facilitate stable object segmentation and limit region growing. Segmented objects are finally evaluated by some fundamental shape features to eliminate non-road objects.

In yet another study, Zhou *et al.* (2019) used a multi-scale segmentation algorithm to segment the images, and fast marching method (FMM) algorithm for feature extraction to get the initial road. Introduced by Sethian (1999) and Hassouna and Farag (2007) for an evolution case of front evolution, the FMM aimed at obtaining the boundary distance field and the source distance field. Considering an interface  $\Gamma$  (i.e., the boundary of road),  $\Gamma$  can be a point, a curve, or a surface. For a front moving with speed ( $F(x)$ ), where  $F$  is always either positive or negative. Then, let  $T(x)$  be the time at which  $\Gamma$  crosses the point  $x$ . In the one-dimensional case, where *distance* = *speed*  $\times$  *time*, the equation of motion can be expressed as:

$$F(x) = \frac{dx}{dT} \quad (6)$$

In multiple dimensions, the equation of evolution is:

$$|\nabla T(x)| F(x) = 1 \quad \Gamma(\Gamma_0) = 0 \quad (7)$$

where  $F(x)$  represents the speed when  $\Gamma$  passes by the point  $x$ ,  $\nabla T(x)$  represents the time gradient of  $\Gamma$  crossing the point  $x$ , and  $\Gamma(\Gamma_0) = 0$  indicates that the initial arrival time of  $\Gamma$  is 0.

The FMM road width of each initial centerline is calculated by combining the boundary distance fields before a tensor field is applied for connecting the broken centerline to gain the final centerline. Finally, matching of the final centerline is performed with its road width when the final road is reconstructed.

## The Study Area

Covering a geographical area of 218 km<sup>2</sup>, Nagpur city, the study area, forms part of Nagpur district of Maharashtra state, central India (Figure 1). The soils of the area are basically black soils ranging in colors from light gray to dark and very dark gray, which exhibits ample amount of similarity with the tarred roads. In order to account for variations in terrain conditions within the city, three test sites representing (1)

compact built-up site, (2) sparse built up site, and (3) predominantly vegetated site were selected for extraction of roads.

## Database and Software

Cartosat-2F high resolution multispectral (HRMX) digital (standard product) data with 1.65 m spatial resolution covering the test sites and acquired on 27 January 2018 were used for realizing the objective of the study (<https://www.isro.gov.in/Spacecraft/cartosat-2-series-satellite-2>). The standard products are georeferenced and generated after accounting for radiometric and geometric distortions. Launched on 12 January 2018, Cartosat-2F carries a panchromatic sensor with better than 1 m resolution and an HRMX collecting co-registered multispectral images in four spectral bands, viz., 0.43–0.52  $\mu\text{m}$  (blue); 0.52–0.61  $\mu\text{m}$  (green); 0.61–0.69  $\mu\text{m}$  (red), and 0.76–0.90  $\mu\text{m}$  near-infrared reflectance (NIR) with 11-bit radiometric resolution, 1.65 m spatial resolution, and 10 km swath. The satellite crosses over the equator at 9:30 A.M. (descending node).

The eCognition Developer 9.0 was used for image segmentation and feature extraction. Besides, ERDAS/IMAGINE 2015 (64-bit) and ArcGIS 10.1, an Environmental Systems Research Institute product was used for processing, classification, analysis of multispectral data, and for displaying the outputs.

## Approach

The approach consists of image preprocessing and feature extraction including image segmentation and classification, and accuracy estimation. Besides, the approach includes Gaussian maximum likelihood classification of Cartosat-2F multispectral data.

## Image Preprocessing

The preprocessing of digital Cartosat-2F HRMX data was carried as a prelude to image analysis. Included in the image preprocessing operations are radiometric corrections related to sensor, namely dead-pixel correction, geometric lens distortion; atmospheric effects followed by conversion of digital number values to radiance, and ultimately to reflectance values (Figure 2). In addition, corrections for distortions in image geometry due to Earth rotation, panoramic distortions, and platform-related errors were also carried out. In order to improve the image contrast, the linear stretching was performed using image enhancement tool available in ERDAS/IMAGINE version 2015.

## Image Analysis

The object-oriented image analysis data involves preprocessing, multi-resolution image segmentation, extraction of road network using fuzzy rule-based algorithm, morphological

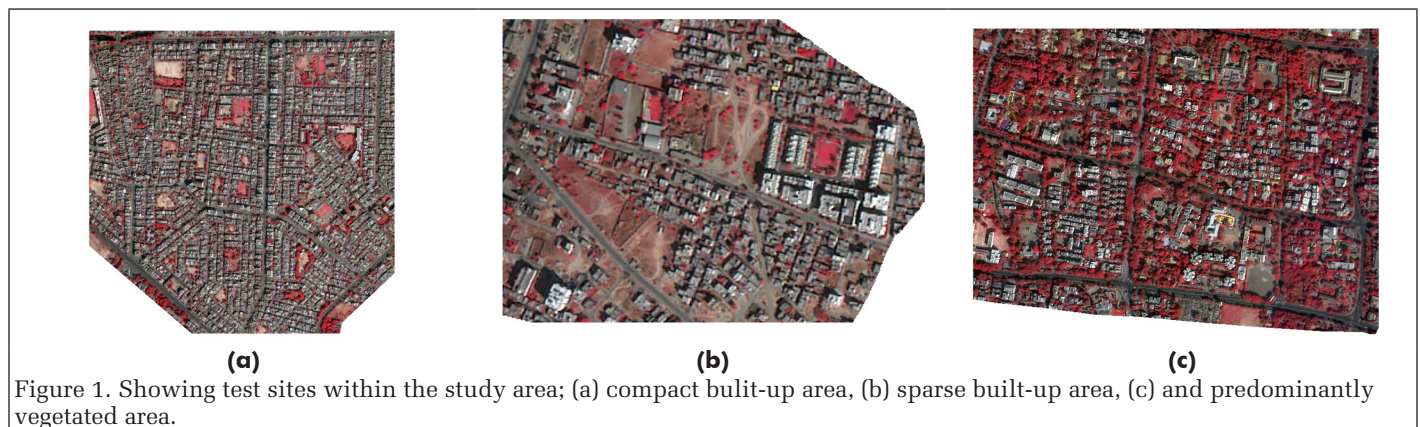


Figure 1. Showing test sites within the study area; (a) compact built-up area, (b) sparse built-up area, (c) and predominantly vegetated area.

operation, and accuracy assessment. The classical per-pixel Gaussian maximum likelihood classification algorithm was used to evaluate the performance of fuzzy rule-based algorithm for extraction of road network.

#### Image Segmentation

The image segmentation was carried out following mutual-best-fitting approach (Definiens 2007) Two types of image segmentation, namely MRS, and SDS were performed (Figure 3). Initially, MRS begins with single image object/segment of 1 (one) pixel size and merges them in several loops iteratively in pairs to larger units until it reaches an upper threshold of homogeneity limit. The homogeneity criteria were defined as a combination of spectral homogeneity and shape homogeneity (image layer weight, i.e., weight assigned to each spectral band image, scale, shape, and compactness). The homogeneity criterion is calculated as a combination of color and shape properties of both the initial and the resulting image objects of the intended merging (Figure 4). The color homogeneity is based on the standard deviation of the spectral colors. The shape homogeneity is based on the deviation of a compact or a smooth shape.

The scale determines the maximum heterogeneity among different objects. The larger the scale parameter, the larger the object area generated, and fewer the number of resultant objects (Luo *et al.* 2013). Scale parameters were modified manually. Shape refers to the outline or configuration of an object. It plays an increasingly important role during segmentation process when objects grow larger particularly in case one or more of the subobjects that form the target object have significantly different spectral information (Tong *et al.* 2012). Shape can be portrayed by such geometric parameters as compactness “C” and smoothness “S”. It can be simply computed by dividing the de facto border length *l* by the square root of the number of pixels comprising the concerned image object *n* (Benz *et al.* 2004):

$$C = \frac{1}{\sqrt{n}} \quad (8)$$

The values for *C* range between 0 and 1.

Smoothness refers the ratio of the *de facto* border length *l* to the shortest possible border length *b*,

$$S = \frac{l}{b} \quad (9)$$

For performing SDS we used the output image generated from the previous step (Figure 5). The image-object domain and level settings were done as appropriate, followed by setting the maximum spectral difference. As mentioned in section “Image Segmentation”, the algorithm merges neighboring image objects that have a spectral difference less than the user-defined maximum to modify the results of the segmentation (Figure 5).

#### The Extraction of Road Network

The road network was extracted from the segmented image using a fuzzy rule-based algorithm. A fuzzy rule-based system is essentially based on fuzzy logic and fuzzy set theory. Introduced by Lotfi Zadeh in 1965 (Zadeh 1965), fuzzy logic is an extension of deterministic logic, i.e., fuzzy truth values are continuous, which are ranged from 0 to 1, unlike binary truth values (0 or 1). The fuzzy set theory treats each element *x<sub>i</sub>* having a certain degree of membership to the set *S*, i.e., it partially belongs to the set. The value of the membership degree is determined by the membership function *f<sub>s</sub>(x<sub>i</sub>)* defined for the fuzzy set *S*. Fuzzy rule-based systems (FRBS) are an extension of classical rule-based systems, also known as production systems or expert systems (Bujard 2012). Basically,

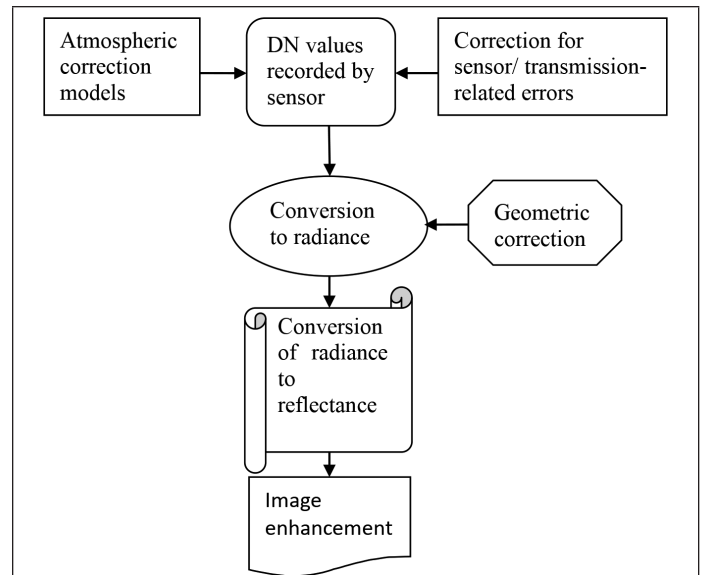


Figure 2. Schematic of the image processing steps.

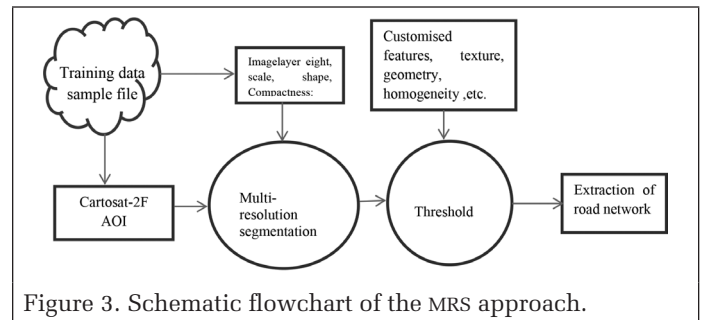


Figure 3. Schematic flowchart of the MRS approach.

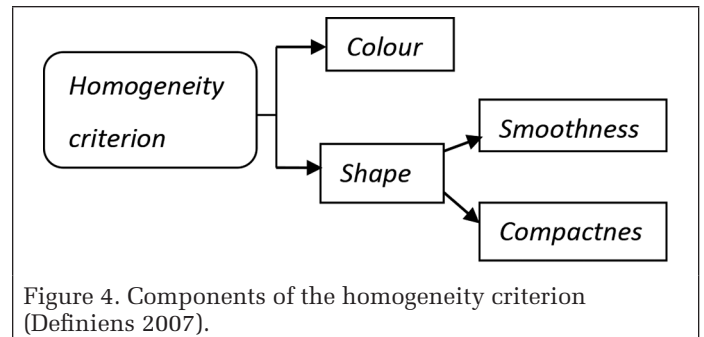


Figure 4. Components of the homogeneity criterion (Definiens 2007).

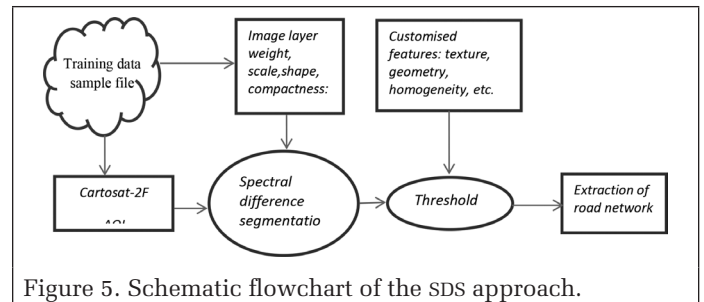


Figure 5. Schematic flowchart of the SDS approach.

FRBS are expressed in the form “IF A THEN B” where A and B are fuzzy sets.

Defining broad spectrum of object features, namely gray-level co-occurrence matrix (GLCM) homogeneity, density, area, rectangular fit, length-to-width ratio, mean NIR values, and normalized difference vegetation index (NDVI) is the first step towards extraction of road network. Homogeneity refers to

the similarity of pixels in terms of reflectance or to one of its derivative values.

$$\text{Homogeneity} = \frac{\sum_{i=1}^{N_g} \sum_{j=1}^{N_g} P_d(i, j)}{1 + |i - j|} \quad (10)$$

where  $N_g$  is the number of gray levels,  $P_d$  is the normalized symmetric GLCM of dimension  $N_g \times N_g$ , and  $P_d(i, j)$  is the  $(i, j)^{\text{th}}$  element of the normalized GLCM (Haralick *et al.* 1973).

A diagonal GLCM gives homogeneity of 1. The density feature describes the distribution of the pixels of an image object in space. Square is the densest shape. The more an object is shaped like a filament the lower the density. The density is calculated by the number of pixels forming the image object divided by its approximated radius, based on the covariance matrix (Definiens 2010):

$$\text{Density} = \frac{\sqrt{\#P_v}}{1 + \sqrt{\text{Var}X + \text{Var}Y}} \quad (11)$$

where  $\sqrt{\#P_v}$  is diameter of a square object with  $\#P_v$  pixels and  $\sqrt{\text{Var}X + \text{Var}Y}$  is diameter of the ellipse.

The area refers to the number of pixels of the objects. Based on in situ information, an upper limit threshold and a lower limit threshold are set to eliminate features which are not of user's interest. The definition of upper and lower limit threshold depends on the spatial resolution of the image used. The length-width ratio in another object feature used in object-oriented classification. It is defined as:

$$R = \frac{L_{\text{MER}}}{R_{\text{MER}}} \quad (12)$$

where  $L_{\text{MER}}$  is the length of the bounding rectangle and  $W_{\text{MER}}$  is the width. A linear object normally has a relatively larger R value. Rectangular fit parameter is another object feature used in classification, which describes how well an image object fits into a rectangle of similar size and proportions. It ranges from 0 to 1, where 0 indicates no fit and 1 means perfect fit. NDVI is the ratio of the difference of the reflectance in NIR from red spectral bands to the sum of the reflectance in NIR with red bands. It is expressed as below:

$$\text{NDVI} = \frac{\rho_{\text{NIR}} - \rho_{\text{RED}}}{\rho_{\text{NIR}} + \rho_{\text{RED}}} \quad (13)$$

where  $\rho_{\text{NIR}}$  refers to reflectance in NIR spectral band and  $\rho_{\text{RED}}$  to reflectance in RED spectral band. The NDVI values range from -1 to +1. In this context, it is used to eliminate vegetation from road features.

#### Morphological Operations

The classified output does not have a uniform shape of road due to nonhomogeneity of the road in real-world scenario. So, in order to get the uniform shape of the road "the Opening" and "the Closing" of the road is applied to the classified output.

#### Accuracy Assessment

For quantitative estimates of the classification accuracy of roads extracted from high-resolution data using OBFE-1 and -2 classifiers sample areas representing roads and nonroads features were selected randomly (Congalton *et al.* 1983). A one-to-one comparison of the roads extracted from multispectral data and reference map was made. Overall accuracy, error of omission and error of commission, and kappa coefficient

(K) were subsequently computed after generating confusion matrix (Congalton and Green 1999). The kappa coefficient (K) was computed as follows (Bishop *et al.* 1975):

$$\hat{K} = \frac{N \sum_{i=1}^r x_{ii} - \sum_{i=1}^r (x_{i+})(x+i)}{N^2 - \sum_{i=1}^r (x_{i+})(x+i)} \quad (14)$$

where  $r$  is the number of rows in the matrix,  $x_{ii}$  is the number of observations in row  $i$ , and column  $i$  (the  $i^{\text{th}}$  diagonal elements),  $x_{i+}$  and  $x+i$  are the marginal totals of row " $r$ " and column  $i$ , respectively, and  $N$  is the number of observations.

#### Per-Pixel Classification

The Gaussian maximum likelihood (GML) classification is a well-established classical per-pixel classification approach. It is based on the premise that the spectral response patterns for each class in each spectral band are normally distributed. The algorithm calculates the probability that a given pixel belongs to a specific class on the ground. Each pixel is assigned to the class that has the highest probability, i.e., the maximum likelihood. However, if the highest probability is smaller than a user-specified threshold, the pixel remains unclassified. For further details on the approach, readers may refer Lillesand *et al.* (2015).

For extraction of roads, spectrally homogenous areas (training sets) representing roads and other land use/land cover features were identified on Cartosat-2F multispectral data and the spectral signature in terms of mean vector, correlation coefficient, and covariance matrix were, initially, generated. The transformed divergence for each training set was subsequently computed for spectral separability analysis. Further refinement in the training sets, if required, was made based on spectral separability analysis. Several iterations were made until an optimal separability was achieved. Finally, using the training set signatures as input, each pixel in the image was assigned to a particular land use/land cover class using per-pixel GML algorithm. The classification accuracy was estimated as the procedure enumerated in the section "Accuracy Assessment".

## Results and Discussion

The results and discussion are organized in two sections: image segmentation and classification. Furthermore, in the classification section, not only we present the results of MRS and SDS but also evaluate the performance of these classifiers vis-a-vis Gaussian maximum likelihood classifier.

### Image Segmentation

#### Multi-Resolution Segmentation

As mentioned in the section "Image Segmentation" for multi-resolution segmentation image object parameters were defined for grouping the image pixels into image objects or segments. It is quite evident from the table that within the same test site the values for image features used for segmentation vary markedly. For instance, the scale value ranges from 15 in predominantly vegetated site (test site 3) to 30 in compact built-up site (test site 1) (Table 1).

The output of multi-resolution part of test site 1 is appended as Figure 6a, and the zoomed version of part of it as Figure 6b. As evident from Figure 6b, despite adequate care taken while assigning values for object features, in some areas especially those marked with arrows in the segmented image, serious anomaly in terms of continuity of segments exists. For instance, in lower-left of Figure 6b, marked with an arrow, vegetation is in a red color, though a single ground feature is seen split into four subobjects. Contrastingly, in areas marked with arrow in the upper right of Figure 6b, wasteland in medium gray and vegetation in red color have been grouped into a single feature.

### Spectral Difference Segmentation

Like MRS, the multi-resolution segmentation of Cartosat-2 multispectral data was performed using object/image parameters like scale, shape, compactness, etc. In addition, the value for spectral difference was also assigned (Table 2). Surprisingly, the spectral values used as spectral differencing parameter in the segmentation step range from 10 in test site 3 to 15 in each of test sites -1 and -2.

### The Extraction of Road Network

The results of all the three test sites are discussed hereunder.

#### Compact Built-Up Site

To begin with, a threshold range of  $>0.23$  to  $<0.67$  was assigned to GLCM homogeneity for extraction of roads from a segmented image fuzzy rule-based algorithm. The threshold range, thus assigned, not only covers roads but also other non-road features like vegetation, soils, and wastelands. In order to refine the feature extraction process other “object”/image parameters like density ( $>1.85$ ), the area ( $<900$  pixels), and rectangular fit ( $>0.45$ ) were assigned to the fuzzy logic-based object-oriented algorithm (Table 3). The roads/road network, thus delineated from the segmented image using MRS, is appended as Figure 7a.

A similar exercise was done for extraction of roads from spectral difference segmented image using a fuzzy rule-based algorithm. Initially, a GLCM homogeneity threshold range of

$>0.23$  to  $<0.54$  was assigned for detection of road network (Table 3). However, like in the case of multi-resolution segmented image here too other nonroad features were misclassified as roads. In order to refine the classification other object/

Table 1. Parameters for multi-resolution segmentation (MRS).

Test Site	Segmentation Parameter	Value
1	Layer weight	1 each for blue, green, and red bands, and 2 for NIR band
	Scale	30
	Shape	0.5
	Compactness	0.1
2	Layer weight	1 each for blue, green, and red bands, and 2 for NIR band
	Scale	18.00
	Shape	0.20
	Compactness	0.10
3	Layer weight	1 each for blue, green, and red bands, and 2 for NIR band
	Scale	15
	Shape	0.8
	Compactness	0.1

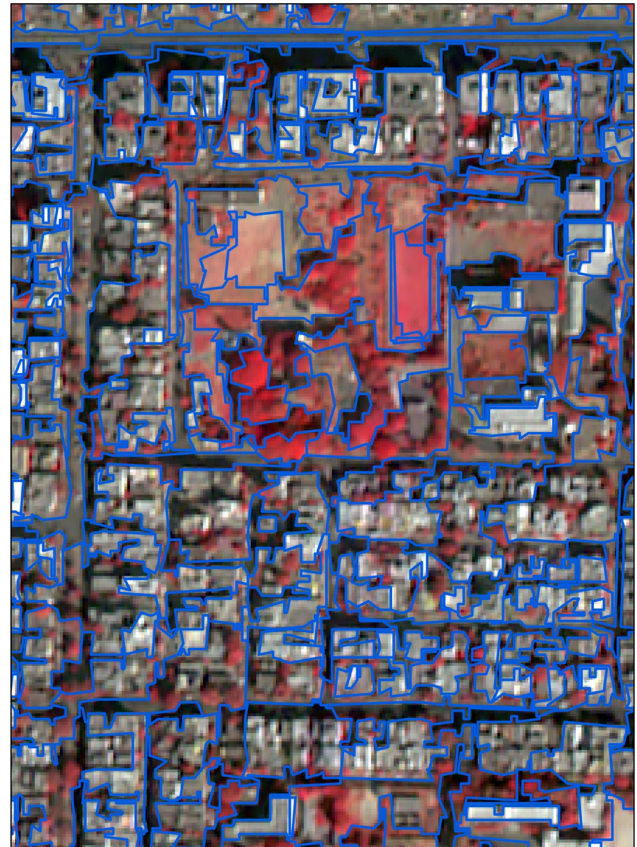
**N.B.** Test site 1: compact built-up site, test site 2: sparse built-up site, and test site 3: predominantly vegetated site.

Table 2. Parameters for spectral difference segmentation (SDS).

Test Site	Segmentation Parameter	Value
1	Layer weight	1 each for blue, green, and red bands, and 2 for NIR band
	Scale	15
	Shape	0.5
	Compactness	0.1
	Spectral difference	10
2	Layer weight	1 each for blue, green, and red bands, and 2 for NIR band
	Scale	15.00
	Shape	0.40
	Compactness	0.00
	Spectral difference	5.0
3	Layer weight	1 each for blue, green, and red bands, and 2 for NIR band
	Scale	15
	Shape	0.5
	Compactness	0.1
	Spectral difference	15



(a)



(b)

Figure 6. Segmented image for part of compact built-up area-1 (a) using MRS approach and (b) a zoomed version of part of the segmented image.

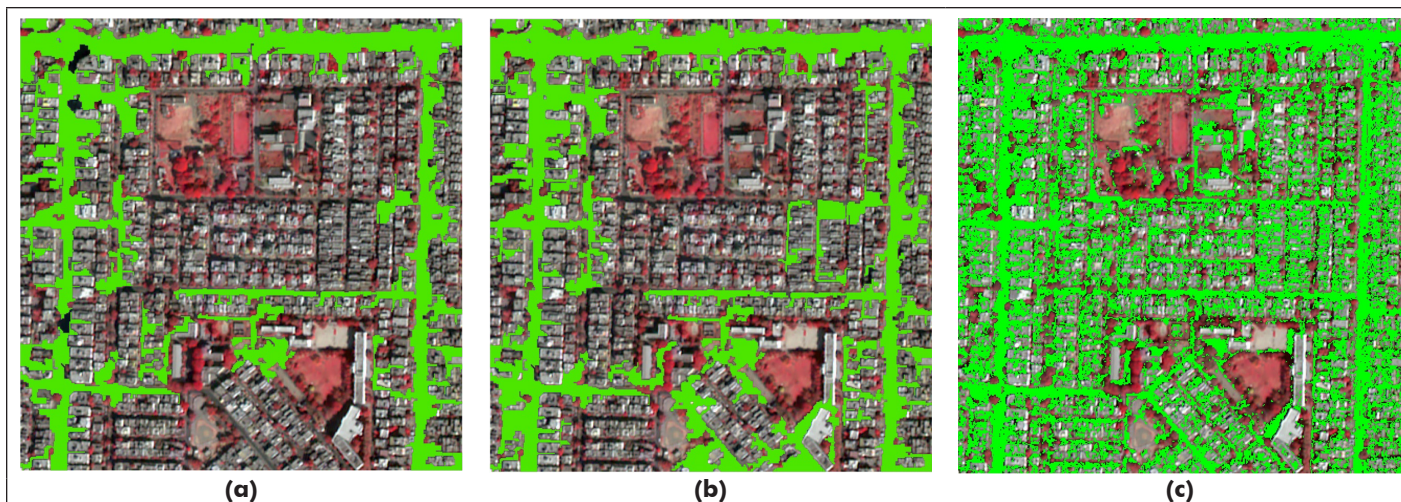


Figure 7. (a) Road layer extracted from MRS, (b) SDS, and (c) maximum likelihood classifier. Green color indicates roads in compact built-up test site 1.

image parameters, namely density, area, and rectangular fit were used, and a value of 1.85, 900 pixels, and 0.45 were assigned to the density, area and rectangular fit, respectively. Output, thus obtained, is appended as Figure 7b.

A comparison of road network extracted MRS with those detected from SDS brings out the fact that a considerable amount of smoothening of road edges could be observed in case of the latter (road feature marked with arrow) (Figures 7a and 7b). Although both primary and secondary roads are mapped using GML-per-pixel classifier (Figure 7c), there is a considerable amount of misclassification. In fact, a fairly large area under built-up land (buildings) has been categorized (misclassified) as road network (green color).

As evident from Figure 7a, MRS could afford the detection of mostly main roads (green color). However, a few link roads passing through residential areas could be delineated as well. An overall classification accuracy of 85% with kappa statistics value of 0.813 could be achieved from MRS image (Table 5). Furthermore, with an overall accuracy of 92% and a kappa value of 0.892 the SDS over scores the MRS in terms of classification accuracy. Interestingly, both of these classifiers scored over classical GML-per pixel classifier which could afford an overall accuracy of 70.0% with a kappa value of 0.685 (Table 5).

The arrows in Figure 7a and 7b indicate the visual impact additional level of image segmentation (spectral difference) done in case of SDS. The smoothness of the road edges in Figure 7b as compared to Figure 7a is quite clear.

#### Sparse Built-Up Site

In sparsely built-up area the density of buildings is relatively low. As a result, the occlusion effect of buildings is relatively smaller. Consequently, the reliability of detection of roads based on spectral response pattern is relatively better. To delineate road network from MRS, a GLCM homogeneity threshold range of  $>0.17$  to  $<0.42$  was assigned which enabled detection of some roads (Table 3). In this process some of the nonroad features like vegetation, bare soils, and wastelands too were classified as roads. For further refining the classification other object/image parameters, viz. density ( $>1.37$ ), and NDVI value ( $<1.0$ ) were defined (Table 3).

Similar steps were followed approach for detection of road network from SDS image. To begin with, a GLCM homogeneity threshold range of  $>0.194$  to  $<0.67$  was defined which permitted detection of some roads (Table 4). Apart from roads some of the nonroad features like vegetation, bare soils, and wastelands too were misclassified as roads. For refining the classification, other object/image parameters viz. density ( $>1.37$ ) and bare area index (BAI) ( $<0.45$ ) were used (Table 4).

Table 3. Object feature values for road extraction using MRS approach.

Features	Site 1	Site 2	Site 3
GLCM homogeneity	$>0.23$ – $<0.67$	$0.17$ – $<0.42$	—
Density	$>1.85$	$>1.65$	—
Area (pixels)	$<900$	$<900$	$<500$
Rectangular fit	$>0.45$	—	—
Blue to NIR ratio	—	—	$>0.15$ – $<0.45$
NDVI	—	$\geq 0.10$	$\geq 0.0$

**N.B.** Compact built-up area (site 1), sparse built-up area (site 2), and predominantly vegetated area (site 3).

Table 4. Object feature values for road extraction using SDS approach.

Features	Site 1	Site 2	Site 3
GLCM homogeneity	$>0.23$ – $<0.54$	$0.194$ – $<0.67$	—
Density	$>1.85$	$>1.37$	—
Area (pixels)	$<900$	—	$<1000$
Rectangular fit	$>0.45$	—	$>0.70$
BAI	—	$<0.45$	$>0.08$ – $<0.35$
NDVI	—	—	$\geq 0.06$

**N.B.** Compact built-up area (site 1), sparse built-up area (site 2), and predominantly vegetated area (site 3).

Table 5. Summary of classification accuracies.

Test Site	Classifiers	Overall Accuracy (%)	Kappa Coefficient
Compact built-up site	MRS	85.00	0.813
	SDS	92.00	0.892
	GML	70.00	0.685
Sparse built-up site	MRS	75.00	0.731
	SDS	88.90	0.862
	GML	62.50	0.613
Predominantly vegetated site	MRS	60.46	0.594
	SDS	77.14	0.768
	GML	50.00	0.489

**N.B.** MRS = Multi-resolution segmentation, SDS = Spectral difference segmentation, and GML = Gaussian maximum likelihood classifier.

As evident from Figure 8a, using MRS approach not only main roads but also a few secondary and even tertiary roads serving the residential areas also could be extracted because of ample image contrast with background, and because of very little occlusion from buildings' shadows. The MRS-spectral-differencing segmentation facilitated the extraction of a few additional secondary/tertiary roads in the eastern peripheral areas of the test site (Figure 8b). The fact is supported by an improvement in overall classification accuracy. Whereas an overall accuracy of 75% with kappa value of 0.731 has been achieved in case of MRS, the corresponding figures for SDS are 88.9% and 0.862, respectively (Table 5).

A comparison of overall accuracies figures realized from MRS and SDS with that of per-pixel classifier reveals the better performance of the former over the latter which could provide an overall accuracy of 62.5% with a kappa value of 0.613 (Table 5). The poor accuracies values from per-pixel classifier may be attributed to spectral similarity of roads with that of background terrain and roof tops, and to the fundamental differences in the classification algorithm (Figure 8c). Whereas intraclass variability resulting from higher spatial resolution multispectral data has been addressed at the segmentation stage in case of object-based feature extraction, the per-pixel classifier relies only on spectral response pattern of an individual pixel.

The arrows in Figure 8a and 8b indicate the visual impact of additional level of image segmentation done in SDS that has resulted in extraction of additional roads.

#### Predominantly Vegetated Site

For extraction of road network from multi-resolution MRS image a blue to NIR ratio threshold of  $>0.15$  to  $<0.45$  was applied. The output image shows up not only road network but non-road features as well. In order to exclude the nonroad feature, another image parameter an NDVI threshold of  $\geq 0$  in conjunction with area threshold value of  $<500$  pixels was assigned (Table 3). In case of SDS for detection of road network a BAI threshold range of  $>0.08$  to  $<0.35$  was defined for extraction of roads (Table 4). The resultant output image included some nonroad features too. Further improvement in classification was made by using NDVI, area, and rectangular fit parameters with values  $\geq 0.06$ ,  $<1000$  pixels, and  $\geq 0.7$ , respectively.

The success of the extraction of road network has not been encouraging. In case of MRS (Figure 9a) only a few vegetation features have been misclassified as roads. In contrast, apart from roads, many trees, and other vegetation features have been delineated as roads from SDS image (Figure 9b). It may be because of the fact that the advanced level segmentation has been performed on already segmented image resulting, thereby in further smoothing of already segmented image. An overall accuracy of delineation of 60.46% with a kappa



Figure 8. (a) Road layer extracted in part of the test site from MRS, (b) SDS, and (c) maximum likelihood classifier (test site 2).

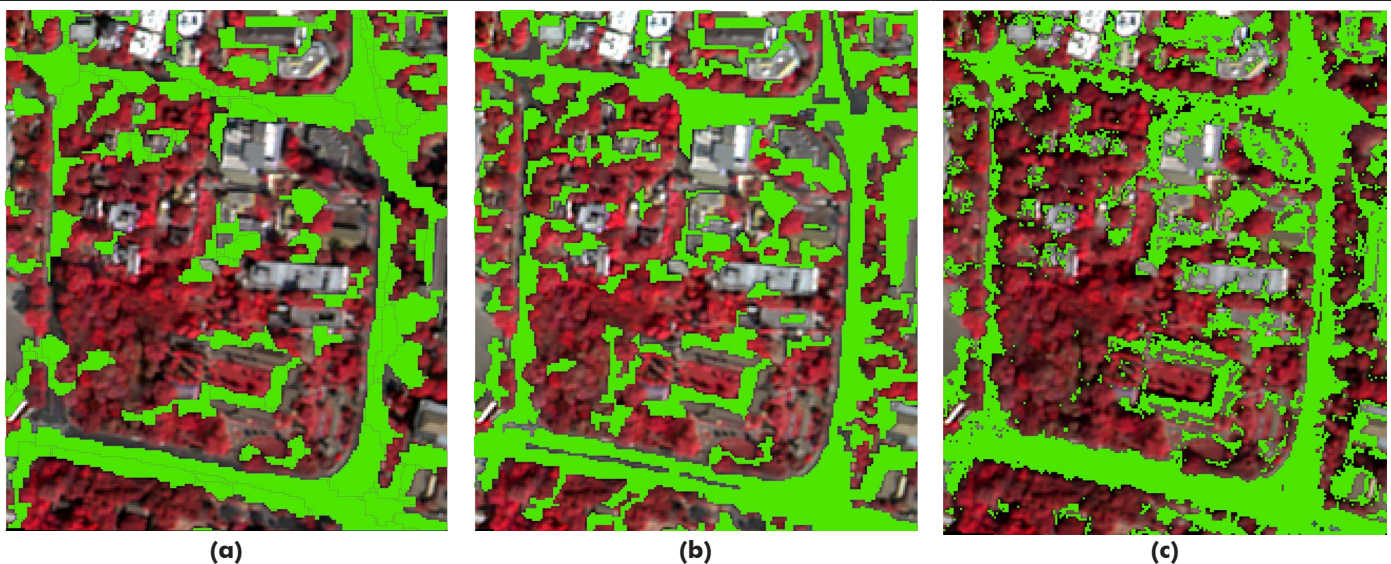


Figure 9. (a) Road layer extracted using MRS, (b) SDS, and (c) supervised classification (test site 3).

coefficient of 0.594 has been achieved in case of MRS was used as against 77.46% achieved from SDS.

Contrastingly, the overall classification accuracy value for GML per-pixel classifier-based output is 50% with a kappa coefficient of 0.489 (Table 5). Furthermore, it is amply clear from Figure 9c that although all the major roads have been extracted, due to spectral similarity between roads and terrain features like roof tops most of the built-up areas have been misclassified as roads (green color in Figure 9c).

## Conclusions

The study has vividly demonstrated the potential of fuzzy logic-based object-oriented classifier in the extraction of roads from high resolution spaceborne multispectral data. The fuzzy logic-based object-oriented classifier better performed classical Gaussian maximum likelihood classifier. Furthermore, within object-oriented approach SDS approach has been found to score over multi-resolution segmentation approach in terms of extraction of roads network. Like classical per-pixel classifier, in-object-oriented classifiers also the involvement of analyst in defining the values of objects' features and in refining the output is required. It introduces an element of subjectivity which calls for automation and optimization of defining these parameters in the classification process. Some efforts have, however, already been made in this direction (Dragut *et al.* 2014; Zheng 2015). More systematic studies are needed to address the segmentation optimization process. Lastly, owing to the existing complexities in road features like discontinuities, occlusion, or shadows, near-parallel boundaries with inconstancy in width and sharp curves, it is almost impossible to model all these situations and to incorporate them into a single module. Multi-model approach, therefore, needs to be developed for road extraction using high to very high resolution remote sensing data.

## Acknowledgments

The authors wish to sincerely thank Dr. Santanu Chowdhary, Director, and Dr. T. Ravi Sankar, Group Director, Land Resources Land Use Cover Monitoring Group, and Dr. G. Ravi Shankar Scientist/Engineer "SG", National Remote Sensing Centre (NRSC) for providing necessary facilities to carry out the project work. Furthermore, technical support provided by Ms. Thara Nair, Head, IODPD, DPA, NRSC is duly acknowledged. Ms. Leena and R.S. Dwivedi express their gratitude to Prof. B. Venkateswara Rao, Director, and Prof. C. Sarala Head, Centre for Spatial Information Technology, Jawaharlal Nehru Technological University, Hyderabad for evincing keen interest in the study and for timely reviewing the progress of the study and for their valuable suggestions.

## References

- Anselin, L. 1995. Local indicators of spatial association—LISA. *Geographical Analysis* 27 (2):93–115.
- Bezdek, J. C., R. Ehrlich and W. Full. 1984. FCM: The fuzzy c-means clustering algorithm. *Computers and Geosciences* 10:191–203.
- Benz, U. C., P. Hofmann, G. Willhauck, I. Lingenfelder and M. Heynen. 2004. Multi-resolution, object-oriented fuzzy analysis of remote sensing data for GIS-ready information. *ISPRS Journal of Photogrammetry and Remote Sensing* 58 (3–4):239–258.
- Bieniek, A. and A. Moga. 2000. An efficient watershed algorithm based on connected components. *Pattern Recognition* 33:907–916.
- Bishop, Y., S. Fienberg and P. Holland. 1975. *Discrete Multivariate Analysis-Theory and Practices*. Cambridge, Massachusetts: MIT Press.
- Burnett, C. and T. Blaschke. 2003. A multi-scale segmentation/object relationship modelling methodology for landscape analysis. *Ecological Modeling* 168 (3):233–249.
- Bujard, A. 2012. fugeR: Fuzzy Genetic, a Machine Learning Algorithm to Construct Prediction Model Based on Fuzzy Logic. R package Version 0.1.2. <<http://CRAN.R-project.org/package=fugeR>>
- Chen, L., Q. Zhu, X. Xie, H. Hu and H. Zeng. 2018. Road extraction from VHR remote-sensing imagery via object segmentation constrained by Gabor features. *ISPRS International Journal of Geo-Information* 7:362. doi: 10.3390/ijgi7090362.
- Congalton, R. S. and K. Green. 1999. *Assessing the Accuracy of Remotely Sensed Data: Principles and Practices*. Boca Raton, Florida: CRC/Lewis Press.
- Congalton, R., R. Oderwald and R. Mead. 1983. A quantitative method to test for consistency and correctness in photo interpretation. *Photogrammetric Engineering on Remote Sensing* 49 (1):69–74.
- Definiens. 2007. *Definiens, User Guide*, 2007. München, Germany: Definiens AG.
- Definiens. 2010. *Definiens Developer Reference Guide*. München, Germany: Definiens AG.
- Dragut, L., O. Csillik, C. Eisank and D. Tiede. 2014. Automated parameterisation for multi-scale image segmentation on multiple layers. *ISPRS Journal of Photogrammetry and Remote Sensing* 88:119–127.
- ENVI. 2013. *ENVI Help*, Exelis Visual Information Solutions. Boulder, Colorado: ENVI.
- Gao, J. 2009. *Digital Analysis of Remotely Sensed Imagery*. New York: McGraw Hill.
- Gao, L., W. Shi, Z. Miao and Z. Lv. 2018. Method based on edge constraint and fast marching for road centreline extraction from very high-resolution remote sensing images. *Remote Sensing* 10:900.
- Gao, Y., J. F. Mas, N. Kerle and J. A. Navarrete Pacheco. 2011. Optimal region growing segmentation and its effect on classification accuracy. *International Journal of Remote Sensing* 32 (13):3747–3763.
- Grote, A., C. Heipke and F. Rottensteiner. 2012. Road network extraction in suburban areas. *Photogrammetric Record* 27 (137):8–28.
- Hamilton, R., K. Megown, T. Mellin and I. Fox. 2007. *Guide to automated stand delineation using image segmentation*. RSAC-0094-RPT1. Salt Lake City, Utah: U.S. Department of Agriculture, Forest Service, Remote Sensing Applications Center.
- Haralick, R., M. K. Shanmugam and I. Dinstein. 1973. Textural features for image classification. *IEEE Transactions on Systems, Man and Cybernetics* 3 (6):610–621.
- Hassouna, M. S. and A. A. Farag. 2007. Multistencils fast marching methods: A highly accurate solution to the eikonal equation on cartesian domains. *IEEE Transactions on Pattern Analysis and Machine Intelligence* 29:1563–1574.
- Kahraman, I., I. R. Karas and A. E. Akay. 2018. Road extraction techniques from remote sensing images: A review. In *Proceedings 2018 International Conference on Geomatics and Geospatial Technology (GGT 2018)*, held in Kuala Lumpur, Malaysia, 3–5 September 2018. The International Archives of the Photogrammetry, Remote Sensing and Spatial Information Sciences, vol. XLII-4/W9.
- Kamarainen, J.-K. 2012. Gabor features in image analysis. Pages 13–14, 34 in *Proceedings of the 2012 3rd International Conference on Image Processing Theory, Tools and Applications (IPTA)*, held in Istanbul, Turkey, 15–18 October 2012.
- Kim, M., T. A. Warner, M. Madden and D. S. Atkinson. 2011. Multi-scale GEOBIA with very high spatial resolution digital aerial imagery: Scale, texture and image objects. *International Journal of Remote Sensing* 32 (10):2825–2850.
- Kumar S. and M. Hebert. 2006. Discriminative random fields. *International Journal of Computer Vision* 68 (2):179–201.

- Lafferty, J., A. McCallum and F. C. Pereira. 2001. Conditional random fields: Probabilistic models for segmenting and labeling sequence data. Pages 282–289 in *Proceedings 18th International Conference on Machine Learning (ICML)*. San Francisco, California: Morgan Kaufmann Publishers Inc.
- Lillesand, T., M. Ralph, W. Kiefer and J. W. Chipman. 2015. *Remote Sensing and Image Interpretation*. Wiley.
- Luo, K. S, R. D. Li and B. R. Chang. 2013. Survey method of large scale land cover based on object classification technology. *Journal of University of Chinese Academy of Science*, 6th ed. 30:770–777.
- Mena, J. B. 2003. State of the art on automatic road extraction for GIS update: A novel classification. *Pattern Recognition Letters* 24 (16):3037–3058.
- Ok, A. O. 2017. Automated detection of buildings and roads in urban areas from VHR satellite images. *Journal of Geodesy and Geoinformation* 3 (1): 29–38.
- Otsu, N. 1979. A threshold selection method from gray-level histograms. *IEEE Transactions on Systems, Man, and Cybernetics* 9:62–66.
- Poullis, C. and S. You. 2010. Delineation and geometric modeling of road networks. *ISPRS Journal of Photogrammetry and Remote Sensing* 65 (2):165–181.
- Sethian, J. A. 1999. Fast marching methods. *Siam Review* 41:199–235.
- Shi, W., Z. Miao and J. Debayle. 2014. An integrated method for urban main-road centerline extraction from optical remotely sensed imagery. *IEEE Transactions on Geoscience and Remote Sensing* 52:3359–3372.
- Sun, X. X., J. X. Zhang and Z. J. Liu. 2006. Object-oriented classification method to extract the river and the road. In *IKONOS Panchromatic Image, Science of Surveying and Mapping*, 1st ed., vol. 31, 62–63.
- Tong, H., T. Maxwell, Y. Zhang and V. Dey. 2012. A supervised and fuzzy-based approach to determine optimal multi-resolution image segmentation parameters. *Photogrammetric Engineering & Remote Sensing* 78 (10):1029–1044.
- Wagstaff, K., C. Cardie, S. Rogers and S. Schrödl. Constrained k-means clustering with background knowledge. Pages 577–584 in *Proceedings of the ICML*, held in Williamstown, Massachusetts, 28 June–1 July 2001.
- Wang, W., N. Yang, Y. Zhang, F. Wang, T. Cao and P. Eklund. 2016. A review of road extraction from remote sensing images. *Journal of Traffic and Transportation Engineering (English edition)* 3 (3):271–282.
- Wang, Y. and Q. Zheng. 1998. Recognition of roads and bridges in SAR Images. *Pattern Recognition* 31 (7):953–962.
- Zadeh, L. A. 1965. Fuzzy sets. *Information and Control* 8 (3):338–353. doi: 10.1016/s0019-9958(65)90241-x.
- Zheng, L. 2015. Parameter optimization in multi-scale segmentation of high resolution remotely sensed image and its application in object-oriented classification. *Proceedings of the 2015 International Conference on Environmental Engineering and Remote Sensing*.
- Zhong, Y., J. Zhao and L. Zhang. 2014. A hybrid object-oriented conditional random field classification framework for high spatial resolution remote sensing imagery. *IEEE Transactions on Geoscience and Remote Sensing*, 11th ed. 52:7023–7035.
- Zhou, T., C. Sun and H. Fu. 2019. Road information extraction from high-resolution remote sensing images based on road reconstruction. *Remote Sensing* 11:79. doi: 10.3390/rs11010079.

# Digital Surface Model Refinement Based on Projected Images

Jiali Wang and Yannan Chen

## Abstract

Currently, the practical solution to remove the errors and artifacts in the digital surface models (DSM) through stereo images is still manual or semiautomatic editing those affected patches. Although some degrees of semiautomation can be gained, the DSM refinement remains a labor consuming and expensive process. This paper proposes a new method to correct errors in DSM or/and refine an existing coarse DSM. The method employs the concept of projected images together with some image matching techniques to correct/refine the affected regions in DSM. Since projected images are used, the proposed method can greatly simplify the complicated coordinate transformations and pixel resampling; therefore, the errors/artifacts in DSM can be amended more efficiently and accurately. Several experiments demonstrate the practical usefulness of the proposed method under some scenarios, and some potential improvements are also pointed out to accommodate the various needs during refining DSM.

## Introduction

The digital surface model (DSM) is probably one of the most popular products widely used in photogrammetric and remote sensing applications. DSM also has its role in many other application areas. For example, the prerequisite for the recently popular digital twins for cities (Ruohomaki *et al.* 2018) is the replicas of physical cities' appearances that is basically the detailed virtual photorealistic DSM. High-resolution three-dimensional (3D) urban DSM can be used for urban planning, environment monitoring, infrastructure asset management, and so on. With the advance of digital imaging technology, very high-resolution imagery can be captured from airborne camera systems. DSM can be derived from those multiple overlapped images in unprecedented detail using some of the latest 3D surface reconstruction commercial photogrammetric systems, such as ContextCapture (Bentley Systems), Correlator 3D (Simactive Inc.), Inpho Match-T (Trimble Navigation Ltd.), Metashape (Agisoft), Pix4Dmapper (Pix4D), Pixel Factory (Airbus Defence and Space), SocetSet (BAE System), SURE (nFrames), UltraMap (Vexcel Imaging), and so on.

Automatic matching algorithms are essential to DSM generation in 3D surface reconstruction systems. There are several classic matching techniques such as the normalized correlation coefficients (NCC) (Bourke 1996), least squares multi-point matching (Rosenholm 1987), dynamic programming matching techniques (Cormen *et al.* 1990), relaxation method matching techniques (Christmas *et al.* 1995; Geman and Geman 1984), semiglobal matching technology (Hirschmüller 2008), etc. Although the latest matching techniques in 3D surface reconstruction systems can achieve great matching

accuracy and efficiency, it is true that, more or less, various errors and artifacts exist in almost every DSM that is automatically reconstructed using image matching techniques, especially in image areas where less information is available (Gruen 2012). These DSM artifacts may be caused by a variety of imaging phenomena, such as occlusions, moving objects, illumination oversaturation, surface reflections, lack of surface texture, etc., and/or due to the limitations of image matching algorithms (Zhang 2005).

In recent years, many researchers have put forth efforts to improve matching techniques from various aspects to reduce matching errors: for example, using redundant information of multiple images to improve the DSM accuracy (Zhang and Gruen 2006; Zhang *et al.* 2017; Zhao *et al.* 2018; Zhu *et al.* 2010); using geometric feature information to obtain highly accurate DSM (Alobeid *et al.* 2010; Gao *et al.*, 2018; Jiang and Jiang 2019); and adopting the multi-view stereo matching method to reconstruct the surfaces (Furukawa and Ponce 2010; Zhu *et al.* 2020). With all the efforts, the DSM refinement still remains a labor consuming and expensive process, since processing all images may remove previous errors but introduce new errors and artifacts somewhere else. Because no perfect matching algorithms exist yet, some commercial photogrammetric systems provide DSM editing tools that allow manually correcting errors and artifacts in DSM.

This paper proposes a new method to refine an existing DSM based on projected images, the new method is inspired by the Vertical Line Locus (VLL) method (Chen *et al.* 2012; Cogan *et al.* 1988; Li 1988). Unlike VLL, which is based on the geometric relationships between the original images and the ground surface, this proposed method first projects the original images onto a common reference plane (horizontal) to form so called "projected images", then applies image matching algorithms on the projected images in the hope that errors in DSM can be corrected. The main contribution of this paper is utilization of the concept of projected images during image matching and 3D coordinate calculations to greatly simplify (1) expensive coordinate transformations between the image space and the object space and (2) correlation window resampling.

In the following sections, the proposed methods are presented in detail (section "Methods"): the principle of the proposed method is illustrated through a single-point correction experiment (Experiment A, section "Single-Point Correction"), followed by an experiments that shows a coarse DSM patch can be refined effectively (Experiment B, section "Coarse DSM Patch Refinement"), and a wrong DSM patch can be corrected through rematching (Experiment C, section "Wrong DSM Patch Correction"); in the last experiment (Experiment D, section "DSM Patch Refinement and Editing Comparisons"), the results from the proposed method are compared with common manual editing tools, and some

---

Jiali Wang is with the College of Information Technology, Shanghai Ocean University, 999 Hucheng Huanlu Road, Shanghai, China (jl-wang@shou.edu.cn).

Yannan Chen is with the College of Marine Science, Shanghai Ocean University, 999 Hucheng Huanlu Road, Shanghai, China.

---

Photogrammetric Engineering & Remote Sensing  
Vol. 87, No. 3, March 2021, pp. 181–187.  
0099-1112/21/181–187

© 2021 American Society for Photogrammetry  
and Remote Sensing  
doi: 10.14358/PERS.87.3.181

elevation accuracies against reference elevations are also analyzed. Finally, some conclusions are drawn, and further improvements are pointed out to accommodate various needs while refining DSM.

## Methods

Assuming a DSM with some errors/artifacts inside is provided and required for refinement, and also assuming that the stereo images which cover the DSM extents are also provided, the common ways to fix those errors/artifacts are either reprocessing these images with some adjusted processing parameters (Ling *et al.* 2019), which is a time-consuming process and may fix some errors but could introduce new errors, or fitting the affected DSM region with a plane or surface (Wang and Yu 2011; Zheng *et al.* 2019), which is purely arbitrary data manipulation without taking into account the actual image information. In photogrammetric literature, image matching approaches usually can be sorted into area-based matching and feature-based matching; image matching approaches can also be sorted into image space-based matching and object space-based matching based on the main coordinate system used during matching (Lemmens 1988; Wang 1990). Both kinds of matching approaches are popular and have their places in certain applications. The proposed method uses the concept of projected images, integrates the image space and the object space. This method takes advantage of both the image space-based matching approach (simple geometry via epipolar lines), and the object space-based matching approach (direct elevation deriving via collinear equations). Once the extent of an affected DSM region is given, the proposed method can correct DSM errors efficiently and accurately. In the following subsections, the projected image, projected locus, and image matching method based on projected images are described in detailed.

## Projected Image

A projected image is a special orthoimage generated using a horizontal plane as DSM. Figure 1 illustrates the relationships of a projected image with its original image's projection center  $S(X_s, Y_s, Z_s)$  and the horizontal plane (assuming the plane's elevation is a constant  $Z_0$ ).

Point  $P(X_p, Y_p, Z_0)$  on the horizontal plane is projected onto the projected image as  $P'(X_p, Y_p)$ , and the projection center  $S(X_s, Y_s, Z_s)$  is projected onto the projected image as  $S'(X_s, Y_s)$ .  $P'$  and  $S'$  have the same elevation  $Z_0$  as  $P$ . The coordinates  $X_p, Y_p$  of  $P'$  can be calculated using collinear Equation 1:

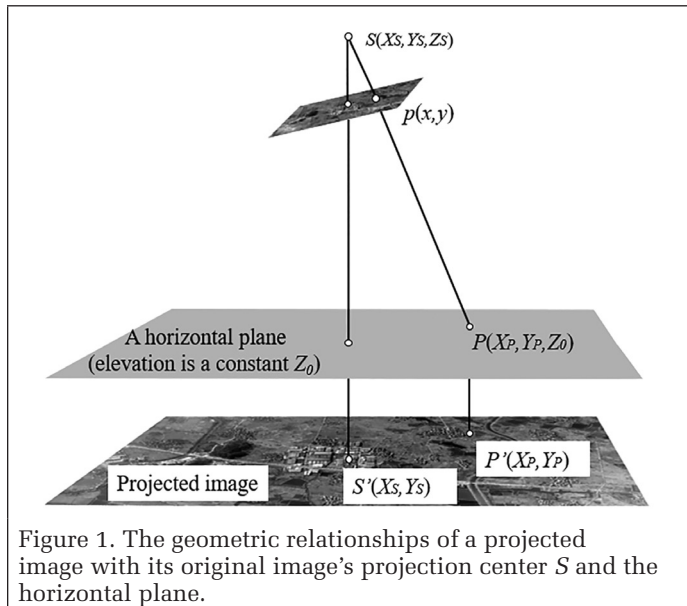


Figure 1. The geometric relationships of a projected image with its original image's projection center  $S$  and the horizontal plane.

$$\begin{cases} X_p = \left( \frac{a_1(x-x_0)+a_2(y-y_0)-a_3f}{c_1(x-x_0)+c_2(y-y_0)-c_3f} \right) (Z_0 - Z_s) + X_s \\ Y_p = \left( \frac{b_1(x-x_0)+b_2(y-y_0)-b_3f}{c_1(x-x_0)+c_2(y-y_0)-c_3f} \right) (Z_0 - Z_s) + Y_s \end{cases} \quad (1)$$

where  $x, y$  denote the image coordinates of  $P$  on the original image;  $Z_0$  is the constant elevation value of the horizontal plane (for simplification  $Z_0$  can be set to 0);  $x_0, y_0$ , and  $f$  are the camera's internal parameters (the principal point and the focal length);  $X_s, Y_s, Z_s$  are the coordinates of the image projection center  $S$ ; and  $(a_i, b_i, c_i)$  ( $i = 1, 2, 3$ ) are the nine elements of the rotation matrix of the original image (Wang 1990, p. 8).

The projected image can be imagined as a giant "image" on the ground. It shares the same projected center with the original image, but its three rotation angles are 0, and the projected image has a huge focal length ( $Z_s - Z_0$ ). Based on the definition of a projected image, the image space of a projected image is the same as the object space of the projected image. This property of the projected image greatly simplifies the coordination calculation between image space-based and object space-based matching and avoids the repeated pixel resampling during subsequent image matching and DSM reconstruction stages; therefore, the improved processing efficiency can be gained.

## Projected Locus

According to the VLL method, the elevation of pending point  $P$  can be determined by finding the optimal matching score through searching up and down along its vertical direction. The VLL method is slow because the points' image and object coordinates need to be calculated using the collinearity equations each time and the image patches on the left and right original images need to be resampled each time. Utilizing the projected image's property, those coordinate calculations and image resampling can be greatly simplified. For the stereo image case, assuming all candidate points  $P_i$  ( $i = 1, 2, 3, \dots, n$ ) passing through the left and right images centers  $S_j$  ( $j = 1, 2$ ) are projected onto the left and right projected images. It can be seen from Figure 2a that all projected points  $P_{ij}$  ( $i = 1, 2, 3, \dots, n; j = 1, 2$ ) either on the left or the right projected image form a locus (projected locus). The corresponding point pair on the left and right projected loci (linked with dots in Figure 2a) are therefore the potential matching candidate pair. Figure 2b depicts the simple geometric relationship among the projected point  $P_i$ , candidate point  $P_i$ , and projected center  $S$ . Due to the simplicity of the geometric relationships among points and unified coordinate system, the coordinate calculation and image resampling become very obvious.

The image and object coordinates of projected point  $P_i$  can be easily obtained using Equation 2.

$$\begin{cases} X_{pi}' = \frac{\lambda X_s - X_p}{\lambda - 1} \\ Y_{pi}' = \frac{\lambda Y_s - Y_p}{\lambda - 1} \end{cases} \quad (2)$$

where  $\frac{Z_i}{Z_s} = \frac{X_p - X_{pi}'}{X_s - X_{pi}'} = \frac{Y_p - Y_{pi}'}{Y_s - Y_{pi}'} = \lambda$ ,  $Z_i = Z_0 + i \cdot \Delta Z$  ( $i = 0, 1, 2, \dots, n$ ).

## Image Matching Techniques

Using the abovementioned projected image and projected locus concepts to find the corrected elevation for any point becomes to find the best matching pair among the candidate pairs, therefore the popular image matching techniques can be employed and adapted easily to solve the projected image-based matching problems. Since developing new matching techniques is not the primary purpose of this

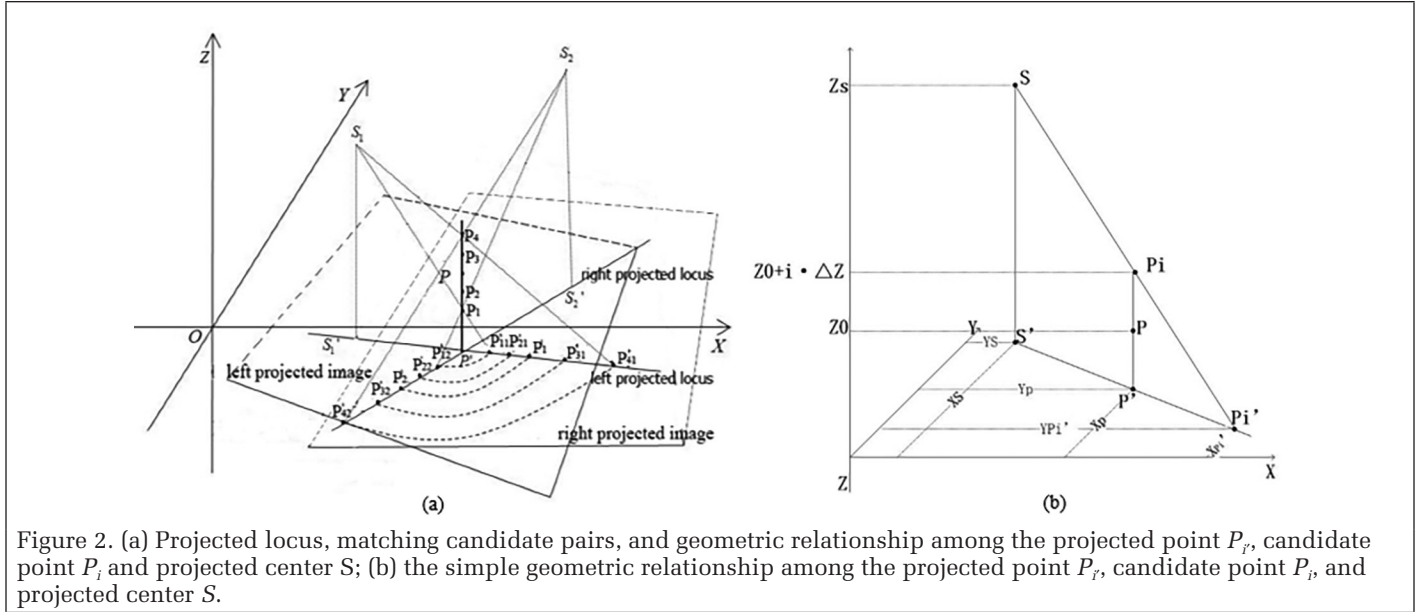


Figure 2. (a) Projected locus, matching candidate pairs, and geometric relationship among the projected point  $P_i$ , candidate point  $P_j$  and projected center  $S$ ; (b) the simple geometric relationship among the projected point  $P_i$ , candidate point  $P_j$ , and projected center  $S$ .

paper, commonly used correlation-based relaxation matching technique is described next in order to demonstrate how matching can be performed on projected images. The NCC image matching technique is chosen as an example to illustrate the process of correcting and refine elevation values. NCC is defined in Equation 3, through coordinate calculation and image resampling, all NCC for candidate pairs of point  $P$  can be obtained, the optimal score is usually the highest NCC, and the corrected elevation is then obtained.

$$NCC_i(P, Z_i) = \frac{\sum_{s \in W} (I_{i1}(s_{i1}) - \bar{I}_{i1})(I_{i2}(s_{i2}) - \bar{I}_{i2})}{\sqrt{\sum_{s \in W} (I_{i1}(s_{i1}) - \bar{I}_{i1})^2} \sqrt{\sum_{s \in W} (I_{i2}(s_{i2}) - \bar{I}_{i2})^2}} \quad (3)$$

where  $\bar{I}_{i1} = 1/m \times n \sum_{s \in W} I_{i1}(s_{i1})$ ,  $\bar{I}_{i2} = 1/m \times n \sum_{s \in W} I_{i2}(s_{i2})$ .

Here,  $I_{i1}$ ,  $I_{i2}$  denote the image intensity values of the points  $P_{i1}$ ,  $P_{i2}$  on its projected images with respect to search point  $P_i$  and the correlation window  $W$ .  $s_{i1}$ ,  $s_{i2}$  are the pixels within the correlation-window  $W$  in the search projected points  $I_{i1}$ ,  $I_{i2}$ , respectively.  $I_{i1}(s_{i1})$ ,  $I_{i2}(s_{i2})$  are the grey values of the search projected points  $P_{i1}$ ,  $P_{i2}$ ,  $m$  and  $n$  are the size dimensions of window  $W$ .

When there are more than two overlapped images available for point  $P$ , each candidate can form multiple pairs to calculate multiple NCC. Some technique approaches described in (Okutomi and Kanade 1993; Zhang and Gruen 2006) can be used to determine the optimal score and final elevation value, such as using the average values of the multiple NCC to find the maximum correlation coefficient and its corresponding elevation as the optimal value.

To an extent, the above single point correction processing to a patch refinement, a mesh grid is defined over the patch, and instead of finding the single optimal matching score, a global optimization process is performed. In this paper, a global relaxation image matching method, which is similar to Zheng *et al.* (2004), is adapted as the projected image space-based matching to correct and refine the patch.

The global relaxation image matching method can be expressed using Equation 4.

$$P^{(n+1)}(i, j) = \frac{P^{(n)}(i, j) Q^{(n)}(i, j)}{\sum_{s=a}^{m_j} P^{(n)}(i, s) Q^{(n)}(i, s)} \quad (4)$$

where  $Q^{(n)}(i, j) = \prod_{I_h \in \Omega(a)} \sum_{k=1}^{m_k} P^{(n)}(h, k) C(i, j; h, k)$ ;  $(i, j)$  is the

candidate matching pair, and  $(h, k)$  is its neighbor pair.  $P(i, j)$  is the probability of pair  $(i, j)$  and is updated iteratively.  $C(i, j; h, k)$  is the compatible coefficient function between pair  $(i, j)$  and its neighboring pair  $(h, k)$ ;  $Q^{(n)}(i, j)$  expresses the support pair  $(i, j)$  received at the  $n$ th iteration from all its neighbor pairs  $(h, k)$  in its neighborhood  $\Omega(a)$ .

In addition, smoothness constraints can be introduced into the relaxation process to handle less texture or homogeneous areas, discontinuities also can be achieved through relaxing the smoothness constraints.

### The Proposed DSM Correction and Refinement Approach

An approach to refine an existing DSM has been developed based on the abovementioned projected images and projected image based matching techniques. Figure 3 shows the workflow chart of the proposed approach. The proposed approach first generates projected images from the original images, followed by image matching and DSM reconstruction based on the projected images. Several experiments (single-point correction, patch refinement, patch correction, and patch refinement validation) are conducted in order to demonstrate the feasibility of the proposed approach.

### Experiment Results

Two regions are chosen to test the proposed method: one region (Figure 4a) covers very flat terrains (elevations vary from 0 to 40 m) while another region (Figure 4b) covers undulating rough terrains (elevations vary from 15 to 430 m). Each region is covered by three consecutive aerial images to form stereo pairs. Those images were acquired using a photogrammetric imaging system (UltraCamXp). The camera focal length is 70.50 mm, image size is 103.86 × 67.86 mm, panchromatic image pixel size is 17 310 × 11 310, the ground sample distance is 0.3 m, the flight height is around 3500 m above the sea level, and the overlap percentages of adjacent images are about 70%. These images were triangulated for the two regions and two DSM with 0.4 m resolution were generated using an in-house algorithm that is similar to that of Zheng *et al.* 2004.

Figure 4 has shown the two orthoimages (Figure 4a and 4b) of the test regions, which include two single points ( $P_1$  and  $P_2$  in Figure 4a) of Experiment A, and the patches (Boxes  $A_1$ ,  $A_2$ , and  $A_3$  in Figure 4a and 4b) of Experiments B, C, and D, respectively. It is not difficult to find that some buildings are reconstructed inaccurately (Box  $A_1$ ), and a few DSM artifacts (the

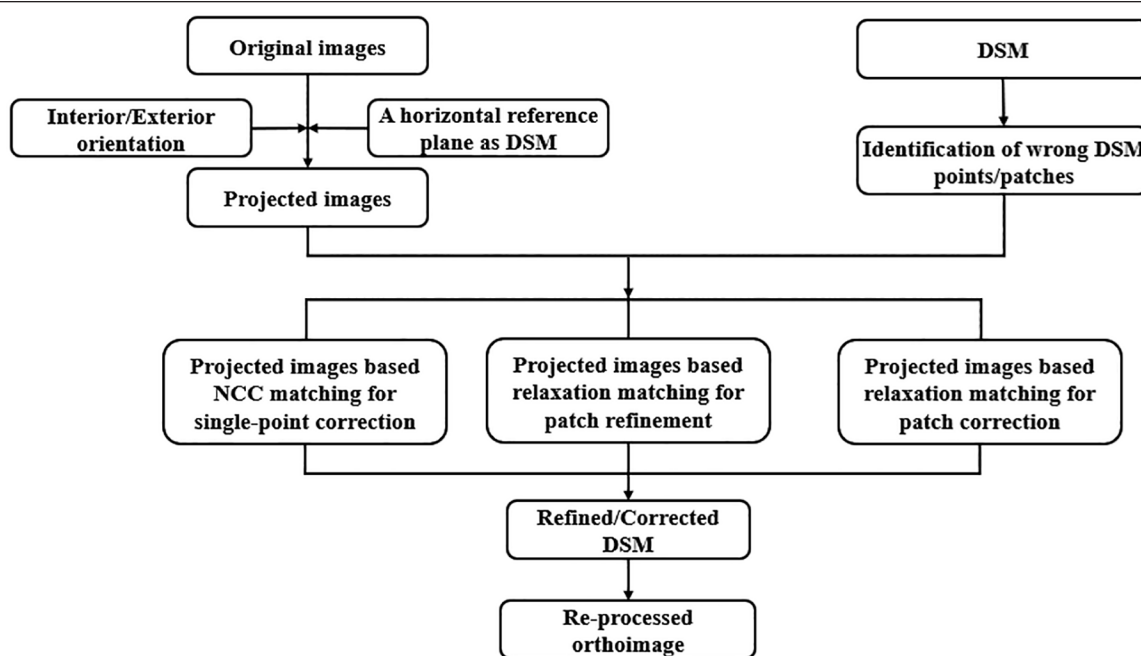


Figure 3. The workflow chart of the proposed DSM correction and refinement approach. DSM = digital surface model; NCC = normalized correlation coefficient.

bright spots in Boxes  $A_2$ ,  $A_3$  in Figure 4a and 4b). As mentioned previously, those errors/artifacts are due to various reasons such as occlusions, moving objects, illumination oversaturation, surface reflections, etc., or due to the limitations and difficulties of image matching algorithms. Although it is not always the case, it is assumed here that those errors/artifacts can be corrected using improved/different image matching techniques. In the following three subsections, some DSM correction/refinement attempts are made to demonstrate the feasibilities of the proposed method. Experiment A is for single-point correction ( $P_1$  and  $P_2$ ). Both Experiments B and C demonstrate how to refine the coarse DSM patches of buildings (Box  $A_1$  covers an area of  $180\text{ m} \times 180\text{ m}$ ) and the totally wrong DSM patches of agricultural land (Box  $A_2$  covers an area of  $200\text{ m} \times 200\text{ m}$ ), respectively. Experiment D compares DSM refinement/correction results from the proposed method and common DSM editing tools in a dense forest area (Box  $A_3$  covers an area of  $288\text{ m} \times 341\text{ m}$ ), and accuracy assessment is also performed against a reference DSM. The reference DSM was generated using the previous year's aerial images without errors (assuming the heights of tree growth can be ignored during a one-year period).

### Single-Point Correction

The single-point correction is very similar to the single-point matching technique except it is performed on a projected image pair. The proposed single-point correction employs NCC matching technique and the detailed processing steps are as follows:

1. Locating the single-point  $P$ 's positions ( $X, Y, Z$ ) on the projected images, choosing an initial elevation value  $Z_0$  for  $P$ , an increment value  $k$  and downward searching range  $S_d$  and upward searching range  $S_u$  (assuming the corrected elevation is within the searching range);
2. Choosing an appropriate correlation window size ( $m \times n$ ) ( $m$ : rows,  $n$ : columns). A larger window is good for flat surfaces, but it blurs the disparity edges. In contrast, a smaller window gives sharper disparity edges at expense of noisy surfaces (Kanade and Okutomi 1994). Based on this principle and experience, a larger window size ( $21 \times 21$ ) is suggested in the flat region and a smaller window size ( $11 \times 11$ ) for the undulating region;

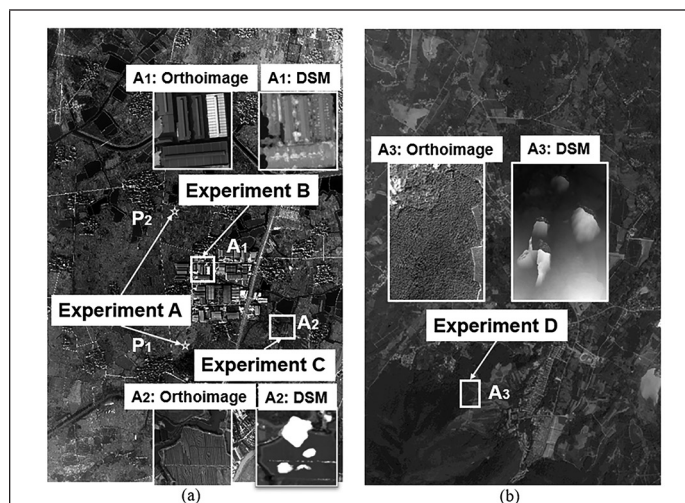


Figure 4. (a) The orthoimage of a very flat region (elevations vary from 0 to 40 m) and the locations of Experiments A, B, and C; (b) the orthoimage of an undulating rough region (elevations vary from 15 to 430 m). The insets show the corresponding orthoimages and DSM patches of the experiments. DSM = digital surface model.

3. Computing the correlation coefficients: using Equation 2 to find the corresponding windows for each candidate  $Z_i$  on all projected images, collecting the image values for the given correlation window size and computing the correlation coefficients using Equation 3;
4. Determining the corrected elevation value: for the purpose of simplicity, the final correlation coefficient at each  $Z_i$  is averaged from all corresponding correlation coefficients (if more than two images are used) and the elevation value who has the highest correlation coefficient is chosen as the final corrected elevation.

In Experiment A, the proposed method is applied to two single points  $P_1$  and  $P_2$ , respectively. The correlation coefficients correspond to the search points of the correct point

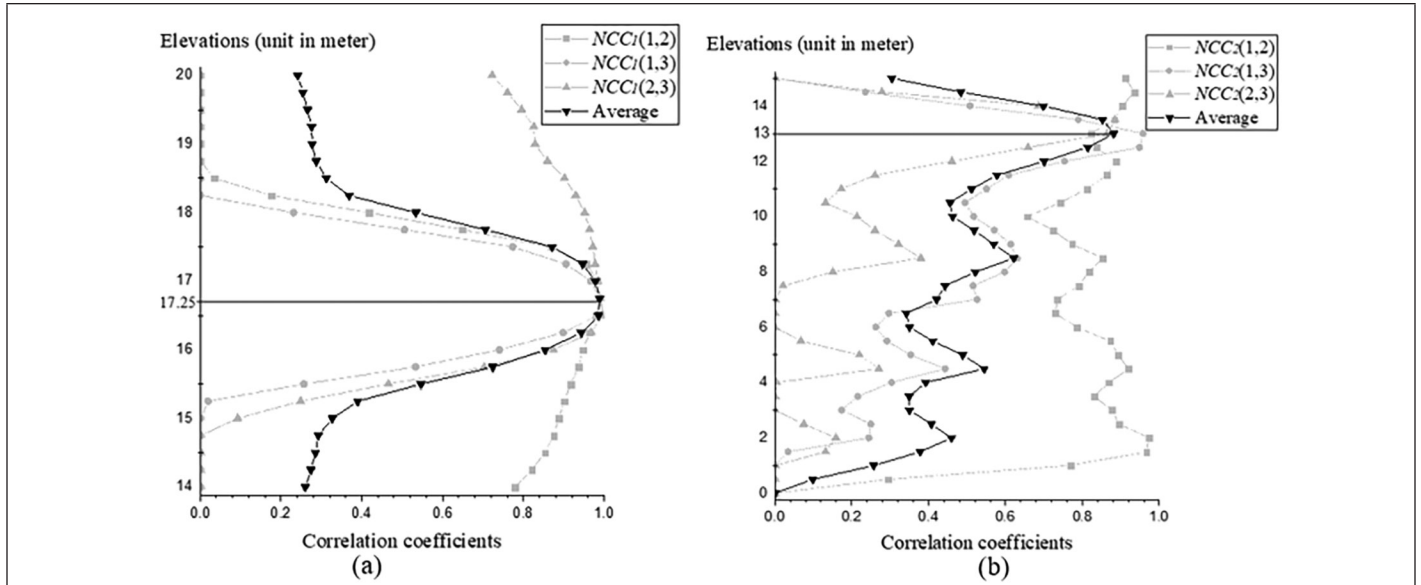


Figure 5. Experiment A: single-point correction. (a) point  $P_1$  elevation correction; (b) point  $P_2$  elevation correction (correction parameters used for  $P_1$ :  $Z_0 = 16$  m,  $k = 0.25$  m,  $S_u = 4$  m,  $S_d = 2$  m,  $m \times n = 21 \times 21$ ; correction parameters used for  $P_2$ :  $Z_0 = 2$  m,  $k = 0.5$  m,  $S_u = 13$  m,  $S_d = 2$  m,  $m \times n = 11 \times 11$ ). NCC = normalized correlation coefficient.

$P_1$  and  $P_2$ ; they are shown in Figure 5a and 5b, respectively.  $NCC_i(1, 2)$  ( $i = 1, 2$ ),  $NCC_i(1, 3)$  ( $i = 1, 2$ ), and  $NCC_i(2, 3)$  ( $i = 1, 2$ ) in Figure 5 represent correlation coefficients corresponding to  $P_1$  and  $P_2$  between the first and the second projected images, the first and the third projected images, and the second and the third projected images, respectively; “Average” shows the averaged values of three correlation coefficients.

For  $P_1$ , the correlation coefficients obtained from the three groups have a more obvious distribution because of the small discrepancy in elevations near the point. The optimal elevation is 16.75 m. For  $P_2$  the final elevation is found to be 13 m.  $P_2$  is actually an electricity pole, whose length is 11 m measured by a laser rangefinder during the filed validation exercise. It is interesting that the ground elevation (the bottom of the pole) is 2 m, which can be found at one of coefficient peaks in Figure 5b (dark line).

This experiment briefly illustrates how the proposed method works for single-point correction. There are many options can be made to improve the results, such as changing the amount of increment, trying different correlation window sizes, fitting a curve for coefficients to find the optimal elevation etc.

### Coarse DSM Patch Refinement

Experiment B chooses coarsely reconstructed buildings to refine using the proposed method. The building edges are not in the correct locations and neighboring should-be standalone buildings are mixed together (Box  $A_1$  in Figure 4) due to the occlusions or/and over-smoothing in the matching process is a pervasive phenomenon in urban environments. For building refinement using the proposed method, instead of giving initial starting elevation values, the following are used: elevation values from the coarse DSM are the initial values; the correlation window size is set to  $(11 \times 11)$ ; the elevation increment is 0.5 m; the searching range is 10 m in both downward and upward directions; and the global matching technique (see section “Image Matching Techniques”) is applied. After the refinement process, the buildings have much clearer edges and individual buildings now can be more easily seen (in Figure 6d–e) when compared with the coarse images (Figure 6b–c).

### Wrong DSM Patch Correct

Sometimes a small area’s elevations may be totally wrong. For example, Box  $A_2$  in Figure 4 shows the DSM reconstructed

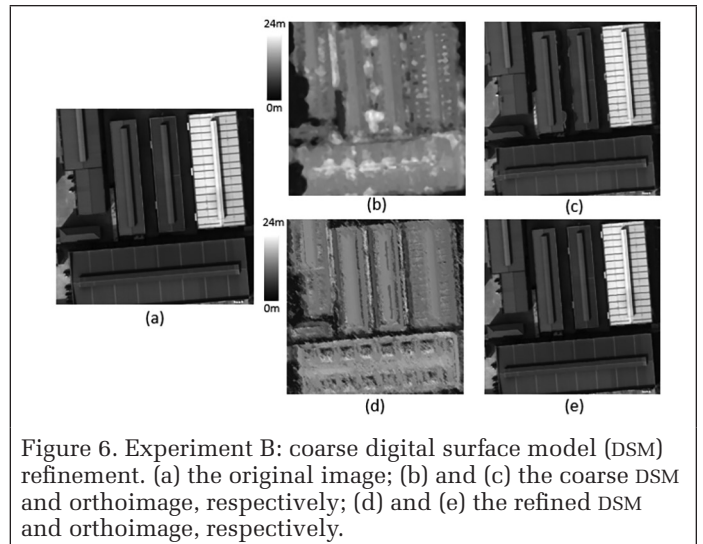


Figure 6. Experiment B: coarse digital surface model (DSM) refinement. (a) the original image; (b) and (c) the coarse DSM and orthoimage, respectively; (d) and (e) the refined DSM and orthoimage, respectively.

from automatic matching process. It is obvious that a couple of patches in the agriculture field have incorrect elevations. The errors could be due to the repeated texture patterns, which confuse the matching algorithms. In Experiment C, the following proposed process are conducted to correct the patch errors. Because the wrong elevation values are far away from the correct ones, an initial elevation value is set to 2 m, which is roughly the elevation of the field. A grid is selected around the affected area, and each node of the grid is applied the similar processing as the single point correction’s except the global matching (see section “Image Matching Techniques”) is applied during the image matching and DSM reconstruction process. An increment of 0.3 m is chosen to search the correct elevations in 3 m downward and 3 m upward directions, and the correlation window size is  $21 \times 21$  because the correct area has a similar texture and almost the same elevations. The results are shown in Figure 7.

Repeated texture pattern is one of main reasons for causing image matching to failure. Experiment C demonstrates that it is possible to correct wrong matches caused by repeated texture patterns using projected images. The preliminary results are encouraging; however, more experiments are needed to

investigate the potential of using projected images to handle difficult matching problems.

In addition to the resolution used in the above correction, the proposed method is further applied to DSM corrections using several different resolutions to demonstrate DSM correction applications for various image resolutions. The DSM with 2 and 5 m resolutions are smoothed and reduced from the 0.4 m resolution DSM, and the resolutions of projected images are also reduced accordingly. Figure 8a–c shows the wrong DSM patch  $A_2$  with different resolutions of 0.4, 2, and 5 m, and Figure 8d–f shows the corresponding correction effect of the proposed method which demonstrate that the new method can equally work well to the lower resolution images.

### DSM Patch Refinement and Editing Comparisons

For any wrong DSM patches, the common practical editing approaches are manually digitizing the wrong patches using any graphic user interface and then apply a first-order/second-order quadratic surface fitting or other interpolations to the affected patches. In order to compare the effects using such editing approaches to the proposed method, an area which contains three bad matching patches (Box  $A_2$  in Figure 4b) are chosen for Experiment D, and the reference elevations for these patches are obtained (Figure 9c). The bad matching patches are in dense forest area (Figure 9a), it is suspected that the matching errors could be caused due to similar texture. The wrong DSM patches (Figure 9b) are refined using the similar process as above experiments and the refined DSM patches are shown in (Figure 9d). In contrast to automatic matching corrections, a first-order and second-order quadratic surface fittings are applied to the patches using only the vertices on the outlines, the resultant first-order (three parameters) and second-order (six parameters) quadratic surface fitted DSM patches are shown in Figure 9e and Figure 9f, respectively. The refined or edited elevations against the reference elevations are difficult to compare visually among Figure 9c–f; therefore, the elevation differences are further generated as images for better comparisons and visualization. Figure 10a–d represent, respectively, the elevation differences of the wrong, refined, first-order quadratic surface fitted, and second-order quadratic surface fitted patches when compared with the reference elevation patches. The images only show the elevation differences ( $dZ$ ) inside the patches: the darkest color represents  $-5$  m or below and the brightest color represents 5 m or above; the statistical differences are shown in Table 1. The means of differences in Table 1 indicate the proposed method is the closest one to the reference elevations. Though the root-mean-square error (RMSE) of the proposed method is also the smallest it does reveal some variations for two “corrected” elevation data sets (the reference and refined ones). The variations could be the results due to the strategies used during matching. In general, from both the visual images and RMSE, it clearly demonstrates that the proposed refine method is superior to the manual editing approaches.

Results from all experiments demonstrate that the proposed method can effectively correct elevation errors in DSM

Table 1. Elevation residuals compared with the reference elevations (unit: in meters).

Editing/ Refinement Methods	Wrong DSM Patches	Proposed Refinement	First-Order Quadratic- Fitting	Second-Order Quadratic- Fitting
Mean (dZ)	29.669	0.191	1.129	1.975
RMSE (dZ)	39.318	1.766	3.448	5.562
Number of pixels	150 086	150 148	150 188	150 188

DSM = digital surface model; RMSE = root-mean-square error.

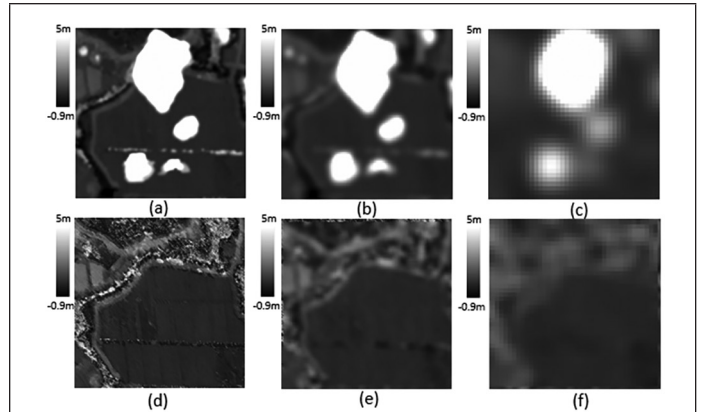
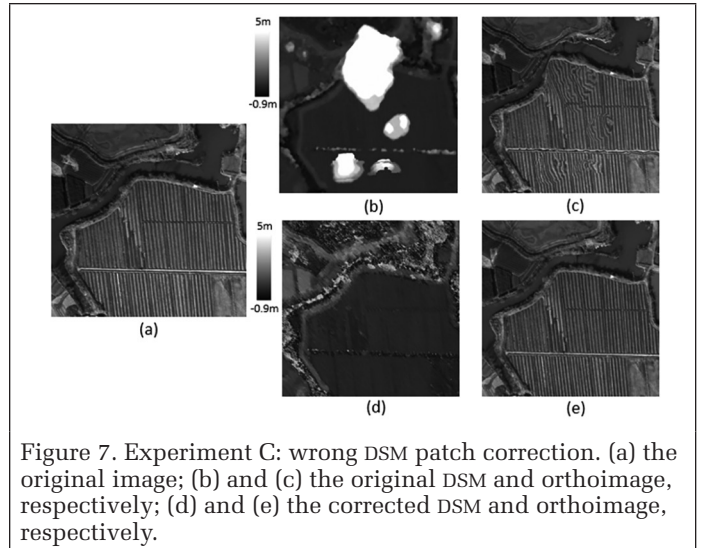


Figure 8. Digital surface model (DSM) corrections with different resolutions. (a to c) the wrong DSM patches with resolutions of 0.4, 2, and 5 m, respectively; (d to f) the corrected DSM patches with resolutions of 0.4, 2, and 5 m, respectively.

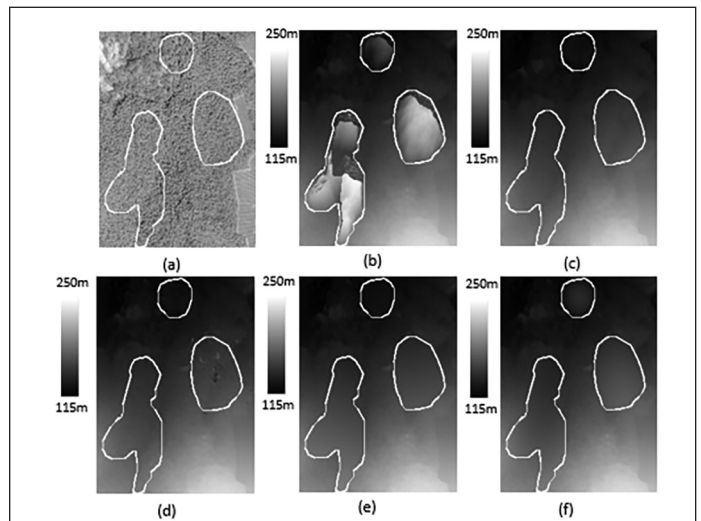


Figure 9. Experiment D: digital surface model (DSM) refinement/editing results. (a) the orthoimage; (b) three wrong DSM patches due to matching errors; (c) reference elevations; (d) refined DSM patches using the proposed method; (e) the first-order quadratic surface fitted DSM patches; (f) the second-order quadratic surface fitted DSM patches.

especially for wrong DSM patches or refine coarse DSM patches. Although there is still room for improvement, the idea of using projected images to perform image matching seems to work well in those circumstances.

## Conclusions

Errors and artifacts are very common in many DSM generated using automatic matching techniques. Currently there is a lack of efficient and effective ways to remove those errors to improve the quality of DSM. Aiming to correct and refine contaminated DSM, this paper proposes to use the concept of projected images, which can act as the bridge between the original image space and object space. As such, they greatly simplify the complicated coordinate transformations between the image space and the object space, and eliminate the repeated pixel resampling; therefore, the errors/artifacts in DSM can be amended efficiently and effectively.

The details of the concept of projected images and the proposed DSM patch correction/refinement method are presented. Although the preliminary results from four experiments (single-point correction, wrong patch correction, coarse patch refinement, and refinement comparisons) are promising and encouraging, there are still areas that can be explored further to accommodate the various needs while refining/correcting DSM. These areas include implementing and evaluating the latest matching algorithms, which can correct different matching error types using some standard test data sets; integrating various matching strategies (pyramid data structures, box filtering) to gain further computational efficiency; applying algorithms to larger areas; and extending projected images for nonframe (satellite) imagery.

## Acknowledgments

The authors thank the anonymous reviewers for their helpful comments that improved the manuscript and valuable recommendations to further improving the method.

## References

- Alobeid, A., K. Jacobsen and C. Heipke. 2010. Comparison of matching algorithms for DSM generation in urban areas from IKONOS imagery. *Photogrammetric Engineering and Remote Sensing* 76 (9):1041–1050.
- Bourke, P. 1996. *Cross Correlation: Auto Correlation—2D Pattern Identification*. Research Paper. Oxford University, Oxford, United Kingdom.
- Cormen, T. H., C. Stein, R. L. Rivest and C. E. Leiserson. 1990. *Introduction to Algorithms*. London, England: The MIT Press, 774–792.
- Christmas, W. J., J. Kittler and M. Petrou. 1995. Structural matching in computer vision using probabilistic relaxation. *IEEE Transactions on Pattern Analysis and Machine Intelligence* 17 (8):749–764.
- Cogan, L., D. Guan, D. Hunter, S. Lutz and C. Peny. 1988. Kern DSP 1—Digital stereo photogrammetric system. *International Archives of Photogrammetry and Remote Sensing Commission II*, 71–83.
- Chen, Y. C., Y. H. Tseng, C. Y. Hsieh, P. C. Wang and P. C. Tsai. 2012. Object-space multi-image matching of mobile-mapping-system image sequences. *International Archives of the Photogrammetry, Remote Sensing and Spatial Information Sciences* 39 (5):465–470.
- Furukawa, Y. and J. Ponce. 2010. Accurate, dense, and robust multiview stereopsis. *IEEE Transactions on Pattern Analysis and Machine Intelligence* 32 (8):1362–1376.
- Geman, S. and D. Geman. 1984. Stochastic relaxation, Gibbs distributions, and the Bayesian restoration of images. *IEEE Transactions on Pattern Analysis and Machine Intelligence* 6 (6):721–741.
- Gruen, A. 2012. Development and status of image matching in photogrammetry. *The Photogrammetric Record* 27 (137):36–57.
- Gao, X., L. Hu, H. Cui, S. Shen and Z. Hu. 2018. Accurate and efficient ground-to-aerial model alignment. *Pattern Recognition* 76:288–302.
- Hirschmüller, H. 2008. Stereo processing by semiglobal matching and mutual information. *IEEE Transactions on Pattern Analysis and Machine Intelligence* 30 (2):328–341.
- Jiang, S. and W. Jiang. 2019. Reliable image matching via photometric and geometric constraints structured by Delaunay triangulation. *ISPRS Journal of Photogrammetry and Remote Sensing* 153:1–20.
- Kanade, T. and M. Okutomi. 1994. A stereo matching algorithm with an adaptive window: Theory and experiment. *IEEE Transactions on Pattern Analysis and Machine Intelligence* 16 (9):920–932.
- Li, P. 1988. Utilization of existing elevation data base to improve correlation on Kern DSR-11 analytical plotter. *International Archives of Photogrammetry and Remote Sensing* 27 (3):466–475.
- Ling, X., X. Huang, Y. Zhang and G. Zhou. 2019. Matching confidence constrained bundle adjustment for multi-view high-resolution satellite images. *Remote Sensing* 12 (1):20.
- Lemmens, J.P.M. 1988. A survey on stereo matching techniques. *International Archives of Photogrammetry and Remote Sensing* 27 (B8):11–23.
- Okutomi, M. and T. Kanade. 1993. A multiple-baseline stereo. *IEEE Transactions on Pattern Analysis and Machine Intelligence* 15 (4):353–363.
- Rosenholm, D. 1987. Multi-point matching using the least-squares technique for elevation of 3-dimensional models. *Photogrammetric Engineering and Remote Sensing* 6 (53):621–626.
- Ruohomaki, T., E. Airaksinen, P. Huuska, O. Kesaniemi, M. Martikka and J. Suomisto. 2018. Smart city platform enabling digital twin. Pages 155–161 in *Proceedings International Conference on Intelligent Systems*, held in Madeira Island, Portugal.
- Wang, J. and Z. Yu. 2011. Quadratic curve and surface fitting via squared distance minimization. *Computers & Graphics* 35 (6):1035–1050.
- Wang, Z. 1990. *Principle of Photogrammetry (with Remote Sensing)*. Beijing, China: Publishing House of Surveying and Mapping.
- Zhang, L. 2005. *Automatic Digital Surface Model (DSM) Generation from Linear Array Images*. Zurich, Switzerland: Institute of Geodesy and Photogrammetry Swiss Federal Institute of Technology (ETH) CH-8093.
- Zhang, L. and A. Gruen. 2006. Multi-image matching for DSM generation from IKONOS imagery. *ISPRS Journal of Photogrammetry and Remote Sensing* 3 (60):195–211.
- Zhang, Y., Y. Zhang, D. Mo, Y. Zhang and X. Li. 2017. Direct digital surface model generation by semi-global vertical line locus matching. *Remote Sensing* 9 (3):214.
- Zhao, W., L. Yan and Y. Zhang. 2018. Geometric-constrained multi-view image matching method based on semi-global optimization. *Geo-spatial Information Science* 23 (1):75–86.
- Zheng, S., Z. Zhang and J. Zhang. 2004. Image relaxation matching based on feature points for DSM generation. *Geo-spatial Information Science* 7:243–248.
- Zhao, W., L. Yan and Y. Zhang. 2018. Geometric-constrained multi-view image matching method based on semi-global optimization. *Geo-spatial Information Science* 23 (1):75–86.
- Zheng, Y., J. Liu, Z. Liu, T. Wang and R. Ahmad. 2019. A primitive-based 3D reconstruction method for remanufacturing. *International Journal of Advanced Manufacturing Technology* 103 (4):3667–3681.
- Zhu, Q., Y. Zhang, B. Wu and Y. Zhang. 2010. Multiple close-range image matching based on a self-adaptive triangle constraint. *The Photogrammetric Record* 25 (132):437–453.
- Zhu, Q., Z. Wang, H. Hu, L. Xie, X. Ge and Y. Zhang. 2020. Leveraging photogrammetric mesh models for aerial-ground feature point matching toward integrated 3D reconstruction. *ISPRS Journal of Photogrammetry and Remote Sensing* 166:26–40.

---

## IN-PRESS ARTICLES

- Wei Wang, Yuan Xu, Yingchao Ren, Gang Wang. Parsing of Urban Façades from 3D Point Cloud Based on A Novel Multi-View Domain.
- Qimin Cheng, Yuan Xu, Peng Fu, Jinling Li, Wei Wang, and Yingchao Ren. Scene Classification of Remotely Sensed Images via Densely Connected Convolutional Neural Networks and an Ensemble Classifier.
- Nahed Osama, Bisheng Yang, Yue Ma, and Mohamed Freeshah. A Digital Terrain Modeling Method in Urban Areas by the ICESat-2.
- Ting Bai, Kaimin Sun, Wenzhuo Li, Deren Li, Yepi Chen, and Haigang Sui. A Novel Class-specific Object-based Method for Urban Change Detection using High-Resolution Remote Sensing Imagery.
- Yang Liu, Yujie Sun, Shikang Tao, Min Wang, Qian Shen, and Jiru Huang. Discovering potential illegal construction within building roofs from UAV images using semantic segmentation and object-based change detection.
- Yongtai Chen, William C. Tang, Jinkui Chu, Ran Zhang, and Song Li. Error Analysis and Optimization of Sky Full-Polarization Imaging Detection System.
- Yang Han, Haiyan Yao, Ziyi Li, Haofang Niu, Tianyi Hao, and Yuyu Zhou. Inversion of Solar-Induced Chlorophyll Fluorescence Using Polarization Measurements of Vegetation.
- Neema Nicodemus Lyimo, Fang Luo, Qimin Cheng, and Hao Peng. Quality Assessment of Heterogeneous Training Datasets for Classification of Urban Area with Landsat imagery.
- Shalini Gakhar and Kailash Chandra Tiwari. Comparative assessment of target detection algorithms for urban targets using hyperspectral data.
- Long Chen, Bo Wu, Yao Zhao, and Yuan Li. A Real-Time Photogrammetric System for Acquisition and Monitoring of 3D Human Body Kinematics.
- Letícia Ferrari Castanheiro, Antonio Maria Garcia Tommaselli, Adilson Berveglieri, Mariana Batista Campos, and José Marcato Junior. Modeling hyperhemispherical points and calibrating a dual-fisheye system for close-range applications.
- Jonathan Li, Qiutong Yu, Wei Liu, Wesley Nunes Gonçalves, and José Marcato Junior. Spatial Resolution Enhancement for Large-scale Land Cover Mapping via Weakly Supervised Deep Learning.
- Binbin He, Guoming Li, Liang Li, Miao Yang, Qiongyi Huang, and Zihan Guo. Ecological Functions and Human-activity Interferences Evaluation in Ecological Protection Redline for Urban Environment.
- Fang Gao, Yihui Li, Wentao Li, Peng Zhang, Yuan An, Xing Zhong, and Yuwei Zhai. A High-Resolution Satellite DEM Filtering Method Assisted with Building Segmentation.
- Xueyan Li, Yu Hou, Ruifeng Zhai, Junfeng Song, Xuehan Ma Shuzhao Hou, and Shuxu Guo. Three-dimensional reconstruction of single input image based on point cloud.
- Hui Luo and Nan Chen. A Combined Unmixing Framework for Impervious Surface Mapping on Medium-Resolution Images with Visible Shadows.
- Zezhong Zheng, Mujie Li, Mingcang Zhu, Yue He, Jun Xia, Xueye Chen, Qingjun Peng, Yong He, Xiang Zhang, and Pengshan Li. The spatio-temporal evolution of urban impervious surface for Chengdu, China.
- Lei Zhang, Hongchao Liu, Xiaosong Li, and Xinyu Qian. Optimizing the segmentation of a high-resolution image by using a local scale parameter.
- Akib Javed, Qimin Cheng, Hao Peng, Orhan Altan, Yan Li, Iffat Ara, Enamul Huq, Yeamin Ali, and Nayyer Saleem. Review of Spectral Indices for Urban Remote Sensing.
- Qinghong Sheng, Rui Ren, Weilan Xu, Hui Xiao, Bo Wang, and Ran Hong. Spinor-based Attitude Determination with Star Sensor Considering Depth.
- Bharath H Aitha and Prakash PS. Digital building height preparation from satellite stereo images.
- Yanfei Zhong, Xiaoman Li, Yu Su, and Richen Ye. Scene Change Detection based on Multi-feature Fusion Latent Dirichlet Allocation Model for High Spatial Resolution Remote Sensing Imagery.
- Wenhui Wan, Jia Wang, Zhaoqin Liu, Man Peng, Yexin Wang, Tianyi Yu, Chuankai Liu, Lichun Li, and Kaichang Di. Enhanced Lunar Topographic mapping using Multiple Stereo Images Taken by Yutu-2 Rover with Changing Illumination Conditions.
- Jiabao Li, M.D, Wei Han, Ruyi Feng, Lizhe Wang, and Fengpeng Li. Unsupervised representation high-resolution remote sensing image scene classification via contrastive learning convolutional neural network.
- Longjie Ye, Wen Xiao, Yehua Sheng, Dong Su, Pengbo Wang, Shan Zhang, Na Zhao, Hui Chen, and Ka Zhang. Gaussian mixture model of ground filtering based on hierarchical curvature constraints for airborne LiDAR point clouds.

# Remote Sensing for Ecosystem Services and Urban Sustainability

John C. Trinder

## Abstract

*The purpose of this paper is to demonstrate how geospatial technologies, especially remote sensing, can play a leading role in defining urban sustainability based on the evaluation of demand and supply of ecosystem services (ES). A brief review of sustainable development and urban sustainability will be given followed by demonstrations of the need for green spaces in cities, and the consequences of fragmentation of green spaces on biodiversity. Although there are no substantive figures for desirable levels of green spaces in urban areas for the benefit of inhabitants, the paper proposes minimum desirable areal percentages. The paper defines natural capital and ES and the procedures adopted by researchers in balancing the supply and demand for ES for urban areas. The genuine progress indicator is presented as a measure of assessing human welfare, but it is not pursued as an indicator of sustainability. Examples of the applications of remote sensing technologies for determining supply and demand of ES are reviewed as are the potential of the supply and demand of ES to support decision-making in urban areas, to ensure that development decisions are sustainable and are in the best interests of the urban residents who depend on ES for their life support.*

## Introduction

The growth of cities is causing increasing stress on many aspects of urban environments. The United Nations (UN) Economic and Social Council reported in 2017 that 54% of world's population lived in cities, and some estimates indicate global urban populations may reach 65% of the world's population by 2050. Challenges and opportunities for the development of Megacities is discussed in Li *et al.* (2019). Sustainable development has been proposed for many years as a means of ensuring that human impacts are within the capacity of the Earth's environment to cope with changes. While there have been many definitions presented, *sustainability* in this paper refers to the adoption of practices in relation to environmental use and management which provide a satisfactory standard of living for today's population, and which do not impair the capacity of the environment to provide for and support the needs of future generations. Alternatively, sustainable development is that which meets the needs of society today without foreclosing the needs or options of the future (Blanco *et al.* 2001). Sustainability "focuses on interactions between resources, its users, and the governance required to sustain ecosystems while also delivering what people need and value" (Newlands 2017, p. 16). This last description suggests that the provision by the environment of benefits and services to users' needs to be controlled by governance from local administrations or higher-level governments. While there are numerous examples of controls over human behavior within various national administrations, such controls should be managed by the assessment of appropriate measures, often prescribed as sustainability indicators (SI). Many examples of

SI have been provided in literature including Trinder (2016), for a range of aspects of urban environments and cities.

## Urban Environments

### Sustainability of Urban Environments

A sustainable city, or eco-city, which can be described as a complex adaptive system (Newlands 2017), is a city designed considering the three pillars of sustainability, namely social, economic, and environmental impact. Such a city will be a resilient habitat for existing populations with the capacity to respond to disruptions or disturbances and recover quickly. That city will also not compromise the ability of future generations to experience similar habitat conditions. The environments in which cities have been located have clearly been changed significantly from their original states. However, their new states require assessment using appropriate measures, which, according to a definition above, also need to be assessed as to whether they can provide a satisfactory standard of living for its current inhabitants and future generations. While Costanza and Patten (1995) state somewhat negatively that sustainability can only be assessed after the fact and not in advance, it is essential that the sustainability of existing urban environmental practices are assessed in consideration of future generations.

Berger (2014) states that cities are unsustainable, while Gardner (2016) in providing a significant review of the sustainability of cities, provides a negative projection for the future of the world's environment. This environment will be dominated by cities and, if the majority of the world's population achieves a similar standard of living as the affluent populations today, global material use will grow by 3 to 5 times current levels. Even technology gains will not reduce the use of materials, since in the past 500 years technology developments are estimated to have increased environmental impacts by 1.5 times. "Creating sustainable cities for all will require great creativity as well as decidedly lower levels of consumption. It will only be possible if a new relationship between humans, energy, and materials is achieved" (Gardner 2016). Experiences with global forums are discussed in Holden *et al.* (2008) and, although written before the development of *Agenda 2030 and the Sustainable Development Goals* (United Nations 2016), it contrasts actions that are presented to achieve sustainability of urban areas, which include a *paradigm shift* that must occur before a major global crisis occurs. Mori and Christodoulou (2012) argue that no satisfactory sustainability indicators have been developed for cities because such indicators should do the following: (a) take into account the three components of sustainability—social, economic, environmental impacts; (b) include consideration of

Photogrammetric Engineering & Remote Sensing  
Vol. 87, No. 3, March 2021, pp. 189–195.  
0099-1112/21/189–195

© 2021 American Society for Photogrammetry  
and Remote Sensing  
doi: 10.14358/PERS.87.3.189

School of Civil and Environmental Engineering, The  
University of New South Wales, UNSW Sydney, NSW 2052  
Australia (j.trinder@unsw.edu.au).

the effects of the use of resources from neighboring areas; (c) be created specifically for assessing city sustainability in both developed and developing countries; (d) be based on absolute measures; and (e) use “total environmental impact and/or eco-efficiency as a threshold or a criterion”. In EU (2015), a range of indices is considered, and the authors conclude “that efficient governance informed by science-driven policies is a critical component of sustainable development”. In the recommendation for a systems approach for sustainable cities, Bai *et al.* (2016) referred to cities as being open systems, complex, encompass multiple actors, and are embedded in a range of structures and processes.

Urbanization has major impacts on the quality of urban life and its sustainable development. Shao *et al.* (2020) refer to the negative impacts of urbanization on ecosystem services (ES), which are described in the section “Natural Capital and Ecosystem Services”, because environments that provide such services as carbon sequestration and support for biodiversity have been replaced by built-up land cover. Shao *et al.* (2020) have developed two indicators (fraction of vegetation coverage and surface urban heat island intensity) to analyze the characteristics of urban environments.

### The Importance of Green Space in Urban Areas

The benefits of exposure to green spaces have been described by many authors and as stated below, green space is considered as part of urban ES. For example, Twohig-Bennett and Jones (2018) list a number of significant health benefits for inhabitants from exposure to green space, including reduced blood pressure, heart rate, and reduced incidence of a number of health risks. They further encourage policy and decision-makers to create, improve, and maintain green spaces especially in deprived city areas. Shanahan *et al.* (2017) listed the beneficial experiences of tree cover in various parts of two cities, one in the United Kingdom and the other in Australia, which were measured by a Nature Relatedness scale, where the percentage of tree cover varied from less than 10% to more than 60%. The Natural Relatedness scale correlates well with attitudes towards nature and differentiates between those who are enthusiastic or otherwise about nature. The benefits of tree cover include reduced stress and asthma, and “psychological restoration”. Similarly, Cox *et al.* (2018) determined “nature dose intensity” in the form of trees taller than 2 m, derived by airborne light detection and ranging (lidar) and Normalized Difference Vegetation Index images from *Landsat 8*, and found that people with low levels of nature dose have poorer mental health and lower levels of social cohesion, but also can gain the most from exposure to nature. Mennis *et al.* (2018) referred to the importance of exposure to vegetation and natural areas leading to reduced stress, attention restoration, and reduction in fatigue in adolescents, and recommended that these findings should influence urban development policies for the inclusion of green space, highlighting that access to green space is being recognized as an environmental justice issue (Wolch *et al.* 2014). Metrics have been discussed in literature regarding desirable sizes of green spaces and distances to them. The minimum size of green space suggested by several authors varied between 0.5 ha and 1 ha, and a threshold distance of 300 m is likely to have better health benefits than longer distances. Van Den Bosch *et al.* (2015) recommend “a 300 m maximum linear distance to the boundary of urban green spaces of a minimum size of 1 hectare”. Environmentally conscious cities worldwide are taking actions to ensure cities are sustainable and provide adequate green spaces, but projecting the impact of these actions into the future, which should be a key aim for sustainable urban areas, presents considerable uncertainties.

Even though it is generally agreed that compact cities are more efficient for the provision of infrastructure, they concentrate buildings and impervious surfaces with a consequent loss of vegetation and hence green spaces. Increasing

compactness beyond a certain limit is undesirable for the health and well-being of the population and energy consumption, as well as the health of local fauna and flora. For example, Tian *et al.* (2012) have described measures taken to overcome the high levels of compactness of developments in Hong Kong, which have led to extremely low green cover in built-up areas. Holden and Norland (2005) refer to studies in which energy use per capita decreases as densities of cities increase, but it increases if compactness increases beyond a certain limit. Rapid urbanization has brought about growth of urban vegetation, which has a higher heterogeneity and therefore more mixed pixels when medium and low-resolution remotely sensed data are used to interpret urban areas (Zhang and Shao 2020).

### Fragmentation in Urban Areas

Fragmentation of green spaces and therefore habitats is a typical consequence of urbanization and there has been considerable discussion in literature about its significance. Based on a review of about 100 research papers, Fahrig (2003) determined that while fragmentation can have significant impacts on biodiversity, the relationship is complex and may have negative as well as positive effects. The paper asks, “How much habitat is enough?” To answer the question, it is necessary to determine which species are most affected by the habitat loss. Fragmentation itself, therefore, is not necessarily a suitable measure of the effects on habitat loss, and behaviors of species may vary according to the characteristics and changes in habitats caused by humans (Fischer and Lindenmayer 2006; Lortie *et al.* 2004). Therefore, habitat fragmentation should be considered as being dependent on the spatial context, the multiple interacting drivers, and the various species associated with the landscape. Perring *et al.* (2010) referred to proposed biodiversity targets set for 2020 in 2010 that were not achieved and that the underlying causes of losses in biodiversity need addressing.

Haddad *et al.* (2015), in providing a comprehensive study in five continents and multiple biomes, demonstrates that fragmentation has degraded biodiversity by 13% to 75%, and it also impairs key ecosystem functions by decreasing biomass and altering nutrient cycles. Pettorelli *et al.* (2018) have presented a detailed discussion of available remote sensing technologies for a global biodiversity monitoring strategy and stress that biodiversity is in crisis. They recommend better understanding of the relationships between biodiversity and ES, which are defined in the section “Natural Capital and Ecosystem Services” in this paper. Pettorelli *et al.* (2018) have proposed a global biodiversity monitoring strategy by adopting a set of definitions, a typology for ecosystem functions, reviews of current opportunities, and the potential limitations of satellite remote sensing technology to support the monitoring process worldwide.

### Future Status of Urban Areas

It is clear from the foregoing that urbanization will be the dominant environmental structure for many future communities. Urban environments have experienced serious degradation not only within the urban areas, but also in surrounding areas as resources are consumed from ever widening areas. Taking into consideration the above findings, it is clear that green spaces are increasingly fragmented; this, in turn, results in a deterioration in habitat biodiversity in cities, such that fewer species of flora and fauna will be resilient enough to adapt to the changes in environmental conditions. Conversely, it has been demonstrated that urban green spaces can reduce the effects of urban heat islands, ensuring energy flow, clean air, and water, while providing aesthetic enjoyment, recreational opportunities, and improved physical and psychological well-being of inhabitants. Cities will continue to exist because of the increases in population around the world, said to reach about 8.5 billion by 2030. Trinder and Liu (2020) proposed that a desired minimum green cover

should be of the order of 15% to 20% in central business districts and industrial areas, 25% to 30% in residential and light commercial areas, and up to 50% in suburban areas. Meanwhile, Goal 11 of the UN Sustainable Development Goals and Agenda 2030 (United Nations 2016) proposes to alleviate poverty and improve the environment of urban areas.

This paper proposes that assessment of ES should be used as a basis for sustainability of urban areas. Therefore, natural capital and ES as well as the supply and demand for ES will be presented in the next sections, followed by a discussion of the contributions of remote sensing to the assessment of ES.

## Natural Capital and ES

Ecosystem services have been studied extensively over approximately the past four decades, as described in Costanza *et al.* (1997), who presented details of seventeen ES across sixteen biomes as listed in Table 1. These details have been updated in many recent research publications including Costanza *et al.* (2014). Costanza *et al.* (1997) state that “natural capital” comprises trees, minerals, ecosystems, and the atmosphere; manufactured capital includes machines and buildings; human capital comprises physical bodies; and intangible forms, such as knowledge held by individuals, computers, in species, or ecosystems. Ecosystem services are those provided by the natural environment and properly functioning ecosystems, for the benefit of humans. They demonstrate the extent of dependence of humans on the natural environment, in the context of more than 54% of the world’s population now living in urban areas. They are represented by flows of material, energy, and information from natural capital stocks, which combine with manufactured and human capital services to produce human welfare (Costanza *et al.* 2014). Expressed another way, human well-being is dependent on interactions between built, social, human, and natural capital.

Table 1. Ecosystem services according to Costanza *et al.* (1997).

Services	
Gas regulation	Pollination
Climate regulation	Biological control
Disturbance regulation	Refugia
Water regulation	Food production
Water supply	Raw materials
Erosion control and sediment retention	Genetic resources
Soil formation	Recreation
Nutrient cycling	Cultural
Water treatment	

A broader based index that estimates the economic welfare generated by economic activity is the genuine progress indicator (GPI). GPI estimates personal consumption expenditures which are adjusted by 24 different components, including income distribution, environmental costs, and negative activities, such as crime and pollution amongst others (Kubiszewski *et al.* 2013). GPI has been presented as an alternative to gross domestic product (GDP) which only measures current production. Kubiszewski *et al.* (2013) have provided a detailed justification for the use of GPI instead of other measures that express the welfare of a nation. Globally GPI/capita maximized in about 1978 and has tended to decline or remain constant since then, while GDP/capita has continued to increase. The conclusion is that policy focus should shift away from increasing production and hence, GDP, and concentrate on improving genuine human well-being through the use of such indices as GPI.

Maechler and Graz (2019) state that “natural capital accounting builds on the relationship between ES on one hand, and environmental accounting on the other”. They indicate that various organizations, including multi-national

accounting firms, have adopted methods of translating environmental data into monetary units to manage environmental crises. The International Standards Organization (ISO) has developed standards for environmental management published in the ISO 14000 family of standards, described in some detail by Maechler and Graz (2019), which they claim can be used as a basis for future sustainable finance.

Guerry *et al.* (2015) aimed to raise awareness of the interdependence of ecosystems and human well-being, advancing the characteristics of the interdisciplinary science of ES, and implementing that science in decision-making to reestablish the sustainable use of natural capital. They suggest that a path forward should include the following:

- developing evidence linking decisions in an urban environment to impacts on natural capital and ES, and consequently to human well-being,
- working with decision-makers in government, business, and civil society to integrate consideration of natural capital and ES as inherently part of normal decision-making,
- reforming policies and building capacity to better align private short-term goals of the decision-making process with societal long-term goals.

In describing a cascade model for ES, Rugani *et al.* (2019) have demonstrated how the quality of ES can impact human well-being.

The descriptions of ES are complex, but the understanding is that if ES is diminished for any reason, such as by human actions, then human well-being and ability to prosper maybe adversely affected. Breuste *et al.* (2013) have attempted to assess ES of parks and green spaces in several cities in Asia and Latin America and suggest that ES should become part of the urban planning process, including targets and quantities of required services. Hansen *et al.* (2015) recommend that ES should be considered in urban planning, so that the needs of the inhabitants of urban areas can be considered during this process. They reviewed the uptake of ES in the planning processes in six cities in Europe and U.S.A. and concluded that more than half of the cities revealed a recognition of the dependence of urban inhabitants on ES. In October 2015, the Obama Administration in the U.S.A. (Obama 2015) released a memorandum directing federal agencies to factor the value of natural infrastructure and ES into federal planning and decision-making. Members of the European Union (EU) have also been requested to take ES into consideration for decision-making.

## Defining the Benefits of ES to Human’s Well-Being

### Determining ES

According to Costanza *et al.* (2014), the global value of ES decreased by a conservatively estimated USD 20 trillion/year between 1997 and 2011 or between 9% and 14%, due to changes in land use. While the significance of estimating the value of ES in monetary terms has been disputed in literature, Costanza *et al.* (2014) stress that the estimates refer to the current relative contribution of the assets or activities to human well-being derived from the interaction of the basic types of capital referred to in the section “Natural Capital and Ecosystem Services”.

Wang *et al.* (2018) showed that building areas increased by 3.5 times in Dongying, China from 1994 to 2015, which resulted in an estimated reduction in ES on the order of 13%. However, Trinder and Liu (2020) showed that over a period of 30 years from 1987 to 2017, building developments in Wuhan, China and western Sydney, Australia, caused estimated reductions in ES of about 20% and about 3%, respectively.

The issue is *How to assess the impact of losses of ES on the well-being of humans?* While GPI (Kubiszewski *et al.* 2013) was presented to assist in assessing human welfare, it is based more on economics and is not meant as a means of

determining sustainability. For the future, GPI assessment should consider environmental protection, employment, social equity, better product quality, and durability, and efficient resource use (Kubiszewski *et al.* 2013). This paper will not attempt to include assessment of these issues but concentrate on the supply and demand of ES.

Recent considerations of the prescription of ES have been based on MA (2005) and TEEB (2010) publications, in four major categories: provisioning, regulating, cultural and amenity service, and supporting and habitat services. Gómez-Baggethun *et al.* (2013) describe these services as shown in Table 2. Maes *et al.* (2016), together with many other researchers in the EU, undertook the fourth mapping and assessment of ecosystems and their services for urban ecosystems, together with specific treatment of 10 cities in Europe. The detailed report demonstrates the progress being made in the EU in assessing the quality of ES. It states that a “pristine urban ecosystem” against which to judge the results in the report is not credible nor would it be an appropriate framework. The conclusion was that urban ecosystems are considered in “good condition” if the living conditions for humans and urban biodiversity are good, in terms of provision of the services, there exists a high level of species diversity, and there is a balance between green and built-up areas. The report provides a table of key indicators against which to judge the provision of ES together with a table of approaches for defining a reference condition of urban ecosystems.

Table 2. Categories of ecosystem services derived from MA (2005) and TEEB (2010).

Ecosystem Services	Benefits Gained
Provisioning	Material products—food, fibre, fresh water, and genetic resources
Regulating	Regulation of climate, water, pollination, and some human diseases
Cultural	Nonmaterial benefits—spiritual enrichment, cognitive development, reflection, recreation, and aesthetic experience, and their role in supporting knowledge systems, social relations, and aesthetic values
Supporting and habitat—necessary for all ES	Biomass production, nutrient cycling, water cycling, provisioning of habitat for species, maintenance of genetic pools, and evolutionary processes

### Provision of ES Expressed as Supply and Demand

Burkhard *et al.* (2012) have defined *supply* of ES, which refers to the capacity of a region to supply a service, and *demand* for ES being the amount actually consumed. Therefore, these two services are combined to form the *ecosystem footprint* which is the area needed to generate the ES required by a certain region in a timeframe. The assessment of the provision of ES to a region requires appropriate indicators, which are sensitive to change over time. Such indicators are similar to sustainability indicators referred to in the section “Urban Sustainability” in this paper, but are based on ES. Burkhard *et al.* (2012) have suggested that provisioning services are relatively easy to quantify, but assessment of cultural services is more subjective. They have followed a process whereby *ecological integrity* is determined for provisioning, regulating, and cultural services to preserve them against nonspecific ecological risks, such as disturbances of the self-organizing capacity of ecological systems. The ecological integrities of ES in the case of cities in Europe were derived for the land cover in Corine databases (European land cover inventory), together with potential indicators and the relative capacity to supply the ES. The demands for the ES were determined for a test site in Leipzig/

Halle in Germany in Burkhard *et al.* (2012). By comparing the ES demands against their supply, for some urban industrial and commercial areas, demand exceeds supply while for other areas supply exceeds demand. Changes in energy supply and demand, from fossil fuel to renewable sources, were reflected in the changes in supply/demand values determined for years 1990 and 2007. This is a vexed process because the demand for ES may not occur in the same location as supply and therefore decisions are required as to where these values should be assigned. Gómez-Baggethun and Barton (2013) provide details of the supply of categories of ES and disservices in urban areas, the latter being inconveniences or pests in urban living, but they do not relate the supply to demand. They refer to a range of approaches for estimating values of urban ES with examples and describe challenges in relation to urban planning, where there is significant variation and fragmentation in urban ecosystems. Gaston *et al.* (2013) have referred to the supply, flow, and demand for ES, especially green space.

Haas and Ban (2017a) determined changes in urban land cover over Shanghai, China from 2000 to 2009, using high-resolution satellite images from *Geo-Eye-1* and *IKONOS*. They stated that high-resolution images are essential for the analysis of land cover classes in urban areas, despite the problems in dealing with shadows cast by tall buildings. Urban land use and land cover (LULC) classes were valued in terms of their capacity or supply, and demand for 22 regulating, provisioning, and cultural ES according to Burkhard *et al.* (2012), which were based on those listed in MA (2005). The results demonstrated an increase in ES of about 20% over the nine-year period, with the largest increase brought about by increases in green spaces.

Haas and Ban (2017b) fused *Sentinel 1* with simulated *Sentinel 2* images over the city of Zurich, Switzerland to determine land cover patches. The influence of four geometric parameters of the extracted land cover patches on the relative demand and supply of ES were derived as follows: (a) distances to patches, since easily accessible patches are of more benefit to urban dwellers; (b) perimeter to area ratio, since the shape of a patch will influence benefit of ecosystems; (c) area, since larger areas are likely to provide greater benefit through diversity and recreation benefit; and (d) contiguity, since less fragmented patches will enable greater diversity and recreational benefit to inhabitants. Since the authors were of the view that definitive monetary values of ES are uncertain, no values were assigned to the ES, and service units per hectare were assigned.

While not referring to urban ES, Schröter *et al.* (2014) used the terms capacity and flow to describe supply and demand. They discussed the differences between capacity and flow, their spatial extent, rivalry, or congestion that prevents other beneficiaries from using the services, and measurement of the services. Therefore, a spatial assessment of capacity and flow can be used to support monitoring sustainability of ecosystem consumption, which they believe can be used as a contribution to ecosystem accounting. They provide a table of ES indicators for the area of Telemark in Norway as well as capacity-flow-balance for four ES.

Ortiz and Geneletti (2018) studied the “mismatches” in the provision of ES in the city of Havana, Cuba which should be assessed spatially and temporally, by mapping and comparing capacity of flow (or supply) and demand, which were limited to examples of two ES: food and recreation. These examples are based on two typologies of mismatches, as shown conceptually in Figure 1. The typologies are “unsustainable flow” and “unsatisfied demand”; they involve assessing how much and where the flow was unsustainable, the location of the unsatisfied demand, and the extent of the deficit considering the demand. The demand for recreation areas was based on the distance for residents to travel to reach recreation

areas and was presented graphically, while supply of food was based on the supply of at least 45% of food requirements. Both case studies revealed that there were supply mismatches. The paper supported the proposal for considering supply and demand as a measure of sufficiency of ES.

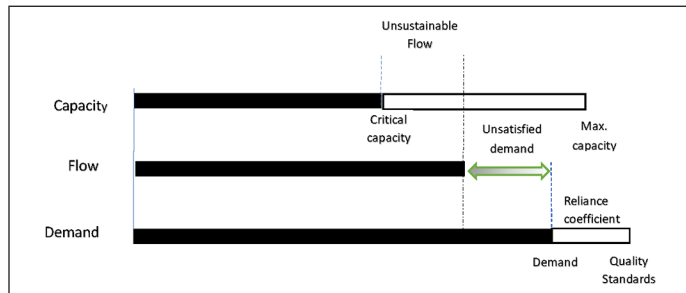


Figure 1. Conceptual framework of mismatches between capacity and demand after Ortiz and Geneletti (2018). Quality standards represent ES demand, which are reduced by the reliance coefficient. Critical capacity may rely on conditions of unsustainability and will always be less than maximum capacity. Unsatisfied demand occurs when demand is higher than ES flow. Unsustainable flow occurs when flow exceeds critical capacity.

In the book by Geneletti *et al.* (2020b) emphasis is placed on consideration of ES for decision-making for urban planning with special reference to Italy. Green space is considered an essential element of the planning process, while there is a need for equity of supply and demand for ES (Geneletti *et al.* 2020a). Colavitti *et al.* (2020) refer to the need for planning processes to be changed in Italy from being based on a traditional standard approach to a more innovative solution based on assessment of ES, as described in the scientific literature. However, in identifying several cities in Italy, they indicate the difficulties in integrating a comprehensive evaluation of the demand and supply of public services into the decision-making processes of governance in Italy. The definition of new standards must consider the changing factors affecting the well-being of urban inhabitants in Italy.

### Contributions of Geospatial Technologies to Determining ES

Costanza *et al.* (2017) referred to the need for access to remote sensing data at a range of resolutions, as well as volunteer collection of data to achieve rapid compilation of ES. Burkhard *et al.* (2012) suggest that while Corine data was available for the study described above, higher spatial and temporal resolution earth observation data would be required for more detailed analysis. Similarly, Gaston *et al.* (2013) refer to the need to use high-resolution remote sensing data for analyzing ES, while Gómez-Baggethun *et al.* (2013) point out that the type and scale of ES will vary for individual environmental and geographic characteristics of each region; some of the ES can be determined by remote sensing technologies.

With the recent and continued developments of remote sensing technologies, assessment of urban ES is becoming possible. These developments include the following: (a) increased spatial, temporal, and spectral resolutions, from high-resolution agile satellites that can provide high-resolution repeat coverage; (b) multiple medium- to high-resolution small satellites launched by private companies; (c) piloted and remotely piloted aerial systems (RPAS); (d) multi-polarized synthetic aperture radar systems with a range of frequencies; and (e) airborne lidar systems,

While sensors on satellite platforms are available with a very broad range of spatial resolutions, because of the requirements of urban remote sensing to detect buildings, pavements, roads, parking lots, the fragmentation of open space and similar issues, airborne sensors have been specifically designed for urban mapping by several

companies. RPAS systems are rapidly developing and are available for very high-resolution imaging with very small ground sampling distances.

Spectral resolution refers to the range and width of wavelengths that can be resolved by a sensor, while temporal resolution refers to the frequency of coverage of a certain area on the terrain surface by a sensor. In the design of sensors on satellites, there is necessarily a compromise between the demands for spatial, spectral, and temporal resolutions. On the other hand, currently available airborne hyperspectral sensors have very high spectral resolutions in hundreds of spectral bands but a relatively coarse spatial resolution.

Airborne lidar, (also written as LiDAR) data is based on a scanning pulsed laser, with wavelengths in the infrared region of the electromagnetic spectrum, so that distances from the platform, either piloted or RPAS to the terrain surface is determined from the time of travel of the laser pulse. Together with knowledge of the position and attitude of the aircraft, a dense point cloud on the terrain surface can be determined to represent the positions and elevations of discrete posts at a density in excess of 10 posts per m<sup>2</sup>. Airborne lidar can be acquired simultaneously with aerial images for the extraction of three-dimensional information about man-made features and therefore details of the built environment.

The two publications by Haas and Ban, referred to above, have demonstrated how the evaluation of ES for urban areas could be based on satellite remote sensing technologies. In particular, in Haas and Ban (2017b), ES supply and demand were determined by extracting 13 land use classes from satellite remotely sensed data, with an accuracy of the order of 80%. The classes were attributed to 22 ecological integrity, regulating, provisioning, and cultural services and seven integrity measures (Burkhard *et al.* 2012) to derive capacities of ecosystems and their functions for supplying services. The supply services attributed to each class are defined as the sum of all ecological integrity, regulating, provisioning, and cultural services. Areas that lack the provision of these services are considered neutral or being in service demand based on human interaction, their structural design, use, and functioning. A demand map was generated with modified service values through addition and averaging of all influence maps and through multiplication with original budget values from Burkhard *et al.* (2012). Interurban supply and demand comparisons were made by multiplying the LULC extracted area with attributed budget values per class.

In de Araujo Barbosa *et al.* (2015) a review is given of papers published on the topic of remote sensing for determining characteristics of ES. There is not only a lack of coverage of urban areas, but the paper has not considered the most recent developments in determining ES or remote sensing technologies. They note that there is no definitive list of ES and therefore have chosen those provided in the MA (2005). They identified 211 peer-reviewed papers covering the applications of remote sensing for determining ES as listed in Table 3. The paper argues that identifying the relationship between locations of changes in ES and those who receive the benefits is important.

Table 3. ES that were determined by remote sensing for determining ES according to de Araujo Barbosa *et al.* (2015), separated into “significant” and “less significant” topics.

Significant Topics	Less Significant Topics
Food provision	Water regulation
Climate regulation	Biological refugia
Genetic resources	Cultural heritage
Raw materials	
Water provision	
Erosion regulation	

While it would be appropriate to present remote sensing technologies that would be suitable for detecting more ES than are listed in Table 3 or as described by Haas and Ban (2017b), this would not be possible in the space available. Indeed, the parameters that would be measured by the current remote sensing or by other means are listed against the 22 ecological integrity, regulating, provisioning, and cultural services and seven integrity measures in Table 1 of Burkhard *et al.* (2012). Pettorelli and her 27 coauthors (2018) provide a comprehensive list of current remote sensors that could be used for assessing ES. As technologies develop, it is likely that further sensors will be available for assessing ES. Both publications are derived by multiple authors who have expertise in a broad range of ES.

Finally, Scott and Rajabifard (2017) have provided a framework for the development of national policies incorporating geospatial information. They stress the opportunities for the geospatial community to play a significant role in global sustainable development.

## Conclusions

The starting point for this review on urban sustainability and ES was to describe the concept of sustainability and the importance of green spaces in urban areas. Ecosystem services, which were defined in the paper as providing the life support systems for human's well-being, have been studied for about four decades, but there is still much to be learned about how they can be assessed and how they can be applied as an assessment tool for decision-makers and sustainability of urban areas. Ecosystem services adopted in this paper are based on the contributions in MA (2005) and TEEB (2010) which comprise 22 regulating, provisioning, and cultural ES and seven integrity measures. The assessment of some of the ES by remote sensing technologies has been described, but future remote sensing systems will enable more of the ES to be determined and therefore, contribute to assessing urban sustainability based on their supply and demand. Published works demonstrate types of remote sensing systems that should allow more of the ES to be assessed. The impact of urban developments has had a very significant, and in some cases disastrous, impact on biodiversity and fragmentation of habitats, which is reflected in a reduction in ES.

The process by which the supply and demand for ES are assessed and change over time has been adopted as a guide for assessing urban sustainability. The assessment of ES should enable determining these impacts on quality of life of inhabitants of cities. We posed the question *How to assess the impact of losses of ES on the well-being of humans?* Progress has been made in some aspects of this work. Geospatial technologies, including remote sensing, should play a significant role in the future assessment of ES.

## References

Bai, X., A. Surveyer, T. Elmqvist, F. W. Gatzweiler, B. Guneralp, S. Parnell, A.-H. Prieur-Richard, P. Shrivastava, J. G. Siri, M. Stafford-Smith, J.-P. Toussaint and R. Webb. 2016. Defining and advancing a systems approach for sustainable cities. *Current Opinion in Environmental Sustainability* 23:69–78.

Berger, M. 2014. The unsustainable city. *Sustainability* 6:365–374.

Blanco, H., F. Wautiez, A. Llaverro and C. Riveros. 2001. Sustainable development indicators in Chile: To what extent are they useful and necessary? *Eure-Revista Latinoamericana de Estudios Urbano Regionales* 27:85–95.

Breuste, J., S. Qureshi and J. Li. 2013. Scaling down the ecosystem services at local level for urban parks of three megacities. *Hercynia N. F.* 46:1–20.

Burkhard, B., F. Kroll, S. Nedkov and F. Müller. 2012. Mapping ecosystem service supply, demand and budgets. *Ecological Indicators* 21:17–29. doi: 10.1016/j.ecolind.2011.06.019.

Colavitti, A. M., A. Floris and S. Serra. 2020. Urban standards and ecosystem services: The evolution of the services planning in Italy from theory to practice. *Sustainability* 12 (2434):20. doi: 10.3390/su12062434.

Costanza, R., R. d'Arge, R. de Groot, S. Farber, M. Grasso, B. Hannon, K. Limburg, S. Naeem, R. V. O'Neill, J. Paruelo, R. G. Raskin, P. Sutton and M. van den Belt. 1997. The value of the world's ecosystem services and natural capital. *Nature* 387:253–260.

Costanza, R., R. de Groot, P. Sutton, S. van der Ploeg, S. J. Anderson, I. I. Kubiszewski, S. Farber and R. K. Turner. 2014. Changes in the global value of ecosystem services. *Global Environmental Change* 26:152–158. doi: http://dx.doi.org/10.1016/j.gloenvcha.2014.04.002.

Costanza, R. R., R. de Groot, L. Braat, I. Kubiszewski, L. Fioramonti, P. Sutton, S. Farber and M. Grasso. 2017. Twenty years of ecosystem services: How far have we come and how far do we still need to go? *Ecosystem Services* 28:1–16. doi: 10.1016/j.ecoser.2017.09.008.

Costanza, R. R. and B. C. Patten. 1995. Defining and predicting sustainability. *Ecological Economics* 15:193–196.

Cox, D. T. C., D. F. Shanahan, H. L. Hudson, R. A. Fuller and K. J. Gaston. 2018. The impact of urbanisation on nature dose and the implications for human health. *Landscape and Urban Planning* 179:234–244.

de Araujo Barbosa, C. C., P. M. Atkinson and J. A. Dearing. 2015. Remote sensing of ecosystem services: A systematic review. *Ecological Indicators* 52:430–443. doi: http://dx.doi.org/10.1016/j.ecolind.2015.01.007.

EU (European Commission). 2015. In-depth report: Indicators for sustainable cities. *Science for Environment Policy* (12):24p. doi: 10.2779/121865.

Fahrig, L. 2003. Effects of habitat fragmentation on biodiversity. *Annual Review of Ecology, Evolution, and Systematics* 34:487–515.

Fischer, J. and D. B. Lindenmayer. 2006. Beyond fragmentation: The continuum model for fauna research and conservation human-modified landscapes. *Oikos* 112:473–480.

Gardner, G. 2016. Cities in the arc of human history: A materials perspective. In *Can a City be Sustainable?*, 11–25. Washington, D.C.: The World Watch Institute, Island Press.

Gaston, K. J., M. L. Avila-Jimenez and J. L. Edmondson. 2013. Managing urban ecosystems for goods and services. *Journal of Applied Ecology*:11. doi: 10.1111/1365-2664.12087.

Geneletti, D., C. Cortinovis, L. Zardo and B. A. Esmail. 2020a. Chapter 6: Towards equity in the distribution of ecosystem services in cities. In *Planning for Ecosystem Services in Cities*, edited by D. Geneletti, C. Cortinovis, L. Zardo and B. A. Esmail. Cham, Switzerland: Springer Nature Switzerland AG.

Geneletti, D., C. Cortinovis, L. Zardo, and B. A. Esmail. 2020b. *Planning for Ecosystem Services in Cities, Springer Briefs in Environmental Science*. Cham, Switzerland: Springer Nature Switzerland AG.

Gómez-Baggethun, E. and D. N. Barton. 2013. Classifying and valuing ecosystem services for urban planning. *Ecological Economics* 86:235–245. doi: 10.1016/j.ecolecon.2012.08.019.

Gómez-Baggethun, E., Å. Gren, D. N. Barton, J. J. Langemeyer, T. McPhearson, P. O'Farrell, E. Andersson, Z. Hamstead and P. Kremer. 2013. Urban Ecosystem services. In *Urbanization, Biodiversity and Ecosystem Services: Challenges and Opportunities—A Global Assessment*, edited by T. Elmqvist, M. Fragkias, J. Goodness, B. Güneralp, P. J. Marcotullio, R. I. McDonald, S. Parnell, M. Schewenius, M. Sendstad, K. C. Seto and C. Wilkinson, 77. Dordrecht, Netherlands: Springer.

Guerry, A. D., P. Polasky, J. Lubchenko, R. Chaplin-Kramer, G. C. Daily, R. Griffin, M. Ruckelshaus, I. J. Bateman, A. Duraipappah, T. Elmqvist, M. W. Feldman, C. Folke, J. Hoekstra, P. M. Kareiva, B. L. Keeler, S. Li, E. McKenzie, Z. Ouyang, B. Reyers, T. H. Ricketts, J. Rockström, H. Tallis and B. Vira. 2015. Natural capital and ecosystem services informing decisions: From promise to practice. *Proceedings of the National Academy of Sciences of the United States of America (PNAS)* 112 (24):7348–7355. doi: 10.1073/pnas.1503751112.

Haas, J. and Y. Ban. 2017a. Mapping and monitoring urban ecosystem services using multitemporal high-resolution satellite data. *IEEE Journal of Selected Topics in Applied Earth Observations and Remote Sensing* 10 (2):669–680. doi: 10.1109/JSTARS.2016.2586582.

- Haas, J. and Y. Ban. 2017b. Sentinel-1A SAR and Sentinel-2A MSI data fusion for urban ecosystem service mapping. *Remote Sensing Applications: Society and Environment* 8:41–53. doi: 10.1016/j.rsase.2017.07.006.
- Haddad, N. M., L. A. Brudvig, J. Clobert, K. F. Davies, A. Gonzalez, R. D. Holt, T. E. Lovejoy, J. O. Sexton, M. P. Austin, C. D. Collins, W. M. Cook, E. I. Damschen, R. M. Ewers, B. L. Foster, C. N. Jenkins, A. J. King, W. F. Laurance, D. J. Levey, C. R. Margules, B. A. Melbourne, A. O. Nicholls, J. L. Orrock, D.-X. Song and J. R. Townshend. 2015. Habitat fragmentation and its lasting impact on Earth's ecosystems. *Science Advances* 1 (2):1–9.
- Hansen, R., N. Frantzeskaki, T. McPhearson, E. Rall, N. Kabisch, A. Kaczorowska, J.-H. Kain, M. Artmann and S. Pauleit. 2015. The uptake of the ecosystem services concept in planning discourses of European and American cities. *Ecosystem Services*. doi: 10.1016/j.ecoser.2014.11.013i.
- Holden, E. and I. T. Norland. 2005. Three challenges for the compact city as a sustainable urban form: Household consumption of energy and transport in eight residential areas in the greater Oslo region. *Urban Studies* 42:2145–2166. doi: 10.1080=00420980500332064.
- Holden, M., M. Roseland, K. Ferguson and A. Perl. 2008. Seeking urban sustainability on the world stage. *Habitat International* 32:305–317.
- Kubiszewski, I., R. Costanza, C. Franco, P. Lawn, J. Talberth, T. Jackson and C. Aylmer. 2013. Beyond GDP: Measuring and achieving global genuine progress. *Ecological Economics* 93:57–68. doi: 10.1016/j.ecolecon.2013.04.019.
- Li, D., J. Ma, T. Cheng, J. L. van Genderen and Z. Shao. 2019. Challenges and opportunities for the development of MEGACITIES. *International Journal of Digital Earth* 12 (12):1382–1395. doi: 10.1080/17538947.2018.1512662.
- Lortie, C. J., R. W. Brooker, P. Choler, Z. Kikvidze, R. Michalet, F. I. Pugnaire and R. M. Callaway. 2004. Rethinking plant community theory. *Oikos* 107:433–438.
- MA (Millennium Ecosystem Assessment). 2005. *Ecosystems and Human Well-Being: Synthesis*. Washington, D.C.: Island Press.
- Maechler, S. and J.-C. Graz. 2019. Environmental management systems standards facing natural capital accounting: ISO 14007 & ISO 14008. In *Proceedings 24th EURAS Annual Standardisation Conference—'Standards for a Bio-Based Economy'*, held in Verlagshaus Main, Germany.
- Maes, J., M. Erhard and A. Teller. 2016. Mapping and Assessment of Ecosystems and their Services—Urban ecosystems. 4th Report. Publications Office of the European Union, Luxembourg.
- Mennis, J., M. Mason and A. Ambrus. 2018. Urban greenspace is associated with reduced psychological stress among adolescents: A geographic ecological momentary assessment (GEMA) analysis of activity space. *Landscape and Urban Planning* 174:1–9.
- Mori, K. and A. Christodoulou. 2012. Review of sustainability indices and indicators: Towards a new City Sustainability Index (CSI). *Environmental Impact Assessment Review*:94–106.
- Newlands, N. K. 2017. *Future Sustainable Ecosystems: Complexity, Risk and Uncertainty*. Boca Raton, Fla.: CRC Press.
- Obama, B. 2015. Obama administration memo directs incorporation of ecosystem services in federal decision-making. *WEF Stormwater Report*. <<https://stormwater.wef.org/2015/10/obama-administration-memo-directs-incorporation-ecosystem-services-federal-decision-making/>>.
- Ortiz, O.M.S. and D. Geneletti. 2018. Assessing mismatches in the provision of urban ecosystem services to support spatial planning: A case study on recreation and food supply in Havana, Cuba. *Sustainability* 2018 10 (2165):21. doi: 10.3390/su10072165.
- Perrings, C., S. Naeem, F. Ahrestani, D. E. Bunker, P. Burkill, G. Canziani, T. Elmqvist, R. Ferrati, J. Fuhrman, F. Jaksic, Z. Kawabata, A. Kinzig, G. M. Mace, F. Milano, H. Mooney, A.-H. Prieur-Richard, J. Tschirhart and W. Weisse. 2010. Ecosystem services for 2020. *Science* 330 (6002):323–324. doi: 10.1126/science.1196431.
- Pettorelli, N., H. Schulte to Buhne, A. Tulloch, G. Dubois, C. Macinnis-Ng, A. M. Queiros, D. A. Keith, M. Wegmann, F. Schrodt, M. Stellmes, R. Sonnenschein, G. N. Geller, S. Roy, B. Somers, N. Murray, L. Bland, I. Geijzendorffer, J. T. Kerr, S. Broszeit, P. J. Leitao, C. Duncan, G. El Serafy, K. S. He, J. L. Blanchard, R. Lucas, P. Mairota, T. J. Webb and E. Nicholson. 2018. Satellite remote sensing of ecosystem functions: Opportunities, challenges and way forward. *Remote Sensing in Ecology and Conservation* 4 (2):71–93. doi: 10.1002/rse2.59.
- Rugani, B., D. Maia de Souza, B. P. Weidema, J. Bared, B. Bakshi, B. Grann, J. M. Johnston, A.L.R. Pavan, X. Liu, A. A. Laurent and F. Verones. 2019. Towards integrating the ecosystem services cascade framework within the Life Cycle Assessment (LCA) cause-effect methodology. *Science of the Total Environment* 690:1284–1298. doi: 10.1016/j.scitotenv.2019.07.023.
- Schröter, M., D. N. Bartonb, R. P. Remmea and L. Hein. 2014. Accounting for capacity and flow of ecosystem services: A conceptual model and a case study for Telemark, Norway. *Ecological Indicators* 36:539–551. doi: 10.1016/j.ecolind.2013.09.018.
- Scott, G. and A. Rajabifard. 2017. Sustainable development and geospatial information: A strategic framework for integrating a global policy agenda into national geospatial capabilities. *Geo-spatial Information Science* 20 (2):59–76. doi: 10.1080/10095020.2017.1325594.
- Shanahan, D. F., D. T. Cox, R. A. Fuller, S. Hancock, B. B. Lin, K. Anderson, R. Bush and K. J. Gaston. 2017. Variation in experiences of nature across gradients of tree cover incompact and sprawling cities. *Landscape and Urban Planning* 157:231–238.
- Shao, Z., L. Ding, D. Li, O. Altan, Md. E. Huq and C. Li. 2020. Exploring the relationship between urbanization and ecological environment using remote sensing images and statistical data: A case study in the Yangtze River Delta, China. *Sustainability*:12. doi: 10.3390/su12145620.
- Shao, Z., N. S. Sumari, A. Portnov, F. Ujoh, W. Musakwa and P. J. Mandela. 2020. Urban sprawl and its impact on sustainable urban development: A combination of remote sensing and social media data. *Geo-spatial Information Science*. doi: 10.1080/10095020.2020.1787800.
- TEEB. 2010. The economics of ecosystems and biodiversity in local and regional policy and management. In *Earthscan TEEB*, edited by H. Wittmer and H. Gundimeda. London/Washington, D.C.: Routledge.
- Tian, Y., C. Y. Jim and Y. Tao. 2012. Challenges and strategies for greening the compact city of Hong Kong. *Journal of Urban Planning and Development* 138 (2):101–109. doi: 10.1061/(ASCE)UP.1943-5444.0000076.
- Trinder, J. C. 2016. Extraction of parameters from remote sensing data for environmental indices for urban sustainability. In *Remote Sensing for Sustainability*, 3–24. Boca Raton, Fla.: CRC Press Taylor & Francis Group.
- Trinder, J. and Q. Liu. 2020. Assessing environmental impacts of urban growth using remote sensing. *Geo-spatial Information Science* 23 (1):20–39. doi: 10.1080/10095020.2019.1710438.
- Twohig-Bennett, C. and A. Jones. 2018. The health benefits of the great outdoors: A systematic review and metaanalysis. *Environmental Research* 166:628–637.
- United Nations. 2016. *UN Sustainable Development Goals*. <<https://unstats.un.org/sdgs/report/2016/>>. Accessed 2 June 2020.
- Van Den Bosch, M. A., M. Pierpaolo, U. Valdas, M. Barndahl, A. Kulinkina, B. Staatsen, and W. Swart, H. Kruijze, I. Zurlyte and A. I. Egorov. 2015. Development of an urban green space indicator and the public health rationale. *Scandinavian Journal of Public Health*, 44 (2):159–67.
- Wang, C., Y. Wang, R. Wang and P. Zheng. 2018. Modeling and evaluating land-use/land-cover change for urban planning and sustainability: A case study of Dongying city, China. *Journal of Cleaner Production* 172:1529–1534. doi: 10.1016/j.jclepro.2017.10.294.
- Wolch, J. R., J. Byrne and J. P. Newell. 2014. Urban green space, public health, and environmental justice: The challenge of making cities “just green enough”. *Landscape and Urban Planning* 125:234–244.
- Zhang, Y. and Z. Shao. 2020. Assessing of urban vegetation biomass in combination with LiDAR and high-resolution remote sensing images. *International Journal of Remote Sensing*. doi: 10.1080/01431161.2020.1820618.

# WHO'S WHO IN ASPRS

## BOARD OF DIRECTORS

### BOARD OFFICERS

#### President

Jeff Lovin  
*Woolpert*

#### President-Elect

Jason M. Stoker, Ph.D.  
*U.S. Geological Survey*

#### Vice President

Christopher Parrish, Ph.D.  
*Oregon State University*

#### Past President

Thomas Jordan, Ph.D.  
*University of Georgia*

#### Treasurer

Stewart Walker, Ph.D.  
*photogrammetry4u*

#### Secretary

Lorraine B. Amenda, PLS, CP

### BOARD MEMBERS

#### Sustaining Members Council – 2021

Chair: Joe Cantz  
[www.asprs.org/About-Us/Sustaining-Members-Council.html](http://www.asprs.org/About-Us/Sustaining-Members-Council.html)

#### Committee Chairs Council – 2022

Chair: Mike Zoltek  
Vice-Chair: TBA

#### Early-Career Professionals Council – 2021

Chair: Bobby Arlen  
Vice Chair: Melissa Martin

#### Region Officers Council – 2021

Chair: Lorraine B. Amenda, PLS, CP  
Vice Chair: Demetrio Zourarakas

#### Student Advisory Council – 2021

Chair: Youssef Kaddoura  
<http://www.asprs.org/Students/Student-Advisory-Council.html>

#### Technical Division Directors Council – 2021

Chair: Bandana Kar, Ph.D.  
Vice Chair: Denise G. Theunissen

### TECHNICAL DIVISION OFFICERS

#### Geographic Information Systems Division – 2021

Director: Xan Fredericks  
Assistant Director: Denise G. Theunissen  
[www.asprs.org/Divisions/GIS-Division.html](http://www.asprs.org/Divisions/GIS-Division.html)

#### Lidar Division – 2022

Director: Joshua Nimetz, CMS  
Assistant Director: Ajit Sampath  
[www.asprs.org/Divisions/Lidar-Division.html](http://www.asprs.org/Divisions/Lidar-Division.html)

#### Photogrammetric Applications Division – 2022

Director: Kurt Rogers  
Assistant Director: Benjamin Wilkinson  
[www.asprs.org/Divisions/Photogrammetric-Applications-Division.html](http://www.asprs.org/Divisions/Photogrammetric-Applications-Division.html)

#### Primary Data Acquisition Division – 2021

Director: Jon Christopherson  
Assistant Director: J. Chris Ogier  
[www.asprs.org/Divisions/Primary-Data-Aquisition-Division.html](http://www.asprs.org/Divisions/Primary-Data-Aquisition-Division.html)

#### Professional Practice Division – 2022

Director: Harold W. Rempel, III, CP  
Assistant Director: Bill Swope  
[www.asprs.org/Divisions/Professional-Practice-Division.html](http://www.asprs.org/Divisions/Professional-Practice-Division.html)

#### Remote Sensing Applications Division – 2022

Director: Raechel A. Portelli, Ph.D.  
Assistant Director: Amr Abd-Elrahman  
[www.asprs.org/Divisions/Remote-Sensing-Applications-Division.html](http://www.asprs.org/Divisions/Remote-Sensing-Applications-Division.html)

#### Unmanned Autonomous Systems (UAS) – 2022

Director: Megan Ritelli, Ph.D.  
Assistant Director: Dan Hubert

### REGION PRESIDENTS

#### Alaska Region

David Parret  
<http://www.asprsalaska.org/>

#### Cascadia Region

Robert Hairston-Porter

#### Eastern Great Lakes Region

Shawana P. Johnson, Ph.D, GISP  
<http://egl.asprs.org/>

#### Florida Region

Xan Fredericks  
<http://florida.asprs.org/>

#### Heartland Region

Whit Lynn  
<http://heartland.asprs.org/>

#### Mid-South Region

<https://www.asprs.org/all-regions/mid-south.html>

#### Northeast Region

(representing the merger of The New England and Central New York Regions)  
Trevis Gigliotti, Interim President

#### North Atlantic Region

Richard W. Carlson, Jr., P.L.S., C.P.  
<http://natlantic.asprs.org/>

#### Pacific Southwest Region

Omar G. Mora  
<https://pswasprs.org/>

#### Potomac Region

Dave Lasko  
<http://www.asprspotomac.org/>

#### Rocky Mountain Region

<http://www.asprs-rmr.org/>

#### Western Great Lakes Region

Brandon Krumwiede  
<http://wgl.asprs.org/>

# Monitoring Work Resumption of Wuhan in the COVID-19 Epidemic Using Daily Nighttime Light

Zhenfeng Shao, Yun Tang, Xiao Huang, and Deren Li

## Abstract

*This study analyzes the characteristics of nighttime light (NTL) radiance variation, aiming to demonstrate the possibility of using NTL to monitor work resumption and evaluate the impact of COVID-19 on economic activities in Wuhan, China. The results show that NTL radiance generally decreased during the epidemic. Despite the fact that increased NTL radiance was observed after lifting the lockdown, it was still lower than normal, indicating that socioeconomic activities have been largely resumed but the production scale has not been fully restored, and the decrease in nitrogen dioxide concentration verified this phenomenon. We find that central urban areas and distant suburban areas present different modes of NTL radiance variation. We further observed a decrease in NTL radiance from different urban functional areas, including industrial parks, airports, business districts, loop lines, and residential area, that corresponds to the impact of the COVID-19 epidemic on both industrial production and the service sector.*

## Introduction

The COVID-19 epidemic broke out in Wuhan, China, at the end of December 2020. This virus has greater transmissibility than severe acute respiratory syndrome and Middle East respiratory syndrome (Tomar and Gupta 2020). Within a few months, it had spread at a drastic rate and covered almost the whole world as of March 2020. The World Health Organization (WHO) estimated that the virus has an incubation period of 2 to 10 days, which makes the control measures of the epidemic more intractable. Additionally, asymptomatic and pre-symptomatic infections have become significant factors in preventing the epidemic from spreading and rebounding. These infected cases can transmit the virus without displaying any symptoms. According to WHO, the cumulative number of confirmed COVID-19 cases worldwide exceeded 20 million on 12 August, the cumulative number of deaths exceeded 730,000, and these numbers are still growing rapidly. Thus, the global epidemic prevention and control situation remains grim. With the strong contagions of the COVID-19 epidemic, many countries have enforced a series of emergency measures, including city lockdowns, ceasing industrial production, and restricting population movement (Pervaiz *et al.* 2020). Wuhan adopted lockdown measures to reduce the spread of COVID-19 from 23 January to 8 April. Soon afterward, a majority of provinces in mainland China carried out rigorous measures to restrict social activities, production, and transportation. Thus, analyzing the impact of the lockdown on people's daily lives and

enterprise production becomes a significant scientific research not only to China but to other countries and regions as well.

At present, many studies that conduct analysis for the epidemic spread and impact of COVID-19 have been published. Research has investigated the future patterns and temporal dynamics of COVID-19 using time series models (Feroze 2020; Griffith *et al.* 2020; Li *et al.* 2020; Zhou *et al.* 2020), estimated and predicted the impact of different factors on the outbreak and spread of COVID-19 (Buckee *et al.* 2020; Luo *et al.* 2020; Oliveiros *et al.* 2020; Sajadi *et al.* 2020), illustrated the impact of containment measures on people's daily lives (Liu *et al.* 2020), analyzed the improvement of air quality (Adams 2020; Griffith *et al.* 2020; Liu *et al.* 2020; Pervaiz *et al.* 2020; Tao *et al.* 2020), and presented the spatiotemporal characteristics of the epidemic spread (Liu 2020; Liu *et al.* 2020; Wang *et al.* 2020). However, few studies have focused on analyzing the impact of epidemic prevention and control measures on the progress of work resumption. During the COVID-19 epidemic, especially during the city lockdown, most enterprises were unable to execute production and business activities, and the governments made unified arrangements for work resumption in accordance with the improvement in prevention and control measures for the epidemic. This study aims to monitor the work resumption of Wuhan in the COVID-19 epidemic and understand the impact of the epidemic at the city level, providing evidence that can help governments adjust lift-lockdown strategies and better evaluate economic losses.

Nighttime light (NTL) remote sensing data have been widely used to estimate socioeconomic parameters and serve as an indication of economic activity (Bennie *et al.* 2014; Shi *et al.* 2014; Li *et al.* 2016, 2018; Hu and Huang 2019) given their capability of demonstrating enterprise production, energy consumption, transportation, and other socioeconomic activities. Scholars have applied NTL data to understand the progress and impacts of critical threats as well as to monitor economic recovery in near real time at low cost (Hudecheck *et al.* 2020). NTL data provide an opportunity to understand people's movements and activity changes during the lockdown. The Earth Observation Group utilizes cloud-free average radiance composites to calculate brightness changes between the pre-epidemic period and the lockdown period. The results show that light intensity was decreased in many parts of China in February 2020, the peak of the epidemic (Elvidge *et al.* 2020). NASA has presented the NTL results of Wuhan, showing the comparisons before and during the lockdown. Their results demonstrated significant dimming, especially in certain districts and highways. Furthermore, NTL changes reflect the shutdown of business and transportation around Hubei province (NASA Earth Observatory 2020). The Gauteng City-Region Observatory has released comparisons of light intensity before the beginning of lockdown (March 2020) and

---

Zhenfeng Shao and Deren Li are with the State Key Laboratory of Information Engineering in Surveying, Mapping, and Remote Sensing, Wuhan University, Wuhan 430079, China (shaozhenfeng@whu.edu.cn).

Yun Tang is with the School of Remote Sensing and Information Engineering, Wuhan University, Wuhan 430079, China.

Xiao Huang is with the Department of Geosciences, University of Arkansas, Fayetteville, AR 72701.

---

Photogrammetric Engineering & Remote Sensing  
Vol. 87, No. 3, March 2021, pp. 197–206.  
0099-1112/21/197–206

© 2021 American Society for Photogrammetry  
and Remote Sensing  
doi: 10.14358/PERS.87.3.197

during the level 5 lockdown (April 2020) as well as the light intensity comparison from the level 5 lockdown to the level 4 lockdown (May 2020). Their data present distinct dimming of lights during the level 5 lockdown, and many residential areas also show an overall dimming. Compared with the level 5 lockdown, brightness during the level 4 lockdown show an overall increase (Naidoo and Maree 2020). Hudecheck *et al.* (2020) found that the NTL intensity of peripheral industrial regions was reduced in January and February compared with the pre-epidemic period, and dense city centers showed a consistent pattern, indicating the impact of COVID-19 on China's service sector. Anand and Kim (2020) used NTL data to assess the economic activity in African protected areas during the COVID-19 epidemic and found that 75% of the protected areas (a total of 8427) showed varying degrees of reduction in light intensity. However, the aforementioned studies focus mainly on qualitative analyses, and the spatial scales are national, provincial, and municipal, so it is necessary to perform quantitative analysis at a finer spatial and temporal resolution. In this study, we calculate monthly average NTL radiance variation in Wuhan before, during, and after the lockdown. We further analyze the impact of the epidemic in different urban functional areas (Zhou *et al.* 2020).

Industrial production, commercial activities, and transportation have a significant impact on the natural environment (e.g., air quality). These anthropogenic activities shrank abruptly during the lockdown of cities, resulting in improved air quality and lower pollutant concentrations. Nitrogen dioxide (NO<sub>2</sub>), sulfur dioxide (SO<sub>2</sub>), and ozone (O<sub>3</sub>) come primarily from traffic emissions, power plants, and factory production. They can serve as representative indicators of industrial activities. An industrial and commercial slowdown will consequently result in reduced concentrations of NO<sub>2</sub>, SO<sub>2</sub>, and O<sub>3</sub>. Therefore, detecting the concentration of these three indicators can monitor the energy consumption of industrial enterprises and indirectly reflect the status of work resumption. Several studies have stressed the effect of the lockdown on air quality (Collivignarelli *et al.* 2020; Kerimray *et al.* 2020; Nakada and Urban 2020; Stratoulas and Nuthamachot 2020). NASA and the European Space Agency (ESA) have observed a significant reduction of NO<sub>2</sub> over China using modified Copernicus Sentinel-5P data, and the reduction is correlated with the economic slowdown following the outbreak of the epidemic (NASA Earth Observatory 2020). The Royal Netherlands Meteorological Institute utilized data from the TROPospheric Monitoring Instrument (TROPOMI) from Sentinel-5P and found that the NO<sub>2</sub> concentrations in Madrid, Milan, and Rome dropped by around 45% from 13 March to 13 April 2020, while Paris saw an arresting decrease of 54%, coinciding with the strict quarantine measures implemented across Europe (ESA Earth Online 2020).

This study utilizes daily NTL radiance images to detect the impact of the COVID-19 epidemic and the lockdown measures on Wuhan. The NO<sub>2</sub> concentration data are used as an auxiliary validation. The changes in economic activities and industrial production reflected from NTL data during the epidemic are revealed in different administrative regions and urban functional areas. These results are expected to offer suggestions for decision-makers to assess economic losses and the progress of work resumption.

## Materials and Methods

### Data Set

#### Visible Infrared Imaging Radiometer Suite NTL Data

The Visible Infrared Imaging Radiometer Suite (VIIRS) Day Night Band (DNB) onboard the Suomi National Polar-orbiting Partnership satellite provides global daily measurements of nocturnal visible and near-infrared light. The VIIRS/DNB

has a spectral range of 500 to 900 nm and is highly sensitive to low-light conditions, significantly improving the ability to detect anthropogenic lighting from buildings, roads, and other city infrastructures at night without the influence of moonlight (Hillger *et al.* 2013). NASA's Black Marble nighttime lights product suite (VNP46) has been available at 500-m resolution since January 2012 with the data from VIIRS/DNB. The routine global processing retrieval algorithm utilizes all high-quality, cloud-free, and atmospheric-, terrain-, vegetation-, snow-, lunar-, and stray light-corrected radiances to estimate daily NTL and other intrinsic surface optical properties, which are described in detail in the algorithm theoretical basis document, and provides rigorous quality assurance and uncertainty information (Román *et al.* 2018). The cloud masks associated with NTL imagery were performed using the VIIRS thermal band (M15) with a spectral range of 10.26 to 11.26 μm (Román *et al.* 2019). This study utilizes the VNP46A1 product with temporal periods from 1 December 2019 to 31 August 2020 and from 1 December 2018 to 31 August 2019. The products are archived at NASA's LAADS DAAC data center (<https://ladsweb.modaps.eosdis.nasa.gov>).

### Pollutant Data

The Sentinel-5 precursor mission provides daily global information at a city-scale spatial resolution on the concentrations of trace gases and aerosols. The TROPOMI onboard the Sentinel-5P satellite is a push-broom spectrometer with ultraviolet, visible spectrum, near-infrared, and short-wave infrared spectral bands, allowing for the retrieval of key atmospheric constituents, namely, NO<sub>2</sub>, O<sub>3</sub>, formaldehyde (CH<sub>2</sub>O), SO<sub>2</sub>, methane (CH<sub>4</sub>), carbon monoxide (CO), aerosol, and clouds (SRON 2020). In order to monitor the induced changes during the different periods of the epidemic, statistics for the periods from 1 December 2019 to 31 August 2020, and from 1 December 2018 to 31 August 2019 were calculated. Earth Observation data were collected from the Sentinel-5P TROPOMI sensor and processed in Google Earth Engine (Gorelick *et al.* 2017).

### Data Preprocessing

The VNP46A1 product contains 26 scientific data set layers. The "QF\_Cloud\_Mask" and "DNB\_At\_Sensor\_Radiance\_500m" layers were extracted from VNP46A1. The "QF\_Cloud\_Mask" layer provides the identity information of pixels that are disturbed by clouds, cirrus clouds, and shadows. This identifier was used to filter the "DNB\_At\_Sensor\_Radiance\_500m" layer to obtain a high-quality image. The "DNB\_At\_Sensor\_Radiance\_500m" layer provides pixel radiance with nW·cm<sup>-2</sup>·sr<sup>-1</sup> as the unit. Clouds affect both the intensity and the location of lights in DNB imagery by reducing the intensity of the lights and blurring the spatial detail of the light features (Baugh *et al.* 2013). Therefore, the "probably clear," "confidentially cloudy," and "probably cloudy" pixels were marked as invalid according to the cloud mask.

The lockdown measure was implemented from 23 January to 8 April 2020, inducing far-reaching impacts on Wuhan. This study calculates the average NTL radiance of cloud-free pixels in different periods. HMA (half month ago) in 2020 represents the period from 9 January to 23 January 2020, corresponding to the half month before the lockdown. HML (half month later) in 2020 represents the period from 24 January to 7 February 2020, corresponding to the half month after the lockdown. Similarly, HMA in 2019 represents the period from 20 January to 3 February 2019. HML in 2019 represents the period from 4 February to 18 February 2019, corresponding to the same periods in 2020. Moreover, the average NTL radiance of January to August 2020 and 2019 were calculated. The NTL radiance of December 2019 and December 2018 were averaged to create a pre-epidemic composite data set and the same periods in 2018's composite data set; these two data sets were

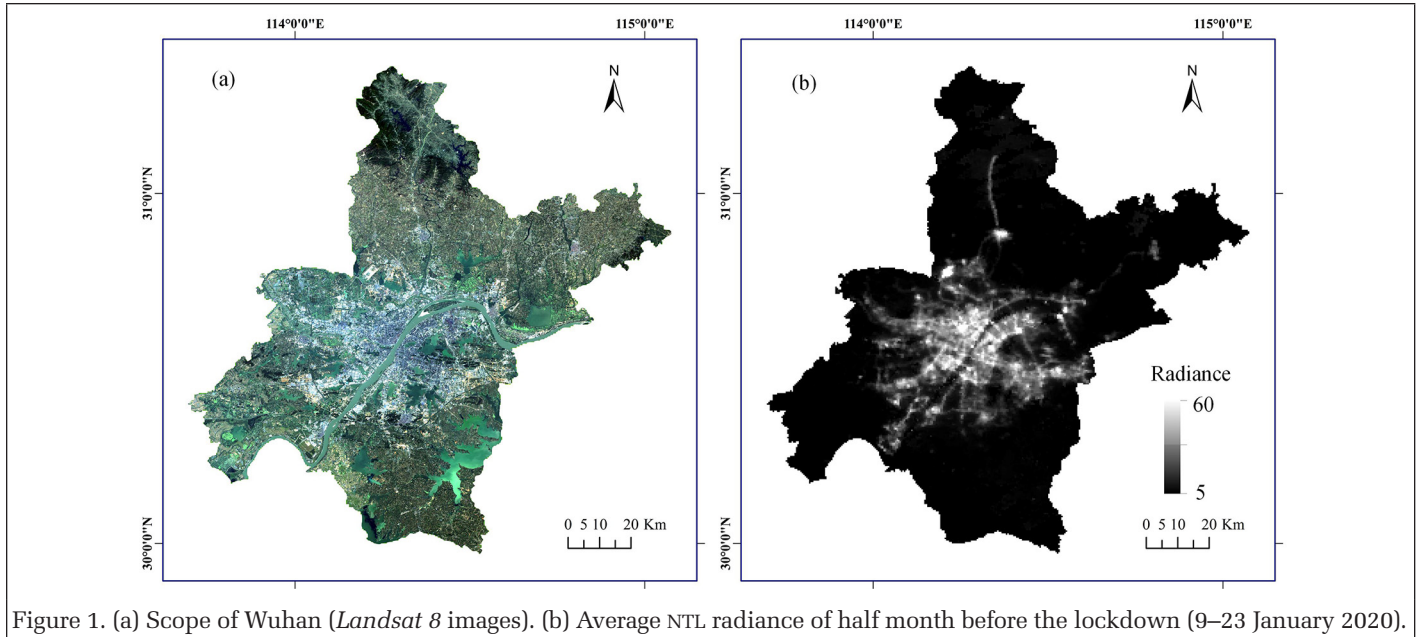


Figure 1. (a) Scope of Wuhan (*Landsat 8* images). (b) Average NTL radiance of half month before the lockdown (9–23 January 2020).

treated as NTL intensity under normal economic activity and industrial production. The scope of the whole of Wuhan and the average NTL radiance image of the half month before the lockdown are shown in Figure 1 (pixels with radiance values lower than  $5 \text{ nW}\cdot\text{cm}^{-2}\cdot\text{sr}^{-1}$  were excluded).

### General Work Flow

Figure 2 shows the work flow described in the previous section.

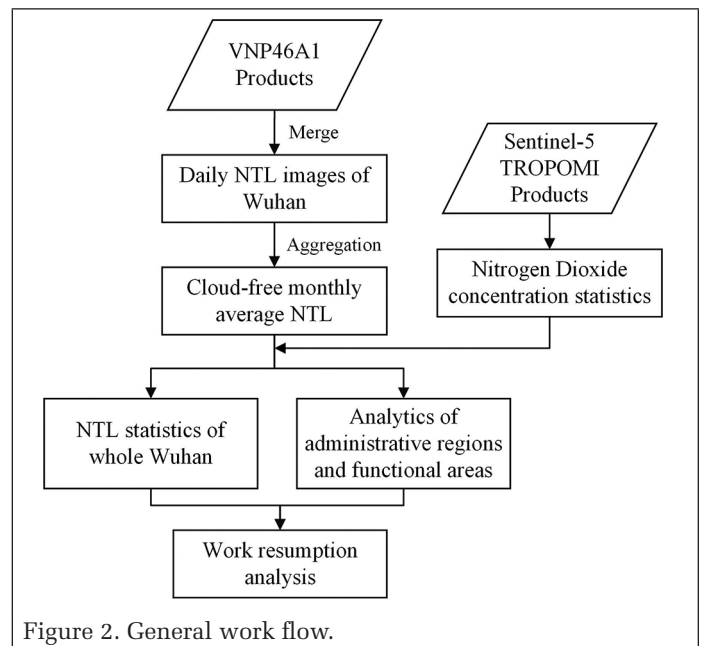


Figure 2. General work flow.

## Results

### Change of NTL Intensity by Administrative Regions

#### Change of NTL Intensity in the Whole City

Figure 3 shows the change ratios of total NTL radiance in Wuhan within different periods. The values at HML in 2020 represent the change ratio of NTL radiance from HML to December 2019, the values at HML in 2019 represent the change ratio of NTL radiance from HML to December 2018, and so on for the other periods and months. We can observe that NTL radiance decreased dramatically during the half month after the lockdown. To comply with the quarantine measures, factories, business centers, and schools were closed, and people continued to be quarantined by ceasing their daily activities from February to March, evidenced by the fact that all the change ratios are negative during the lockdown period.

On 8 April, Wuhan lifted the lockdown measures. The consumption of electricity by enterprises above a designated size had recovered over 80%, the employee attendance rate had reached 60.5% in early April, and the electricity load was expected to return to 90% by the end of April (Xinhuanet 2020). NTL radiance was found to increase greatly compared to March but was still lower than NTL radiance in December 2019. The change ratios of total NTL radiance decreased in May and June 2019 compared with April, and the same is true in 2020, which can be attributed to the influence of seasonal factors. We further found that NTL radiance gradually increased after Wuhan lifted the lockdown measures, but the total NTL radiance was still lower than before the lockdown, indicating that work resumption had been significantly improved but the production scale had not fully recovered. However, a drastic reduction in the NTL radiance change ratio was observed in July 2020, which can be explained by the lots of rainy days in July.

We further investigated the total NTL radiance difference value during different periods. The NTL radiance in Figure 4

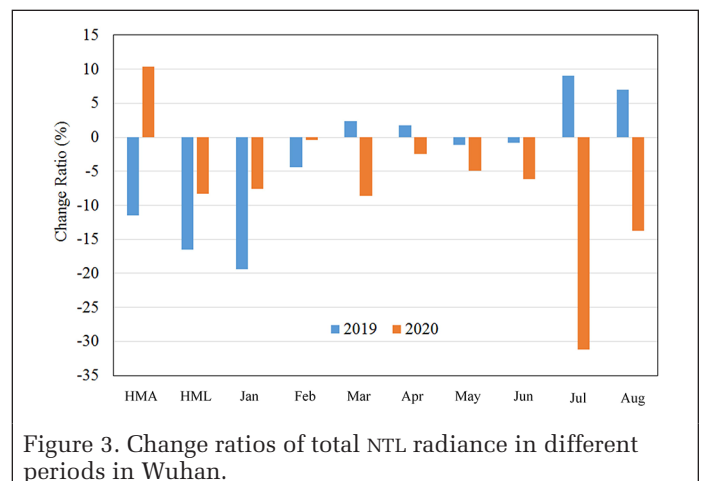


Figure 3. Change ratios of total NTL radiance in different periods in Wuhan.

was centered on the artificial lights that exist mainly in residential, urban, and built-up areas, excluding the outliers and the pixels with radiance values less than  $5 \text{ nW}\cdot\text{cm}^{-2}\cdot\text{sr}^{-1}$  (Liu *et al.* 2020). In Figure 4, the values at HMA in 2020 represent the difference value of total NTL radiance between the same period in 2019 and December 2019, the values at HMA in 2019 represent the difference value of total NTL radiance between the half month before the lockdown and December 2018, and so on for the other periods and months. All the median and mean total NTL radiance difference values are negative during and after the lockdown. After lifting the lockdown, the difference values of April are considerably lower than March. All of the above results indicate that the lockdown measures have greatly impacted economic activities, industrial manufacturing, and population mobility in Wuhan.

Figure 5 presents the year-on-year growth rates of average  $\text{NO}_2$  concentrations over the different periods of the epidemic. Compared to the same period in 2019, we found a sharp reduction in  $\text{NO}_2$  concentration during the half month before the lockdown. After that, the year-on-year growth rates continued to decline during the lockdown until March. With the improvement of the epidemic situation, the growth rate in March shows an increase compared to February. Especially after the lockdown, the growth rate increased dramatically. Rainfall has little effect on the changes in  $\text{NO}_2$  concentration (YangFan 2015), although Wuhan suffered heavy rainfall in July, and the growth rate of  $\text{NO}_2$  concentration increased in July and reached a positive value, indicating that work resumption in July plays well. Therefore, the progress of work resumption, reflected by the changes in growth rate of  $\text{NO}_2$  concentrations, is consistent with the results demonstrated by the change ratios of total NTL radiance.

The change ratios of total NTL radiance in different periods reveal that during and after the lockdown, the whole of Wuhan saw a decrease in total NTL radiance. Figure 6 demonstrates the change ratios of six major economic indicators (Wuhan Bureau of Statistics 2020). Compared with 2019, all the indicators dropped significantly during the epidemic, consistent with the decrease in NTL radiance. The change ratios of the six major economic indicators show upward

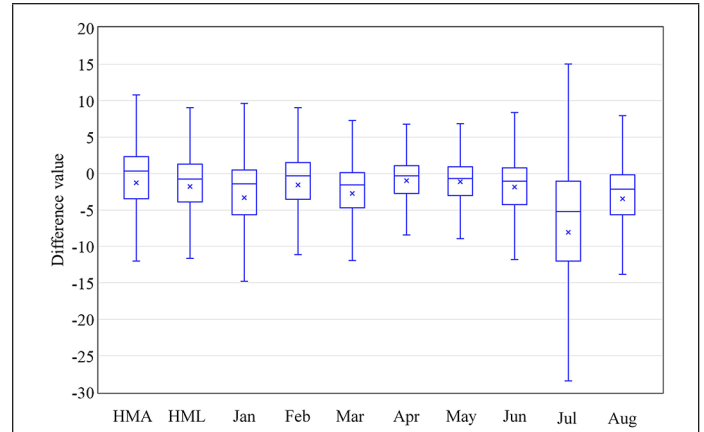


Figure 4. Comparison of NTL radiance difference value in different periods.

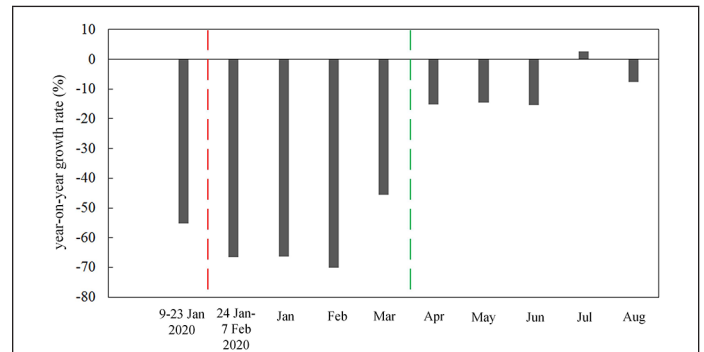


Figure 5. Year-on-year growth rate of average  $\text{NO}_2$  concentration over Wuhan in different periods (the period before the red line represents the half month before the lockdown, the period between the red line and the green line represents the lockdown, and the period after the green line represents after the lockdown).

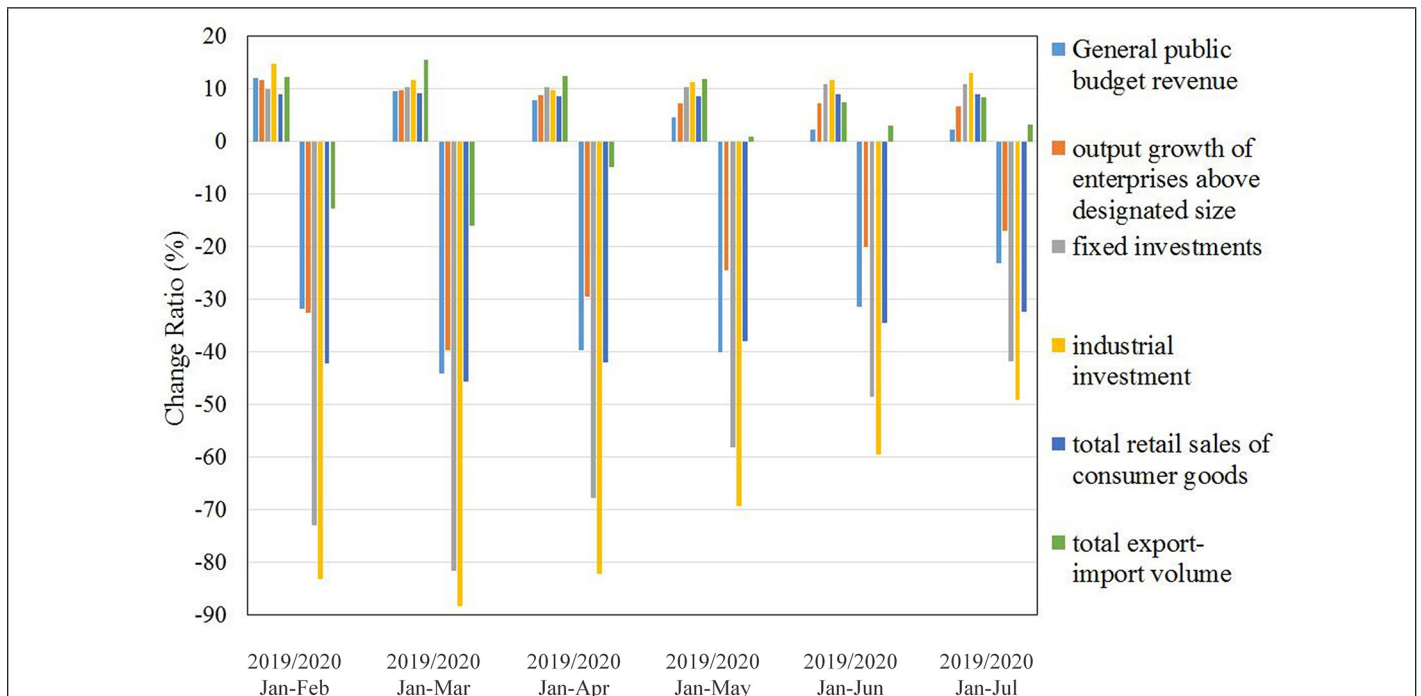


Figure 6. Change ratio of major economic indicators in Wuhan.

trends after the lockdown, indicating that economic activities and industrial production improved when the epidemic was under control.

### Changes in Different Regions

This study compared the NTL radiance change ratio across different regions of Wuhan. Figure 7 shows the change ratios of 13 administrative regions, which can be categorized into central urban areas and distant suburban areas. We observe

that the central urban areas and distant suburban areas demonstrate different patterns of the NTL radiance change ratio. For all the periods before, during, and after the lockdown, most NTL radiance change ratios in seven central urban areas are negative (Jiang'an, Jianghan, Qiaokou, Hanyang, Wuchang, Qingshan, and Hongshan districts). Although seasonal factors are taken into account, the degree of decrease in NTL radiance in seven central urban areas before the lockdown is considerably higher than 2019, suggesting that citizens started

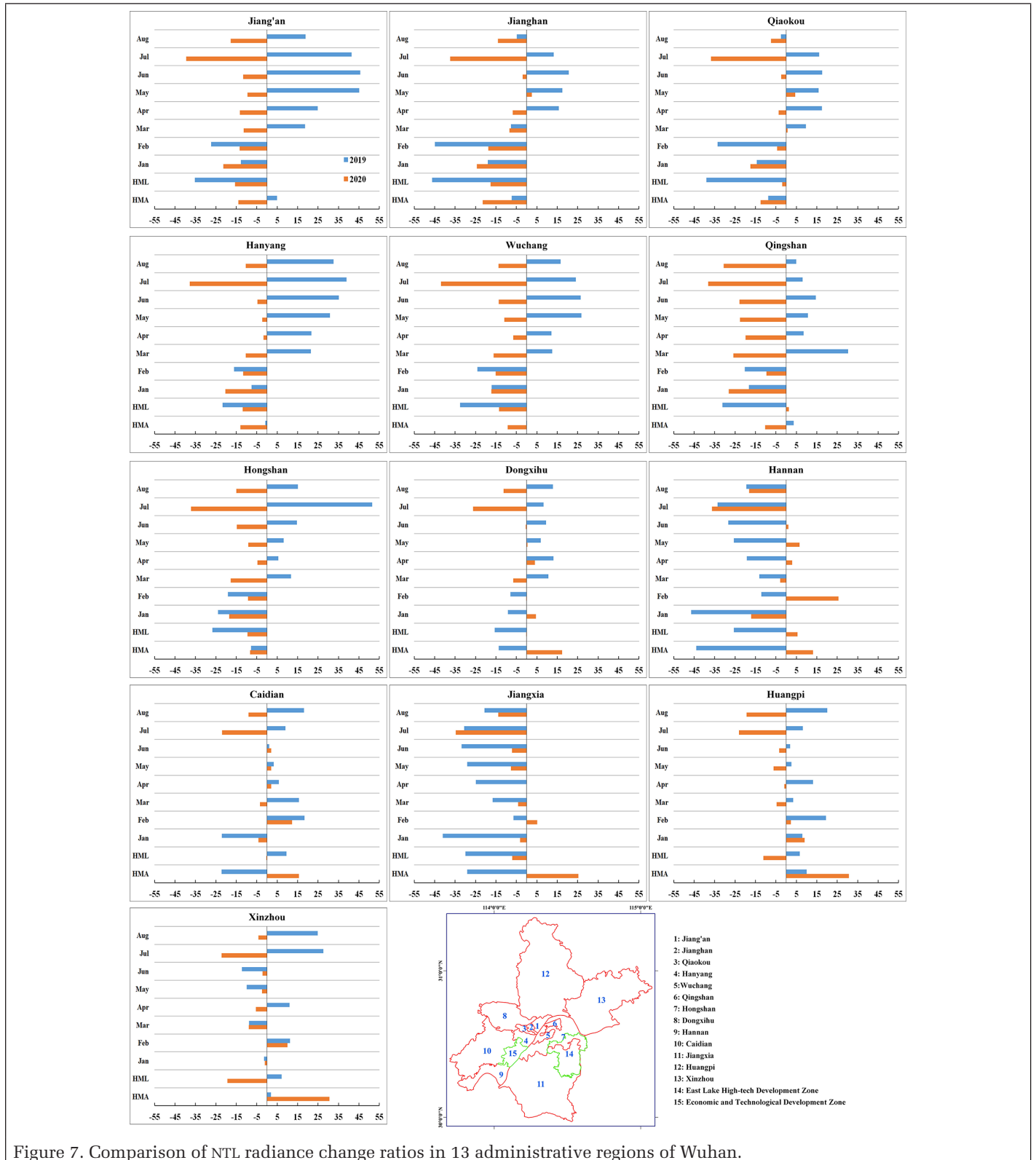


Figure 7. Comparison of NTL radiance change ratios in 13 administrative regions of Wuhan.

self-isolating before the official quarantines, and the similar NTL emissions reduction was observed in China's northern regions (Hudecheck *et al.* 2020).

On the other hand, the NTL radiance change ratio of seven central urban areas in the half month after the lockdown and February 2020 are obviously higher than the same periods in 2019. According to the *Wuhan Statistical Yearbook* (2018), central urban areas are known to have high population densities, and people stay at home in compliance with epidemic prevention measures to reduce social contact and the risk of transmission during the lockdown, resulting in more pixels being lit in the residential category and brighter pixels being found in the residential areas. The same periods in 2019 are during the Spring Festival holiday, which explains the more frequent population movement than other months. As the migrant population returns to their hometowns and the residents go out to visit relatives and friends or travel, a decrease in NTL intensity of residential areas was observed.

The change ratios in six distant suburban areas (Dongxihu, Hannan, Caidian, Jiangxia, Huangpi and Xinzhou districts) present different patterns. The change ratios in the half month before the lockdown 2020 are positive, but they are negative in the seven central urban areas in the same period. Figure 3 shows that the change ratio of the whole of Wuhan in the half month before the lockdown is 10.33%, which is considerably higher than that in all central urban areas. This insight indicates that the NTL radiance increase of Wuhan in the half month before the lockdown is due largely to the NTL radiance increase in distant suburban areas. Figures 3 and 7 illustrate that the patterns of NTL radiance change in the same periods in 2019 are different from those in 2020, and they do not vary between the distant suburban areas and the central urban areas in the same periods in 2019. Furthermore, we calculate the NTL radiance change ratios over the same periods in 2018; these also did not show the discrepancies. The change ratio of the whole of Wuhan in the same periods in 2018 is 14.43%, and most administrative regions show varying degrees of NTL radiance increase, except for Qingshan district. However, the change ratios in the distant suburban areas are negative in the half month after the lockdown, except for Hannan district, which indicates that the NTL radiance of the distant suburban areas dropped sharply with the implementation of the lockdown measures.

After the 2019 Spring Festival holiday, industries, commercial centers, entertainment venues, and individual business have completely resumed production, and employees returned to work. The NTL radiance in central urban areas has increased remarkably. From March to August 2020, lower NTL radiance change ratios were found than during the same periods in 2019 across all 13 administrative regions. The negative change ratios after the lockdown indicate that the production scale or capacity of enterprises has not been fully restored.

Figure 8 demonstrates the NTL radiance change ratios of two national development zones, i.e., East Lake High-Tech Development Zone (ELHTDZ) and Economic and Technological Development Zone (ETDZ), which are the top two districts with the highest gross domestic product in Wuhan. The ELHTDZ is dominated by the optoelectronic information industry, high-end equipment manufacturing, and the bioengineering and high-tech medicine industries. The automobile and automobile parts and the electronic and electrical industries are two pillar industries of the ETDZ.

Compared with the same period in 2019, these two zones present similar characteristics of NTL radiance variation. From the half month before the lockdown to February, most NTL radiance change ratios are negative (except for the ETDZ in February), and all of them are higher than the same period in 2019. According to the *Wuhan Statistical Yearbook* (2018), these two

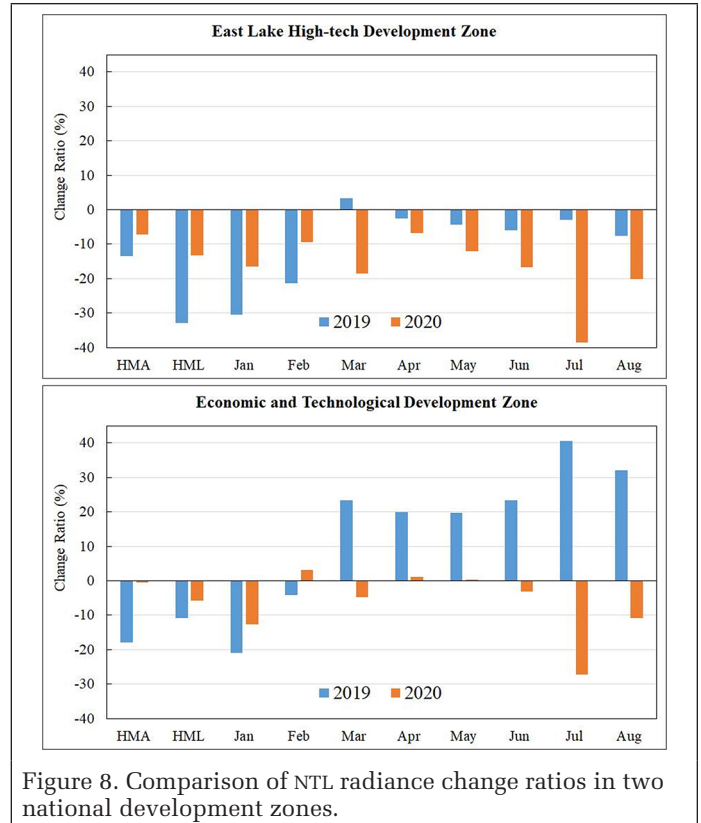


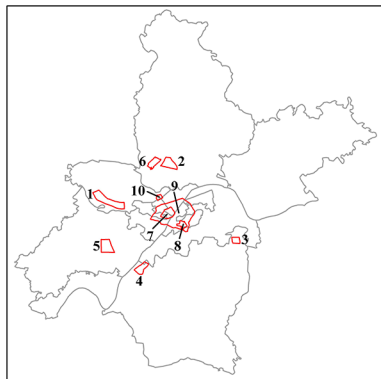
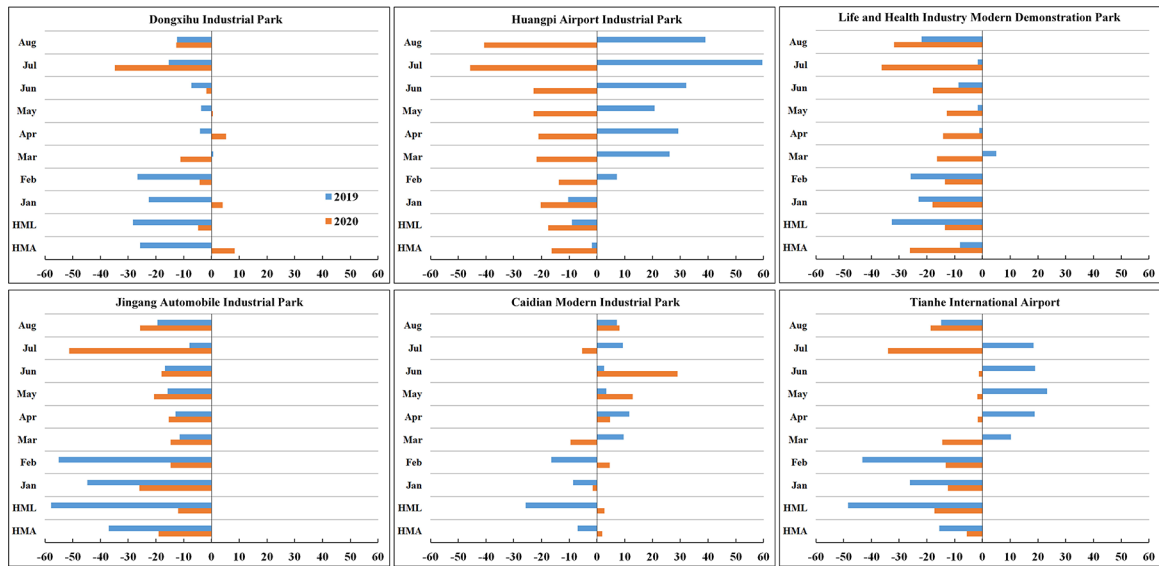
Figure 8. Comparison of NTL radiance change ratios in two national development zones.

zones have higher population densities than majority distant suburban areas, and the migrant population in the ELHTDZ and ETDZ accounts for 44.0% and 31.8%, respectively, of the total population in 2015. The mobility from the migrant population is presumably responsible for the reduction of NTL radiance for the ELHTDZ and ETDZ around Spring Festival holiday.

After February, the NTL radiance variation of the two zones present different patterns. Compared with December 2018, the NTL radiance of the ELHTDZ from March to August 2019 have slightly changed, indicating that the NTL intensity after February has reached a normal level in 2019. It indicates that social activities and industrial production have generally returned. However, compared with December 2019, the NTL intensity after February 2020 was still below the normal level before the epidemic, but the difference values of NTL radiance change ratios between 2020 and 2019 in the ELHTDZ are significantly lower than in most of the administrative regions, suggesting that the progress of work resumption in the ELHTDZ is better than in other regions. This results are supported by the fact that the gross regional production and growth rate of the ELHTDZ ranked first among all districts in Wuhan in the first half of 2020. We can also observe that the NTL radiance of the ETDZ are close to pre-epidemic levels from March to August 2020, but the NTL radiance change ratios are significantly lower than in the same period in 2019, suggesting that social activities and production have returned to pre-epidemic levels but are still lower than the same period in 2019.

#### Change in NTL Intensity by Urban Functional Areas Categories

We further calculate the change ratio of NTL radiance in different urban functional area categories (i.e., industrial production, airports, business districts, loop lines, and residential areas) to investigate the impact of the lockdown measures. Figures 9 and 10 present the change ratio of five industrial parks, airports, business districts, city centers, and residential communities, demonstrating their different change characteristics. Before, during, and after the lockdown of Wuhan,



1. Dongxihu Industrial Park
2. Huangpi Airport Industrial Park
3. Life and Health Industry Modern Demonstration Park
4. Jingang Automobile Industrial Park
5. Caidian Modern Industrial Park
6. Tianhe International Airport
7. Jiangnan Road and Hanzheng Street Business Districts
8. Zhongnan Road Business Districts
9. Within Second Ring Road
10. Changqing Garden Community

Figure 9. Comparison of NTL radiance change ratios across industrial parks and the international airport.

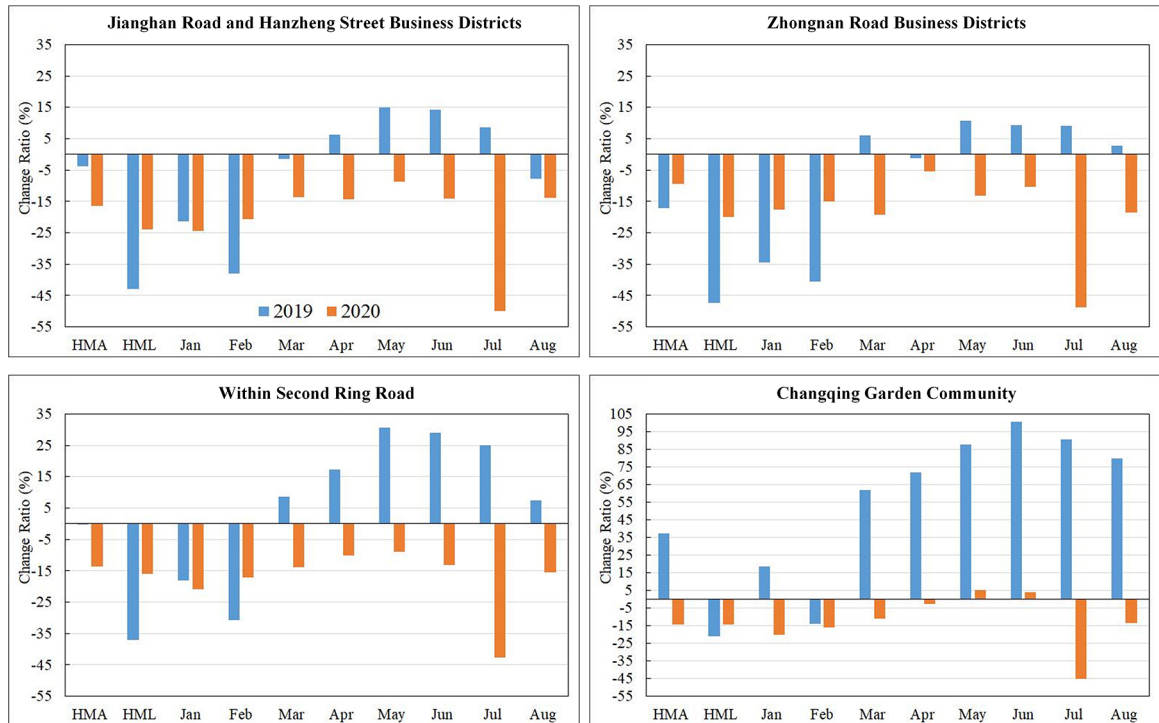


Figure 10. Comparison of NTL radiance change ratios across business districts, the second ring road, and the community.

decreased NTL radiance were found in most urban functional areas. Dongxihu Industrial Park consists of an industrial food park and a logistics industry park. With the lockdown of the city, the NTL radiance was found to have decreased, and the food process industries and express-delivery enterprises did not resume work and production until late March. We observe that the NTL radiance after the lockdown is close to that of December 2019, suggesting that the production capacity and scale have recovered. As the core area of Wuhan Airport Economic Zone, Huangpi Airport Industrial Park was composed of five major industrial sectors, including new energy and new materials, jewelry and clothing design, intelligent manufacturing, biomedical industries, and logistics e-commerce. The NTL radiance change ratios in Huangpi Airport Industrial Park are negative throughout the temporal period before, during, and after the lockdown.

In Life and Health Industry Modern Demonstration Park, located in the ELHTDZ, the change ratios are obviously lower than in December 2019. Since the outbreak of the COVID-19 epidemic, a number of medical enterprises in the park have maintained production and given full play to their advantages in research, production, and transportation and strengthened the production of testing methods, preventive drugs, and protective equipment to support the prevention and control of the epidemic, and those actions from the medical enterprises are presumably responsible for the high NTL radiance in the half month after the lockdown and in February. After the lockdown of Wuhan, the change ratios are still lower than the same periods in 2019, indicating that the production capacity has not fully recovered. After the lockdown, the NTL radiance change characteristics of Jingang Automobile Industrial Park are similar to those of Huangpi Airport Industrial Park and Life and Health Industry Modern Demonstration Park. Caidian Modern Industrial Park focuses on high-end equipment manufacturing, including new-energy vehicles and intelligent connected vehicles, intelligent manufacturing, and modern logistics, and the NTL radiance change ratios increased obviously after the lockdown, suggesting that the production scale has been restored. Before, during, and after the lockdown, the change ratios of Tianhe International Airport are negative. Despite the fact that the NTL radiance has returned to the level of December 2019, the change ratios are significantly lower than the same periods in 2019, indicating that the production scale has not fully recovered to the levels of the same periods in 2019. Until mid-June, international scheduled passenger flights had not resumed due to the overseas epidemic. Daily flights recovered only 40%, and the passenger throughput recovered 25%. It was not until mid-September 2020 that the daily flight volume returned to the same level as the previous year (Changjiang Daily 2020).

We also observe a consistent variation in light emission in dense city centers and residential areas. The Jiangnan Road and Hanzheng Street business districts are the two most prosperous areas in Wuhan, and dimmed NTL was found for those two districts before and during the lockdown. With the resumption of work since March, the change ratios are still negative and considerably lower than in 2019. A similar pattern can also be observed in the Zhongnan Road business district and within the second ring road. Compared with the same period in 2019, the NTL radiance change ratios of the dense city centers and business districts have been significantly reduced, indicating a sharp reduction of non-industry-related activities, corresponding to the impact of the COVID-19 epidemic on the service sectors.

In comparison, the change ratios in residential areas present different characteristics. As one of the communities with the largest permanent populations in Wuhan, the change ratios of Changqing Garden Community have generally shown

an upward trend after the ease of the epidemic situation, indicating an increase in the return of residents and work resumption.

## Discussion

The COVID-19 epidemic has greatly impacted economic activities, industrial production, and human activities. Some of these impacts can be monitored via light intensity from DNB images. By using NO<sub>2</sub> concentration as auxiliary validation data and showing the characteristics of NTL radiance variation before, during, and after the lockdown in Wuhan, we monitor the light intensity dynamics in Wuhan to provide a comprehensive understanding of the impact of COVID-19 on both the economic activities and the work resumption process for decision-makers and citizens. To comply with the quarantine measures, most people stayed at home during the lockdown by reducing their daily outdoor activities. From the beginning of the lockdown to mid-March 2020, Wuhan's electricity load dropped by nearly 40% compared with the same period in 2020, which has been confirmed by the NTL intensity decrease, suggesting that the economy has been greatly impacted. Moreover, we found that the impacts of the epidemic on different administrative regions and urban functional areas vary, reflected by the characteristics of the NTL. This type of information offers knowledge for decision-makers and the public on how the economy has recovered and provides a reference for the other countries to make their own policies to control the spread of the epidemic and resume work and production. In the future, we can utilize higher-spatial-resolution NTL data to analyze the impact of COVID-19 on a subregional scale, such as high-spatial-resolution color Jilin-1 imaging. Furthermore, the combinations of remote sensing data and statistical data, such as gross domestic product, consumption, and the unemployment rate, should be used to help in understanding the impacts of the epidemic. NTL has been used as an indicator of economic activity and provides a direct signature of human activity (Li *et al.* 2013; Levin *et al.* 2020). NTL emissions are particularly effective at quantifying the economic and social impact of COVID-19. VIIRS/DNB data can quickly recognize decreases in economic activity, which is almost impossible to identify in time through statistical data issued by the government. Therefore, it can be used to investigate post-epidemic socioeconomic situations as well. However, NTL radiance is affected by deviations from clouds and aerosols, similar to daylight sensing in the visible band. Opaque clouds can completely block NTL radiance, while a thinner and transparent or semitransparent atmosphere partially blocks the radiance and scatters the light, creating a fuzzy image (Elvidge *et al.* 2017). In addition, uncertainties originating from seasonal variation and surface optical properties also lead to measurement error in NTL. These types of uncertainty affect the estimation of socioeconomic status based on NTL data, and these factors need to be removed from the NTL radiance variation trends in future research. These challenges may be addressed with future sensors.

This study utilizes spatiotemporal patterns in artificial NTL to investigate the impact of the epidemic and to monitor work resumption at different scales and regions, proving the feasibility of NTL remote sensing for studying the impact of public health emergencies. Furthermore, the breadth of NTL remote sensing applications can be improved and extended. Natural disasters can damage electrical equipment and infrastructure, interrupt human activities and production, and affect NTL emissions, and related power outages will be mapped on the NTL images. NTL remote sensing can monitor the extent and scope of disasters and the recovery from disasters.

NO<sub>2</sub> concentrations show sharp reductions before and during the lockdown, and the growth rates of NO<sub>2</sub> concentrations increased after the lockdown. Due to the reduction of industrial production and transportation, the emissions of pollutants have been greatly reduced during the lockdown, improving air quality. On the other hand, as the epidemic has broken out in many regions and countries, some cities have adopted lockdown measures to suppress the spread of the epidemic. The investigation of variation of pollutants and air quality during the epidemic should be expanded to larger study areas, and the comprehensive impacts of the epidemic on the urban environment should be analyzed in future studies.

## Conclusions

The outbreak of the COVID-19 epidemic has greatly disrupted human lives, economic activities, and industrial manufacturing. From 23 January to 8 April 2020, Wuhan adopted 76-day lockdown measures to reduce the spread of COVID-19. This study analyzes the impact of COVID-19 on human lives and economic activities as reflected by NTL and NO<sub>2</sub> concentration and provides detailed spatiotemporal characteristics of the progress of work resumption. From the results of the experiments and statistics, we conclude the following:

1. The average NTL radiance in Wuhan has dropped significantly with the implementation of the lockdown measures. Although the NTL radiance has increased after lifting the lockdown, it is still lower than normal, indicating that compared with the lockdown period, work resumption has been improved, but the production scale and capacity have not been fully restored in Wuhan.
2. NO<sub>2</sub> concentration reduced dramatically because of the shutdown of industrial production and transportation during the epidemic and shows a significant increase with the improvement of the epidemic situation, especially after the lockdown. The decrease of NO<sub>2</sub> concentration in Wuhan has also confirmed the phenomenon demonstrated by the NTL radiance.
3. The central urban areas and distant suburban areas show different patterns of NTL radiance variation. NTL radiance in most central urban areas decreased before, during, and after the lockdown, and citizens started self-isolating before the official quarantines. During the half month before the lockdown, the increase of NTL radiance in Wuhan was accompanied by an increase of NTL radiance in distant suburban areas. Compared with December 2019, NTL radiance in 13 administrative regions was significantly reduced from March to August 2020.
4. The progress of work resumption in the ELHTDZ is better than all other administrative regions. Social activities and the production scale in the ETDZ have returned to pre-epidemic levels.
5. NTL radiance in different urban functional areas all decreased during the epidemic, including industrial parks, airports, business districts, loop lines, and residential areas, indicating that the lockdown measures have a significant impact on industrial production, commercial activities, daily human life, and transportation. NTL radiance in the business districts has been remarkably reduced, indicating a sharp reduction of non-industry-related activity, corresponding to the impact of the COVID-19 epidemic on the service sectors.

## Acknowledgments

The authors are sincerely grateful to the editors as well as the anonymous reviewers for their valuable suggestions and comments that helped us improve this article significantly.

## References

- Adams, M. D. 2020. Air pollution in Ontario, Canada during the COVID-19 State of Emergency. *Science of the Total Environment* 742:140516. doi:10.1016/j.scitotenv.2020.140516.
- Anand, A. and D.-H. Kim. 2020. Pandemic induced changes in economic activity around African protected areas captured through night-time light data. <https://doi.org/10.32942/osf.io/kzdxr>.
- Baugh, K., F.-C. Hsu, C. D. Elvidge, and M. Zhizhin. 2013. Nighttime lights compositing using the VIIRS day-night band: Preliminary results. *Proceedings of the Asia-Pacific Advanced Network* 35:70–86.
- Bennie, J., T. W. Davies, J. P. Duffy, R. Inger, and K. J. Gaston. 2014. Contrasting trends in light pollution across Europe based on satellite observed night time lights. *Scientific Reports* 4 (1):1–6.
- Buckee, C. O., S. Balsari, J. Chan, M. Crosas, F. Dominici, U. Gasser, Y. H. Grad, B. Grenfell, M. E. Halloran, and M. U. Kraemer. 2020. Aggregated mobility data could help fight COVID-19. *Science* 368 (6487):145.
- Changjiang Daily. 2020. Daily flight volume exceeded 200, Tianhe airport returned to 40% of the normal level before the epidemic. <https://baijiahao.baidu.com/s?id=1669302017077595371&wfr=pider&for=pc>. Accessed 10 August 2020.
- Collivignarelli, M. C., A. Abbà, G. Bertanza, R. Pedrazzani, P. Ricciardi, and M. C. Miino. 2020. Lockdown for CoViD-2019 in Milan: What are the effects on air quality? *Science of the Total Environment* 732:139280. doi:10.1016/j.scitotenv.2020.139280.
- Elvidge, C. D., K. Baugh, M. Zhizhin, F. C. Hsu, and T. Ghosh. 2017. VIIRS night-time lights. *International Journal of Remote Sensing* 38 (21):5860–5879.
- Elvidge, C. D., F.-C. Hsu, T. Ghosh, and M. Zhizhin. 2020. World tour of COVID-19 impacts on nighttime lights. <https://payneinstitute.mines.edu/world-tour-of-covid-19-impacts-on-nighttime-lights>. Accessed 10 August 2020.
- ESA Earth Online. 2020. Sentinel-5P news. <https://earth.esa.int/web/guest/missions/esa-ee-missions/sentinel-5p/news>. Accessed 1 October 2020.
- Feroze, N. 2020. Forecasting the patterns of COVID-19 and causal impacts of lockdown in top ten affected countries using Bayesian structural time series models. *Chaos, Solitons and Fractals* 140:110196. doi:10.1016/j.chaos.2020.110196.
- Gorelick, N., M. Hancher, M. Dixon, S. Ilyushchenko, D. Thau, and R. Moore. 2017. Google Earth Engine: Planetary-scale geospatial analysis for everyone. *Remote Sensing of Environment* 202:18–27.
- Griffith, S. M., W.-S. Huang, C.-C. Lin, Y.-C. Chen, K.-E. Chang, T.-H. Lin, S.-H. Wang, and N.-H. Lin. 2020. Long-range air pollution transport in East Asia during the first week of the COVID-19 lockdown in China. *Science of the Total Environment* 741:140214. doi:10.1016/j.scitotenv.2020.140214.
- Hillger, D., T. Kopp, T. Lee, D. Lindsey, C. Seaman, S. Miller, J. Solbrig, S. Kidder, S. Bachmeier, and T. Jasmin. 2013. First-light imagery from Suomi NPP VIIRS. *Bulletin of the American Meteorological Society* 94 (7):1019–1029.
- Hu, T. and X. Huang. 2019. A novel locally adaptive method for modeling the spatiotemporal dynamics of global electric power consumption based on DMSP-OLS nighttime stable light data. *Applied Energy* 240:778–792.
- Hudecheck, M., C. Sirén, D. Grichnik, and J. Wincent. 2020. Monitoring the COVID-19 crisis from space. *MIT Sloan Management Review*, 17 April. <https://sloanreview.mit.edu/article/monitoring-the-covid-19-crisis-from-space>.

- Kerimray, A., N. Baimatova, O. P. Ibragimova, B. Bukenov, B. Kenessov, P. Plotitsyn, and F. Karaca. 2020. Assessing air quality changes in large cities during COVID-19 lockdowns: The impacts of traffic-free urban conditions in Almaty, Kazakhstan. *Science of the Total Environment* 730:139179. <https://doi.org/10.1016/j.scitotenv.2020.139179>.
- Levin, N., C. C. Kyba, Q. Zhang, A. S. de Miguel, M. O. Román, X. Li, B. A. Portnov, A. L. Molthan, A. Jechow, and S. D. Miller. 2020. Remote sensing of night lights: A review and an outlook for the future. *Remote Sensing of Environment* 237:111443. <https://doi.org/10.1016/j.rse.2019.111443>.
- Li, D., X. Zhao, and X. Li. 2016. Remote sensing of human beings—A perspective from nighttime light. *Geo-spatial Information Science* 19 (1):69–79.
- Li, Q., X. Guan, P. Wu, X. Wang, L. Zhou, Y. Tong, R. Ren, K. S. Leung, E. H. Lau, and J. Y. Wong. 2020. Early transmission dynamics in Wuhan, China, of novel coronavirus-infected pneumonia. *New England Journal of Medicine* 382 (13):1199–1207.
- Li, X., S. Liu, M. Jendryke, D. Li, and C. Wu. 2018. Night-time light dynamics during the Iraqi civil war. *Remote Sensing* 10 (6):858.
- Li, X., H. Xu, X. Chen, and C. Li. 2013. Potential of NPP-VIIRS nighttime light imagery for modeling the regional economy of China. *Remote Sensing* 5 (6):3057–3081.
- Liu, Q., D. Sha, W. Liu, P. Houser, L. Zhang, R. Hou, H. Lan, C. Flynn, M. Lu, and T. Hu. 2020. Spatiotemporal patterns of COVID-19 impact on human activities and environment in mainland China using nighttime light and air quality data. *Remote Sensing* 12 (10):1576.
- Liu, Y., Y. Li, Z. Li, and F. Han. 2020. The diffusion characteristics of an outbreak of 2019 novel coronavirus diseases (COVID-19) in Guangdong province. *Tropical Geography* 40 (3):367–374.
- Liu, Z., Y. Ye, H. Zhang, X. Guohong, J. Yang, and J. Wang. 2020. Analysis of the spatio-temporal characteristics and transmission path of COVID-19 cluster cases in Zhuhai. *Tropical Geography* XX (XX):XXX–XXX.
- Luo, W., M. Majumder, D. Liu, C. Poirier, K. Mandl, M. Lipsitch, and M. Santillana. 2020. The role of absolute humidity on transmission rates of the COVID-19 outbreak. medRxiv. <https://doi.org/10.1101/2020.02.12.20022467>.
- Naidoo, Y. and G. Maree. 2020. Gauteng going dark. <https://www.gcro.ac.za/outputs/map-of-the-month/detail/gauteng-going-dark>. Accessed 12 August 2020.
- Nakada, L. Y. K. and R. C. Urban. 2020. COVID-19 pandemic: Impacts on the air quality during the partial lockdown in São Paulo state, Brazil. *Science of the Total Environment* 730:139087. [doi:10.1016/j.scitotenv.2020.139087](https://doi.org/10.1016/j.scitotenv.2020.139087).
- NASA Earth Observatory. 2020a. Nighttime images capture change in China. <https://earthobservatory.nasa.gov/images/146481/nighttime-images-capture-change-in-china>. Accessed 10 August 2020.
- NASA Earth Observatory. 2020b. Airborne nitrogen dioxide plummets over China. <https://earthobservatory.nasa.gov/images/146362/airborne-nitrogen-dioxide-plummets-over-china>. Accessed 1 October 2020.
- Oliveiros, B., L. Caramelo, N. C. Ferreira, and F. Caramelo. 2020. Role of temperature and humidity in the modulation of the doubling time of COVID-19 cases. medRxiv. <https://doi.org/10.1101/2020.03.05.20031872>.
- Pervaiz, S., K. Javid, F. Z. Khan, Y. Zahid, and M. A. N. Akram. 2020. Preliminary assessment of air during COVID-19 lockdown: An unintended benefit to environment. *Environment and Natural Resources Journal* 18 (4):363–375.
- Román, M. O., Z. Wang, R. Shrestha, T. Yao, and V. Kalb. 2019. *Black Marble User Guide Version 1.0*. Washington, D.C.: NASA.
- Román, M. O., Z. Wang, Q. Sun, V. Kalb, S. D. Miller, A. Molthan, L. Schultz, J. Bell, E. C. Stokes, and B. Pandey. 2018. NASA's Black Marble nighttime lights product suite. *Remote Sensing of Environment* 210:113–143.
- Sajadi, M. M., P. Habibzadeh, A. Vintzileos, S. Shokouhi, F. Miralles-Wilhelm, and A. Amoroso. 2020. Temperature, humidity, and latitude analysis to predict potential spread and seasonality for COVID-19. *JAMA Network Open*. [doi:10.2139/ssrn.3550308](https://doi.org/10.2139/ssrn.3550308).
- Shi, K., B. Yu, Y. Huang, Y. Hu, B. Yin, Z. Chen, L. Chen, and J. Wu. 2014. Evaluating the ability of NPP-VIIRS nighttime light data to estimate the gross domestic product and the electric power consumption of China at multiple scales: A comparison with DMSP-OLS data. *Remote Sensing* 6 (2):1705–1724.
- SRON. 2020. Sentinel-5 Precursor/TROPOMI. <https://www.sron.nl/missions-earth/sentinel-5p-tropomi>. Accessed 29 September 2020.
- Stratoulas, D. and N. Nuthammachot. 2020. Air quality development during the COVID-19 pandemic over a medium-sized urban area in Thailand. *Science of the Total Environment* 746:141320. [doi:10.1016/j.scitotenv.2020.141320](https://doi.org/10.1016/j.scitotenv.2020.141320).
- Tao, J. H., F. M., J. B. Gu, and L. F. Chen. 2020. Satellite observations of the return-to-work over China during the period of COVID-19. *Journal of Remote Sensing* 24 (7):824–836.
- Tomar, A. and N. Gupta. 2020. Prediction for the spread of COVID-19 in India and effectiveness of preventive measures. *Science of the Total Environment* 728:138762. [doi:10.1016/j.scitotenv.2020.138762](https://doi.org/10.1016/j.scitotenv.2020.138762).
- Wang, X., C. Liao, Z. Li, H. Hu, X. Cheng, Q. Li, and J. Lu. 2020. Preliminary analysis on the early epidemic and spatiotemporal distribution of new coronavirus pneumonia in Guangdong Province. *Journal of Tropical Medicine* 20 (4):427–430.
- Wuhan Bureau of Statistics. 2020. Main national economic indexes of Wuhan. <http://tjj.wuhan.gov.cn>. Accessed 10 August 2020.
- Wuhan Statistical Yearbook. 2018. Wuhan, Hubei, China: Hubei Provincial People's Government.
- Xinhuanet. 2020. Central enterprises press the “fast forward” button to resume work and production in Wuhan. [http://www.xinhuanet.com/politics/2020-04/15/c\\_1125856258.htm](http://www.xinhuanet.com/politics/2020-04/15/c_1125856258.htm). Accessed 18 October 2020.
- YangFan. 2015. *The Removal Efficiency and Mechanism of Rainfall to Gaseous Particles and Pollutants*. NanChang: NanChang University.
- Zhou, T., Q. Liu, Z. Yang, J. Liao, K. Yang, W. Bai, X. Lu, and W. Zhang. 2020. Preliminary prediction of the basic reproduction number of the Wuhan novel coronavirus 2019-nCoV. *Journal of Evidence-Based Medicine* 13 (1):3–7.
- Zhou, W., D. Ming, X. Lv, K. Zhou, H. Bao, and Z. Hong. 2020. SO-CNN based urban functional zone fine division with VHR remote sensing image. *Remote Sensing of Environment* 236:111458. [doi:10.1016/j.rse.2019.111458](https://doi.org/10.1016/j.rse.2019.111458).

# Progressive TIN Densification with Connection Analysis for Urban Lidar Data

Tao Wang, Lianbin Deng, Yuhong Li, and Hao Peng

## Abstract

Urban lidar data are advantageous for capturing the terrain surface of built-up areas, which can be directly used to provide digital surface models. Cloud points are classified into ground points to obtain digital terrain models. This study proposes a method to improve the progressive triangulated irregular network (TIN) densification method using a TIN connection analysis algorithm, namely, connection analysis via slope analysis. The proposed method comprises five steps: selection of seed points, connection and slope analysis, increasing the seed points, construction of the TIN model of the seed points, and an iterative construction of the final TIN. Seven data sets from the International Society for Photogrammetry and Remote Sensing Working Group are used to test whether the proposed method can preserve discontinuities of landscapes and reduce omission and total errors by an average of 9% and 5%, respectively; achieving such results can reduce the amount of workload required for result modification during posttreatment, thus decreasing costs.

## Introduction

With ongoing urbanization, the urban–rural fringe has gradually become built-up areas, thus affecting the quality of urban life and sustainable development (Ding *et al.* 2016). In developing countries, the problems are severe (Shao *et al.* 2020) and may lead to new challenges to urban development.

For example, if the proportion of urban buildings and roads is too large, it may lead to the decrease in permeable surfaces, such as vegetation. Moreover, the unreasonable distribution of impervious surfaces increases urban surface run-off, leading to waterlogging (Shao *et al.* 2019); the reduction of vegetation also results in the decrease in urban above-ground biomass (Zhang and Shao 2020).

Airborne light detection and ranging (lidar) has become increasingly popular for creating digital terrain models. With lidar data, cultivated land is easily distinguished from buildings (Shao *et al.* 2020). Lidar can measure the distance between the sensor and a target. Airborne and satellite remote sensing are precise and useful (Shao *et al.* 2020), but substantial work is required for automatic extraction from airborne lidar data.

Sithole and Vosselman (2004) compared different filter methods, concluding that filters that incorporate a surface concept perform better than others; however, no good segmentation-based filters are available at present. Four algorithms, i.e., weighted linear least squares, multi-scale curvature

classification, progressive morphological filter, and progressive triangulated irregular network (TIN) were compared for filtering in a forest environment (Silva *et al.* 2018). Chen *et al.* (2017) classified existing methods into six categories: surface-based adjustment, morphology-based filtering, TIN-based refinement, segmentation and classification, statistical analysis, and multi-scale comparison.

Digital elevation model (DEM) extraction algorithms use several methods to judge if a point is a ground point (Vosselman and Klein 2010). Lidar data are three-dimensional points. In remote sensing, images are usually processed in two dimensions. Thus, if lidar data are converted to an image format, many image processing methods can be used to process point cloud data. However, the precision is changed after conversion. (Shan and Charles 2009; Markus and Hanspeter 2007).

Filtering algorithms can be divided into four categories: morphological filtering, progressive densification, interpolation, and segmentation algorithms.

Morphological filtering algorithms use a morphological method to process the images converted from lidar data (Broelli *et al.* 2003). These algorithms mostly detect height differences, whereas surface-based filters also consider surface trends (Chen *et al.* 2007). Therefore, surface-based filters can obtain more reliable outcomes than morphological ones. On the one hand, morphological algorithms remove the object points through slope analysis. On the other hand, features on flat areas must be maintained. The simple morphological filter algorithm uses increasing window sizes to remove the object points with a slope threshold and fills the empty cell (Thomas *et al.* 2013). Hui *et al.* (2016) improved the morphological method by using multi-level Kriging interpolation. Liu and Lim (2018) used a voxel-based multi-scale morphological filtering method to extract DEMs under forest areas. Li *et al.* (2017) made a geodesic transformation of mathematical morphology. Bigdeli *et al.* (2018) included two main sections, i.e., iterative geodesic morphology and scan labeling. Ozcan and Unsalan (2016) proposed a novel filter based on two-dimensional empirical mode decomposition. Wang *et al.* (2018) created a terrain relief index to tune the slope-related parameters of ground filtering methods.

Progressive densification constructs terrain TIN models by detecting ground points increasingly. Axelsson (2000) divided data into grid cells. The point with the lowest height in each cell is selected as the seed point. Then, these points are triangulated to construct the initial TIN model. If a point is located in a triangle of the TIN model, then it is added to the TIN model. Zhang and Lin (2013) improved the above model using the segmentation method, and Zhao *et al.* (2016) improved this method using a morphological algorithm. He *et al.* (2018) proposed a method that progressively detects terrain points through energy minimization using a graph cut.

Photogrammetric Engineering & Remote Sensing  
Vol. 87, No. 3, March 2021, pp. 207–215.  
0099-1112/21/207–215

© 2021 American Society for Photogrammetry  
and Remote Sensing  
doi: 10.14358/PERS.87.3.207

Tao Wang and Lianbin Deng are with Zhuhai Dahengqin Technology Development Co., Ltd.

Tao Wang is also with Guangzhou Institute of Geography.

Yuhong Li is with CAUPD Planning & Design Consultants Co., 10 Chegongzhuang West Road, Beijing 100037, China.

Hao Peng is with State Key Laboratory of Information Engineering in Surveying, Mapping and Remote Sensing, Wuhan University, Wuhan 430079, China (pphaopeng@gmail.com).

Dong *et al.* (2018) improved the progressive TIN densification method by considering the density and standard variance of point clouds. Shi *et al.* (2018) proposed a novel parameter-free progressive TIN densification filtering method. Ma *et al.* (2018) combined the full-waveform and progressive TIN densification to extract ground points. Zhang *et al.* (2018) used LAS Ground to extract DEM from the photogrammetric dense matching cloud point. Dong *et al.* (2017) proposed a novel method to filter cloud points from image matching by considering the density of the TIN, the distance threshold, and the angle threshold. Nie *et al.* (2017) improved the classic progressive TIN method by combining the Douglas–Peucker algorithm and changing iterative judgment criteria.

Interpolation algorithms use an interpolated DEM to calculate residuals from lidar data to the DEM (Kraus and Pfeifer 1998). If lidar data are above the interpolated DEM, they have less weight on the shape of the DEM shape in the next interpolation (Pfeifer *et al.* 2001). A multi-resolution hierarchical classification algorithm interpolates a raster surface with different resolutions by using the thin plate spline (TPS) method and calculates the residuals of the point between neighbor cells; if four residuals are smaller than the parameters, then the point is regarded as a ground point, and this iteration is repeated with different resolutions and residuals (Chuanfa *et al.* 2013). Adaptive surface filters use an adaptive threshold by calculating bending energy and handle noise with regularization (Han *et al.* 2014). Gomroki *et al.* (2017) proposed an intelligent interpolation method to filter lidar data under forest areas. Qin *et al.* (2017) filtered urban areas with region growing on the basis of moving-window weighted iterative least-square fitting. Hui *et al.* (2019) proposed a parameter-free filtering method using expectation-maximization. Chen *et al.* (2017) improved the TPS-based interpolation filter on the basis of finite difference TPS computation to create a fast and robust filter.

Segmentation methods, such as region-growing techniques and the normal vector, can be used to divide different classes in the object space. Usually, the planar surface can be detected (Shan and Charles 2009). A multi-directional ground filtering algorithm uses slope and elevation difference to distinguish ground from nonground points in two directions (Xueliang *et al.* 2009). Ozcan *et al.* (2018) extracted ground points by using probabilistic voting and segmentation. Yang

*et al.* (2016) combined segment-based filtering and multi-scale morphological filtering to extract ground points. Ural and Shan (2016) used min-cut based filtering to extract ground points. The method proposed by Kumar *et al.* (2018) has two stages: first, nonground objects are removed from pre-processed airborne laser scanning data based on geometrical reasoning; second, ground points that are falsely recognized as nonground in the first stage are retrieved using geometrical similarity of ground points in their surroundings.

To improve the filtering method, this study proposes a new surface-based method that can remove nonground features and maintain ground characteristics in steep mountains and areas with cities and forests. The important contribution of this study is the use of TIN model connection analysis to detect additional ground points, which can be used as seed points; therefore, omission errors during processing can be reduced remarkably. To test the capacity of the proposed method, it is compared with classic progressive triangulated irregular network densification (PTD) methods, using data provided by the International Society for Photogrammetry and Remote Sensing (ISPRS) Working Group. The dataset includes seven urban and rural sites with different scenes.

### Algorithm

The PTD algorithm is improved by connection analysis. Our method is described as follows (Figure 1):

1. Determination of outliers and removal of repeated points. Outliers are points that have a long distance to the DEM. If these points exist, then the lowest point from the terrain cannot be selected from the entire scene; these points are called outliers. A TIN model of all points is constructed; if the triangles around the point have high normal values and the points around it have high differences, then this point is removed from the list. Many points have the same coordinates; such points are removed.
2. Selection of seed points and construction of the TIN model of the seed points. After calculating the area of the point cloud, the maximum and minimum values of the width, length, and height are obtained. The data set is divided into small blocks in accordance with width and length.

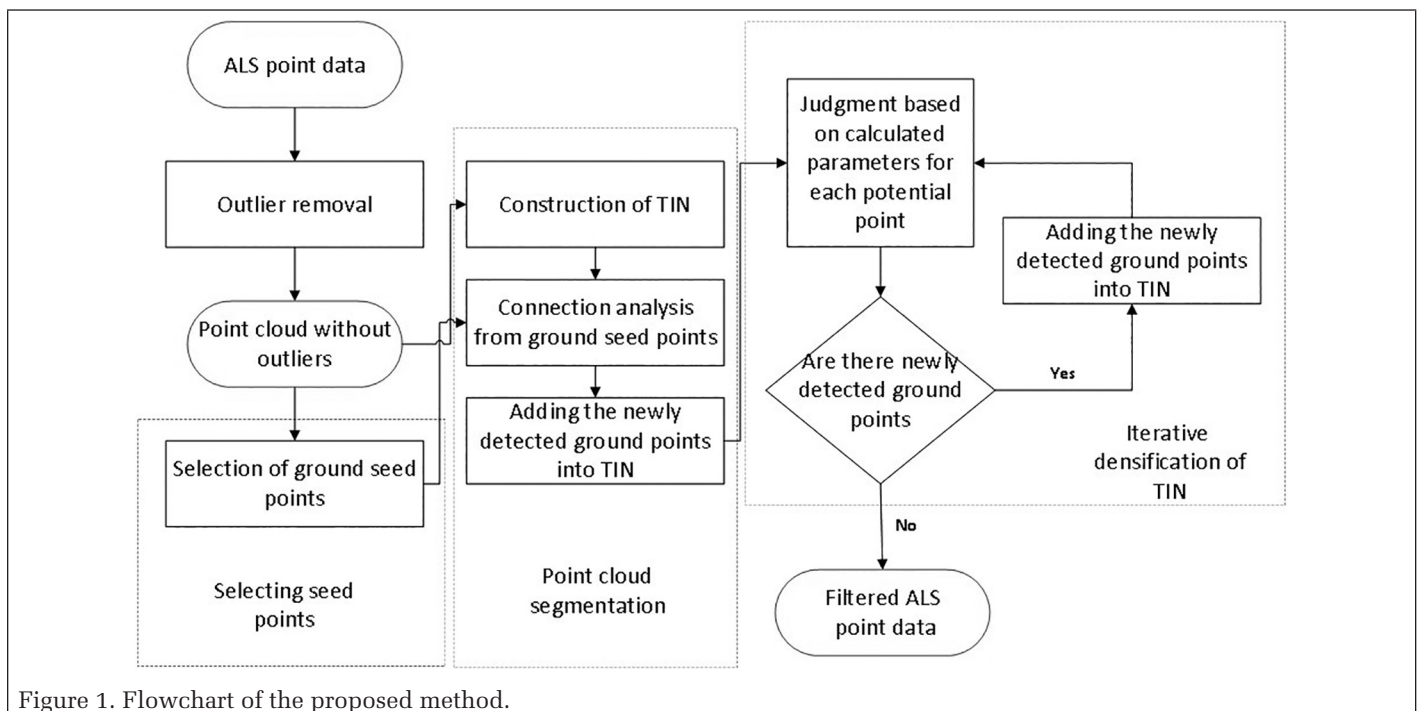


Figure 1. Flowchart of the proposed method.

In each cell, the lowest point is chosen as a seed point. After selecting seed points, the TIN model is created from all the points, the triangle that contains each seed point is identified, and the triangles around this triangle are checked. If their normal values and height differences are smaller than the thresholds, then these triangles are added to the checklist. Connection analysis is used to obtain additional ground points using the above method. Afterward, the points in these triangles are used as initial points; then, the TIN of these points is constructed.

3. Selection of parameters. Three important parameters must be set in the proposed method.
  - a. Grid cell length,  $m$ : If the grid cell length is set to a value smaller than the maximum building size, then the seed point may be selected from the roof of the building.
  - b. Maximum angle,  $\theta$ : A point is connected to the triangle vertexes; three lines exist. Then, the angles between these lines and the triangle plane are calculated, and the maximum angle in the angles ( $\alpha, \beta, \gamma$ ) is  $\theta$ , as shown in Figure 2. If a point is not in the TIN model, then its angle is larger than the maximum angle, and it is considered an object point and then considered a ground point.
  - c. Maximum distance,  $d$ : If a point is not in the TIN model, then the distance  $l$  to the triangle plane is calculated. If the distance  $l$  is larger than  $d$  (as shown in Figure 1), then it is considered an object point; otherwise, it is considered a ground point.

In conclusion, these three parameters must be preset for the PTD herein.

4. Iterative densification of the TIN. In each iteration, the points are judged one by one using the parameters. If the distance from the point to the triangle plane is smaller than  $d$  and the maximum angle is smaller than  $\theta$ , then the point is considered a ground point; otherwise, the point is considered an object point. Iteration is repeated until no point joins the part of the ground points.

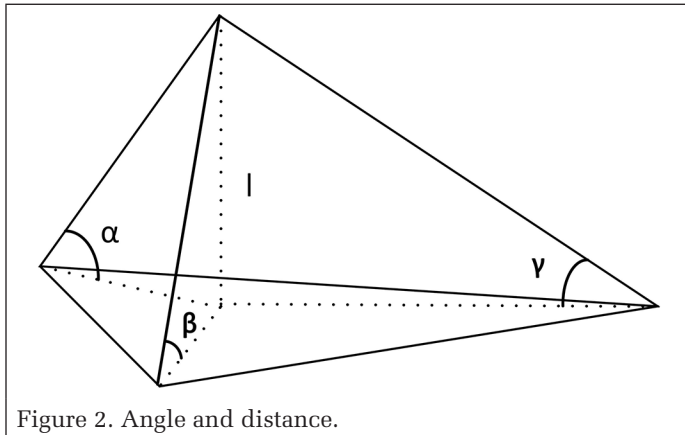


Figure 2. Angle and distance.

## Experiment and Results

A program for processing airborne laser scanning cloud point is developed in C++ using Visual Studio 2010 on Windows 8. Cloud points are triangulated using Triangle, an open-source Delaunay triangulator (Shewchuk 2005; Isenburg *et al.* 2006).

### Testing Data

ISPRS Commission III provides eight free data sets to test filtering algorithms. These data are scanned using an Optech ALTM scanner. The eight data sets are as follows: CSite1, CSite2, CSite3, CSite4, FSite5, FSite6, FSite7, and FSite8. Fifteen reference samples from the eight data sets are manually classified for testing. These data sets and reference samples are used to test the proposed method and the classic algorithm.

CSite1–4 contain urban regions, whereas FSite1–4 consist of forest regions. These data have different resolutions. CSite1 is characterized by a mixture of vegetation and buildings on hillsides, steep slopes, and data gaps. CSite2 comprises bridges, large buildings, and irregularly shaped buildings. CSite3 is characterized by densely packed buildings with vegetation between them, buildings with eccentric roofs, and open spaces with a mixture of low and high features. CSite4 is composed of railway stations with trains and data gaps. FSite5 is a rural scene where steep slopes with vegetation and vegetation on riverbanks are found. FSite6 is composed of large buildings and roads with embankments. FSite7 consists of bridges and road embankments.

### Specification of Parameters

Compared with the classic method, the proposed method requires two additional parameters. In this study, the three shared parameters of the filters have the same value. All the parameters are determined by TerraScan software experience. The parameters used for sites 1–7 are set in Table 1.

Table 1. Parameters in the two algorithms for each scene.

Scene	Parameters		Classic PTD Method			Our Method	
	Points	Outlier	$m(m)$	$\theta(^{\circ})$	$d(m)$	$d(m)$	$\theta(^{\circ})$
CSite1	2 732 814	2362	60	6	1.4	0.2	45
CSite2	973 598	1360	60	6	1.4	0.2	45
CSite3	754 054	391	60	6	1.4	0.2	45
CSite4	1 036 114	574	60	6	1.4	0.2	45
FSite5	1 256 894	96	60	6	1.4	0.2	45
FSite6	1 101 952	11 510	60	6	1.4	0.2	45
FSite7	786 134	9208	60	6	1.4	0.2	45

## Results

CSite2 and FSite7 are selected to show the effect of processing. The reference data of sample11, sample23, sample42, and sample53 are compared to show the effect of processing. CSite2 is in an urban area, including large buildings, irregularly shaped buildings, bridges, and a small tunnel, along with some data gaps. The original data have 973 598 points, of which 1360 are detected as noise points and removed from the process. The remaining points and the resulting digital surface models are shown in Figures 3a and 3b. In the process, 54 seed points are selected for the two methods (Figure 3c). The classic algorithm obtains 96 061 ground points (Figure 3e). A total of 133 960 ground points are identified by the connection analysis method (Figure 3d). Overall, 152 059 ground points are identified (Figure 3f). The differences between Figures 1e and 1f are shown in Figure 1g. By contrast, the proposed method can preserve ground points in the rectangle area (Figure 3f).

FSite5 is a forested area, including small buildings, a bridge, and steep slopes, as well as some data gaps. The original data contain 314 160 points, of which 96 are detected as noise points and removed from the process. The remaining data and the TIN are shown in Figures 3a and 3b. During the process, 182 814 points are selected as seed points for the two methods. A total of 246 631 points are detected as ground points for the classic filter (Figure 4e). A total of 212 483 ground points are identified by the connection analysis method (Figure 4d). Overall, 269 632 points are identified as ground points (Figure 4f). In contrast to the PTD method, the proposed method preserves steep slopes, as shown in Figure 4g.

Furthermore, in some situations (e.g., buildings and vegetation on a steep slope (Figure 5), big houses and complex buildings (Figure 6), train stations with trains (Figure 7), steep slopes (Figure 8)), the proposed algorithm can identify more

ground points from the results of reference samples in comparison with the classic method.

However, the proposed algorithm cannot detect nonground points in the following cases: when some objects, such as bridges (Figure 3), connect to the terrain surface; small objects are considerably low on the ground (Figure 8).

### Comparison

The two filters are compared by using the images of results and table of accuracies. The result shows that the classic algorithm and the proposed algorithm work well in different scenes, such as big houses, complex buildings, and mixtures of buildings and vegetation on flat ground, as well as data gaps. If a mountain slope is steep or buildings and vegetation stay together, then the classic algorithm removes ground points. By contrast, the proposed method can identify ground points successfully where the classic method fails. However, compared with the classic method, the proposed algorithm cannot detect object points connected to the ground through a smooth connection, such as bridges, as represented in the elliptical area (Figures 3e–3g). The classic method can detect ground points under this condition successfully.

In addition, the two filters are compared in accordance with the proposals in the ISPRS lidar filter comparison. Three types of errors are detected. Type I errors occur when ground points are classified as object points; type II errors happen when object points are classified as ground points; total error is the rate

of misclassified points. These three types of errors resulting in the two filters for the 15 references are listed in Table 2.

The results in Table 2 show that type I and total errors are lower in the proposed algorithm than those in the classic algorithm. Except for samp11, samp22, and samp24, 12 samples have lower type I errors in the proposed algorithm compared with those of the classic algorithm in the 15 samples. In addition, except for samp21, samp12, samp24, and samp51, the total errors of our method are lower than those of the classic method in 11 samples (Figures 9a and 9c). However, the classic algorithm can avoid type II errors. The result in Table 2 shows that type II errors in our algorithm is higher than that in the classic method in 13 cases (Figure 9b). After automatic processing, it still needs substantial manual operation to repair all the errors. Type I and total errors are lower in the proposed algorithm; thus, less postprocessing is required.

One disadvantage of the proposed method is that it needs more computation time compared with the classic method because connection analysis is time consuming. Nevertheless, this research focuses on accuracy rather than efficiency; if parallel computing is used, then this issue can be easily resolved.

The proposed method has two advantages. First, TIN segmentation is adopted in the process of filtering. If the natural terrain is smooth, then the proposed method can expand the seed points with connection analysis from the TIN model of the cloud points. Therefore, it can extract additional ground points. Second, the classic PTD method and connection analysis are combined. The PTD algorithm is widely used in

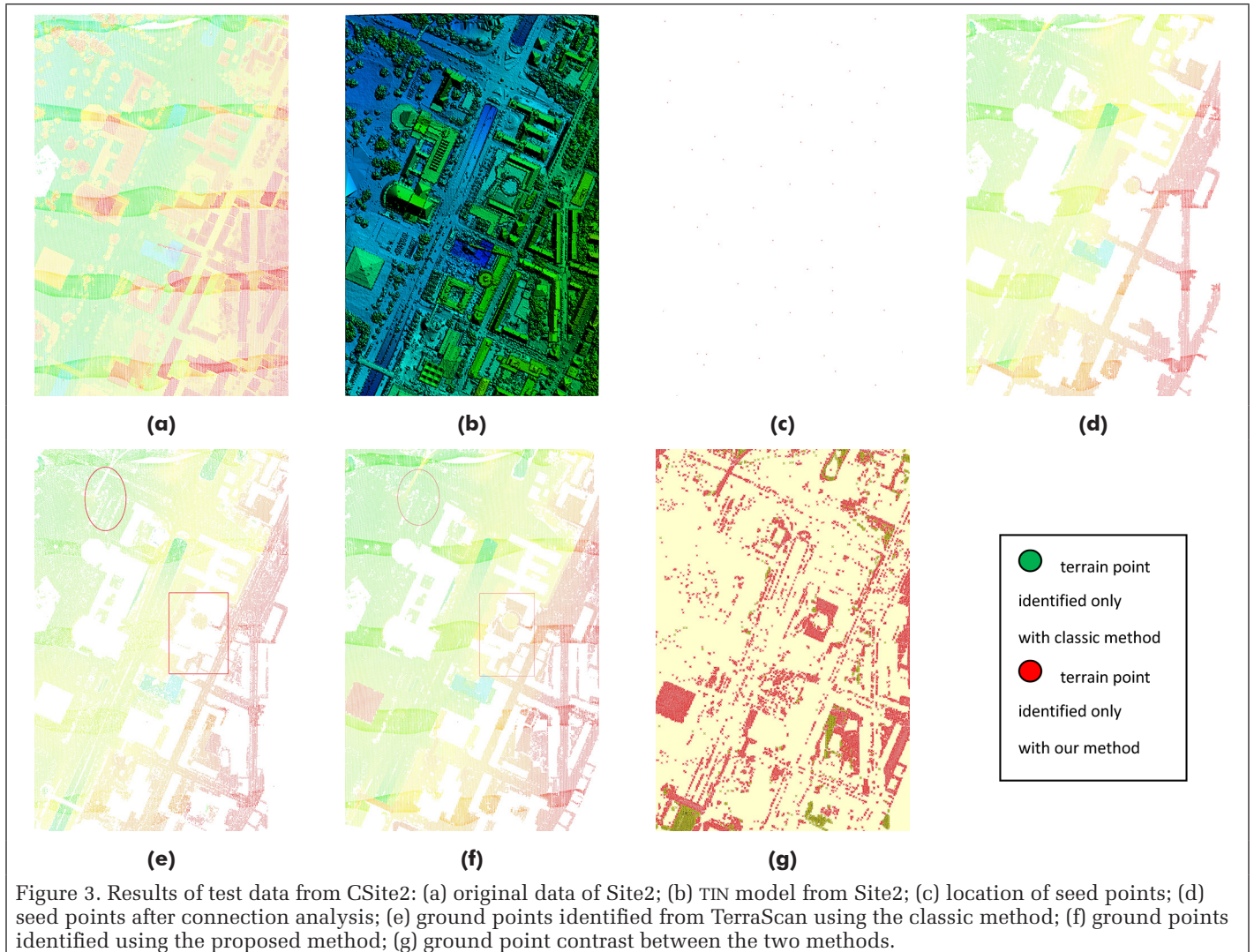


Figure 3. Results of test data from CSite2: (a) original data of Site2; (b) TIN model from Site2; (c) location of seed points; (d) seed points after connection analysis; (e) ground points identified from TerraScan using the classic method; (f) ground points identified using the proposed method; (g) ground point contrast between the two methods.

Table 2. Three kinds of errors in the classic and the proposed methods.

Data No.	Error	Classic (%)	Proposed (%)
Sample11	I	12.5	13.0
	II	18.2	16.9
	T	14.9	14.6
Sample12	I	3.4	2.6
	II	6.8	5
	T	5.1	3.8
Sample21	I	2.5	1.9
	II	1.0	30.3
	T	2.2	8.2
Sample22	I	7.9	8.4
	II	0.5	17.9
	T	5.6	11.3
Sample23	I	20.5	4.6
	II	0.8	5.8
	T	11.2	5.4
Sample24	I	7.5	7.9
	II	1.9	11.8
	T	5.9	9.0
Sample31	I	6.5	0.6
	II	0.2	5.2
	T	3.6	2.7
Sample41	I	45.1	4.0
	II	0.3	15.0
	T	22.7	9.5
Sample42	I	4.1	2.5
	II	0.8	0.9
	T	1.3	1.4
Sample51	I	1.4	0.2
	II	2.2	14.2
	T	1.5	3.2
Sample52	I	23.5	4.7
	II	2	15.0
	T	21.2	5.8
Sample53	I	36.0	5.9
	II	0.3	18.5
	T	34.6	6.4
Sample54	I	9.0	2.4
	II	1.4	5.2
	T	4.9	3.9
Samp61	I	11.1	1.1
	II	0.2	36.2
	T	10.7	2.3
Sample71	I	15.1	0.4
	II	0.7	66.1
	T	13.4	7.8
Minimum	I	1.4	0.2
	II	0.2	0.9
	T	1.3	1.4
Maximum	I	45.1	13
	II	12.5	66.1
	T	34.6	14.6
Average	I	13.7	4
	II	2.5	17.6
	T	10.5	6.4

commercial software and has been proven to be a good filter. The proposed method can obtain good results by combining the PTD method with connection analysis. However, the connection analysis of the TIN model cannot remove the object points attached to the terrain. Thus, the proposed method increases type II errors.

### Conclusion

The extraction of building, road, and other terrain information is a requirement of urban sustainable development and is considered a technical means to monitor urban changes (Shao

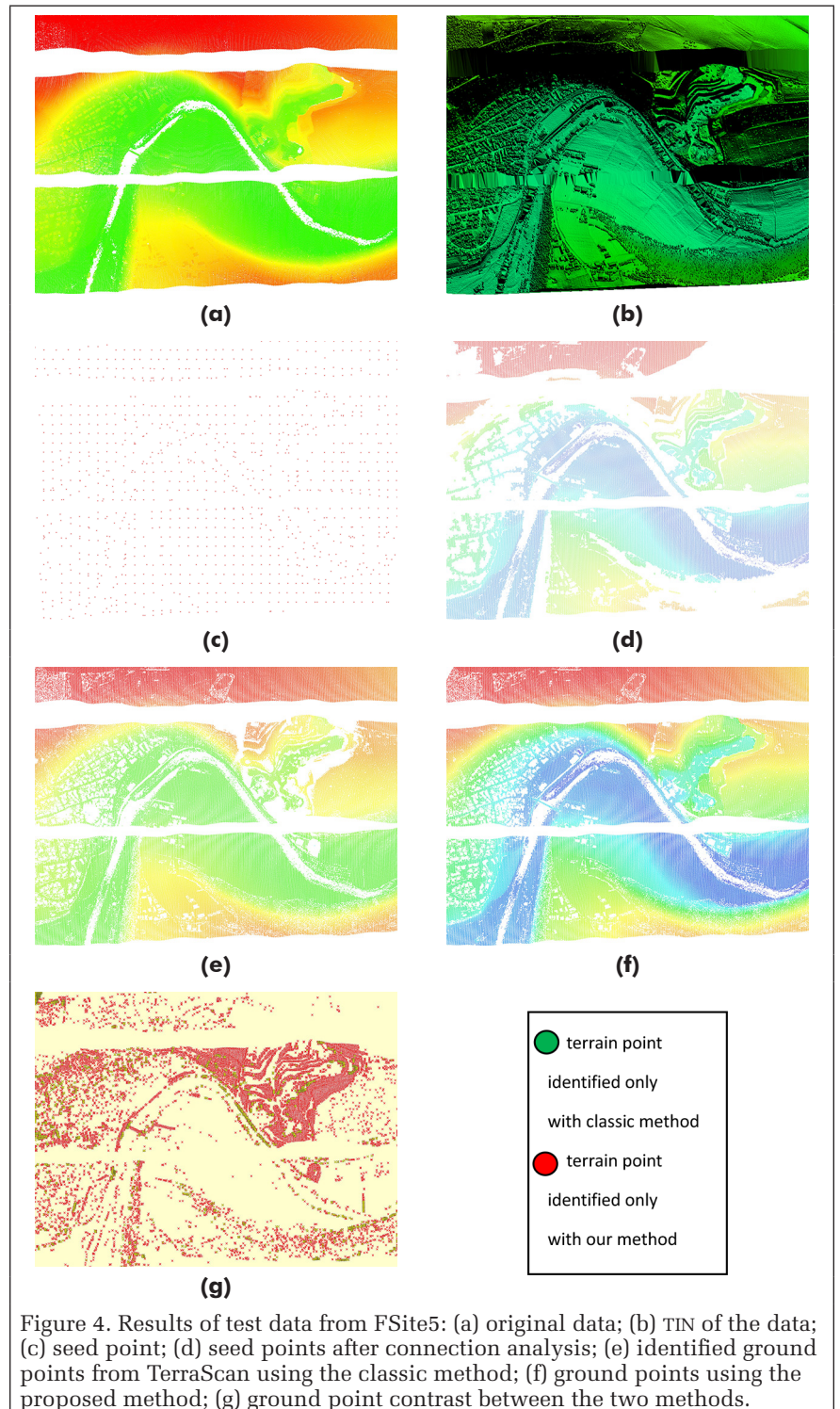


Figure 4. Results of test data from FSite5: (a) original data; (b) TIN of the data; (c) seed point; (d) seed points after connection analysis; (e) identified ground points from TerraScan using the classic method; (f) ground points using the proposed method; (g) ground point contrast between the two methods.

et al. 2020; Zhang 2019). Urban lidar data have the advantages to capture the terrain surfaces of built-up areas directly.

Obtaining ground points is an important step in point cloud processing, and many filters can be used to perform this task. PTD has been used in TerraScan commercial software successfully. It removes ground points in steep terrain places. This method is improved by combining it with connection analysis to expand the seed points based on the smooth terrain. According to the result, the proposed method is useful to obtain additional ground seed points.

Seven ISPRS data sets are used in the proposed method; 15 reference samples cut from them are compared for the accuracies. The comparison shows that the two methods are useful to the eight data sets. However, the proposed method is better than the classic PTD method in terms of maintaining ground characteristics. In particular, despite having higher type II errors, the proposed method may have lower type I and total errors than the classic algorithm; thus, the costs of manual operation for repair may be reduced. Future work will improve connection analysis with artificial intelligence and fuse full waveform data to classify point clouds.

### Acknowledgments

This work was funded by the National Key Research and Development Program of China (2017YFB0503801), the forestry science and technology innovation of Guangdong province, China (grant No.2020KJ CX003); Natural Science Foundation of Guangdong province (2015A030313882), the Key Research and Development Program of Yunnan province in China (2018IB023), the Research Project from the Ministry of Natural Resources of China under Grant 4201-240100123.

### References

- Axelsson, P. 2000. DEM generation from laser scanner data using adaptive TIN models. *ISPRS—International Archives of the Photogrammetry, Remote Sensing and Spatial Information Sciences* 33:111–118.
- Bigdeli, B., H. Amirkolaee and P. Pahlavani. 2018. DTM extraction under forest canopy using LiDAR data and a modified invasive weed optimization algorithm. *Remote Sensing of Environment* 216:289–300.

- Broelli, M., M. Cannata and U. Longoni. 2003. Lidar data filtering and DTM interpolation within GRASS. *Transactions in GIS* 8:155–174.
- Chen, C., Y. Li, W. Li and H. Dai. 2013. A multiresolution hierarchical classification algorithm for filtering airborne LiDAR data. *ISPRS Journal of Photogrammetry and Remote Sensing* 82:1–9.
- Chen, C. F., Y. Y. Li, N. Zhao, J. Y. Guo and G. L. Liu. 2017. A fast and robust interpolation filter for airborne LiDAR data. *Measurement* 104:70–77.
- Chen, Q., P. Gong, D. Baldocchi and G. Xie. 2007. Filtering airborne laser scanning data with morphological methods. *Photogrammetric Engineering & Remote Sensing* 73 (2):175–185.

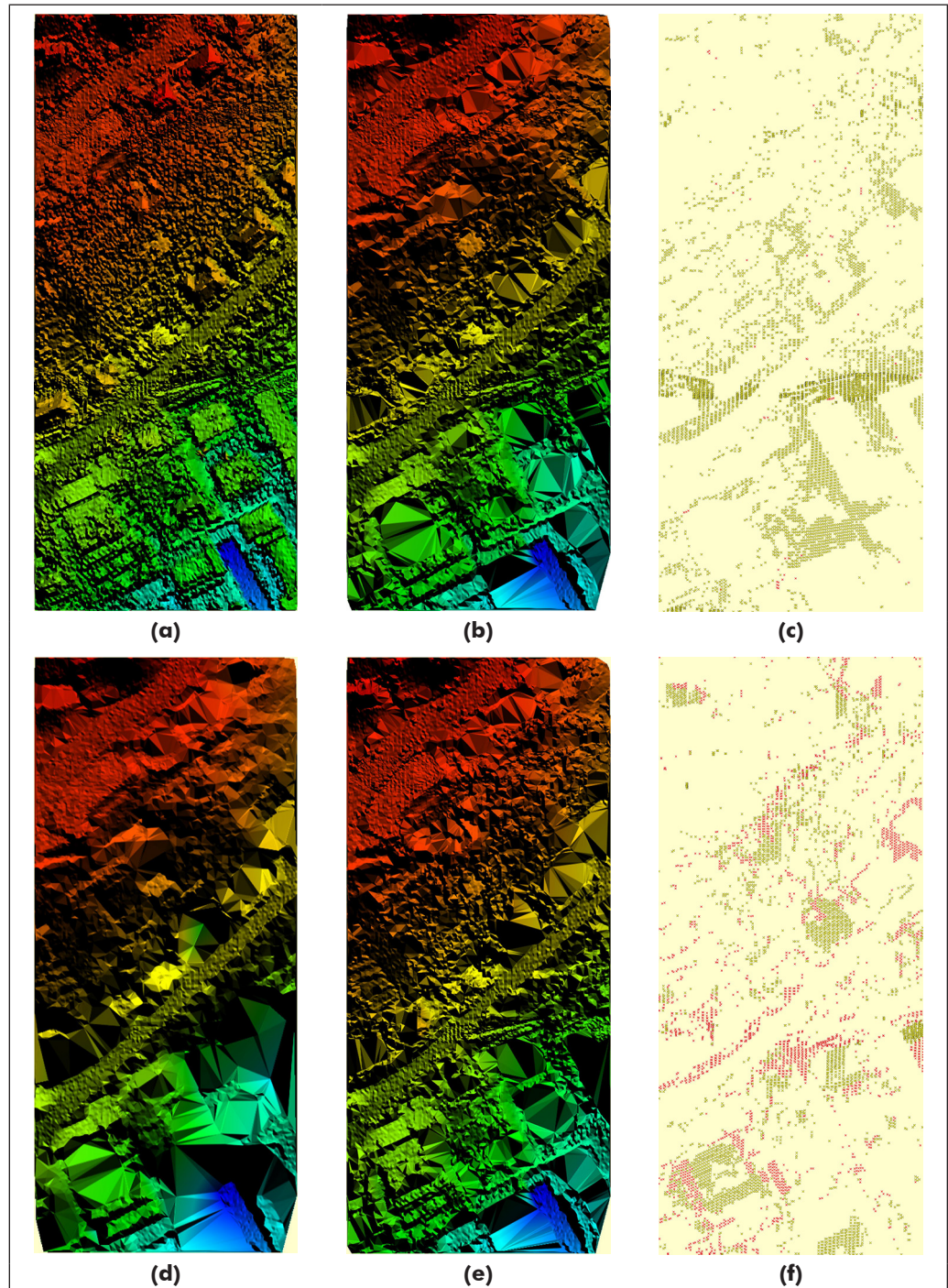
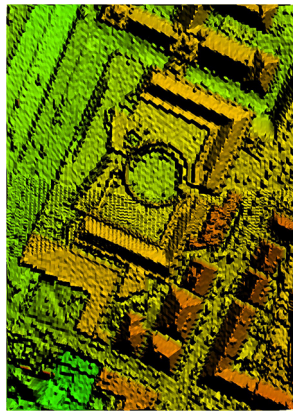
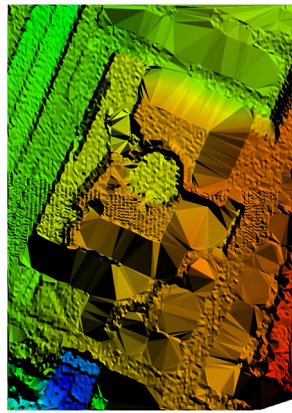


Figure 5. Results of samp11: (a) TIN model of original data; (b) TIN model of ground data of reference data; (c) type I (red points) and II (green points) errors of the classic method; (d) DEM created by TerraScan using the classic method; (e) DEM created using the proposed method; (f) type I (red points) and II (green points) errors of the proposed method.



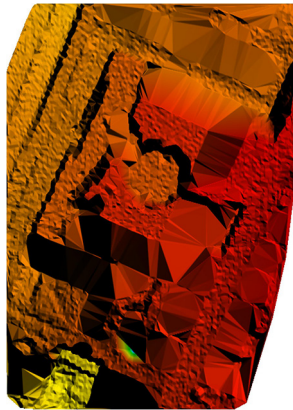
(a)



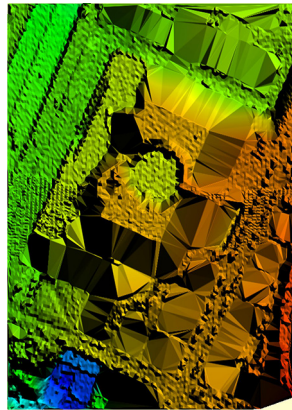
(b)



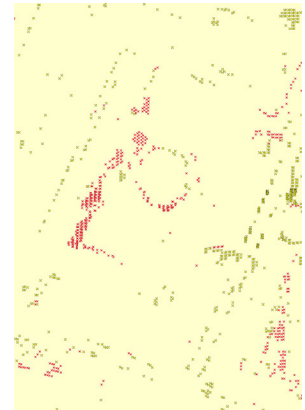
(c)



(d)

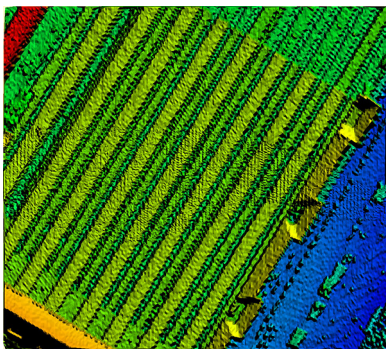


(e)

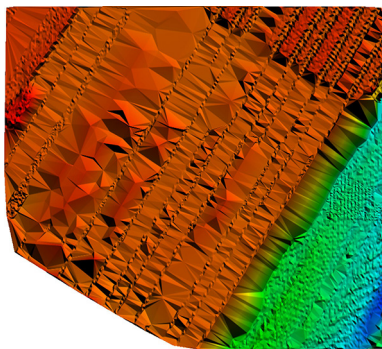


(f)

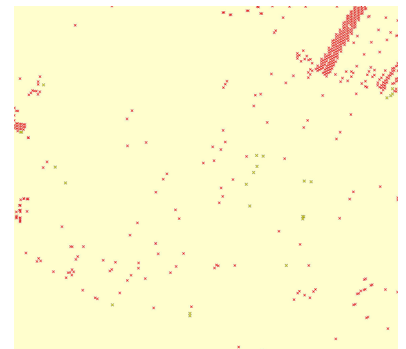
Figure 6. Results of samp23: (a) TIN model of original data; (b) TIN model of ground data of reference data; (c) type I (red points) and II (green points) errors in the classic method; (d) DEM created by TerraScan using the classic method; (e) DEM created using the proposed method; (f) type I (red points) and II (green points) errors in the proposed method.



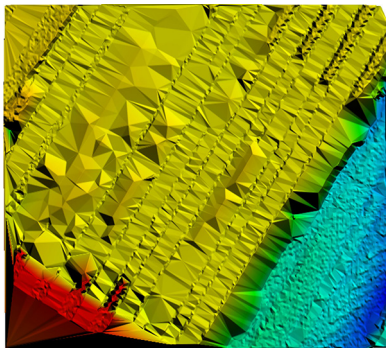
(a)



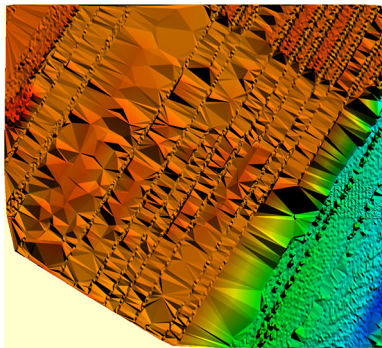
(b)



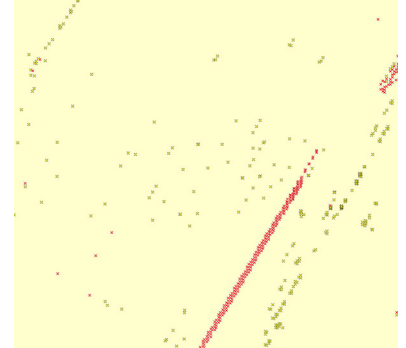
(c)



(d)



(e)



(f)

Figure 7. Results of samp42: (a) TIN model of original data; (b) TIN model of ground point of reference data; (c) type I (red points) and II (green points) errors in the classic method; (d) DEM created by TerraScan using the PTD method; (e) DEM created using the proposed method; (f) type I (red points) and II (green points) errors in the proposed method.

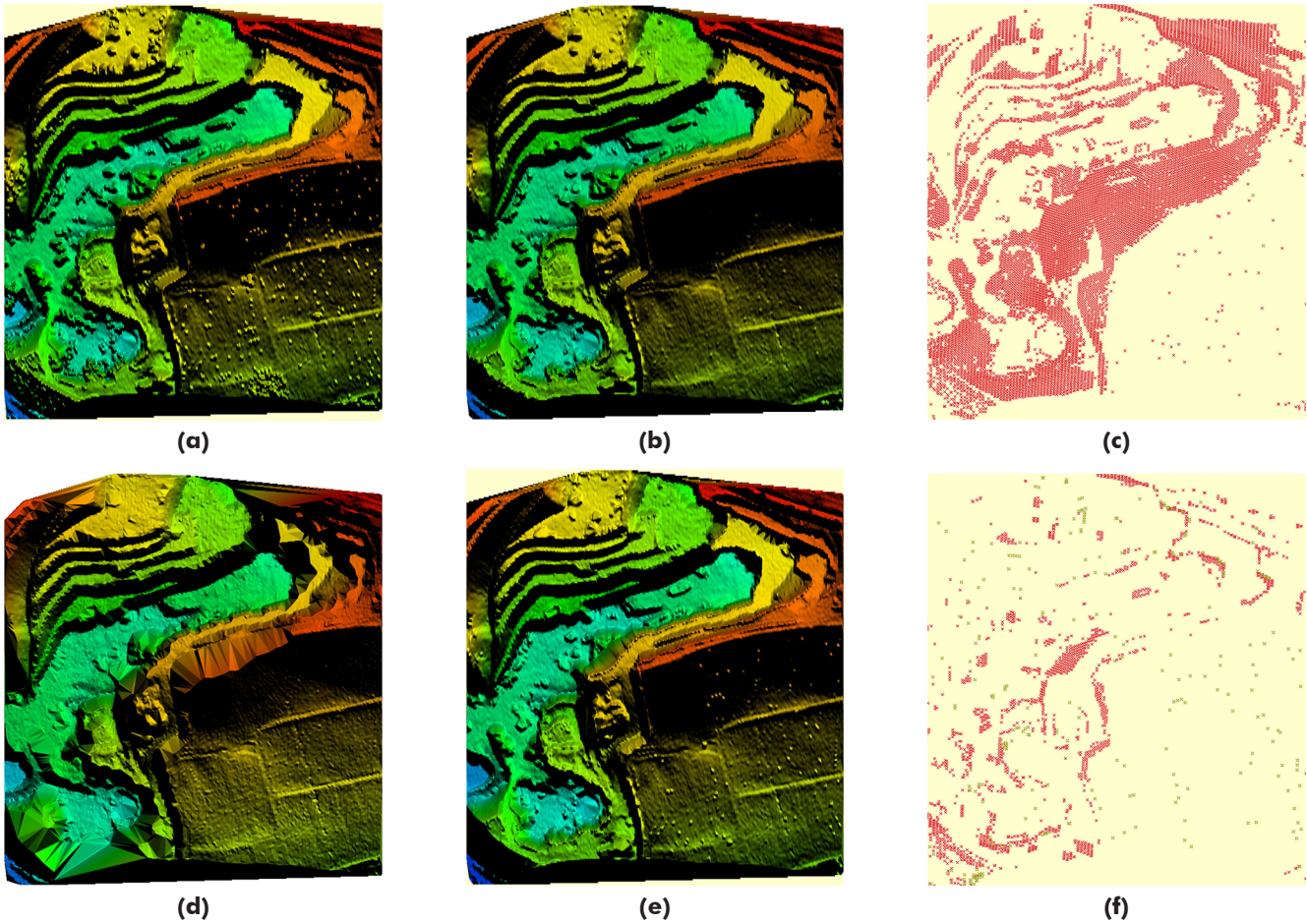


Figure 8. Results of samp53: (a) TIN model of original data; (b) TIN model of the ground points of reference data; (c) type I (red points) and II (green points) errors in the classic method; (d) DEM created by TerraScan using the PTD method; (e) DEM created using the proposed method; (f) type I (red points) and II (green points) errors in the proposed method.

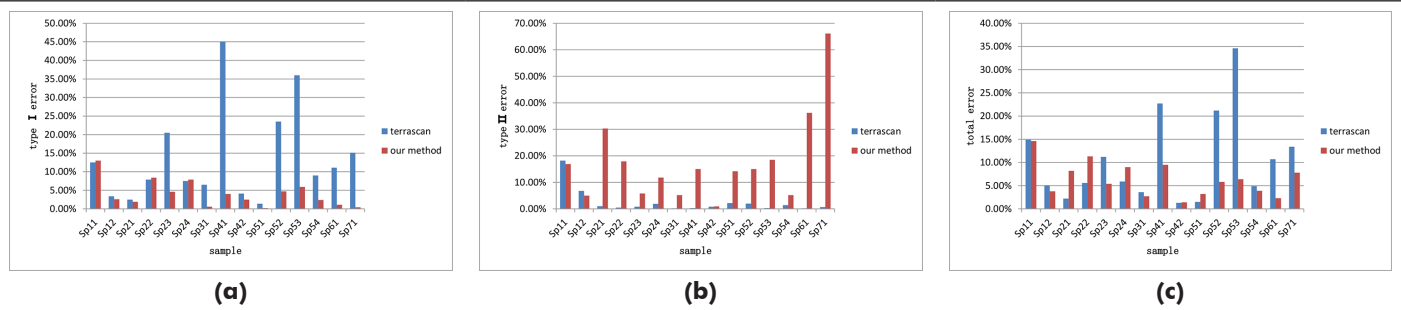


Figure 9. Error comparison between the two algorithms: (a) type I errors; (b) type II errors; (c) total errors. Note: “Sp” denotes “Sample”.

Chen, Z. Y., B. B. Gao and B. Devereux. 2017. State-of-the-art: DTM generation using airborne LiDAR data. *Sensors* 17:150.

Ding, L., Z. Shao, H. Zhang, C. Xu and D. Wu. 2016. A comprehensive evaluation of urban sustainable development in China based on the TOPSIS-entropy method. *Sustainability* 8 (8):746.

Dong, Y. Q., X. M. Cui, L. Zhang and H. Ai. 2018. An improved progressive TIN densification filtering method considering the density and standard variance of point clouds. *ISPRS International Journal of Geo-information* 7:409.

Dong, Y. Q., L. Zhang, X. M. Cui and H. B. Ai. 2017. An automatic filter algorithm for dense image matching point clouds. *ISPRS International Archives of the Photogrammetry, Remote Sensing and Spatial Information Sciences*, XL II-2/W7:703–709.

Gomroki, M., M. Jafari, S. Sadeghian and Z. Azizi. 2017. Application of intelligent interpolation methods for DTM generation of forest areas based on LiDAR data. *PFG-Journal of Photogrammetry Remote Sensing and Geoinformation Science* 85:227–241.

Gross, M. and H. Pfister, eds. 2007. *Point-Based Graphics*. Burlington, Mass.: Morgan Kaufmann.

He, Y., C. Zhang and C. Fraser. 2018. Progressive filtering of airborne LiDAR point clouds using graph cuts. *IEEE Journal of Selected Topics in Applied Earth Observations and Remote Sensing* 11:2933–2944.

Hui, Z., Y. Hu, Y. Z. Yeveyo and X. Yu. 2016. An improved morphological algorithm for filtering airborne LiDAR point cloud based on multi-level Kriging interpolation. *Remote Sensing* 8 (1):35.

- Hui, Z. Y., D. J. Li, S. G. Jin, Y. Y. Ziggah, L. Wang and Y. Hud. 2019. Automatic DTM extraction from airborne LiDAR based on expectation-maximization. *Optics & Laser Technology* 112:43–55.
- Hu, H., Y. Ding, Q. Zhu, B. Wu, H. Lin, Z. Du, Y. Zhang and Y. Zhang. 2014. An adaptive surface filter for airborne laser scanning point clouds by means of regularization and bending energy. *ISPRS Journal of Photogrammetry and Remote Sensing* 92:98–111.
- Kraus, K. and N. Pfeifer. 1998. Determination of terrain models in wooded areas with airborne laser scanner data. *ISPRS Journal of Photogrammetry and Remote Sensing* 53 (4):193–203.
- Kumar, B., M. Yadav, B. Lohani and A. Singh. 2018. A two-stage algorithm for ground filtering of airborne laser scanning data. *International Journal of Remote Sensing* 39:6757–6783.
- Li, Y., B. Yong, P. Van Oosterom, M. Lemmens, H. Wu, L. Ren, M. Zheng and J. Zhou. 2017. Airborne LiDAR data filtering based on geodesic transformations of mathematical morphology. *Remote Sensing* 9:1104.
- Liu, L. and S. Lim. 2018. A voxel-based multiscale morphological airborne lidar filtering algorithm for digital elevation models for forest regions. *Measurement* 123:135–144.
- Ma, H. C., W. W. Zhou and L. Zhang. 2018. DEM refinement by low vegetation removal based on the combination of full waveform data and progressive TIN densification. *ISPRS Journal of Photogrammetry and Remote Sensing* 146:260–271.
- Meng, X., L. Wang, J. L. Silván-Cárdenasa and N. Currita. 2009. A multi-directional ground filtering algorithm for airborne LiDAR. *ISPRS Journal of Photogrammetry and Remote Sensing* 64:117–124.
- Nie, S., C. Wang, P. L. Dong, X. H. Xi, S. Z. Luo and H. M. Qin. 2017. A revised progressive TIN densification for filtering airborne LiDAR data. *Measurement* 104:70–77.
- Ozcan, A. H. and C. Unsalan. 2016. LiDAR data filtering and DTM generation using empirical mode decomposition. *IEEE Journal of Selected Topics in Applied Earth Observations and Remote Sensing* 10:360–371.
- Ozcan, H., C. Unsalan and P. Reinartz. 2018. Ground filtering and DTM generation from DSM data using probabilistic voting and segmentation. *International Journal of Remote Sensing* 39:2860–2883.
- Pfeifer, N., P. Stadler and C. Briese. 2001. Derivation of digital terrain models in the SCOP++ environment. In *Proceedings of OEEPE Workshop on Airborne Laserscanning and Interferometric SAR for Digital Elevation Models*, held in Stockholm, Sweden.
- Pingel, J., C. Keith and A. William. 2013. An improved simple morphological filter for the terrain classification of airborne LiDAR data. *ISPRS Journal of Photogrammetry and Remote Sensing* 77:21–30.
- Qin, L. J., W. Wu, Y. G. Tian and W. Xu. 2017. LiDAR filtering of urban areas with region growing based on moving-window weighted iterative least-squares fitting. *IEEE Geoscience and Remote Sensing Letters* 14:841–845.
- Shan, J. and K. Charles. 2009. *Topographic Laser Ranging and Scanning Principles and Processing*. Boca Raton, Fla.: CPC Press.
- Shao, Z., L. Ding, D. Li, O. Altan, Md. E. Huq and C. Li. 2020a. Exploring the relationship between urbanization and ecological environment using remote sensing images and statistical data: A case study in the Yangtze River Delta, China. *Sustainability* 12:5620. doi: 10.3390/su12145620.
- Shao, Z., H. Fu, D. Li, O. Altan and T. Cheng. 2019. Remote sensing monitoring of multi-scale watersheds impermeability for urban hydrological evaluation. *Remote Sensing of Environment* 232:111338. doi: 10.1016/j.rse.2019.111338.
- Shao, Z., C. Li, D. Li, O. Altan, L. Zhang and L. Ding. 2020b. An accurate matching method for projecting vector data into surveillance video to monitor and protect cultivated land. *ISPRS International Journal of Geo-Information* 9:448. doi: 10.3390/ijgi9070448.
- Shao, Z., N. S. Sumari, A. Portnov, F. Ujoh, W. Musakwa and P. J. Mandela. 2020c. Urban sprawl and its impact on sustainable urban development: A combination of remote sensing and social media data. *Geo-spatial Information Science*. doi: 10.1080/10095020.2020.1787800.
- Shao, Z., W. Wu and S. Guo. 2020d. IHS-GTF: A fusion method for optical and synthetic aperture radar data. *Remote Sensing* 12:2796. doi: 10.3390/rs12172796.
- Shi, X. T., H. C. Ma, Y. W. Chen and L. Zhang. 2018. A parameter-free progressive TIN densification filtering algorithm for lidar point clouds. *International Journal of Remote Sensing* 39:6969–6982.
- Silva, C. A., C. Klaueberg, A. Hentz, A. Corte, U. Ribeiro and V. Liesenberg. 2018. Comparing the performance of ground filtering algorithms for terrain modeling in a forest environment using airborne LiDAR data. *Floresta e Ambiente* 25 (2):e20160150.
- Sithole, G. and G. Vosselman. 2004. Experimental comparison of filter algorithms for bare-Earth extraction from airborne laser scanning point clouds. *ISPRS Journal of Photogrammetry and Remote Sensing* 59 (1):85–101.
- Ural, S. and J. Shan. 2016. A min-cut based filter for airborne LiDAR data. Pages 395–401 in *Proceedings ISPRS—International Archives of the Photogrammetry, Remote Sensing and Spatial Information Sciences* vol. XLI-B3, XXIII ISPRS Congress, held in Prague, Czech Republic, 12–19 July 2016.
- Vosselman, G. and R. Klein. 2010. Visualization and structuring of point clouds. *Airborne and Terrestrial Laser Scanning*:43–79.
- Wan, P., W. M. Zhang, K. Andrew, J. B. Qi and X. L. Jin. 2018. A simple terrain relief index for tuning slope-related parameters of LiDAR ground filtering algorithms. *ISPRS Journal of Photogrammetry and Remote Sensing* 143:181–190.
- Yang, B. S., R. G. Huang, Z. Dong, Y. F. Zang and J. P. Li. 2016. Two-step adaptive extraction method for ground points and breaklines from LiDAR point clouds. *ISPRS Journal of Photogrammetry and Remote Sensing* 119:373–389.
- Zhang, H., X. Ning, Z. Shao and H. Wang. 2019. Spatiotemporal pattern analysis of China's cities based on high-resolution imagery from 2000 to 2015. *ISPRS International Journal of Geo-Information* 8 (5):241.
- Zhang, J. and X. Lin. 2013. Filtering airborne LiDAR data by embedding smoothness constrained segmentation in progressive TIN densification. *ISPRS Journal of Photogrammetry and Remote Sensing* 81:44–59.
- Zhang, Y. and Z. Shao. 2020. Assessing of urban vegetation biomass in combination with LiDAR and high-resolution remote sensing images. *International Journal of Remote Sensing*. doi: 10.1080/01431161.2020.1820618.
- Zhang, Z., M. Gerke, G. Vosselman and M. Y. Yang. 2018. Filtering photogrammetric point clouds using standard lidar filters towards DTM generation. *ISPRS Annals of the Photogrammetry, Remote Sensing and Spatial Information Sciences* IV-2:319–326.
- Zhao, X. Q., Q. H. Guo, Y. J. Su and B. L. Xue. 2016. Improved progressive TIN densification filtering algorithm for airborne LiDAR data in forested areas. *ISPRS Journal of Photogrammetry and Remote Sensing* 117:79–91.

# SUSTAINING MEMBERS

## **Aerial Services, Inc.**

Cedar Falls, Iowa  
www.AerialServicesInc.com  
Member Since: 5/2001

## **Ayres Associates**

Madison, Wisconsin  
www.AyresAssociates.com  
Member Since: 1/1953

## **Cardinal Systems, LLC**

Flagler Beach, Florida  
www.cardinalsystems.net  
Member Since: 1/2001

## **Dewberry**

Fairfax, Virginia  
www.dewberry.com  
Member Since: 1/1985

## **Esri**

Redlands, California  
www.esri.com  
Member Since: 1/1987

## **F.R. Aleman & Associates, Inc.**

Miami, Florida  
https://fr-aleman.com  
Member Since: 7/2020

## **GeoCue Group**

Madison, Alabama  
http://www.geocue.com  
Member Since: 10/2003

## **Geographic Imperatives LLC**

Centennial, Colorado  
http://geographicimperativesllc.com  
Member Since: 9/2021

## **GeoWing Mapping, Inc.**

Richmond, California  
www.geowingmapping.com  
Member Since: 12/2016

## **GPI Geospatial Inc.**

formerly Aerial Cartographics of America, Inc. (ACA)  
Orlando, Florida  
www.aca-net.com  
Member Since: 10/1994

## **Green Grid Inc.**

San Ramon, California  
www.greengridinc.com  
Member Since: 1/2020

## **Half Associates, Inc.**

Richardson, Texas  
www.half.com  
Member Since: 8/2021

## **Keystone Aerial Surveys, Inc.**

Philadelphia, Pennsylvania  
www.kasurveys.com  
Member Since: 1/1985

## **Kucera International**

Willoughby, Ohio  
www.kucerainternational.com  
Member Since: 1/1992

## **L3Harris Corporation**

Broomfield, Colorado  
www.harris.com  
Member Since: 6/2008

## **Pickett and Associates, Inc.**

Bartow, Florida  
www.pickettusa.com  
Member Since: 4/2007

## **Quantum Spatial, Inc.**

Sheboygan Falls, Wisconsin  
www.quantumspatial.com  
Member Since: 1/1974

## **Sanborn Map Company**

Colorado Springs, Colorado  
www.sanborn.com  
Member Since: 10/1984

## **Surveying And Mapping, LLC (SAM)**

Austin, Texas  
www.sam.biz  
Member Since: 12/2005

## **T3 Global Strategies, Inc.**

Bridgeville, Pennsylvania  
https://t3gs.com/  
Member Since: 6/2020

## **Teledyne Optech**

Vaughan, Ontario, Canada  
TeledyneOptech.com  
Member Since: 12/2020

## **Terra Remote Sensing (USA) Inc.**

Bellevue, Washington  
www.terraremove.com  
Member Since: 11/2016

## **Towill, Inc.**

San Francisco, California  
www.towill.com  
Member Since: 1/1952

## **Wingtra**

Zurich, Switzerland  
https://wingtra.com/  
Member Since: 6/2020

## **Woolpert LLP**

Dayton, Ohio  
www.woolpert.com  
Member Since: 1/1985

# SUSTAINING MEMBER BENEFITS

## **Membership**

- ✓ Provides a means for dissemination of new information
- ✓ Encourages an exchange of ideas and communication
- ✓ Offers prime exposure for companies

## **Benefits of an ASPRS Membership**

- Complimentary and discounted Employee Membership\*
- E-mail blast to full ASPRS membership per year\*
- Professional Certification Application fee discount for any employee
- Discounts on *PE&RS* Classified Ad
- Member price for ASPRS publications
- Discount on group registration to ASPRS virtual conferences
- Sustaining Member company listing in ASPRS directory/website
- Hot link to company website from Sustaining Member company listing page on ASPRS website
- Press Release Priority Listing in *PE&RS* Industry News
- Priority publishing of Highlight Articles in *PE&RS* plus, 20% discount off cover fee, one per year
- Discount on *PE&RS* full-page advertisement
- Exhibit discounts at ASPRS sponsored conferences (exception ASPRS/ILMF)
- Free training webinar registrations per year\*
- Discount on additional training webinar registrations for employees
- Discount for each new SMC member brought on board (Discount for first year only)

\*quantity depends on membership level

# 2019-2020 PE&RS Reviewers

Thank you to all of the people who make *PE&RS* possible.

Ahmed Abdelhafiz	Min Chen	Norbert Haala
Amr Abd-Elrahman	Wei Chen	Isabel Haase
Elisabeth A. Addink	Yanming Chen	Christian Heipke
Athos Agapiou	Yimin Chen	Erin L Hestir
Davood Akbarl	Gui Cheng	Benjamin W. Heumann
Devrim Akça	Jacky Chow	Joshua Hollick
Perpetual Akwensi	Jinkui Chu	Gang Hong
Ugur Alganci	Cary Cox	Eija Honkavaara
Amin Alizadeh Naeini	Sophie Crommelinck	Weizhen Hou
Shrinidhi Ambinakudige	Davide Cucci	Bin Hu
Ru An	Nusret Demir	Han Hu
Katharina Anders	Ashraf Dewan	Wenjiang Huang
Itiya Aneece	Kaichang Di	Xiao Huang
Gary Atkinson	Lin Ding	Xin Huang
Reza Attarzadeh	Cenk Donmez	Yao Huang
Ugur AVDAN	Diogo Duarte	Yuchun Huang
Ebrahim Babaeian	Oussama Ennafii	Ming-Chih Hung
Krzysztof Bakula	Mustafa Tolga Esetlili	Md Enamul Huq
Gabor Barsai	Ruyi Feng	Md. Enamul Huq
Alexander Becker	Sagi Filin	Jungho Im
Suha Berberoglu	Juan J. Flores	Salahuddin M. Jaber
Ksenia Bittner	Giles Foody	Karsten Jacobsen
Andrew J. Brenner	Heide Friedrich	C. Jeganathan
Meredith Guenevere Longshore Brown	Peng Fu	Wanshou Jiang
Dimitri Bulatov	Tung Fung	Yonghua Jiang
Eric Bullock	Wenxia Gan	Jaehoon Jung
Olivier Burggraaff	Xun Geng	Kaan Kalkan
Robert Burtch	Zan Gojic	Anna Krzyszowska Waitkus
Gurcan Buyuksalih	Valerie Gouet-Brunet	D. Nagesh Kumar
Cai Cai	Wojciech Gruszczyński	Arnaud Le Bris
Michael J. Campbell	Jianyu Gu	Hugo Ledoux
Yanpeng Cao	Haiyan Guan	Ville Lehtola
Laurent Caraffa	Murali Krishna Gumma	Titus Leistner
Ting On Chan	Qinghua Guo	Laman Lelegard
Huijun Chen	Xian Guo	Chang LI
Min Chen	Barry N Haack	Guoyuan Li

Huapeng Li	Kyle T. Peterson	Manning Wang
Jianjun Li	Rongjun Qin	Qiang Wang
Jiayi Li	Munshi Khaled Rahman	Qunming Wang
Peijun Li	Shahinoor Rahman	Xinyu Wang
Peng Li	Nathir Rawashdeh	Zhongyuan Wang
Qinghua Li	Cristina Re	Zongyue Wang
Xiaodong Li	Wenyi Ren	Lukas Winiwarter
Dong Lin	Megan Ritelli	Bo Wu
Xiao Ling	Dora Roque	Hongan Wu
Bin Liu	Ewelina Rupnik	Taixia Wu
Chong Liu	Stefania Russo	Shaobo Xia
Chong Liu	Nayyer Saleem	Linfu Xie
Chong Liu	Stefan Schmohl	Mingming Xu
Shijie Liu	Forrest Schoessow	Xiong Xu
Shishi Liu	Elif Sertel	Zhijia Xu
Siyuan Liu	Mozhdeh Shahbazi	Lei Yan
Wai Chung Liu	Zhenfeng Shao	Bo Yang
Wei Liu	Zhanfeng Shen	Honglei Yang
Tengfei Long	Qian Shi	Nan Yang
Sietse Los	Peter Tian-Yuan Shih	Wei Yao
Bing Lu	Yosio Shimabukuro	Qian Yu
Zhumin Lu	Ramesh Sivanpillai	Li Yuan
Hui Luan	Huihui Song	Han Zhai
Neema Nicodemus Lyimo	Kaishan Song	Caiyun Zhang
Alina Elisabeth Maas	Xiaogang Song	Chunmin Zhang
Mason Maimaitijiang	Alfred Stein	Hongping Zhang
Mathew Maimaitiyiming	Corinne Stucker	Hongsheng Zhang
Kenneth Marr	Yanjun Su	Ka Zhang
Helmut Mayer	Neema S S Sumari	Kui Zhang
James Timothy McClinton	Kaimin Sun	Lei Zhang
Jochen Meidow	Qian Sun	Liangpei Zhang
Zhiguo Meng	Weiwei Sun	Liqiang Zhang
Slawomir Wojciech Mikrut	Xiaobing Sun	Qi Zhang
Charity Mundava	Zhongqiu Sun	Ruiqian Zhang
Yaw Danquah Twumasi Nana	Fayez Tarsha Kurdi	Su Zhang
Paolo Neri	Liqiao Tian	Yongjun Zhang
Ali Ozgun Ok	Hüseyin Topan	Jiangsan Zhao
Adam Oliphant	Yu-Hsuan Tu	Kaichun Zhao
Mohammad Omidalizarandi	Ava Vali	Yongqiang Zhao
Coskun Ozkan	John van Genderen	Cheng Zhong
Jens-André Paffenholz	Bo Wang	Ji Zhou
Spiros Pagiatakis	Chisheng Wang	Mei Zhou
Sidike Paheding	Cuizhen Wang	Weixun Zhou
Hongbo Pan	Di Wang	Yan Zhou
Jiayi Pan	Guoquan Wang	Yilin Zhou
Claudia Paris	Hui Wang	Xiaolin Zhu
Charlotte Pelletier	Lei Wang	Nataliya Zubko

# PE&RS Media Kit 2021

## Special Advertising Opportunities

### FRONT COVER SPONSORSHIP

A *PE&RS* cover sponsorship is a unique opportunity to capture the undivided attention of your target market through three premium points of contact.

#### 1— *PE&RS* FRONT COVER

(Only twelve available, first-come, first-served)

*PE&RS* is world-renowned for the outstanding imagery displayed monthly on its front cover—and readers have told us they eagerly anticipate every issue. This is a premium opportunity for any company, government agency, university or non-profit organization to provide a strong image that demonstrates their expertise in the geospatial information industry.

#### 2— FREE ACCOMPANYING “HIGHLIGHT” ARTICLE

A detailed article to enhance your cover image is welcome but not a condition of placing an image. Many readers have asked for more information about the covers and your article is a highly visible way to tell your story in more depth for an audience keenly interested in your products and services. No article is guaranteed publication, as it must pass ASPRS editorial review. For more information, contact Rae Kelley at rkelley@asprs.org.

#### 3— FREE TABLE OF CONTENTS COVER DESCRIPTION

Use this highly visible position to showcase your organization by featuring highlights of the technology used in capturing the front cover imagery. Limit 200-word description.

**Terms:** Fifty percent nonrefundable deposit with space reservation and payment of balance on or before materials closing deadline.

Cover Specifications:

**Bleed size:** 8 5/8" × 11 1/4" Trim: 8 3/8" × 10 7/8"

Offprints of the cover, Table of Contents page, and highlight article are available at the time of publication. These must be ordered and paid for in advance.

For front cover offprints or other quantities, contact Rae Kelley, ASPRS Assistant Director – Publications 505-819-3599 e-mail rkelley@asprs.org.

### PRICING

	Corporate Member Exhibiting at a 2021 ASPRS Conference	Corporate Member	Exhibitor	Non Member
Cover 1	\$1,850	\$2,000	\$2,350	\$2,500

### Belly Bands, Inserts, Outserts & More!

Make your material the first impression readers have when they get their copy of *PE&RS*. Contact Bill Spilman at bill@innovativemediasolutions.com

### VENDOR SEMINARS

ASPRS Sustaining Members now have the opportunity to hold a 1-hour informational session as a Virtual Vendor Seminar that will be free to all ASPRS Members wishing to attend. There will be one opportunity per month to reach out to all ASPRS Members with a demonstration of a new product, service, or other information. ASPRS will promote the Seminar through a blast email to all members, a notice on the ASPRS web site home page, and ads in the print and digital editions of *PE&RS*.

The Virtual Seminar will be hosted by ASPRS through its Zoom capability and has the capacity to accommodate 500 attendees.

Vendor Seminars	
Fee	\$2,500 (no discounts)

### EMPLOYMENT PROMOTION

When you need to fill a position right away, use this direct, right-to-the-desktop approach to announce your employment opportunity. The employment opportunity will be sent once to all ASPRS members in our regular Wednesday email newsletter to members, and will be posted on the ASPRS Web site for one month. This type of advertising gets results when you provide a web link with your text.

Employment Opportunity	Net Rate
30-Day Web + 1 email	\$500/opportunity
Web-only (no email)	\$300/opportunity

*Do you have multiple vacancies that need to be filled? Contact us for pricing details for multiple listings.*

### NEWSLETTER DISPLAY ADVERTISING

Your vertical ad will show up in the right hand column of our weekly newsletter, which is sent to more than 3,000 people, including our membership and interested parties. **Open Rate: 32.9%**

Newsletter vertical banner ad	Net Rate
180 pixels x 240 pixels max	\$500/opportunity

## PE&RS Digital Edition

### Digital Edition E-mail Blast: 5,800+

*PE&RS* is available online in both a public version that is available to anyone but does not include the peer-reviewed articles, and a full version that is available to ASPRS members only upon login.

The enhanced version of *PE&RS* contains hot links for all ASPRS Sustaining Member Companies, as well as hot links on advertisements, ASPRS Who's Who, and internet references.

### Become a sponsor today!

The e-mail blast sponsorship opportunity includes a **180 x 240 pixel ad** in the email announcement that goes out to our membership announcing the availability of the electronic issue.

Digital Edition Opportunities	Net Rate
E-mail Blast Sponsorship*	\$1,000

For more information, contact Bill Spilman at bill@innovativemediasolutions.com | (877) 878-3260 toll-free | (309) 483-6467 direct | (309) 483-2371 fax

## PE&RS 2021 Advertising Rates & Specs

**THE MORE YOU ADVERTISE THE MORE YOU SAVE!** PE&RS offers frequency discounts. Invest in a three-times per year advertising package and receive a 5% discount, six-times per year and receive a 10% discount, 12-times per year and receive a 15% discount off the cost of the package.

	Corporate Member Exhibiting at a 2021 ASPRS Conference	Corporate Member	Exhibitor	Non Member
<i>All rates below are for four-color advertisements</i>				
Cover 1	\$1,850	\$2,000	\$2,350	\$2,500
<i>In addition to the cover image, the cover sponsor receives a half-page area to include a description of the cover (maximum 500 words). The cover sponsor also has the opportunity to write a highlight article for the journal. Highlight articles are scientific articles designed to appeal to a broad audience and are subject to editorial review before publishing. The cover sponsor fee includes 50 copies of the journal for distribution to their clients. More copies can be ordered at cost.</i>				
Cover 2	\$1,500	\$1,850	\$2,000	\$2,350
Cover 3	\$1,500	\$1,850	\$2,000	\$2,350
Cover 4	\$1,850	\$2,000	\$2,350	\$2,500
Advertorial	1 Complimentary Per Year	1 Complimentary Per Year	\$2,150	\$2,500
Full Page	\$1,000	\$1,175	\$2,000	\$2,350
2 page spread	\$1,500	\$1,800	\$3,200	\$3,600
2/3 Page	\$1,100	\$1,160	\$1,450	\$1,450
1/2 Page	\$900	\$960	\$1,200	\$1,200
1/3 Page	\$800	\$800	\$1,000	\$1,000
1/4 Page	\$600	\$600	\$750	\$750
1/6 Page	\$400	\$400	\$500	\$500
1/8 Page	\$200	\$200	\$250	\$250
Other Advertising Opportunities				
Wednesday Member Newsletter Email Blast	1 Complimentary Per Year	1 Complimentary Per Year	\$600	\$600

A 15% commission is allowed to recognized advertising agencies

Ad Size	Width	Height
Cover (bleed only)	8.625"	11.25"
Full Page (bleed)	8.625"	11.25"
Full Page (trim)	8.375"	10.875"
2/3 Page Horizontal	7.125"	6.25"
2/3 Page Vertical	4.58"	9.625"
1/2 Page Horizontal	7.125"	4.6875"
1/2 Page Vertical	3.4375"	9.625"
1/3 Page Horizontal	7.125"	3.125"
1/3 Page Vertical	2.29"	9.625"
1/4 Page Horizontal	7.125"	2.34"
1/4 Page Vertical	3.4375"	4.6875"
1/8 Page Horizontal	7.125"	1.17"
1/8 Page Vertical	1.71875"	4.6875"

- Publication Size: 8.375" × 10.875" (W x H)
- Live area: 1/2" from gutter and 3/8" from all other edges
- No partial page bleeds.
- Publication Style: Perfect bound
- Printing Method: Web offset press
- Software Used: PC InDesign CS6
- Supported formats: TIFF, EPS, BMP, JPEG, PDF, PC InDesign, Illustrator, and Photoshop

Source: PE&RS Readership Survey, Summer 2017

For more information, contact Bill Spilman at bill@innovativemediasolutions.com | (877) 878-3260 toll-free | (309) 483-6467 direct | (309) 483-2371 fax

**Send ad materials to:**  
 ASPRS/PE&RS Production  
 425 Barlow Place, Suite 210  
 Bethesda, Maryland 20814  
 505-819-3599  
 rkelly@asprs.org

**Ship inserts to:**  
 Alicia Coard  
 Walsworth  
 2180 Maiden Lane  
 St. Joseph, MI 49085  
 888-563-3220 (toll free)  
 269-428-1021 (direct)  
 269-428-1095 (fax)  
 alicia.coard@walsworth.com

# Digital Elevation Model Technologies and Applications: The DEM Users Manual, 3<sup>rd</sup> Edition

Edited by David F. Maune, PhD, CP  
and Amar Nayegandhi, CP, CMS

To order, visit  
<https://www.asprs.org/dem>

The 3rd edition of the DEM Users Manual includes 15 chapters and three appendices. References in the eBook version are hyperlinked. Chapter and appendix titles include:

1. Introduction to DEMs  
*David F. Maune, Hans Karl Heidemann, Stephen M. Kopp, and Clayton A. Crawford*
  2. Vertical Datums  
*Dru Smith*
  3. Standards, Guidelines & Specifications  
*David F. Maune*
  4. The National Elevation Dataset (NED)  
*Dean B. Gesch, Gayla A. Evans, Michael J. Oimoen, and Samantha T. Arundel*
  5. The 3D Elevation Program (3DEP)  
*Jason M. Stoker, Vicki Lukas, Allyson L. Jason, Diane F. Eldridge, and Larry J. Sugarbaker*
  6. Photogrammetry  
*J. Chris McGlone and Scott Arko*
  7. IfSAR  
*Scott Hensley and Lorraine Tighe*
  8. Airborne Topographic Lidar  
*Amar Nayegandhi and Joshua Nimetz*
  9. Lidar Data Processing  
*Joshua M. Novac*
  10. Airborne Lidar Bathymetry  
*Jennifer Wozencraft and Amar Nayegandhi*
  11. Sonar  
*Guy T. Noll and Douglas Lockhart*
  12. Enabling Technologies  
*Bruno M. Scherzinger, Joseph J. Hutton, and Mohamed M.R. Mostafa*
  13. DEM User Applications  
*David F. Maune*
  14. DEM User Requirements & Benefits  
*David F. Maune*
  15. Quality Assessment of Elevation Data  
*Jennifer Novac*
- Appendix A. Acronyms  
Appendix B. Definitions  
Appendix C. Sample Datasets

This book is your guide to 3D elevation technologies, products and applications. It will guide you through the inception and implementation of the U.S. Geological Survey's (USGS) 3D Elevation Program (3DEP) to provide not just bare earth DEMs, but a full suite of 3D elevation products using Quality Levels (QLs) that are standardized and consistent across the U.S. and territories. The 3DEP is based on the National Enhanced Elevation Assessment (NEEA) which evaluated 602 different mission-critical requirements for and benefits from enhanced elevation data of various QLs for 34 Federal agencies, all 50 states (with local and Tribal input), and 13 non-governmental organizations.

The NEEA documented the highest Return on Investment from QL2 lidar for the conterminous states, Hawaii and U.S. territories, and QL5 IfSAR for Alaska.

Chapters 3, 5, 8, 9, 13, 14, and 15 are "must-read" chapters for users and providers of topographic lidar data. Chapter 8 addresses linear mode, single photon and Geiger mode lidar technologies, and Chapter 10 addresses the latest in topobathymetric lidar. The remaining chapters are either relevant to all DEM technologies or address alternative technologies including photogrammetry, IfSAR, and sonar.

As demonstrated by the figures selected for the front cover of this manual, readers will recognize the editors' vision for the future – a 3D Nation that seamlessly merges topographic and bathymetric data from the tops of the mountains, beneath rivers and lakes, to the depths of the sea.

Co-Editors

David F. Maune, PhD, CP and  
Amar Nayegandhi, CP, CMS

---

## PRICING

Student (must submit copy of Student ID)	\$50 +S&H
ASPRS Member	\$80 +S&H
Non-member	\$100 +S&H
E-Book (only available in the Amazon Kindle store)	\$85

---

LEARN  
DO  
GIVE  
BELONG

**ASPRS Offers**

- » Cutting-edge conference programs
- » Professional development workshops
- » Accredited professional certifications
- » Scholarships and awards
- » Career advancing mentoring programs
- » *PE&RS*, the scientific journal of ASPRS

[asprs.org](http://asprs.org)

ASPRS